# Use of airborne hyperspectral data and height information to support urban micro climate characterisation

Dissertation zur Erlangung des
naturwissenschaftlichen Doktorgrades
der Bayerischen Julius-Maximilians-Universität Würzburg

Vorgelegt von

Wieke Heldens

# Abstract

The urban micro climate has been increasingly recognised as an important aspect for urban planning. Therefore, urban planners need reliable information on the micro climatic characteristics of the urban environment. A suitable spatial scale and large spatial coverage are important requirements for such information.

This thesis presents a conceptual framework for the use of airborne hyperspectral data to support urban micro climate characterisation, taking into account the information needs of urban planning. The potential of hyperspectral remote sensing in characterising the micro climate is demonstrated and evaluated by applying HyMap airborne hyperspectral and height data to a case study of the German city of Munich.

The developed conceptual framework consists of three parts. The first is concerned with the capabilities of airborne hyperspectral remote sensing to map physical urban characteristics. The high spatial resolution of the sensor allows to separate the relatively small urban objects. The high spectral resolution enables the identification of the large range of surface materials that are used in an urban area at up to sub-pixel level. The surface materials are representative for the urban objects of which the urban landscape is composed. These spatial urban characteristics strongly influence the urban micro climate.

The second part of the conceptual framework provides an approach to use the hyperspectral surface information for the characterisation of the urban micro climate. This can be achieved by integrating the remote sensing material map into a micro climate model. Also spatial indicators were found to provide useful information on the micro climate for urban planners. They are commonly used in urban planning to describe building blocks and are related to several micro climatic parameters such as temperature and humidity.

The third part of the conceptual framework addresses the combination and presentation of the derived indicators and simulation results under consideration of the planning requirements. Building blocks and urban structural types were found to be an adequate means to group and present the derived information for micro climate related questions to urban planners.

The conceptual framework was successfully applied to a case study in Munich. Airborne hyperspectral HyMap data has been used to derive a material map at sub-pixel level by multiple endmember linear spectral unmixing. This technique was developed by the German Research Centre for Geosciences (GFZ) for applications in Dresden and Potsdam. A priori information on building locations was used to support the separation between spectrally similar materials used both on building roofs and non-built surfaces. In addition, surface albedo and leaf area index are derived from the HyMap data. The sub-pixel material map supported by object height data is then used to derive spatial indicators, such as imperviousness or building density. To provide a more detailed micro climate characterisation at building block level, the surface materials, albedo, leaf area index (LAI) and object height are used as input for simulations with the micro climate model ENVI-met.

The identification of 31 surface materials represented the urban objects and their structure in Munich very well. The unmixing approach could be transferred successfully to the Munich region and a large number of flight lines because of the high level of automatisation of the algorithm. The material abundances could be identified with a mean absolute error of 2.2 % per building block and 16 % per cluster of 3x3 pixels (average of all classes). The use and quality of a priori knowledge on building locations was found to be one of the most important factors influencing the accuracy.

The surface albedo and leaf area index could also be derived with sufficient accuracy to be used as input for the ENVI-met model. The albedo is strongly influenced by illumination effects resulting from sensor viewing angle and object orientation. The estimation of the leaf area index has to be carried out with care in urban areas, amongst others because of the high number of mixed pixels.

The spatial indicators building density, vegetation density, imperviousness, building volume, vegetation volume and dominant roof material were calculated with an absolute mean error of less than 5 %. This is an improvement in comparison to the accuracy of the spatial indicators currently used by the municipality of Munich of around 5 %. For the various urban structural types, typical ranges of the spatial indicators could be identified.

The ENVI-met model was used to simulate the micro climate for 95 building blocks in 16 areas of 400 x 400 m$^2$. Based on the sub-pixel material map, height data, albedo and leaf area index values, the input data for the simulation of the micro climate in these areas could be generated without interactive steps, saving tedious manual editing. The sub-pixel information of the material map helped to solve small co-registration errors between hyperspectral and height data during the generation of the input data for the model. Areas of interest could thus be represented realistically in the micro climate simulation environment. A general limitation of remote sensing data for this application is that tree crows obscure streets and buildings, especially in detached and semi-detached housing areas.

Two approaches were demonstrated to analyse the micro climate simulation results in combination with the spatial indicators, allowing the characterisation of the micro climate for urban structural types.

Concluding, this thesis demonstrated the potential of hyperspectral remote sensing to support urban micro climate characterisation. A detailed mapping of surface materials at sub-pixel level could be performed. This provides valuable, detailed information on a large range of spatial characteristics relevant to the assessment of the urban micro climate.

The developed conceptual framework has been proven to be applicable to the case study, providing a means to characterise the urban micro climate. The remote sensing products and subsequent micro climatic information are presented at a suitable spatial scale and in understandable maps and graphics. The use of well-known spatial indicators and the framework of urban structural types can simplify the communication with urban planners on the findings on the micro climate.

Further research is needed primarily on the sensitivity of the micro climate model towards the remote sensing based input parameters and on the general relation between climate parameters and spatial indicators by comparison with other cities.

# Zusammenfassung

Für die Stadtplanung werden klimatische Aspekte zunehmend wichtiger, weil die Klimaveränderung besonders in Städten die Lebensqualität beeinflussen kann. Hierfür benötigen Stadtplaner detaillierte Basis-Informationen über die mikroklimatischen Eigenschaften des urbanen Gebietes. Dabei sind ein ausreichend detaillierter Maßstab sowie eine großflächige Abdeckung wichtige Voraussetzungen.

Das Ziel dieser Dissertation ist die Entwicklung und Anwendung von einem konzeptionellen Rahmenwerk, wie räumlich und spektral höchst aufgelöste Fernerkundungsdaten zur stadtklimatischen Charakterisierung verwendet werden können. Hierbei sollten die Anforderungen der Stadtplaner berücksichtigt werden. Zusätzliches Ziel ist das Potenzial dieser sog. hyperspektralen Fernerkundung zur Charakterisierung des Mikroklimas zu demonstrieren. Dazu wird das konzeptionelle Rahmenwerk an Hand des Fallbeispiels der Stadt München unter Verwendung von HyMap-Daten angewendet und evaluiert.

Das entwickelte Rahmenwerk besteht aus drei Teilen: Der erste Teil beschreibt, wie relevante Parameter aus Daten eines flugzeuggetragenen Hyperspektralsensors abgeleitet werden können. Die hohe räumliche and spektrale Auflösung dieser Daten ermöglicht es, für die heterogene urbane Landschaft Oberflächenmaterialien auf Subpixel-niveau zu kartieren. Diese Oberflächenmaterialien sind wiederum repräsentativ für urbane Objekte, aus welchen die urbane Landschaft zusammengesetzt ist. Das Mikroklima wird stark durch diese räumlichen Merkmale der Stadt beeinflusst.

Der zweite Teil des Konzepts beschreibt einen Ansatz, wie hyperspektrale Datenprodukte für die Charakterisierung des Mikroklimas angewendet werden können. Dies wird primär durch die Integration von thematischen Produkten (insbesondere die erwähnte Oberflächenmaterialkarte) in ein Mirkoklima-Simulationsmodell erreicht. Zusätzlich haben sich räumliche Indikatoren als hilfreich erwiesen, um Stadtplanern Informationen zu mikroklimatischen Eigenschaften bereitzustellen.

Im dritten Teil des Rahmenwerkes wird angesprochen wie unter Berücksichtigung der Anforderungen der Stadtplaner die abgeleiteten Indikatoren und Klimasimulationen kombiniert und aufbereitet werden können. Hierzu stellte sich die Einteilung der abgeleiteten Datenprodukte nach Stadtstrukturtypen als geeignet heraus. Stadtstrukturtypen basieren auf physischen Indikatoren wie Dichte, Typ und Konfiguration der Bebauung eines Baublocks, und lassen Rückschlusse auf sozio-ökonomische und klimatologische Eigenschaften zu.

Dieses Rahmenwerk wurde für das konkrete Fallbeispiel der Stadt München erfolgreich angewendet. Daten des flugzeuggetragenen HyMap-Hyperspektralsensors wurden verwendet, um die Subpixel-Materialkarten abzuleiten. Mittels einer *multiple endmember spectral mixture analyis*, welche durch das Deutschen GeoForschungszentrum (GFZ) für Anwendungen in Dresden und Potsdam entwickelt wurde, können die Oberflächenmaterialen abgeleitet werden. Zur Verbesserung des Produkts wurden zusätzlich a-priori-Informationen zu den Gebäu-

destandorten integriert, um die Unterscheidung von Gebäudedächern und Freiflächen mit spektral ähnlichen Materialien zu unterstützen. Die resultierende Subpixel-Materialkarte ist das Schlüsselprodukt für den entwickelten Ansatz. Als ein weiters Produkt wurden Albedo und Blattflächenindex aus den Hyperspektraldaten abgeleitet. Im nächsten Schritt wurde die Subpixel-Materialkarte mit den Höhendaten kombiniert und daraus räumliche Indikatoren wie Versiegelungsgrad oder Bebauungsdichte abgeleitet. Solche Indikatoren werden in der Stadtplanung häufig verwendet, um Baublöcke zu charakterisieren. Zusätzlich besteht ein Zusammenhang zwischen diesen Indikatoren und verschiedenen stadtklimatischen Parametern wie der Temperatur oder der Luftfeuchte. Für eine detaillierte Charakterisierung des Mikroklimas innerhalb eines Baublocks wurden die Fernerkundungsprodukte (Oberflächenmaterial, Albedo, Blattflächenindex und Höhendaten) als Inputdaten für das Mikroklimamodell ENVI-met verwendet.

Die Ergebnisse der spektralen Entmischung zeigen, dass mit den 31 identifizierten Materialien die städtischen Objekten und Strukturen in München sehr gut wiedergegeben werden konnten. Der Entmischungsalgorithmus konnte durch einen hohen Grad an Automatisierung erfolgreich auf das Testgebiet München sowie eine großen Anzahl an Flugstreifen übertragen werden. Die Flächenanteile der Materialien konnten mit einem mittleren absoluten Fehler von 2,2 % Flächenanteil per Baublock und 15 % Flächenanteil per Cluster von 3x3 Pixels abgeschätzt werden (Mittelwert für alle Materialien). Die Verwendung und Qualität der Gebäudestandorte wurde als einer der einflussreichsten Faktoren für die Genauigkeit der Materialkarte identifiziert.

Die Albedo und der Blattflächenindex konnten mit ausreichender Genauigkeit für die Verwendung im Mikroklimamodell abgeleitet werden. Die Albedo ist stark beeinflusst von Beleuchtungseffekten bedingt durch den Blickwinkel des Sensors und die räumliche Orientierung der Objekte. Kritisch ist die Ableitung des Blattflächenindex in urbanen Gebieten aufgrund der hohen Anzahl an Mischpixel.

Die räumlichen Indikatoren Bebauungsgrad, Grünanteil, Versiegelungsgrad, Bauvolumen, Grünvolumen und dominantes Dachmaterial konnten mit einem mittleren absoluten Fehler von unter 10 % berechnet werden. Damit ist die Genauigkeit besser als die derzeit von der Stadt München verwendeten Datensätze zu Versiegelungsgrad, Bebauungsgrad und Grünanteil. Auch konnten charakteristische Werte dieser Indikatoren für die verschiedenen Stadtstrukturtypen festgestellt werden.

Für die Simulation des Mikroklimas für 95 Baublöcke in 16 Testgebiete von 400 x 400 m$^2$ wurde das ENVI-met Modell verwendet. Die Inputdaten für die Simulationen wurden ohne interaktive Schritte direkt aus den hyperspektralen Fernerkundungsprodukten und den Höhendaten abgeleitet, wodurch aufwändige manuelle Editierungen vermieden wurden. Durch die Subpixel-Information der Materialkarte konnten kleinere Fehler in der Ko-Registrierung zwischen den Hyperspektralprodukten und den Höhendaten behoben werden. Somit können die Testgebiete in der Simulationsumgebung realistisch dargestellt werden. Allerdings existiert eine generelle Limitierung von Fernerkundungsdaten in der Beschattung von Straßen und Gebäuden durch Baumkronen, was insbesondere in Gebieten mit hohem Vegetationsanteil deutlich wird (z.B. in Einzel- und Doppelhausbebauungen).

Mit zwei beispielhaften Ansätzen für eine synergetische Analyse der räumlichen Indikatoren und der Ergebnisse der Mikroklimasimulation konnten die typischen Unterschiede zwischen

den verschiedene Stadtstrukturtypen, sowohl in Bezug auf deren räumliche als auch klimatische Merkmale demonstriert werden.

Zusammenfassend demonstriert diese Dissertation das Potenzial der hyperspektralen Fernerkundung zur Unterstützung von Mikroklima-Charakterisierung. Oberflächenmaterialien konnten hierfür thematisch detailliert bis auf sub-Pixel Level identifiziert werden. Mit den erzeugten hyperspektralen Fernerkundungsprodukten konnte eine detaillierte Beschreibung der relevanten räumlichen Merkmale erzielt werden, welche von großer Relevanz für die Bewertung des städtischen Mikroklimas sind.

Das entwickelte konzeptionelle Rahmenwerk hat sich für das Fallbeispiel als sehr geeignet erwiesen. Es ermöglichte die Charakterisierung des städtischen Mikroklima auf Basis des ENVI-met Modells. Die Fernerkundungsprodukte und die darauf basierenden Mikroklima-Informationen wurden mit einem geeigneten räumlichen Maßstab und als intuitiv verständliche Karten und Abbildungen dargestellt. Die Verwendung allgemein bekannter räumlicher Indikatoren und das Klassifikationsschema nach Stadtstrukturtypen vereinfachen die Kommunikation mit Stadtplanern über die stadtklimatischen Erkenntnisse.

Weitere Forschungsschritte sind unter anderem notwendig um die Sensitivität des Mikroklimamodells gegenüber den fernerkundungsbasierten Inputparametern genauer zu charakterisieren und um die allgemeine Beziehungen zwischen Klimaparametern und räumlichen Indikatoren durch den Vergleich mit weiteren Städten näher zu untersuchen.

# Samenvatting

Het microklimaat speelt een steeds belangrijker rol in de stedelijke planvorming. Om dit aspect in de ruimtelijke plannen op te nemen hebben planologen informatie nodig over de microklimatologische eigenschappen van het stedelijk gebied. Die informatie moet op een passende ruimtelijke schaal en gebiedsdekkend voor een regio beschikbaar zijn. In dit proefschrift wordt een conceptuele benadering beschreven voor de toepassing van hyperspectrale aardobservatie ter ondersteuning van de karakterisering van het stedelijke microklimaat. De mogelijkheden van hyperspectrale aardobservatie worden gedemonstreerd en geëvalueerd door de toepassing van beelden van de HyMap-sensor aan boord van een vliegtuig, ondersteund door hoogtegegevens, voor een case study in de stad München, Duitsland.

De ontwikkelde conceptuele benadering bestaat uit drie delen. Het eerste deel gaat over de mogelijkheden van hyperspectrale aardobservatie vanuit vliegtuigen om stedelijke eigenschappen te karteren. Deze observaties leveren beelden met een hoge ruimtelijke en spectrale resolutie. Daarmee kunnen de oppervlaktematerialen waaruit het heterogene stedelijke landschap is opgebouwd tot op sub-pixelniveau worden weergegeven. Deze oppervlaktematerialen zijn kenmerkend voor de objecten (gebouwen, bomen, straten, etc.) in de stad die samen het stedelijke landschap vormen. Deze objecten hebben grote invloed op het stedelijk microklimaat. Het tweede deel van de conceptuele benadering beschrijft hoe de uit hyperspectrale beelden afgeleide producten kunnen worden gebruikt om het stedelijke microklimaat te karakteriseren. De producten (o.a. een materiaalkaart) worden gebruikt om de inputparameters voor een microklimaatmodel te definiëren. Ook worden ruimtelijke indicatoren afgeleid. De focus van het derde deel van de conceptuele benadering is het geschikt maken van de afgeleide microklimatologisch relevante informatie voor gebruik in de stedelijke planning. Hiervoor blijken de presentatie van de informatie op bouwblokniveau en de indeling van de resultaten naar stedelijke structuurtypen zeer geschikt.

De ontwikkelde conceptuele benadering is met succes toegepast op een case study in München. De HyMap-beelden zijn gebruikt om een materiaalkaart op sub-pixelniveau te generen door middel van multi-endmember lineare spectrale ontmenging, ontwikkeld door het Duitse Onderzoekscentrum voor Geoinformatie (GFZ) voor de steden Dresden en Potsdam. Om spectraal vergelijkbare materialen op daken en onbebouwde gebieden beter te kunnen onderscheiden is uit andere bronnen bekende (a priori) informatie over de locaties van de gebouwen gebruikt. Verder zijn uit de hyperspectrale beelden de albedo en de bladoppervlakte-index berekend, twee belangrijke parameters voor het microklimaatmodel. In de volgende stap zijn op basis van de materiaalkaart de ruimtelijke indicatoren (zoals bebouwingsdichtheid en bouwvolume) berekend, ondersteund door de hoogtegegevens. Zulke indicatoren worden in de stedelijke planning vaak gebruikt om eigenschappen van bouwblokken te beschrijven. Bovendien bestaat er een relatie tussen deze indicatoren en verschillende klimaatparameters als temperatuur en luchtvochtigheid. Met de invoer van de materiaalkaart en albedo, bladopperlakteindex

en hoogtegegevens in het microklimaatmodel ENVI-met kon een meer gedetailleerde karakterisering van het stedelijk microklimaat worden gegeven.

De objecten en structuren in München konden goed worden weergegeven met de 31 materiaalklassen. Doordat de spectrale ontmengings-methode tot in hoge mate geautomatiseerd is, verliep de omzetting naar een andere stadt (München) en naar een groter gebied (252 km$^2$) soepel. De materiaalaandelen per pixel konden met een gemiddelde absolute afwijking van 2,2 % per bouwblok en 16 % per cluster van 3x3 pixels nauwkeurig gekarteerd worden (gemiddelde voor alle materialen). Het gebruik en de kwaliteit van de a priori informatie met betrekking tot de locaties van de gebouwen bleek de grootste invloed op de nauwkeurigheid van de materiaalkaart te hebben.

De albedo en de bladoppervlakte-index konden met voor het microklimaatmodel toereikende nauwkeurigheid worden afgeleid. Hierbij moet worden opgemerkt dat de albedo sterk beïnvloed wordt door belichtingseffecten als gevolg van de invalshoek van de sensor en de oriëntatie van gebouwen en andere objecten met betrekking tot de zon en de sensor. Bij het berekenen van de bladoppervlakte-index op basis van aardobservatiegegevens moet in stedelijke gebieden voorzichtig te werk worden gegaan, onder andere vanwege het grote aantal gemengde pixels.

De ruimtelijke indicatoren bebouwingsdichtheid, vegetatiedichtheid, bouwvolume, vegetatievolume, percentage ondoorlaatbare oppervlakte en dominant dakbedekkingsmateriaal konden met een absolute gemiddelde afwijking van minder dan 5 % worden berekend. Dat is een verbetering ten opzichte van de nauwkeurigheid van de kaarten met ruimtelijke indicatoren die thans bij de gemeente in München in gebruik zijn. Voor de verschillende stedelijke structuurtypen konden karakteristieke bereiken voor de waarden van de verschillende indicatoren worden waargenomen.

Met behulp van het model ENVI-met werd het microklimaat gesimuleerd voor 95 bouwblokken verdeeld over 16 testgebieden van 400 x 400 m$^2$. Deze testgebieden konden gedetailleerd en automatisch beschreven worden in het ENVI-met bestandsformaat op basis van de sub-pixel materiaalkaart, de hoogtegegevens, de albedo en de bladoppervlakte-index. Dit bespaard het tijdrovende handmatig invoeren van de beschrijving van het testgebied in ENVI-met. De sub-pixel informatie over de materialen kon worden gebruikt om kleine problemen met co-registratie te verhelpen, die hoofdzakelijk in gebieden met vrijstaande huizen optreden tussen de hyperspectrale beelden en de hoogtegegevens. Tests lieten zien dat de locatie van het bouwblok in kwestie binnen het testgebied een grote rol speelt voor de uitkomst van de simulatie in dat bouwblok.

In twee voorbeelden is getoond hoe de ruimtelijke indicatoren en de simulatieresultaten gezamenlijk geanalyseerd kunnen worden om het microklimaat in stadstructuurtypen te karakteriseren.

Concluderend: dit proefschrift demonstreert de mogelijkheden van hyperspectrale aardobservatie om de analyse van het stedelijke micoklimaat te ondersteunen. Er is een gedetailleerde kartering van landbedekkingsmaterialen op sub-pixel niveau uitgevoerd. Dit levert waardevolle informatie voor de beoordeling van het stedelijke microklimaat aan hand van een breed scala aan ruimtelijke kenmerken.

Het in dit proefschrift beschreven onderzoek laat zien dat de ontwikkelde conceptuele benadering toepasbaar is in een concrete situatie. Het verschaft nuttige informatie om het stedelijk

microklimaat te beschrijven. De aardobservatieproducten en de daaruit afgeleide informatie over het microklimaat kunnen op een voor de ruimtelijke ordening geschikte schaal worden gepresenteerd in begrijpelijke kaarten en afbeeldingen. Het gebruik van alom bekende ruimtelijke indicatoren en stedelijke structuurtypen kan de communicatie met planologen over de microklimatologische situatie in de stad vergemakkelijken.

Toekomstig onderzoek is vooral nodig naar de sensitiviteit van het microklimaatmodel voor de aardobservatieproducten die voor dat model als input worden gebruikt. Vergelijking van dit onderzoek met de resultaten van onderzoek in andere steden kan meer zicht geven op de meer algemene relatie tussen klimaatparameters en ruimtelijke indicatoren.

# Contents

# Contents

# List of Figures

# List of Tables

# 1 Introduction

According to prognostics on climate change, both mean temperatures and periods of heat will significantly increase during the coming years (Deutsche Meteorologische Gesellschaft, 2007). In 2008 the surface temperature and near surface temperature reached higher values than the long-time average in almost every month (Deutscher Wetterdienst, 2009). Urban areas have their own climate conditions that differ from rural areas, which results in typical urban phenomena such as urban heat islands. Therefore an increase of temperature in cities has to be feared, which will have even stronger negative effects e.g. on the quality of life or public health (Kuttler, 2004). Because of this, the urban micro climate gains increasing attention by German governments at a national scale and also at a local scale in urban and spatial planning departments (BMBF, 2009). Worldwide more than 50 % of the population lives in cities, in Germany this was even 73 % in 2005 (UN, 2007). The urban micro climate directly influences the well-being of this large and increasing number of inhabitants of the urban areas. With well-defined planning measures the micro climate can be improved or negative effects can be mitigated (Fehrenbach et al., 2001; Gómez et al., 2001). To define such measures urban planners need information on the micro climate situation in their city. However, the urban micro climate is not yet commonly considered during the processes of urban planning, which seems to be the result of a lack of suitable planning tools to protect the urban climate (Wende et al., 2009) and a sub-optimal communication among urban planners and climatologists (Eliasson, 2000; Oke, 2006). Information on the urban micro climate should be communicated to urban planners in a suitable form, e.g. as indicators or maps, which is often lacking (BRIDGE, 2009). Most information regarding the urban climate is available in point measurements which do not meet the area wide information need of urban planners. Simulation and modelling approaches can provide area wide information, but are mainly carried out on synthetic scenes. The acquisition of the input data for the simulation of existing areas in a city is very time consuming and usually requires extensive field surveys.

In order to derive spatial information with a large coverage, remote sensing is a powerful tool. Thermal remote sensing is commonly used for the analysis of surface temperature in the relation to urban climate (Weng, 2009). Especially regional phenomena such as the urban heat island are studied frequently. Surface temperature - which can be measured with thermal remote sensing - is an important climate parameter. However, for the assessment of the influence of the urban micro climate on the well-being of the inhabitants is the surface temperature alone not sufficient. Additional parameters such as air temperature and wind speed are essential for this. Therefore it is useful to map the spatial characteristics which influence the urban micro climate, e.g. land cover types or surface albedo. Such information can be used as input data for climate modelling (Arthur-Hartranfta et al., 2003; Pinty et al., 2006). When the spatial characteristics of the urban area are combined with measurements of climate parameters, relationships can be identified (Xian, 2008). Such relationships and models can help urban planners to gain insight in the influence of the urban area on the micro climate.

So far most studies that used remote sensing to support the analysis of urban climate focused

on a regional scale. Analysis of the micro climate, where small-scale effects of less than two kilometres play the most important role, requires detailed spatial and thematical information on the urban area. However, urban areas are a challenging environment for remote sensing based mapping. They are very heterogeneous: many small objects are located close to each other and there is a large variety of land cover types, e.g. the manifold of roofing materials. Airborne hyperspectral remote sensing has proven to be a useful tool in describing the urban land cover at a local scale (e.g. Ben-Dor et al., 2001; Heiden et al., 2007). It enables us to collect frequent and area wide data which can be analysed by (semi-)automatic image analysis procedures. Airborne hyperspectral data, e.g. recorded by the HyMap sensor, can reach a high spatial resolution of 2 - 10 m. This is required to identify the relatively small objects (Small, 2003). The large variety of urban materials can be identified using the high spectral resolution of the hyperspectral data (Herold et al., 2003a).

However, up until now only few studies where hyperspectral remote sensing has been used for urban micro climatic analysis have been recorded in literature. Xu et al. (2008) use airborne hyperspectral data to derive broad band albedo, vegetation fraction and land cover in five classes to model the urban sensible heat flux at multiple spatial scales. Jung et al. (2007) relate general land cover classes derived from hyperspectral data to surface temperature. Moreover, airborne hyperspectral data is able to derive not only general land cover classes but also detailed surface materials at sub-pixel level (Roessner et al., 2001), which is likely to be valuable information for urban micro climate characterisation.

The studies and initiatives mentioned above indicate that there is a demand for the characterisation of the micro climate for urban planning applications. Especially detailed spatial information about the urban area is required to support micro climate simulations. The possibilities of airborne hyperspectral remote sensing are promising though not fully explored yet. Therefore this thesis aims at the following two objectives:

- The development of a conceptual framework for the use of airborne hyperspectral data to support urban micro climate characterisation in a way which is suitable for urban planning.
- The demonstration and evaluation of the potential of hyperspectral remote sensing for micro climate characterisation by applying HyMap airborne hyperspectral and height data to a case study in the German city of Munich.

To meet the objectives this thesis focuses on the identification of surface material cover from airborne hyperspectral data, the optimisation and application of this remote sensing product for micro climate modelling and mapping of spatial indicators. The information needs and requirements of urban planners guide the definition of the conceptual framework, the remote sensing products and the selection of methods.

The conceptual framework is presented in chapter 2. In chapter 3 the backgrounds and state of the art of the three disciplines urban planning, urban micro climate studies and optical urban remote sensing are provided. The study area and available data are presented in chapter 4. Chapter 5 describes the methods and techniques which have been applied to implement the conceptual framework on the study area of Munich. The results are presented in chapter 6. In chapter 7, the results and the conceptual framework are discussed. Finally, in chapter 8 the findings regarding the conceptual framework and the potential of hyperspectral remote sensing to support urban micro climate characterisation are summarised and directions for further research are suggested.

# 2 Conceptual framework

In this chapter the conceptual framework is presented. The conceptual framework combines the requirements and possibilities of three disciplines: urban planning, urban micro climate studies and remote sensing. It sets up a framework for the selection of the hyperspectral products and methods to characterise the urban micro climate. The underlying theory and state of the art of the three disciplines is explained in more detail in the next chapter.

**Concept**

The urban micro climate is strongly influenced by spatial characteristics of the urban area such as surface cover and land use (see section 3.2.1). In urban planning, spatial indicators form the basis for the classification system of urban structural types, where building blocks with similar characteristics are grouped into one urban structural type (Pauleit, 1998, see also section 3.1). Spatial indicators are here defined as urban characteristics which can easily be measured in order to provide indirect information on another parameter (e.g. urban structure) which cannot be directly measured or described. Examples of spatial indicators are imperviousness, building density and vegetation volume. The spatial scale of the urban structural types, the building block, is comparable to that on which the micro climate is studied, i.e. two kilometers or less (Kuttler, 2004). Because urban structural types are already familiar to urban planners, it would be favourable to use this system as a framework for the characterisation of the urban micro climate for urban planning purposes. Because building blocks of the same urban structural type have many spatial characteristics in common, it is likely that they also have similar micro climatic characteristics. Urban structural types with similar micro climatic characteristics require similar planning measures to improve the climate situation or mitigate unwanted effects (Pauleit, 1998; Fehrenbach et al., 2001).

Climatologists make use of in situ measurements, models and indicators to study and describe the urban micro climate. The main needs are to gather information about the temperature, wind, humidity and air quality parameters. In situ measurements cannot provide information on the spatial patterns of these parameters. Knowledge about the urban characteristics is important in order to provide area wide information on the urban micro climate. These urban characteristics can serve as spatial indicators or as input for simulations with micro climate models. Relevant urban characteristics are for example surface cover type, building configuration and height, thermal properties of roads, roofs and other surfaces (i.e. surface material) as well as location and type of vegetation. For example the percentage of impervious surface is positively correlated to temperature (e.g. Zhang et al., 2009a). Imperviousness can thus be used as an indicator to predict where higher temperatures are to be expected (see also section 3.2.2). As another option to retrieve area wide micro climatic information, urban micro climate models are used to simulate climate parameters over time for a certain area (see also section 3.2.2). This is an

interesting tool for urban planners since it allows them to study the effect of planned measures in advance (e.g. building a new road).

To be able to provide area wide information on the spatial characteristics of urban areas, airborne hyperspectral remote sensing with almost contiguous spectral bands and a spatial resolution of 2 to 10 m pixel size is a suitable tool. Because of the high spectral resolution, hyperspectral data allows the mapping of urban characteristics at a local scale by using the spectral signatures. This is illustrated in figure 2.1. Surface materials each have their own spectral signature. Urban objects (a building, a road, etc.) can be identified by their surface material. In the example in figure 2.1 the identification of clay or concrete roofing tiles allows the mapping of the building. The type and configuration of urban objects characterise the building block and its urban structural type. The urban structural type in the example is a regular block development, which follows from the rectangular shaped buildings which are regularly arranged within the building block and are surrounded by vegetation. Thus, the building block and its urban structural type can be described by their surface materials, e.g. by the area covered with impervious materials or roofing materials of a certain type. These characteristics provide a means to classify building blocks into urban structural types in an objective way (e.g. Sukkop and Wittig, 1998; Pauleit, 1998).

Based on the aspects described above, the following concept for the use of hyperspectral remote sensing to support urban micro climate characterisation is presented, to ensure the suitability for urban planning. The hyperspectral data can be used to map climate relevant spatial characteristics based on surface materials. These characteristics can be aggregated at building block level and can be used as spatial indicators for urban planning and micro climatic applications. In addition the spatial characteristics can also serve as input for urban micro climate models. By relating climate indicators and model results to urban structural types, the micro climate can be characterised in a way which is suitable for urban planners.

This thesis aims at implementing this newly developed concept and analysing the potential of the airborne hyperspectral remote sensing data for urban micro climate characterisation.

**Implementation**

The concept presented in the previous section is applied to a case study of the city of Munich. Figure 2.2 shows an overview of the implementation of the conceptual framework. Based on airborne hyperspectral data of the HyMap sensor supported with height data, remote sensing products which are required as input for the calculation of spatial indicators and a micro climate model are derived. The main emphasis lies on the identification of surface materials. Based on this information both spatial indicators and a large part of the input data for the micro climate model can be derived. In addition, surface albedo and leaf area index are derived from the hyperspectral imagery so as to provide even more information for the micro climate model. The implementation of the remote sensing products in the micro climate model is an important part of this thesis as well. The spatial indicators and the micro climate simulations focus on the building block scale, allowing a micro climatic analysis of various selected urban structural types. In the following paragraphs, the different steps of the conceptual framework are addressed in more detail.
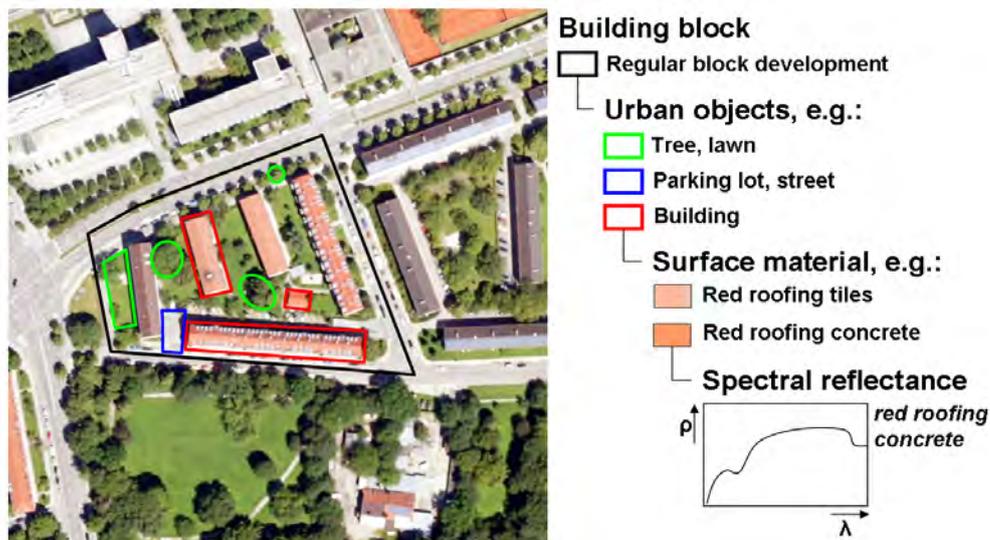
Figure 2.1: *Schematic illustration of the characterisation of a building block*

The first step comprises of data collection and pre-processing, including atmospheric correction and geometric correction of the hyperspectral HyMap data and normalisation of the digital elevation model (DEM). This is described in section 4.3.

Secondly, surface materials are identified using a linear spectral unmixing approach (see section 5.1). Because for different parts of the study area data sets of varying quality are available, several options and settings are tested. The result of the linear spectral unmixing is an abundance map for each surface material, in which the fractional cover of that material is indicated for each pixel. In this way sub-pixel material information is derived from the hyperspectral data.

The albedo is derived using both a function in ATCOR atmospherical correction software (Richter, 2007) and the overall reflectance average. This is described in detail in section 5.2.1. The leaf area index is calculated based on vegetation indices and subsequently used to estimate the leaf area density of trees (see section 5.2.2).

After calculating these remote sensing products, the third step is to calculate the spatial indicators. The spatial indicators imperviousness, building density, vegetation density, building volume, vegetation volume and roof material have been selected for this study. They are important to urban planners to describe the urban area (see also section 3.1). They are relevant for micro climatic analysis as well because there are strong relationships between these characteristics and climate parameters such as temperature (see section 3.2). The selected spatial indicators are calculated per building block based on the material abundances and height data. The approach that is used to accomplish this is described in detail in section 5.3.

The modelling of the urban micro climate is carried out by a model called ENVI-met. This numerical model provides a tool for urban planning by modelling the interaction between urban surface, vegetation and atmosphere (Bruse and Fleer, 1998). The ENVI-met model has been selected because it provides a comprehensive simulation of many aspects of the urban enviroment, it is available at no costs (www.envi-met.com) and is constantly improved. It allows the simulation of the micro climate in the modelled area over a certain period of time. This makes
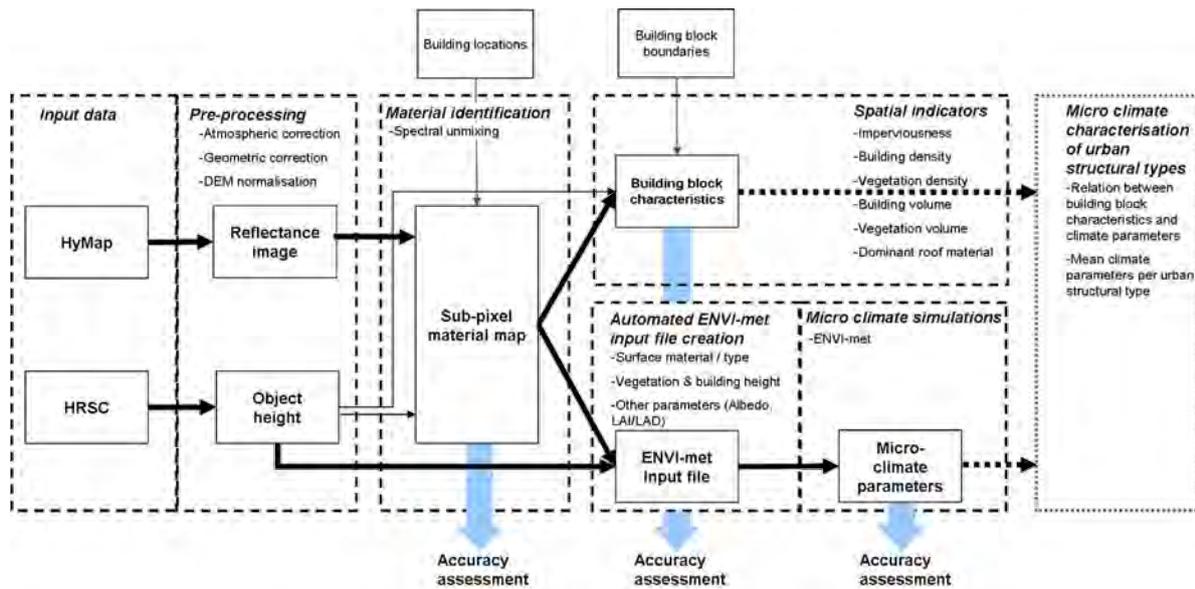
Figure 2.2: *Implementation of the conceptual framework*

ENVI-met - like other micro climate models - a useful planning tool, because different scenarios can be tested. For the case study of Munich, several simulations were carried out for selected building blocks representing different urban structural types. To achieve this, the information provided by the hyperspectral data and the height data are used to create simulation areas which represent these selected areas in Munich. A simulation area is described by parameters on surface cover types, object location and heights and thermal properties of all surfaces. The object location, surface type (surface material), building height and vegetation height are derived from the material abundances and height data. Thermal properties of the surfaces in the simulation area can be assigned according to the identified materials. The surface albedo and the leaf area density (based on the leaf area index), which are retrieved directly from the hyperspectral data, provide further properties of the surfaces and vegetation required by the micro climate model. The model ENVI-met and the generation of the input parameters from the hyperspectral data are described in detail in section 5.4.

Before urban planners and climatologists are able to use the information that was collected with hyperspectral remote sensing, it is of great importance to have insight in both the potentials and the limitations of this technique. Some limitations are inherent to (airborne) remote sensing or imaging spectroscopy, others to the selected methods. An accuracy assessment of the results of the material identification, the indicator calculation and the micro climate modelling is carried out to assess the influence of these factors (see the sections 5.1.4, 5.4.4 and 5.3.3).

# 3 Interdisciplinary background

This chapter provides a background on the disciplines urban planning, urban climate studies and optical remote sensing. The information needs, relevant theories and techniques of these disciplines are described to support a better understanding of the conceptual framework (chapter 2) and the selected methodological approach (chapter 5).

## 3.1 Urban planning

The first discipline which is addressed is that of urban planning. Urban planning is mainly carried out by governmental bodies. This thesis aims at fulfilling the information requirements of urban planning regarding micro climatic analysis. Therefore, first the objectives and information requirements of urban planning are described. Next, urban structural types, being one of the most important frameworks of urban planning to describe the urban area, are explained in detail.

### 3.1.1 Objectives of urban planning

In general, the aim of urban planning is sustainable development of the urban area in which social, economic and environmental needs are balanced. Spatial planning of urban areas is in Germany mainly a task at a regional and municipal level. At the federal level the Building Code (Baugesetzbuch, Bundesministerium für Verkehr, Bau und Stadtentwicklung, 2009) directs the municipalities to formulate detailed spatial plans at a local level (Bauleitplanung). Within those urban planning activities there are two actual plans that have to be developed and updated. The first plan is the more general zoning plan (Flächennutzungsplan) which is developed at a scale of 1:10,000. In the zoning plan areas are designated for desired uses such as residential, commercial or industrial use. The smallest relevant spatial unit for the zoning plan is the building block. The second plan is the legally binding building plan (Bebauungsplan) with a spatial scale of 1:1,000, making single buildings the smallest relevant unit for this plan.

In the Building Code several aspects that have to be taken into account in urban planning are specifically mentioned (Baugesetzbuch §1) such as the availability and preservation of health care, cultural heritage and employment. These three examples show the variety of thematic fields that play a role in urban planning. It also makes one aware that one spatial measure will have consequences on many aspects of society (e.g. social, economic and environmental aspects). An example is the development of a park with the aim to improve the micro climatic situation and to increase the living standard. As a result the housing prices are likely to rise which might cause a shift from residents with a low to average income to residents with high incomes.

Environmental protection is an important topic in urban planning. Nature and landscape conservation and a minimal increase of sealed surface are important in this context. The Building Code in many cases obligates municipalities to write an environmental report (Umweltbericht) in addition to the zoning and building plans. In this report the effect of the proposed measures on the environment has to be assessed. Climate, e.g. in the form of thermal comfort or air pollution, is not explicitly mentioned in the Building Code yet. However, in politics this topic has gained importance. This is shown for example by the implementation of environmental zones (Umweltzonen) in various German cities including Munich (Bayerisches Staatsministerium für Umwelt, Gesundheit und Verbraucherschutz, 2008). In determined zones of these cities high emission vehicles are no longer allowed on certain times of the day with the aim to reduce the amount of particulate matter in the urban area. Another example is the Ministry of Research and Education (Bundesministerium für Bildung und Forschung) which sponsors research that focuses on the effects of climate change on society and on which (planning) measures can be taken to mitigate them (e.g. KlimaZwei, Klimzug; Bundesministerium für Bildung und Forschung, 2009).

### 3.1.2 Information needs of urban planning

From the broad field of aspects that should be taken into account in urban planning it becomes clear that urban planners need a vast amount of information. In order to take the best actions for the public and individuals, information on the status quo and on the effect of the actions is needed. Also some understanding of the system (e.g. local economy, transportation or urban climate) on which the actions have impact is required. The effects of an action on different planning aspects have to be understood and evaluated. Therefore, information from different scientific disciplines is required for planning (Hidding et al., 2002). Information used in planning does not only concern a variety of topics, but also considers a variety of sources such as census data, in situ measurements and a large variety of maps. One thing they all have in common is their spatial component. Statistical data is widely used in social and economic disciplines. This data (e.g. demographic data or income level of inhabitants) is gathered by questionnaires and administrative data collection (for example by a census bureau). Statistical analysis of this data provides planners with information at a suitable level of spatial detail, e.g. for a region, a municipality or a street. However, such data is expensive and time consuming to collect and thus recent information is not often available. In situ measurements are common in several environmental disciplines. Examples are measurements of a weather station or traffic counts. Often this data is interpolated prior to use in urban planning in order to provide information with a larger spatial coverage. Direct area wide information is retrieved by mapping, e.g. of land use or vegetation species. The mapping can be done by field surveys, manual digitising of aerial photographs and other remote sensing imagery or by (semi-)automatic analysis of remote sensing data. A geographical information system (GIS) allows a combined analysis of different thematic characteristics of a certain area. Through this, relations between environmental, social and economic aspects can be identified, understood and if necessary mitigated or improved by planning measures.

Depending on the source of the information and the planning issues that need to be addressed, the most suitable spatial scale should be selected for the presentation of the spatial information. For each scale different spatial units are relevant. Typical examples of spatial units are postal

zip-code zones or administrative boundaries. Such units are especially suitable for the application of spatial measures: within one administrative boundary the same jurisdiction is valid. At a more detailed scale level building blocks are a suitable spatial unit. A building block (Baublock) is bounded by its surrounding streets. An advantage is that the building block boundaries are often equivalents of the property boundaries.

The information requirements of urban planning on the micro climate are difficult to meet, which is one of the reasons why micro climatic aspects are not commonly included in preparations for the building plan yet. Urban planners often do not have enough background knowledge about micro climatic processes and communication with climate experts is difficult because of the different scientific disciplines (Eliasson, 2000). Therefore, understandable information on the urban micro climate is required for urban planners. Important properties of information that are useful for urban planners are the scale and spatial coverage which suit to the requirements of a building plan. Urban micro climatic analysis focuses on a scale smaller than two kilometers (Helbig et al., 1999). The building block can be identified as a suitable spatial unit to analyse the urban micro climate for urban planners, because it suits the scale of micro climatic analysis and because it is a commonly used unit in other planning issues as well. In addition building blocks have been the basic spatial unit for analysis of urban areas in many different studies, for example in mapping urban structural parameters (e.g. in Berlin by Kleinschmit et al. (2007), in Munich by Fischer (2002) or in Tokyo, Japan by Yoshida and Omae (2005)) or for urban micro climate studies (e.g. Shashua-Bar et al., 2004; Arnfield, 2003; Hoyano et al., 1999). Building blocks have defining characteristics regarding building and vegetation structure, land use, location within the urban area, and demographic, socio-economic and ecological parameters. There is also a strong interrelationship between these factors.

Urban structural types (Stadtstrukturtypen) are a useful classification system for urban areas at a building block level (Pauleit and Duhme, 2000a). This descriptive system provides the possibility to group urban areas with similar characteristics. For planning purposes this is useful, because it is likely that building blocks with similar characteristics need the same spatial measures to meet environmental objectives. This is used in urban ecology for example, where urban structural types coincide with urban biotope types and where they are used to describe the biodiversity within the city (Sukkop and Wittig, 1998). Urban structural types are also a useful classification system for urban micro climatic analysis, because the spatial indicators which are used to separate the different structural types also influence the micro climate (e.g. Zhang et al., 2009b; Rigo and Parlow, 2007, see also section 3.2.1). Additionally, urban structural types are a means of communication. They are often considered to be representative for a certain land use, a socio-economic standard, an ecological standard and the quality of life. As an example we look at detached and semi-detached housing (Einzel- und Doppelhausbebauung). One can imagine a building block with detached and semi-detached houses, even without knowing the exact number of houses, inhabitants or income. One could for example expect houses with gardens, families with young children with medium to high income, etc. A land cover map together with demographic data could be used to confirm this expectation (e.g. as applied in Pauleit (1998)). In several studies a direct relationship has been established between different climate parameters and the urban structural type (Helbig et al., 1999; Pauleit, 1998). Links have also been made between temperature and several indicators such as imperviousness, surface albedo and vegetation density (Jenerette et al., 2007; Zhang et al., 2009a), which are in turn

characteristic of the urban structural type.

The above shows that urban structural types are a useful and established system for describing the urban area in a planning and micro climatic context. Therefore, the next section focuses on the various urban structural types that can be distinguished and their characteristics.

### 3.1.3 Urban structural types

Many German cities have mapped the structure of their urban areas. There are many similarities between the different cities. For example, block development can be found in all large German cities and occurs in the maps of urban structural types of Berlin, Hamburg and Munich (Berlekamp and Pranzas (1986) in Heber and Lehmann, 1993; Hanschke and Beddig, 2005; Pauleit, 1998). There are, however, regional differences. Various terms and definitions have been used by the different municipalities within Germany to indicate similar urban structures. Classification schemes based on the main use of the building blocks (residential, commercial, etc.), on the building period, on the building configuration or a combination of those have been used.

The differences between German urban structural types and those of other countries are of course even larger. They are the result of different environmental circumstances (landscape, climate) and differences in planning traditions which, in turn, are influenced by political and environmental events during history (Knox and Marston, 2001). This also complicates the translation of the names of the urban structural types into English, because of the large differences in town planning traditions in Germany and Great Britain or the USA (Campbell and Fainstein, 2003). Being aware of the large variation, the names and descriptions of the urban structural types in this thesis are based on the definitions used in Munich, as described by Pauleit (1998) and Fischer (2002). The names of the urban structural types are translations of German names. The advantage of the definitions of the urban structural types used here is that they are mainly based on building configuration and not only on the use of the block. This is convenient for remote sensing analysis, which can be used to directly derive land cover information, but not for the identification of land use. By identifying roof materials, buildings can be mapped with remote sensing, as is explained in chapter 2. The roof material does not only represent the building, but is also characteristic for the urban structural type. Industrial buildings have often bitumen or synthetic roofs while roofing tiles are most common for residential buildings for example.

This thesis focuses on the 12 most common urban structural types in Munich. Areas with agricultural use and transportation networks (roads, highways, railways) are left out of consideration. In table 3.1 the main characteristics of the selected urban structural types are listed. The mean values of the indicators building density, vegetation density and imperviousness are given for each type. Additionally, the most common roof materials are provided because of their importance to remote sensing based mapping of urban structural types. These characteristics do not only separate the different urban structural types, they also influence the urban micro climate (see section 3.2.1). In the text below the selected urban structural types are described based on analysis of the urban structural types of Munich by Fischer (2002) and aerial photographs.

Although the selected structural types can be found in this form in other German and European cities, some characteristics are typical for Munich. Especially building materials vary

largely among regions. An example is the usage of slate as a roof material. This is rarely found on roofs in Munich because it is not available in the natural environment around Munich. However, in other German regions such as around the river Rhein, e.g. in Bonn, slate is extensively used as a roofing material (Franke et al., 2009). Therefore, the following description of the structural types should be seen as typically German or in this case Munich in particular.

**Dense block development (a1)** has the highest building density and almost the highest percentage of impervious surface of all urban structural types. The buildings form a closed front towards the street. The inner courtyard is often built over or paved. Although from the street it might look as if the block consists of one large building, the roofs can be made of different materials, reflecting different owners and building periods. In the example in table 3.1 the high building density and the variety of roofing materials are clearly visible. Tiles are generally the dominant roof material of this urban structural type. The building height varies between three and six floors. This urban structural type can typically be found in urban centres in Germany. Commonly its occupation is residential or a mixture of residential and commercial use. Because of the little space in the city centres, workshops and storage buildings are regularly located in the inner courtyard.

**Perimeter block development (a2)** has the building configuration and the building height in common with the dense block development. The difference is that only the perimeter of the block is built over, which is clearly shown by the example of a perimeter block development in table 3.1. The inner courtyard is an open space, often covered with vegetation. This results in a lower building density and a lower percentage of impervious surface than a dense block development would generally have. The main use of the perimeter block development structural type is residential, though commercial uses are not uncommon as well.

**Regular block development (a3)** is characterised by the orientation of the buildings within the block. The buildings are organised in a regular pattern, often perpendicular to the streets. This provides a view from the streets on the green spaces between the buildings. Vegetation density, building density and the percentage of impervious surface are medium high compared to the other urban structural types. The buildings are usually between three and six floors high. Since the block is often developed and built as a whole, roofing materials are often the same for the whole block. Tiles are the most common roofing material for this structural type. Regular block developments can be found outside the historical city centre. Since they are usually the result of a larger planning project, they can be found in various suburbs or other areas redeveloped since the beginning of the twentieth century (Hanschke and Beddig, 2005). Their occupation is mainly residential.

**Row house development (a4)** can be described as single houses being connected to building rows, which are in turn regularly ordered within the building block. The building structure is comparable to that of a regular block development. In the aerial photograph of an exemplary row house development in table 3.1 only the slight difference in roofing and the green spaces divided into private gardens show that there are connected single houses with different owners. Other differences between row house development and regular block development are that the

buildings in a row house development are usually lower (two to three floors) and the vegetation density is on average slightly higher. The dominant roofing material is roofing tiles. Row house developments can be found more towards the outskirts of the city. It is a clearly residential structural type.

**Detached and semi-detached houses (a5)**   have the highest vegetation density and the lowest building density and percentage of impervious surface of all urban structural types (not counting parks, urban green and sports fields). It is the dominant urban structural type in Munich both in number of building blocks and in surface area. The buildings are relatively small and surrounded by gardens with many trees. The buildings are mainly placed at the border of the building block. Every house can be a little different from the next by slightly varying shape, roofing material and roofing type. Roofing tiles are the most common roof material, though many types of tiles are used. Usually the houses do not have more than three floors. This structural type is typical for suburban areas and some older areas with urban villas. The houses are mainly used for residential purposes. One or two families usually live in one building. In the older urban villas, which are usually more centrally located in the city, residential use often becomes too expensive and is replaced by offices and medical practices.

**High rise buildings (a6)**   together with row house development and regular block development have the second highest vegetation density, with vegetation covering about two-thirds of the building block on average. The high buildings (more then six floors) are surrounded by park-like vegetation as is shown for an exemplary high rise building block in table 3.1. The shape and size of the buildings and the number of high rise buildings within one building block can vary. They commonly have flat roofs, resulting in bitumen and concrete as the most common roofing materials. In the city centre high rise buildings are frequently occupied by commercial or administrative offices. Often, high rise buildings of companies are located along highways and other well visible locations, where they become an icon for the company. However, high rise buildings are also residentially used.

**Small multi-storey buildings (a7)**   have a building structure similar to detached and semi-detached houses, except that the buildings are larger. Compared to detached and semi-detached houses, this results in a 10 % lower vegetation density and a 10 % higher building density. Sometimes the buildings are connected to complexes. The dominant roofing material varies depending on weather the roofs are flat (bitumen) or pitched (tiles). Also metal roofs are not uncommon. In Munich, the use of small multi-storey buildings is often residential, although it is not uncommon that a part of the building is used by offices or medical practices. Complexes of small buildings are often used for administrative and commercial purposes. Another typical example is a school complex. This structural type is situated throughout the whole city, though usually not in the historical city centre and more often towards the outskirts of the city, where there is more space for green area.

**Large multi-storey buildings (b1)**   are covered with larger buildings than the small multi-storey buildings structural type. Often one building or a complex of buildings covers almost the whole building block as is the case in the example in table 3.1. This type has one of the highest

building densities and percentages of impervious surface and as a result one of the lowest vegetation densities. This structural type is often located within commercial or industrial areas. It can also be found in the city centre: many large historical buildings such as palaces or hospitals belong to this category. As is already clear from the locations, large multi-storey buildings are mainly commercially used or occupied by administrative and governmental services.

**Large halls and storage buildings (b2)**  are characterised by large, not very high buildings. The non-built spaces within building blocks of this structural type are usually impervious as a direct result of the industrial use. Because of this, this urban structural type has the highest percentage of impervious surface, directly after the dense block development as is illustrated by the example in table 3.1. Examples of the occupation of single story buildings are factory halls, storage buildings and large stores (e.g. home improvement stores). The non-built spaces are often used to store construction materials, to park vehicles etc. This needs be taken into account when performing remote sensing analysis, because this occupation influences the recorded spectra. Typical roof materials for this structural type are synthetic materials such as PVC and bitumen. This structural type can be found in industrial areas at the borders of the urban area or near logistic hotspots, such as a railway station or a highway junction.

**Small halls and storage buildings (b3)**  are quite similar to the large halls and storage buildings, except that the buildings are smaller and that the non-built space in the building block is more often covered with vegetation (see table 3.1 for an example). There is also a large variation in roofing materials as is the case with the large halls and storage buildings. The use is commercial/industrial and the urban structural type can be found in industrial areas but also in transitional areas between residentially and commercially used areas. A typical example of small halls and storage buildings are discount supermarkets.

**Parks and urban green (c1)**  are important to the urban eco-system, the urban climate and the landscape quality of an area. This structural type actually has quite little structure, in the sense of buildings. Parks might contain some small buildings. Small footpaths or roads are usually present for example in the small park shown as example in table 3.1. This results in a low percentage of impervious surfaces. Urban green refers to the small public green spaces, such as a lawn between two building blocks. Urban green is usually too small to contain any buildings. For the urban eco-system and the urban climate the vegetation structure of parks and urban green is important. This describes the configuration of trees and lawns.

**Sports fields (c2)**  are characterised by a low building density. Depending on the type of sports field the percentage of impervious surface can be low. However, the sports fields often consist of impervious or partially impervious materials such as synthetic turf (e.g. for hockey) or loose chippings (e.g. for tennis). In the building block in table 3.1 both a partially sealed tennis court and a pervious grass soccer field are present. Large sports fields are often located in peripheral regions of the city. Within the test area many sports fields are located in more densely built urban structures, e.g. near schools. Especially in the more densely built areas they are some of the largest open spaces, which give them an important function in the regulation of the urban micro climate.

Table 3.1: *Characteristics of 12 common urban structural types in Munich derived from Fischer (2002) and aerial photographs. BD = building density; VD = vegetation density and IMP = imperviousness.*

| Urban structural type | Abbr. | Mean BD [%] | Mean VD [%] | Mean IMP [%] | Example |
|---|---|---|---|---|---|
| Dense block development (Blockbebauung) | a1 | 62 | 21 | 79 | |
| Perimeter block development (Blockrandbebauung) | a2 | 44 | 40 | 59 | |
| Regular block development (Zeilenbebauung) | a3 | 34 | 50 | 49 | |
| Row house development (Reihenhausbebauung) | a4 | 30 | 64 | 37 | |
| Detached and semi-detached houses (Einzel- und Doppelhausbebauung) | a5 | 22 | 69 | 31 | |
| High rise buildings (Hochhäuser) | a6 | 38 | 48 | 52 | |

| Urban structural type | Abbr. | Mean BD [%] | Mean VD [%] | Mean IMP [%] | Example |
|---|---|---|---|---|---|
| Small multi-storey buildings (Kleine Geschoßbbauten) | a7 | 36 | 46 | 53 | |
| Large multi-storey buildings (Große Geschoßbauten) | b1 | 44 | 31 | 68 | |
| Large halls and storage buildings (Große Hallen- bebauung und Lager) | b2 | 55 | 3 | 96 | |
| Small halls and storage buildings (Kleine Hallen- bebauung und Lager) | b3 | 24 | 34 | 58 | |
| Parks and urban green (Parkanlagen und Grünflächen) | c1 | 1 | 89 | 9 | |
| Sports fields (Sportanlagen) | c2 | 7 | 75 | 22 | |

## 3.2  Urban micro climate

The World Meteorological Organisation defines climate as the long term average weather, described by the mean and variability of relevant quantities. Those quantities are most often surface variables such as temperature, precipitation and wind (Commission for Climatology, 2009). The climate system consists of the atmosphere, the hydrosphere, the cryosphere, the land surface and the biosphere. The climate is influenced by the interactions between those components, and external influences such as volcanic eruptions, solar variations and anthropogenic actions (e.g. pollution or land use change) (Commission for Climatology, 2009).

Urban climate is the climate in built up areas, which is strongly influenced by human activities. The climate in urban areas differs from that in rural areas in temperature (urban heat island), precipitation (e.g. more rain, less snow) and air quality (e.g. smog), among others (Kuttler, 2004). Urban climate is commonly studied at a regional or local level. At a regional scale (2-250 km) for example urban heat islands are studied. At a local scale (<2 km) micro climatic effects within the urban area are addressed, e.g. the effect of a cooling tower on the surrounding area, or the energy balance of a building (Helbig et al., 1999).

This thesis focuses on the urban micro climate at a local scale. The different aspects of the urban climate and the parameters that influence them are described in the next section. After that, methods to measure and model the urban micro climate are addressed.

### 3.2.1  Aspects of the urban micro climate

The most important climate surface variables that are influenced by the urban area are temperature, wind, precipitation and air quality (Kuttler, 2004). Table 3.2 provides an overview of the influence of the urban spatial characteristics on these four climate parameters. Only those parameters are listed which have influence on the micro climate. Table 3.2 shows that there are a lot of parameters influencing temperature. This explains the large number of studies on temperature in urban areas, ranging from micro climatic studies (e.g. Krayenhoff and Voogt, 2007) to urban heat island studies (e.g. Kato and Yamaguchi, 2007). The fact that temperature also influences wind, humidity and (to some degree) air quality, provides an additional explanation for the large interest in temperature. In the following sections the different climate parameters and the urban spatial characteristics which influence them are addressed in more detail. First, to support the understanding of the influences of the urban area on the urban micro climate, two more general aspects of the urban climate are described: the urban atmosphere and the urban energy balance. If not indicated otherwise, the text is based on Kuttler (1998). For more detailed information the reader is referred to Oke (1987), Helbig et al. (1999) and Kuttler (1998).

**Urban atmosphere**

In figure 3.1 a schematic overview of the urban atmospheric layers is given. Oke (1988) describes the urban atmosphere as follows: the urban canopy layer reaches to the top of the roofs and is dominated by site specific micro scale effects, such as buildings, trees and other urban structure characteristics. The study of the micro climate usually concentrates on this layer. On top of the roofs, the urban boundary layer starts. This layer reaches to a height where the urban area no longer has any influence. This height varies depending on the land use and the weather

Table 3.2: *Summary of urban spatial characteristics influencing the four main climate surface parameters. H/W ratio = height / width ratio.*

| Urban spatial characteristic | Climate surface parameter | | | |
|---|---|---|---|---|
| | Temperature | Wind speed | Humidity & precipitation | Air quality |
| Building structure | ● | ● | ● | ● |
| H/W ratio of street canyons | ● | ● | | ● |
| Sky view factor | ● | | | |
| Land cover | ● | ● | ● | ● |
| Surface material | ● | | | |
| Albedo | ● | | | |
| Emissivity | ● | | | |
| Thermal inertia | ● | | | |
| Impervious area | ● | ● | ● | |
| Vegetation fraction | ● | ● | ● | |
| Surface water | ● | | | ● |
| Land use | ● | | ● | ● |
| Traffic density | ● | | ● | ● |
| Industrial areas | ● | | ● | ● |

situation and can reach up to several hundred meters (Kuttler, 1998). The lower part of the urban boundary layer is influenced by the roughness of the surface (buildings etc.), on top of which a turbulent layer, a surface layer and a mixed layer are positioned. The urban boundary layer as a whole is mainly influenced by local and meso-scale effects, such as major land use.

**Urban energy balance**

The urban energy balance is of importance to understanding how urban spatial characteristics can influence the urban micro climate. The following description of the urban energy balance is based on Oke (1988). The energy balance of the urban canopy layer is described by the
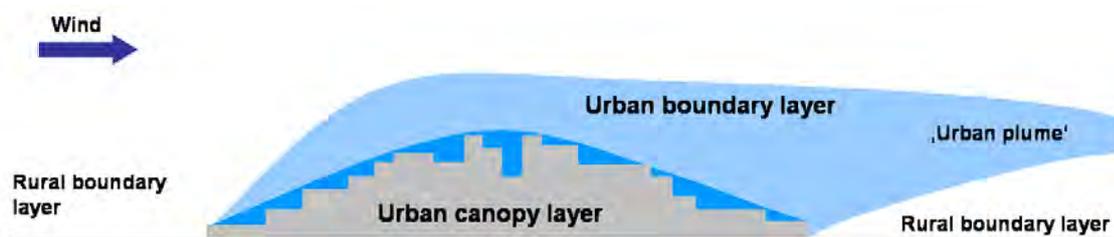


Figure 3.1: *Schematic overview of the influence of urban area on the atmospheric layers. Adapted after Oke (1987).*

following equation:

$$Q* + Q_f = Q_h + Q_e + \Delta Q_s + \Delta Q_a \qquad (3.1)$$

where Q* is the net radiation, $Q_f$ is the heat release by combustion, $Q_h$ it the turbulent sensible heat flux density (energy required for heating of the air), $Q_e$ is the turbulent latent heat flux density (energy required for evapotranspiration), $\Delta Q_s$ is the net heat storage e.g. in buildings and $\Delta Q_a$ is the net heat advection (e.g. hot air currents, wind). The energy balance is illustrated by figure 3.2 a. The amount of available energy is directly influenced by anthropogenic heat production ($Q_f$, by vehicles, factories, etc), but the main part of the energy results from the radiation. The net radiation is defined by the radiation budget:

$$Q* = K \downarrow - K \uparrow + L \downarrow - L \uparrow \qquad (3.2)$$

where $K \downarrow$ and $K \uparrow$ are the incoming, respectively reflected short-wave radiation and $L \downarrow$ and $L \uparrow$ are the incoming respectively outgoing long-wave radiation. Both the emitted and reflected radiation contribute to the outgoing long-wave radiation. The short-wave radiation is subject to scattering and absorption in the atmosphere and between buildings. The long-wave radiation is also subject to absorption and remittance in the atmosphere. This is illustrated in figure 3.2b. Here it is interesting to note that remote sensing measures the outgoing radiation, e.g. with an airborne or satellite based sensor. This provides the possibility to measure a large part of the radiation balance directly with remote sensing (see section 3.3.1).

The amount of energy in the urban canopy layer is reduced by heating of air (sensible heat) and water (latent heat) which then leaves the system with the air flow. The turbulent latent heat flux density $Q_e$ is related to the evapotranspiration. This makes the energy balance sensible to the available amount of water in the system and the potential of the surface to evaporate (which is high for vegetation but low for impervious surface). Also the net storage of energy in buildings and soils reduces the energy in the urban canopy layer, as does the net advection of heat by the wind.

### Temperature

An increase in temperature is one of the most remarkable and best studied effects of the urban influence on the climate. In table 3.3 seven factors are listed which have a positive influence of the temperature in the urban canopy layer. For each of them the urban characteristic that causes this factor is indicated. Combined, these factors are responsible for the urban heat island. The reflectance and absorption properties of the urban surface are the largest influencing factor on the temperature, followed by the change in latent and sensible heat flux and anthropogenic heat production.

Reflectance and absorption properties are mainly material specific. They are described by the material parameters albedo and emissivity. Also the amount of available radiation (reduced e.g. by cloud cover), scattering and absorption in the atmosphere (see figure 3.2b) and building configuration play a role.

The building configuration is often referred to as a system of street canyons in urban climatology (Arnfield, 2003). Street canyons are characterised by their height to width ratio (H/W). They reduce the reflected energy leaving the canyon due to multiple reflections between the
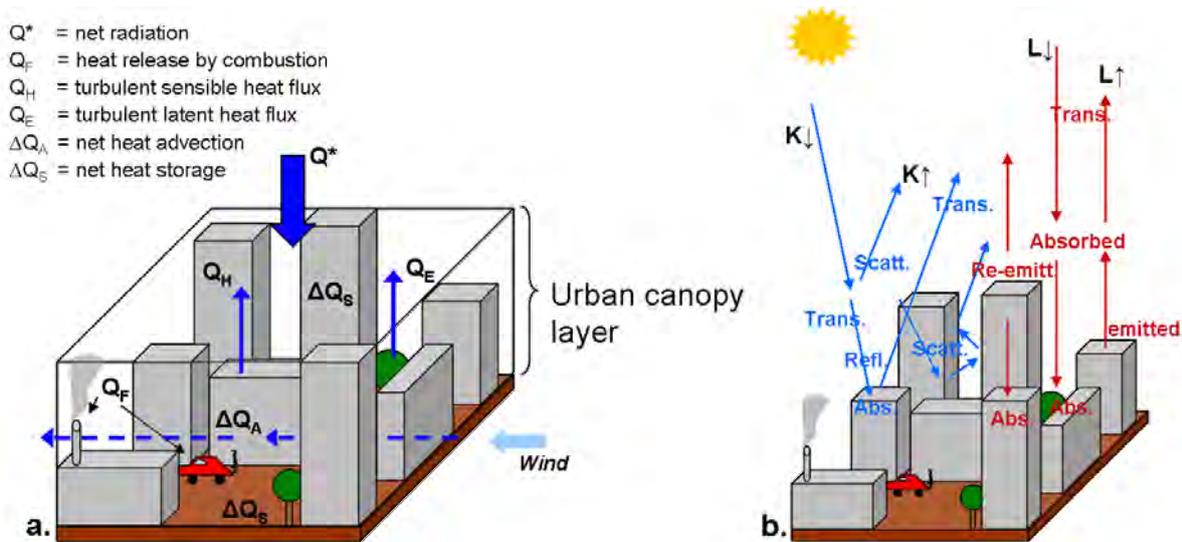
Figure 3.2: *Schematic representation of the urban energy balance (a) and the urban radiation balance (b). Adapted after Oke (1987). $K \downarrow$ and $K \uparrow$ are the incoming, respectively reflected short-wave radiation and $L \downarrow$ and $L \uparrow$ are the incoming respectively outgoing long-wave radiation.*

walls (Offerle et al., 2007). A second parameter related to the urban street canyon is the sky view factor. This factor describes the ratio between the potential visible sky and the actual visible sky from a certain location. This depends on the height to width ratio of the street canyon and influences the amount of direct illumination.

The thermal inertia of buildings causes short wave radiation to first heat up the surfaces in the morning and only heat up the air after that. In the evening the building surfaces release their heat. A result of those two effects is that an urban area heats up slower than a rural area, but stays warm longer.

The latent heat flux is smaller in urban areas in comparison with rural areas because of little evapotranspiration resulting from low vegetation density and fast rain water drainage on sealed surfaces. The sensible heat flux (air temperature) in urban areas is often higher than outside these areas, because the energy is not needed for evapotranspiration and can thus be used for heating the air.

The anthropogenic heat production was mentioned before as a factor influencing the urban climate. The amount of anthropogenic heat that is produced depends on the number of inhabitants, industrial activity and traffic and the time of the day and year. Air pollution caused by these human activities increases the effect. Since pollutants and other particles in the air increase scattering of radiation they keep radiation inside the urban canopy layer and increase the temperature in this layer.

**Wind**

The large surface roughness of an urban area influences vertical wind profiles up to 500 meters because of obstructions by buildings and trees. It also causes a reduction of wind speed of 10-20% in comparison to a rural area. There is a difference in the strength of the reduction of wind

Table 3.3: *Factors causing an increase of temperature in the urban canopy layer. Adapted after Kuttler (1998)*

| Factors | Related urban characteristic |
|---|---|
| Increased absorption of short wave radiation | - air pollution<br>- street canyons (increased and multiple reflections) |
| Increased incoming long-wave radiation | Air pollution (increased absorption and re-emission) |
| Reduced outgoing long-wave radiation | Street canyons (reduced sky view factor) |
| Anthropogenic heat sources | Traffic, industry |
| Increased storage of sensible heat | Heat capacity of buildings |
| Reduced evapotranspiration | Building materials (increase of sealed surfaces) |
| Reduced heat advection | 3D structure of the urban area (reduction of wind speed) |

speed between summer and winter caused by the decrease in obstruction by vegetation that is not in leaf during winter.

During quiet, cloud free weather conditions, thermal gradients within the urban area can also cause wind flow. This thermal gradient depends on the locations and intensity of the urban heat island. Normally, it causes wind flow towards the warmer city centre. This is a desirable effect because it brings fresh air into the city, especially in summer, when this quiet weather situation occurs most often. In urban planning this effect can be facilitated by assigning ventilation corridors (Kaltluftschneisen), e.g. along a river.

**Humidity and precipitation**

In general the humidity in an urban area is lower than in rural areas during daytime, especially over impervious surfaces. This is caused by the reduced evaporation and increased surface water run off. During night-time, the humidity is usually higher. Transport of water vapour from the urban boundary layer up into the urban canopy layer and the low amount of dew forming because of the heat island contribute to this. The percentage of impervious surface and the vegetation density and their impact on the energy and radiation fluxes are the main urban characteristics influencing humidity. Additional anthropogenic factors such as artificial water supply (e.g. for watering of gardens and parks) and moisture release by the combustion process of motor vehicles and industry can increase the humidity.

Studies on precipitation have shown that the amount of precipitation is often higher on the leeward side of the city. The main cause for this is the presence of the city as an obstacle with high surface roughness, but also air pollution can contribute to increased precipitation in urban areas. The heat island over the city can cause convection with clouds as a result.

**Air quality**

The air quality in cities is the result of a complex interaction between natural and anthropogenic environmental conditions (Mayer, 1999). Both the temporal and spatial emission pattern of pollutants and the weather conditions are responsible for air pollution becoming a serious health problem. The main sources of air pollution are strongly related to urban use. Motorised traffic is the largest source for nitrogen oxides ($NO_x$) and carbon monoxide ($CO$) and the second largest source for coarse particulate matter ($PM_{10}$). The amount of emitted pollutants is time dependant. During rush hours and on working days considerably more pollutants are emitted than on Sundays (Mayer, 1999). The emitted air pollutants disperse into the atmosphere. The dispersion is influenced by meteorological parameters such as wind direction and speed, turbulence and atmospheric stability. Also the location of the sources (near to the ground or above the urban canopy, upwind or downwind of the city) influences the concentration of pollutants within the urban area. As shown above, those meteorological parameters are strongly influenced by the urban structure. Once the pollutants are in the atmosphere chemical reactions occur. An example is the production of photochemical ozone. This and other chemical reactions are influenced by short-wave radiation, air temperature and air humidity. These parameters influencing the chemical reactions are also influenced by the urban area themselves (see previous paragraphs of this section), which illustrates the complexity of the urban micro climatic system.

### 3.2.2 Measuring and modelling urban micro climate

As described above, urban areas influence temperature, wind, humidity and air quality. Because of the direct influence of these parameters to the inhabitants of the city, there is a need for urban planners and climatologists to find out what causes undesired micro climatic effects (e.g. hot summer temperatures or air pollution) and how they can be mitigated. Therefore information is needed on temperature, wind, humidity, air quality and other parameters at different times and circumstances. In urban micro climate studies there are three approaches to get this information: direct (in situ) measurements; indirect by indicators and based on simulations.

**In situ measurements**

In situ measurements are usually highly accurate and can provide long-time series of data. Temperature, wind, humidity, air quality and other parameters are directly measured by weather stations. The variation over time is relevant to understand the relations with human activities and seasons or to monitor the change of the situation. However, the spatial variation of the values of the parameters is important to gain an overall impression of the complex climatic structure of the city as well (Xu et al., 2008). This information can seldom be provided by in situ measurements, because the observational network is seldom tight enough. Measurements with equipment installed on vehicles are an improvement, but still cannot provide area wide coverage (Weng, 2009).

In addition to in situ measurement on the ground, remote sensing provides a tool for area wide measurement of some parameters of urban climate (see section 3.3.3). Thermal infrared remote sensing can be used to measure land surface temperature (LST) (Weng, 2009). Optical remote sensing can provide measurements of the broad band albedo (Govaerts et al., 2008).

For other surface parameters indicators or simulation models are needed to generate area wide information.

**Indicators**

Area wide indicators are especially valuable to urban climate, because in situ measurements only seldom can provide area wide information. The indicators can give an estimation of the climatic situation in the complex urban area. In section 3.2.1 it has been shown that spatial characteristics of urban areas, such as land cover and land use, influence certain aspects of the urban micro climate (temperature, wind, humidity or air quality). Each of these characteristics (see table 3.2) can serve as a climate indicator, although the strength of the relationship with the micro climatic aspect of interest may vary. Many studies have been carried out to quantify the relationship between the surface parameter and the climate parameter of interest, e.g. by regression modelling.

In table 3.4 a selection of these studies is listed. The table gives an overview of indicators for which the relationship with one or more climate parameters has been analysed. Many of these indicators can be mapped by remote sensing as can be seen in the fourth column of table 3.4. Also aerial photographs or topographical maps have been used. For social indicators such as population density, census data is used to retrieve the parameters for certain areas or units.

Table 3.4 shows that most relations that have been studied concerned temperature (including surface temperature, air temperature and heat flux). In these cases the temperature is often measured with thermal remote sensing (mainly surface temperature) or in situ measurements.

The majority of the indicators in table 3.4 is positively related to temperature. This means that an increase of the indicator results in an increase in temperature. Exceptions are vegetation, surface albedo, land use, land cover and urban structural types. Vegetation and surface albedo have a negative correlation to temperature. Land use, land cover and urban structural types are nominal classes. Therefore it is impossible to speak about increasing land cover as such. As a result there is no clear positive or negative relationship between this indicator and temperature, but in many studies the presence of a relationship has been proven (e.g. Rigo and Parlow, 2007; Henry and Dicks, 1987; Weng and Quattrochi, 2006; Pauleit, 1998; Hoyano et al., 1999; Weng, 2001).

Besides temperature, also the relation between wind, air pollution and humidity have been studied, although less frequently. An explanation for this is that these parameters are more difficult to measure than temperature, which can be very easily derived from remote sensing imagery. Also the influence of spatial characteristics on these parameters is not as strong and often indirect via changes in temperature. However, several studies have been carried out on these relationships, e.g. on the influence of land use, land cover and urban structure (Weng and Quattrochi, 2006; Weng, 2001; Offerle et al., 2007; Eliasson et al., 2006).

An additional important aspect of urban climate is human comfort. It expresses the influence of the climate aspects temperature, humidity and wind on the well-being of humans, taking into account human physiological characteristics (Helbig et al., 1999). Because human comfort depends on so many variables, several indices have been developed to combine this information into one single number. This is useful for urban planners; one number expresses the effect of the micro climatic situation on the inhabitants of a certain area. A currently widely used index for human comfort is the predicted mean vote (PVM) which ranges from -3.5 (too cold) to 0

(comfortable) to +3.5 (too hot), originally developed by Fanger (1970). The original application of the PVM was to evaluate the indoor climate, but after several modifications it is now applied to describe outdoor effects as well (Bouyer et al., 2007). Also other human comfort indices exist, like OUT_SET* (Pickup and Dear, 1999)) or physiologically equivalent temperature (PET, (Höppe, 1999)). These indices use an empirical relation between air temperature, humidity, wind speed and mean radiant temperature (Ali-Toudert and Mayer, 2007).

**Modelling**

Models can increase the understanding of ongoing processes or the effects of changes in complex systems such as the urban micro climate. Indicators, as addressed above, can be considered empirical, static models. However, such models can only predict one parameter at a certain time. For the next time step, new values of the input parameter are required. Dynamic models, or forward models, do provide the possibility of simulating ongoing processes. The model state at $t+1$ is simulated or modelled using a deterministic or probabilistic function of the model state at the previous time step $t$ (Karssenberg and De Jong, 2005). This functionality is valuable for urban planning since the effects of different scenarios can be tested. Numerical simulations of the urban canyon are an effective method to gain insight in the influence of canyon characteristics on air and energy fluxes and thus the total energy budget within the urban canopy layer (Arnfield, 2003). The URBAN3 model of Terjung and O'Rourke (1980) was one of the early energy budget models which considerably contributed to the understanding of near-surface city climates (Arnfield, 2003). The model MISKAM (Eichhorn, 1989) is often used in Germany for analysis of wind fields and pollutant concentrations For this study the ENVI-met model of Bruse and Fleer (1998) is selected. This model focuses on the interactions between urban surface, vegetation and the atmosphere and thus models the urban micro climate as a whole. Additional advantages of this model are that it is freely available and allows the automated implementation of detailed surface characteristics (see also section 5.4).

Table 3.4: *Examples of spatial indicators for urban climate parameters*

| Indicator | Climate parameter | Correlation | Method to measure/map the indicator | References |
|---|---|---|---|---|
| Land use | Ground heat flux | (1) | Remote sensing | Rigo and Parlow (2007) |
| | Air temperature | (1) | Topographic map | Henry and Dicks (1987) |
| | Air pollution | (1) | Remote sensing | Weng and Yang (2006) |
| Urban structural type | Surface temperature | (1) | Field survey and aerial photographs | Pauleit (1998) |
| Population density | Surface temperature | Positive | Census data | Jenerette et al. (2007) |
| Median household income | Surface temperature | Positive | Census data | Jenerette et al. (2007) |
| Anthropogenic heat | Urban heat island | Positive (2) | Meso-scale numerical climate model | Fan and Sailor (2005) |
| Surface cover/ surface materials | Surface temperature | (1) | Field survey and aerial photographs | Pauleit (1998) |
| | Sensible heat flux | (1) | Standardized in situ measurements | Hoyano et al. (1999) |
| | Air temperature | (1) | Aerial photographs | Henry and Dicks (1987) |
| | Humidity: surface runoff | (1) | Remote sensing | Weng (2001) |
| Impervious area | Surface temperature | Positive | Remote sensing, also image digitalisation | Yuan and Bauer (2007); Xian (2008); Pauleit (1998) |
| Build up area (normalised differentiating building index: NDBI) | Surface temperature | Positive | Remote sensing | Zhang et al. (2009b) |
| Vegetation (vegetation density, vegetation indices e.g. NDVI, REP, SAVI etc.) | Surface temperature | Negative | Remote sensing, image digitalisation | Xian and Crane (2006); Jung et al. (2007); Zhang et al. (2009b); Pauleit (1998); Jenerette et al. (2007) |
| | Ground heat flux | Negative | Remote sensing | Rigo and Parlow (2007) |
| Surface albedo | Air temperature | Negative | In situ measurements | Kolokotroni and Giridharan (2008) |
| Urban structure ( building pattern, street canyon orientation, sky view factor and H/W ratio) | Ground heat flux | Positive (3) | Digital surface model | Rigo and Parlow (2007) |
| | Sensible heat flux | (1) | Topographic map | Hoyano et al. (1999) |
| | Human comfort | (1, 4) | Characteristics/settings for numerical simulations | Ali-Toudert and Mayer (2007) |
| | Wind /air flow patterns | (1,5) | Numerical simulations | Offerle et al. (2007) |
| | Wind /turbulence | (1) | DEM, fisheye photographs | Eliasson et al. (2006) |

(1) For nominal type indicators (e.g. land uses or materials) it is not possible to indicate the nature of the correlation.
(2) Influence strongly time dependent
(3) Parabolic
(4) Broad E-W orientation: less comfort
(5) Only weak effect in this study (stronger expected from other studies)

## 3.3 Optical urban remote sensing

This section provides background information on optical urban remote sensing which is relevant for micro climatic analysis supported by hyperspectral remote sensing. First, a short introduction to optical remote sensing acquaints the reader with the aspects of passive remote sensing that are important in this context. For a detailed introduction on remote sensing and spectroscopy principles, the reader is referred to one of the many text books (e.g. Lillesand et al., 2004; Schowengerdt, 1997; Van der Meer and de Jong, 2003). After this introduction, an overview on how remote sensing has been applied in urban studies so far is given in section 3.3.2. Section 3.3.3 provides an overview of urban climate analysis with remote sensing and section 3.3.4 discusses the potential of hyperspectral remote sensing for urban analysis, respectively.

### 3.3.1 Introduction to optical remote sensing

In Lillesand et al. (2004) remote sensing is described as the collection of data about the surface of the earth with airborne or space borne sensors measuring electromagnetic radiation in order to assist inventorying, mapping and monitoring of the earth. These sensors measure the radiation reflected and emitted by the surface. Using the same figure as in section 3.2.1, a schematic representation of the reflected and emitted radiance is given in section 3.3. The radiance measured by the sensor depends on the properties of the surface within the sensor's field of view. Additionally the radiance is influenced by scattering and absorption in the atmosphere (see section 3.3). Because this hampers the analysis of the surface properties, the atmospheric influences are commonly removed by an atmospheric correction algorithm and the spectral reflectance is calculated:

$$\rho_\lambda = \frac{E_R(\lambda)}{E_I(\lambda)} * 100\% \tag{3.3}$$

in which $\rho_\lambda$ is the spectral reflectance at wavelength $\lambda$ expressed as percentage, $E_R(\lambda)$ is the radiance at wavelength $\lambda$ reflected from the object and $E_I(\lambda)$ is the incoming radiance upon the object at wavelength $\lambda$ (Lillesand et al., 2004). The curve of reflectance against the wavelength is called a spectral signature (or a spectrum in short). Spectral reflection is a property of the surface material and is the result of the particular molecular structure and the chemical composition of the material (Van der Meer, 2004). The knowledge about the interaction of the radiance with the surface can be used to identify the surface cover (classification). In figure 3.4 typical spectra of four land cover classes are shown for the reflective part of the spectrum from 450 to 2500 nm. Water has a very low reflectance over all wavelengths, except for those in the blue part of the spectrum, because water is a strong absorber of radiation. Vegetation has relatively low reflectance in the visible part of the spectrum (VIS) due to strong chlorophyll absorption, with a peak in the green part. In the near infrared (NIR), the reflectance of vegetation increases into the short wave infrared (SWIR) where the spectrum is marked with strong water absorption features at 1400 nm and 1900 nm. At those wavelengths the water in the plant absorbs most of the light. The spectrum of bare soil is low in the visible part of the spectrum and increases in the NIR region. An adsorption feature at 2300 nm indicates the presence of calcite in the soil.
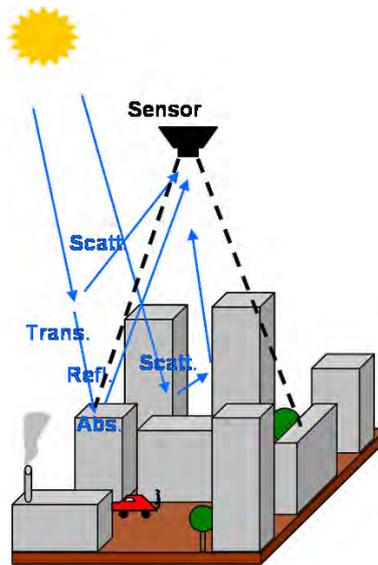
Figure 3.3: *Reflected and emitted radiance in an urban area within a sensor's field of view (adapted after Oke (1988); Schowengerdt (1997))*

The spectrum of roofing tiles also shows an increasing reflectance towards higher wavelengths, clearly showing the adsorption feature caused by iron at 870 nm.

Sensors on a satellite or an airplane do not record the spectral signature continuously over all wavelengths, but only in selected spectral bands (also called channels). The width of those bands ranges from 10 nm for hyperspectral sensors to the complete visible range for a panchromatic sensor (e.g. IKONOS PAN-band covers 450-900 nm) (Lillesand et al., 2004). A multispectral sensor has several spectral bands at selected wavelengths within the spectrum. In comparison, a hyperspectral sensor has many small spectral ($>$40 bands, 10-20 nm band width), contiguously covering the complete spectrum (Van der Meer and de Jong, 2003). In figure 3.5 the spectral bands of the high spatial resolution satellite-based sensor IKONOS, the multispectral satellite based sensor Landsat ETM+ and the airborne hyperspectral sensor HyMap are shown. Also a vegetation spectrum as seen by those sensors is included. This shows the influence of the number and width of the spectral bands of the sensor on the detail of the recorded spectra and therefore the ability to separate different surface covers. This aspect will be addressed in more detail in section 3.3.4.

In addition to the spectral resolution, the spatial resolution is also an important characteristic of satellite and airborne sensors. The spatial resolution is related to sensor design and flight height (Schowengerdt, 1997). Sensors with a high spatial resolution (pixel size $<$10 m) record images on which more and smaller separate objects can be identified. Medium and low spatial resolution sensors provide less spatial detail, but often cover a large area with one image.

The frequency in which a sensor can record a certain area is described by the temporal resolution or revisiting time. This is commonly only indicated as a sensor characteristic for satellite based sensors and not for airborne sensors, because airborne sensors are not bounded by fixed orbits such as satellites. For most urban applications the temporal resolution is not a limiting factor, since seasonal or multi-date acquisitions within one year are seldom necessary. Appli-
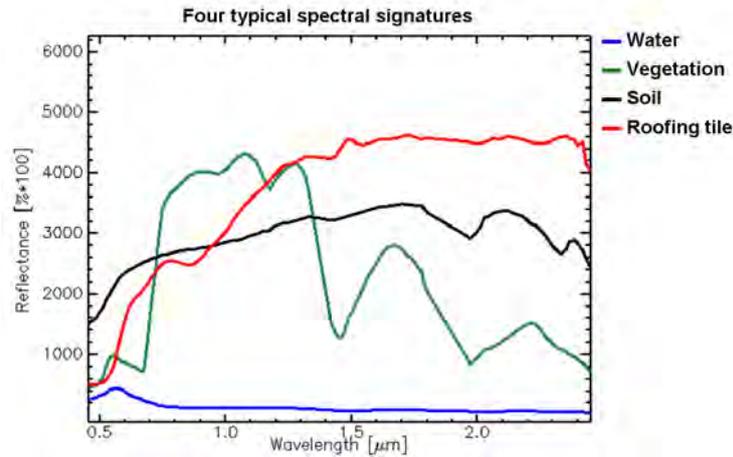
Figure 3.4: *Typical spectra of water, soil, vegetation and clay roofing tile*
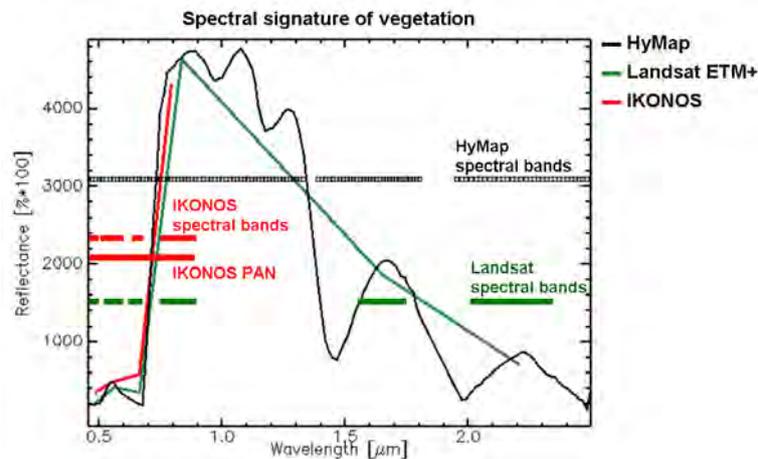


Figure 3.5: *Comparison of a vegetation spectrum as recorded by sensors with different spectral resolution*

cations where a high temporal resolution is important are disaster mapping or the analysis of urban vegetation.

After data acquisition, the images need to be processed and analysed to provide potential users with the desired information. There are many image analysis techniques available to derive maps for a large range of applications. Automatic and semi-automatic image processing techniques allow fast, objective and repeatable classifications. Examples are supervised and unsupervised classifications, spectral indices, spectral unmixing, image segmentation and texture analysis. The next section gives an overview of analysis techniques that have been used to derive maps from urban remote sensing for different applications.

### 3.3.2 Remote sensing data and methods for urban studies

The repeatable and area wide data collection makes remote sensing a highly suitable tool for the mapping of urban areas (Roberts and Herold, 2004; Esch et al., 2009b). However, urban areas are complex environments and certain aspects have to be taken into account. Urban areas are characterised by small scale variation of materials and objects, resulting in a heterogeneous surface cover. In comparison to natural areas, the borders between the different land covers are crisp and most of the man-made materials have distinctive spectral features. If the spectral and spatial resolutions are high enough, this will result in clearly separable spectra and objects (Welch, 1982; Herold et al., 2003a). With lower spatial resolutions many mixed pixels occur, because there are multiple objects within one pixel. Lower spectral resolutions reduce the ability to recognise small spectral features and reduce the differences between the spectra of different materials. Thus, an optimal sensor for urban remote sensing would have both a very high spatial and spectral resolution. However, for such a sensor the spatial coverage and temporal resolution are likely to decrease and costs will increase, with current technical standards. Based on a literature study on the use of remote sensing for different urban applications, four strategies which are commonly applied to deal with this trade-off problem can be distinguished: a first strategy using medium spatial and spectral resolution data, a second strategy using (very) high spatial resolution data, a third strategy using high spectral resolution data and a fourth strategy combining data sets of different spatial and spectral resolutions. These four strategies are described below. It depends on the information need of the user regarding the field of application and the required spatial scale and thematic detail which strategy is most suitable. Common application fields of urban remote sensing are land cover/land use mapping, urban planning, monitoring of urban development, risk analysis, urban ecology and urban climate.

The first strategy uses the advantage of the large coverage of medium resolution data (i.e. around 30 m pixel size). Such data costs little and is frequently available. Studies using this data mainly focus on land cover/land use in general classes (e.g. Song et al., 2005; Lu and Weng, 2006). Also the vegetation-impervious-soil (VIS) concept developed by Ridd (1995) is often applied to map urban area at a regional scale (e.g. Lee and Lathrop, 2005; Powell et al., 2007). The VIS concept was improved by dividing the impervious class into high and low albedo impervious surfaces (e.g. Wu and Murray, 2003; Weng et al., 2008) because imperviousness is an important parameter for many applications which include urban planning and urban climate. Also Xiao et al. (2007) and Esch et al. (2009a) focus on mapping impervious surface at medium spatial resolution, although they do not make use of the VIS concept. The medium resolution data strategy is also suitable for mapping urban growth or land use change as is shown by for example Madhavan et al. (2001) and Jat et al. (2008). Studies using multispectral medium resolution data use mainly traditional classifiers (e.g. maximum likelihood classificatory or ISODATA) or spectral unmixing. The latter is especially popular for classifications according to the VIS concept. Of course other methods are tested as well, such as in Song et al. (2005), Xiao et al. (2007) and Esch et al. (2009a) which use neural networks, a classification and regression tree model and support vector machines, respectively.

The second strategy uses very high spatial resolution imagery (pixel size smaller than 5 m) because of its possibility to identify small urban objects. This strategy becomes more and more popular with the increase of available very high resolution (VHR) satellite based sensors, such

as IKONOS (4 m spatial resolution, since 1999) or QuickBird (2.5 m spatial resolution, since 2001). As a trade off to their high spatial resolution these sensors do not provide so much spectral information (mostly only three or four bands) and the spatial coverage is smaller. Spectral classification methods such as maximum likelihood classification (Jain and Jain, 2006) or spectral unmixing (Small, 2003; Wu, 2009) have been applied, but are less likely to achieve good results because of the high in-class variability due to the small pixels (Wu, 2009). Therefore information on the image texture and the configuration of objects is used intensively. Object-based classification approaches have been applied manifold, e.g. for mapping land cover (Bruzzone and Carlin, 2006; Su et al., 2008), buildings (Durieux et al., 2008) and roads (Inglada, 2007). Texture and spatial metrics are for example used by Herold et al. (2003a) for mapping urban morphology and land cover classes or by Zhang et al. (2009a) for mapping vegetation structure (patchiness) within an urban area.

The third strategy that can be recognised, though not as commonly applied as the previous two, is the use of hyperspectral sensors. Because most of those sensors are airborne, their spatial resolution is high, between 2.5 and 15 meters. In studies following this strategy the main objective is surface cover mapping and identification of man-made materials (e.g. Ben-Dor et al., 2001; Heiden et al., 2007). The potential of hyperspectral remote sensing and recent applications are addressed in section 3.3.4 in more detail because of their importance to this thesis.

A fourth strategy, increasingly drawing attention, is a combination of the above trends, often referred to with the terms *data fusion* or *information fusion*. High resolution imagery, including digital surface models, expands the information content of lower resolution imagery. It allows making use of the full spectral information of the multispectral or even hyperspectral images and, at the same time, takes advantage of the spatial detail of high spatial resolution imagery. For example Gamba et al. (2007) and Niemann et al. (1998) combine hyperspectral data with very high resolution data (QuickBird, aerial photographs) to improve urban classification quality. Greiwe et al. (2004) combines hyperspectral data with a digital surface model and ortho-photos to improve object-based classification of urban surface cover. Also the combination of optical remote sensing data with radar data is being studied. Both integration of multispectral optical data (e.g. Gomez-Chova et al., 2006) or hyperspectral optical data (e.g. Hepner et al., 1998) with radar data are of interest to improve the quality of urban mapping. The combination of data sets faces some difficulties, such as the co-registration of data sets or different scales and types of data. Therefore most research within this strategy still focuses on the development of data fusion and combination techniques and not yet on the development of applications and products.

### 3.3.3 Remote sensing to support urban climate analysis

In section 3.2.2 and table 3.4 it has already been shown that remote sensing can provide valuable indirect information on the urban climate. Thermal remote sensing is applied for mapping surface temperature directly, e.g. for urban heat island (UHI) analysis. Voogt and Oke (2003) and Weng (2009) provide an overview of methods and applications of thermal remote sensing. Commonly, satellite based sensors with medium spatial resolution and one or more thermal

bands such as ASTER (e.g. Gluch et al., 2006; Frey et al., 2007) or Landsat (e.g. Chen et al., 2006; Small, 2006; Weng and Yang, 2006) are used for mapping the thermal landscape at a regional scale. They focus on meso-scale urban climate. At this scale level, remote sensing has been used frequently for analysis of the relationship between temperature patterns and surface characteristics. For example the relationship with imperviousness (e.g. Zhang et al., 2009b; Yuan and Bauer, 2007; Xian, 2008), fractional vegetation cover (e.g. Jenerette et al., 2007; Weng et al., 2004) or albedo (e.g. Pena, 2008) has been studied frequently. Pinty et al. (2006) studied the radiation characteristics of land surfaces (especially vegetation) to support climate modelling.

Applying remote sensing to studying the urban micro climate at a local scale is less common. Airborne thermal sensors are required for the mapping of surface temperature at this scale level. For example Quattrochi and Ridd (1994) used the TIMS airborne thermal sensor to analyse the thermal response of 25 urban surface materials. Ben-Dor and Saaroni (1997) used a thermal video radiometer mounted on a helicopter to map temperature structures at street level. Stone and Norman (2006) used the airborne thermal multispectral sensor ATLAS to calculate heat flux and related this to land-parcel characteristics such as impervious area and number of bedrooms. Xu et al. (2008) use the thermal band of the airborne hyperspectral sensor OMIS to model sensible heat flux supported by a land cover map derived from the hyperspectral data. Also Jung et al. (2007) uses similar sensors to define the correlation between surface temperature and vegetation (using NDVI).

Urban characteristics influencing the urban micro climate (see section 3.2.2) such as land cover and imperviousness are mapped frequently at a local scale, also with hyperspectral sensors. However, these studies do not use their products for urban micro climate studies. For example Franke et al. (2009) performs a land cover classification at different classification levels using HyMap data. Van der Linden (2008) focuses on the analysis of imperviousness, also using HyMap. Urban structure can be expressed by calculating spatial metrics such as shown by Herold et al. (2003b). The spatial metrics they applied were among others patch density and edge density, expressing the average density, shape and spread of objects of the same land cover.

Only very few studies applied urban remote sensing at a local scale and used it for urban micro climatic analysis. Rigo and Parlow (2007) used a digital elevation model to calculate the sky view factor. Wania (2007) used hyperspectral data to characterise urban vegetation and used this knowledge to simulate the effect of vegetation on the urban micro climate. Jung et al. (2007) and Xu et al. (2008) used hyperspectral data in relation to the urban micro climate to derive a land cover map with general classes for the support of thermal remote sensing analysis.

### 3.3.4 Potential of hyperspectral remote sensing

Knowledge of the location and type of urban objects (e.g. buildings or trees) and the used surface materials is of great importance to urban micro climatic analysis, because these aspects influence the urban micro climate directly (see section 3.2.1). Because the different urban objects are characterised by their surface material, the ability of the hyperspectral data to differentiate between many surface materials can be used to identify the urban objects. The information about the different surface materials can additionally be used to characterise the influence of the urban objects on the micro climate. Different roof materials have different thermal inertia
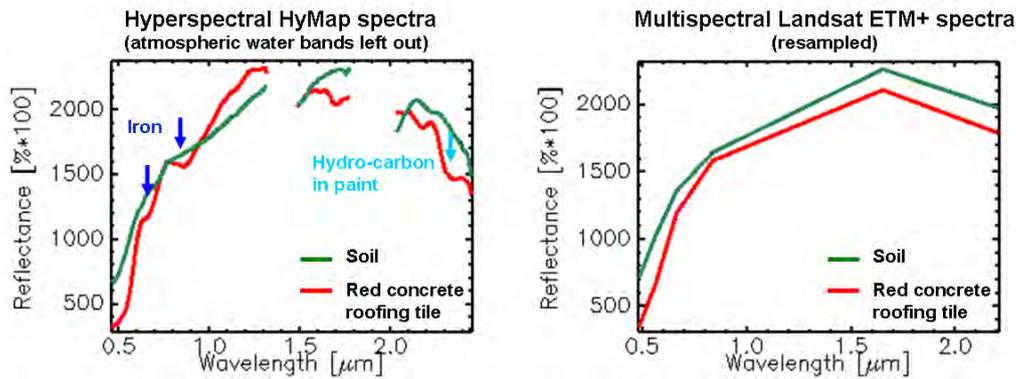
Figure 3.6: *Comparison of hyperspectral and multispectral data. Left: Hyperspectral HyMap spectra of soil and red roofing concrete. Right: The same soil and roofing concrete spectra after resampling to Landsat ETM+ spectral bands*

and albedo properties. Also categorising the different surface materials in classes such as vegetation, impervious surface cover and pervious surface cover provides relevant information for urban micro climatic analysis. The following illustrates what the advantages of a high spectral resolution are for urban mapping and it provides an overview of common approaches for the identification of surface materials and urban objects with hyperspectral remote sensing.

As has been stated before, the urban landscape is characterised by a high heterogeneity. Small objects with clear boundaries are located close to each other. In urban areas there is a large variety of surface materials and thus also a large number of different spectral signatures. Small (2001) showed that the spectral dimensionality of urban areas is up to 2.5 times higher than that of non-urban areas. To represent this higher dimensionality, a higher spectral resolution is required. Herold et al. (2003a) confirmed these findings in a study on the classification ability of urban materials with IKONOS (4 bands), Landsat TM (6 bands) and AVIRIS data (224 bands), where the best classification results were achieved with AVIRIS data. Not only the number of bands, but also the spectral location of the bands is important. Many urban materials have typical features which are only visible in a narrow wavelength range. Therefore, the position, width and number of available spectral bands is important for the separation between different materials. The availability of several bands in the SWIR region is essential, since hydro-carbons and several characteristic minerals (e.g. kaolinite, calcite and dolimite) have absorption features in this region (Heiden et al., 2007; Herold et al., 2004) (see also table 3.5).

Figure 3.6 illustrates the advantage of a high spectral resolution for the identification of different surface materials. The spectra of bare soil and red roofing concrete (tiles) are shown on the left side. The roofing tile shows a peak in the red because of the colour, absorption features of iron at 670 and 870 nm and absorption of hydro-carbons in the synthetic paint at 2300 nm and higher wavelengths (Heiden, 2004). With those features, the roofing tile is clearly separable from the bare soil. However, if only a few spectral bands are available such as in Landsat ETM+ data (figure 3.6, right), these features are no longer visible. The difference between the two spectra is less then 3% in overall albedo, which might be caused by illumination effects (shade, inclined roof) as well. This makes it difficult to separate soil from roofing tiles and also other impervious materials using multispectral data. Since the separation between pervious and

impervious materials is especially important in urban analysis, the use of hyperspectral data is advantageous. A study of Cavalli et al. (2008) shows that a classification of the urban area of Venice, Italy with the hyperspectral sensor Hyperion (30 m pixel size) has similar accuracy as classification results of the higher resolution multispectral sensor MIVIS (8 m pixel size). Because of the high spectral resolution hyperspectral data has much more potential for analysing mixed pixels than multispectral data (see section 5.1).

For hyperspectral mapping of surface materials knowledge on the spectral reflection characteristics of the materials is used. Analysis of the spectral characteristics of urban surfaces is often carried out by field spectroscopy or high resolution airborne hyperspectral data in combination with field spectroscopy. Urban materials can be characterised by using different spectral analysis techniques (e.g. Bassani et al., 2007; Heiden et al., 2007). An overview of the spectral characteristics of a selection of important urban materials is given in table 3.5 based on studies by Heiden et al. (2007), Heiden (2004) and Herold et al. (2004). Absorption features can be numerically described by the mean, standard deviation and ration of the reflectance between two wavelengths, by the area under the feature in the spectrum, and by the absorption depth and position (Heiden et al., 2007).

Several aspects influence the spectra of man-made materials. The effects of ageing on the man-made materials are an important research topic. Usage, dust and erosion can largely change the spectral signature, e.g. for asphalt as described by Herold and Roberts (2005). Also bidirectional reflectance distribution function (BRDF) effects can have a significant effect in urban areas. The BRDF is a function which describes the reflectance properties of a material under different illumination and view angle. This is of importance to roofs, for example. Roofs have varying inclinations and orientations towards the sun. As a result they receive and reflect varying amounts of light in varying angles. In addition, shadows are cast by the large number of buildings. This reduces the albedo of the material in the shadow or even makes the spectra unrecognisable (Lacherade et al., 2005).

Once an overview of the spectral signatures and their variation has been created, a suitable classification scheme and mapping method can be selected to identify the urban objects and surface materials. Depending on the focus of the study and the quality of the spectra in the study area, the detail of the mapped classes can be up to single roof and street cover materials (e.g. Heiden et al., 2007). Because of the relatively small objects in urban areas and the resulting high amount of mixed pixels, spectral unmixing approaches are used frequently (e.g. Ben-Dor et al., 2001; Segl et al., 2003; Franke et al., 2009). Also spectral angle mapper (SAM), a method to classify pixels by comparing image spectra with known spectra of the material (endmember) is often used (e.g. Bhaskaran et al., 2004; Chen and Hepner, 2001). Of course more traditional classification approaches are applied as well, both on original bands as on transformed spectral bands, such as maximum likelihood classification (e.g. Dell'Acqua et al., 2005; Herold et al., 2004). A transformation of spectral bands is applied to reduce the noise, de-correlate bands or reduce data dimensionality, for example with a minimal noise fraction transformation or principal component transformation.

A few research groups work on extensive mathematical approaches such as morphological profiles to analyse urban hyperspectral data (Benediktsson et al., 2004; Plaza et al., 2004). In those approaches the spatial organisation is also explicitly taken into account. Spatial information (e.g. on the neighbouring pixels) can provide very useful a priori information for the

classification of urban areas. Because the borders of urban objects are usually crisp, image segmentation is a promising approach. It attracts more and more attention, also for hyperspectral data. An interesting example is the use of support vector machines (SVM) to model and classify at segment level (e.g. Lizarazo, 2008; Van der Linden et al., 2007).

Often the hyperspectral data is extended with information from other sources for urban analysis. A common aim of using such additional data is to identify buildings a priori to the classification. This is required because several materials are used both as roofing material and as surface material (e.g. bitumen roof and asphalt or red clay tiles and red loose chippings). Because in these cases the same materials are used for different urban objects, it is not possible to separate these objects based on their spectral characteristics. A priori information on the building locations solves this problem. Various data sources are used such as a digital elevation model (DEM) derived by stereo imagery (e.g. Greiwe et al., 2004; Madhok and Landgrebe, 1999), cadastre data (e.g. Heldens et al., 2008), lidar or radar data (e.g. Bochow et al., 2007b; Chen et al., 2003). Also very high resolution imagery is used in combination with hyperspectral data at different levels of data fusion (e.g. Gamba et al., 2007; Niemann et al., 1998).

Section 5.1 describes the methods to identify urban objects and surface materials which are applied in this study.

Table 3.5: *Overview of characteristic spectral features of important urban materials based on studies by Heiden et al. (2007); Herold et al. (2004); Heiden (2004).*

| Material | General spectral shape between 0.4 and 2.5 $\mu$m | Characteristic absorption features | Remarks |
|---|---|---|---|
| *Mineral roofing materials* | | | |
| Clay roofing tiles (red) | Increasing reflectance in NIR and SWIR | Iron oxide at 0.52 $\mu$m, 0.67 $\mu$m and 0.87 $\mu$m. Clay minerals at 2.2 $\mu$m | |
| Roofing concrete | High reflectance | Pulp fibre at 2.1 $\mu$m Calcite at 2.34 $\mu$m | |
| *Metallic roofing materials* | | | |
| Zinc (also galvanised metal) | | Zinc at 1.04 $\mu$m | Albedo strongly depending on sun and sensor angle. |
| Aluminium | | Aluminium at 0.84 $\mu$m | Albedo strongly depending on sun and sensor angle. |
| Copper | Slight decrease in SWIR | Copper peak between 0.47 $\mu$m and 0.7 $\mu$m | Colour of copper (and thus the absorption peak) changes over time from red to green due to erosion |
| *Synthetic roofing materials (hydrocarbons)* | | | |
| Polyethylene | High reflectance, decrease after 2.2 $\mu$m | Hydrocarbon at 1.2 $\mu$m, 1.7 $\mu$m and after 2.2 $\mu$m | Reflectance in VIS depending on the colour |
| PVC | Decrease in reflectance after 0.5 $\mu$m | Hydrocarbon at 1.7 $\mu$m | |
| Bitumen | Low reflectance | Hydrocarbon after 2.2 $\mu$m (2.2 $\mu$m, 2.23 $\mu$m, 2.32 $\mu$m) - weak | |
| *Impervious surface materials* | | | |
| Asphalt | Low reflectance | Silicates at 2.2 $\mu$m - weak    Hydrocarbons after 2.2 $\mu$m - weak | Increase of reflectance when ageing |
| Concrete | High reflectance | Calcite at 2.34 $\mu$m    Dolomite at 2.37 $\mu$m | Depending on the mineral composition of the concrete (regional differences) |
| *Partially impervious surface materials* | | | |
| Cobblestone (granite) | High reflectance | Silicates at 2.2 $\mu$m    Calcite at 2.34 $\mu$m | Depending on the type of stone used. |
| Loose chippings (grey, red) | High reflectance | Clay minerals (kaolinite) at 2.19 $\mu$m and 2.2 $\mu$m Iron oxide at 0.52 $\mu$m, 0.67 $\mu$m and 0.87 $\mu$m (red split) | |

# 4 Study area and data

For the implementation of the conceptual framework a case study has been carried out. In this chapter the study area will be introduced. Next, the available remote sensing data sets will be described. Also the auxiliary data used in this study, e.g. for validation, will be listed here. Finally, the pre-processing of the remote sensing data sets during which the data is prepared for the actual remote sensing analysis will be addressed.

## 4.1 Study area

The analysis of the hyperspectral data to support urban micro climate characterisation was carried out for a case study in the city of Munich. The location of the metropolis nearby DLR - DFD in Oberpfaffenhofen is advantageous to data acquisition and discussion with urban planners. The city, founded in the year 1158 at the shores of the river Isar, covers 310 square kilometres and has over 1.3 million inhabitants (www.münchen.de). In figure 4.1 an illustration of the variety of urban structural types in Munich is given. Dense structural types can be found mainly in the city centre (A), along the river Isar. Between and within the different neighbourhoods are many smaller and larger parks, such as Olympia Park (B) in the north or the park around Castle Nymphenburg (C) in the west. The urban structural type with the largest area coverage is detached and semi-detached housing, resulting in a very green urban area. In 2002, 62% of the municipality is covered with vegetation, 14% is built up. Asphalt (18%) and permeable pavements (6%), which are mainly part of the transportation network, cover the rest of the municipality (Fischer, 2002).

For the development of the methodology a test area of 3 x 5 km$^2$ is selected. The main selection criterion is the presence of a large variety of urban structural types on a close range. In figure 4.2 the test area is presented. It is located east of the city centre of Munich. The eastern railway station (Ostbahnhof) is in the middle of the test area. At the left hand side is the river Isar, with the Museum Island (Deutsche Museum). Along the railway track from north to southwest there is first a large (former) industrial area (Kunstpark Ost, now mainly cultural use) and then a large cemetery (Ostfriedhof). There is a clear gradient of highly urban, dense buildings in the west near the city centre to more open building patterns in the east. The railway track forms an imaginary border between the high and low density built up areas. Because of this gradient a large variety of urban structural types is present. In total 1094 building blocks are present in the test area, with 33 different urban structural types. This study focuses on the 12 main urban structural types, which have been described in section 3.1.3. These urban structural types cover 76% of the building blocks in the test area. In figure 4.3(a) a histogram of the percentage of each urban structural type for Munich and the test area is shown. The variation within the test area mainly corresponds with the variation in Munich. Exceptions are the detached and semi-detached houses (a3) which cover 23% of the building blocks in Munich and only 7% in the
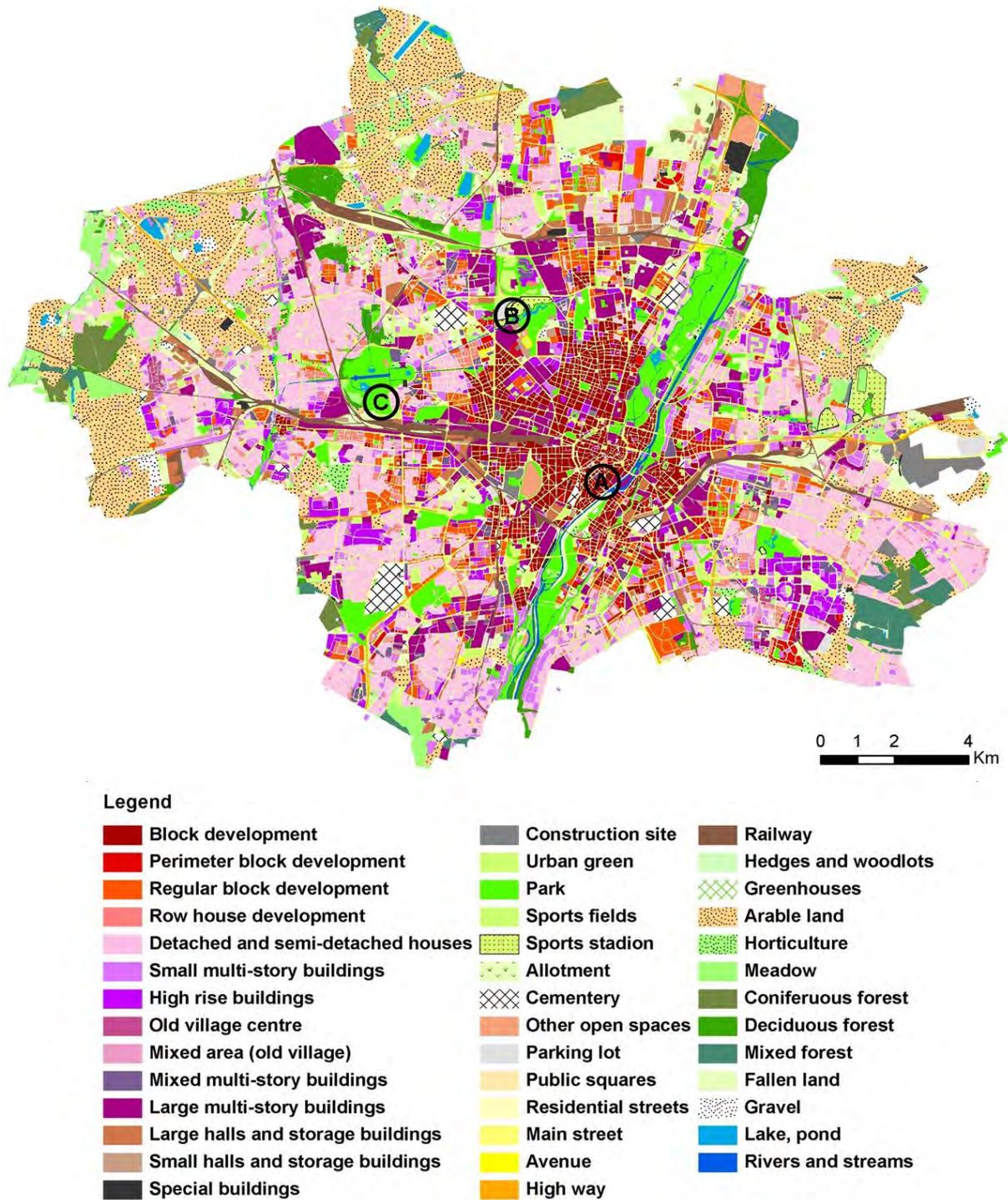
Figure 4.1: *Urban structural types in Munich in 2002 (Data provided by the Municipality of Munich)*
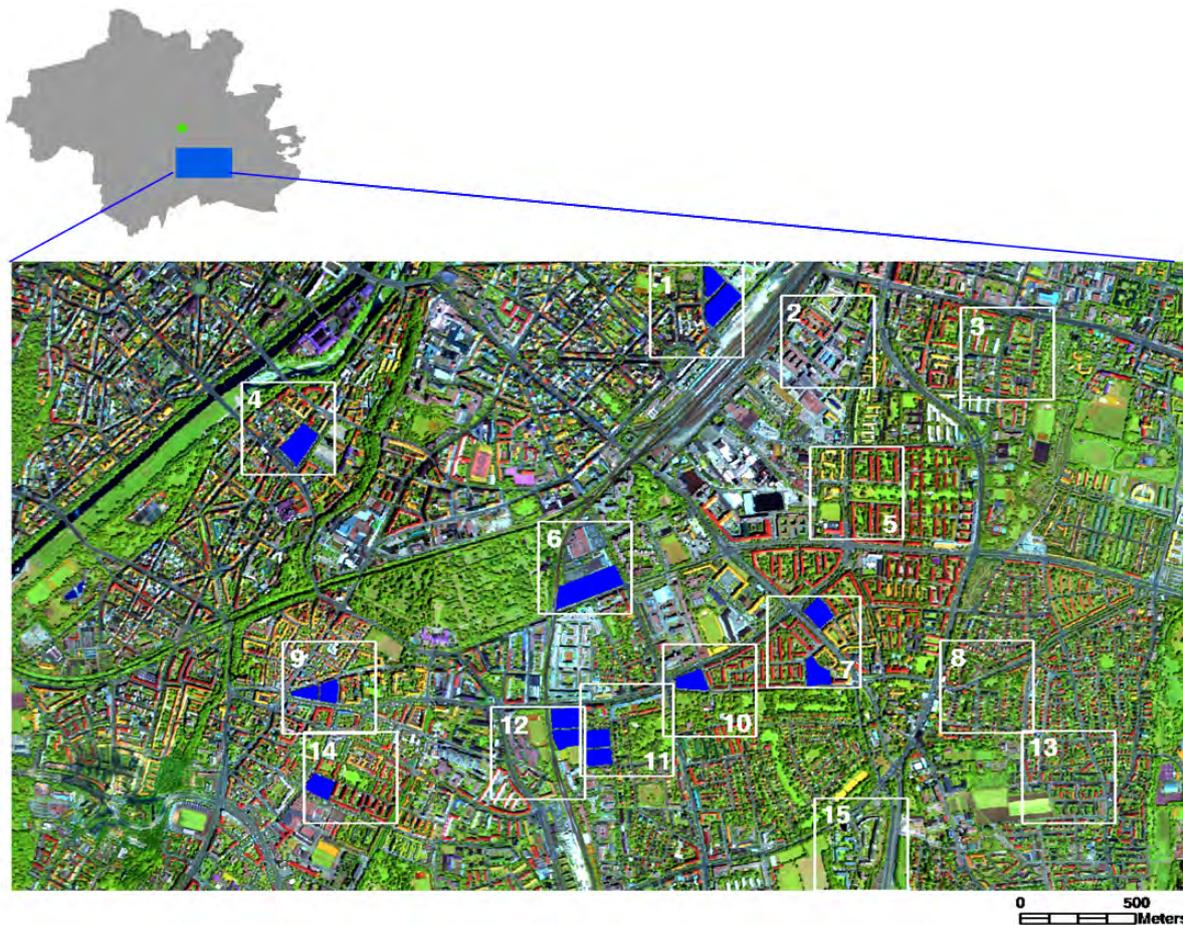
Figure 4.2: *Location of the test area (blue) and the simulation area Theresienstraße (green) in Munich (on top) and a HyMap color composite of the test area with the validation blocks indicated in blue and the location of the simulation areas in white (below)*

test area and the high density block development (a1) which covers 19% of the building blocks in the test area but 7% in Munich. This is a result from the vicinity of the city centre which is dominated by high density structures. However, all 12 urban structural types show enough instances to form a representative test area.

Within the test area, 14 building blocks are selected as validation areas. They cover the most important urban structural types and are used to validate the hyperspectral data products (see section 5.1.4 for a detailed description of the validation concept). Their location is indicated in figure 4.2. For the implementation of the hyperspectral data products into a micro climate model 15 areas of 400 x 400 m$^2$ are selected to test the approach. The simulation areas include the 14 validation blocks. An additional objective was to include a representative number of each urban structural type. The histogram in figure 4.3 (b) shows that the variation of the urban structural types (95 building blocks in total ) is comparable with the variation within the test area.

An additional simulation area of 400 x 560 m$^2$ is located north of the city centre around the Theresienstraße (indicated in green in figure 4.2). A meteorological station of the Lud-
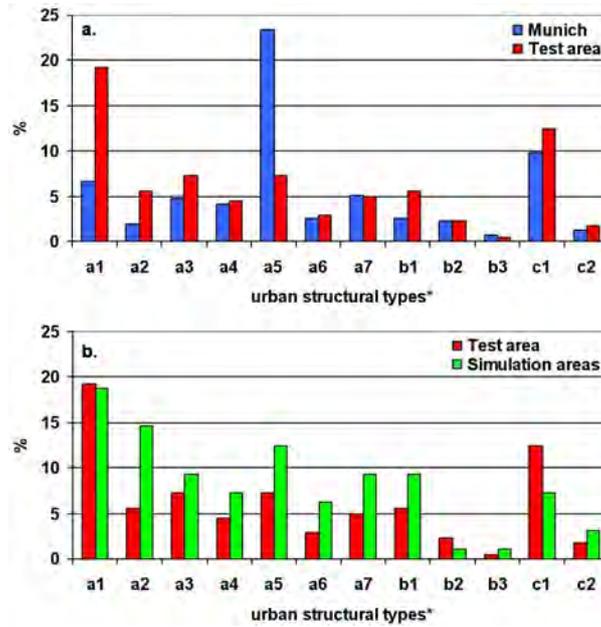
Figure 4.3: *Frequency of the 12 selected urban structural types in Munich and the test area (a) and in the test area and the simulation areas (b). * a1=dense block development, a2=perimeter block development, a3=regular block development, a4=row house development, a5=detached and semi-detached housing, a6=high rise buildings, a7=small multi-storey buildings, b1=large multi-storey buildings, b2=large halls and storage buildings, b3=small halls and storage buildings, c1=parks and urban green, c2=sports fields*

wig Maximilian University of Munich is located there, providing continuous measurements of temperature, wind speed and humidity (www.meteo.physik.uni-muenchen.de). This opens the opportunity to use realistic input parameters for the urban micro climate model and compare its results with the measured values (see also section 5.4). The location of the simulation areas within the test area is shown in figure 4.2. In appendix A aerial photographs of all simulation areas with indication of the urban structural types are included.

## 4.2  Available data

For the research described in this thesis five data sets are available: hyperspectral data, height data, vector data of building blocks and building locations, aerial photographs, and thermal airborne images. The spatial coverage of the data sets is indicated in figure 4.4.

On June 17th and 25th 2007 hyperspectral data, aerial photographs and thermal images of the Munich region were acquired in the context of the REFINA project (Klein et al., 2009) during the HyEurope2007 campaign at DLR. For the REFINA project data on some towns in the rural outskirts of Munich were recorded. This thesis, however, focuses on the city of Munich. The hyperspectral data was recorded with the HyMap sensor (Cocks et al., 1998) in seven north-south oriented flight lines. This airborne whiskbroom sensor has 128 narrow spectral bands, ranging from 450 nm to 2500 nm. At a flight height of 2000 meter, as applied for this study, the
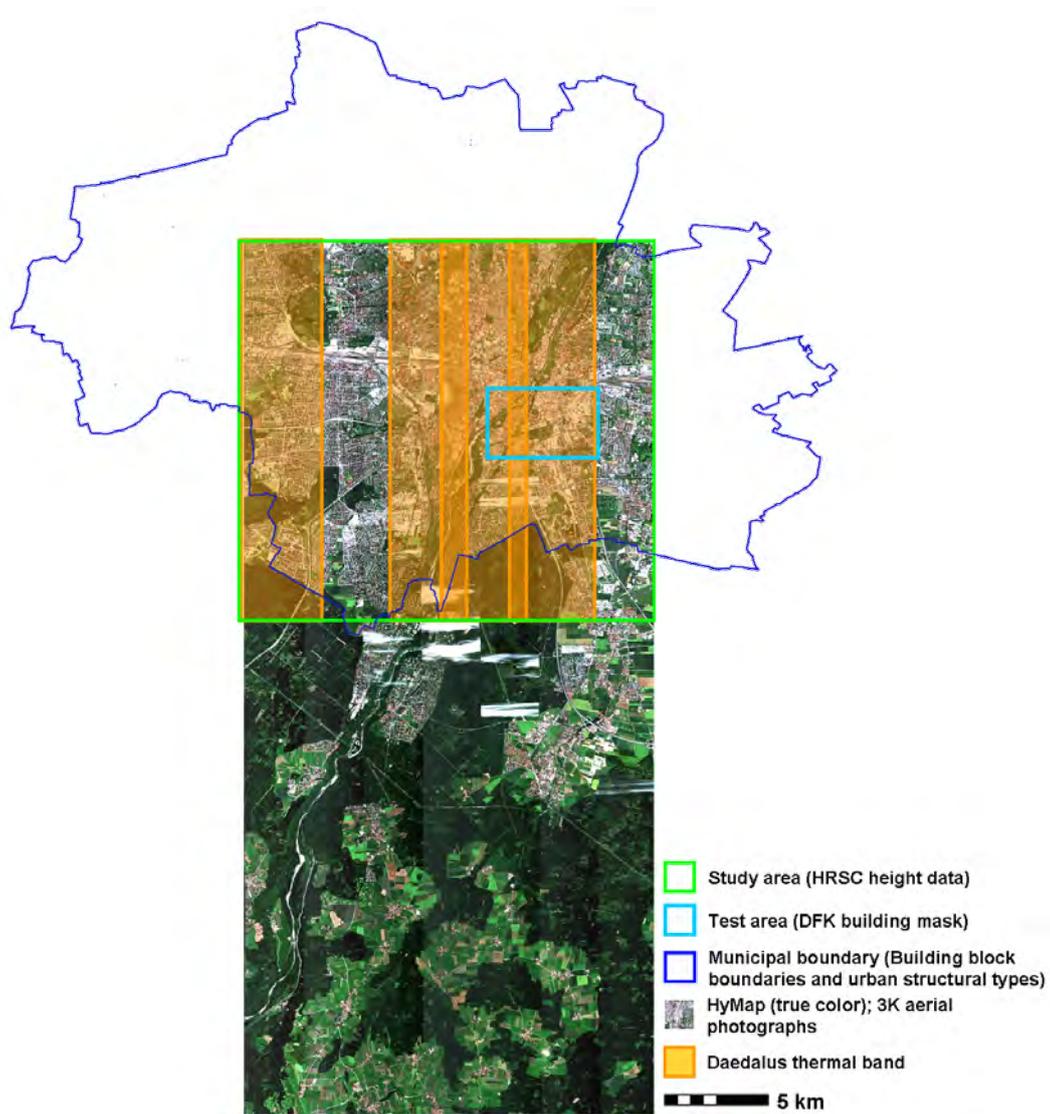
Figure 4.4: *Spatial coverage of the available data sets and spatial extend of the study area and the test area*

Table 4.1: *Spectral characteristics of the HyMap sensor (Cocks et al., 1998)*

| Spectrometer | No. of bands | Bandwidth [nm] | Wavelength range [nm] |
|:---:|:---:|:---:|:---:|
| VIS | 32 | 15 | 400-900 |
| NIR | 32 | 16 | 885-1350 |
| SWIR I | 32 | 16 | 1400-1800 |
| SWIR II | 32 | 20 | 1900-2500 |

spatial resolution is 4 meter. The broad field of view of 61°of HyMap results in a swath width between 2 and 2.5 km at this flight height. The spectral characteristics of the sensor are listed in table 4.1.

The 3K-camera actually consists of three digital cameras mounted on a platform, of which one is pointed nadir, the second pointed to the left and the third is pointed to the right (Kurz et al., 2007). The cameras are combined to broaden the field of view to 111°in total. At a 2000 meter flight height this results in a spatial resolution of 50 cm (25 cm for the nadir pointing camera and 50 cm for the left and right pointing cameras) and a swath width of 5.8 km.

The thermal images were recorded with the multispectral sensor DAEDALUS AADS 1268 Airborne Thematic Mapper (ATM), operated by DLR. The whiskbroom scanner has a total field of view of 86°. The nine channels in the visible and near infrared part of the spectrum are left out of consideration. The thermal band covers the spectral range from 8 to 13 $\mu$m.

The HyMap sensor, the 3K camera and the Daedalus scanner were mounted on the same airplane. The pre-processing of the hyperspectral data is described in section 4.3.1. From the 3K images geo-referenced ortho-photos were derived by DLR-IMF. The ortho-photos are used for validation and referencing purposes. The Daedalus thermal images were also pre-processed by DLR-IMF. The measured radiance was converted to surface temperature using in-flight black body measurements. A geo-correction was carried out, in which the thermal images were resampled to 4 m pixels. However, strong turbulences and a defect in the GPS-system during data acquisition made that the Deadalus images did not reach the geometric accuracy of the HyMap data. This makes a direct, pixel-by-pixel combination of the two data sets impossible. However, the thermal images can still be used to visual compare the results of the micro climate model (see section 5.4.4).

The height data was derived from HRSC stereo aerial photographs by DLR-Berlin. The HRSC images were recorded on September 15th 2004. The height data has a spatial resolution of 1 meter in the x- and y-direction and 10 cm in the z-direction. After further processing (described in section 4.3.2), the height data is used as base data for the urban micro climate model (described in section 5.4) and to support the identification of buildings during the hyperspectral data analysis (see section 5.1).

For the analysis of the urban structural types a vector data set provided by the municipality of Munich is used. This data set contains the boundaries of the building blocks, the urban structural type of each block and according parameters such as degree of impervious surface and vegetation density (Fischer, 2002). The classification of urban structural types was created in 1998 and updated in 2002. The building block boundaries are used as a reference unit for the spatial indicators. The parameters are used for validation of the spatial indicators derived from the hyperspectral data. Several building blocks have been changed during the five years that lay between the hyperspectral data take and the generation of the map of structural types. If these changed building blocks lay within one of the sixteen simulation areas, their urban structural type has been updated. Additionally a vector data set of buildings is provided by the municipality of Munich. It consists of the cadastral building layer of January 2008. This data set is used to support the identification of buildings during the hyperspectral data analysis.

# 4.3 Pre-processing

Pre-processing is a necessary step to bring the available remote sensing data in a form that is suitable for thematic analysis and improves the quality of the data. For this study the pre-processing of the HyMap data set included atmospheric and geo-metric correction, the removal of cloud shadows and a nadir normalisation. The pre-processing of the HRSC digital elevation model consisted of the calculation of a normalised digital elevation model, in which only the urban objects are included. The last and very important step in pre-processing was the co-registration of the four data sets.

## 4.3.1 Pre-processing of the hyperspectral data

The HyMap data set of the study area consists of 7 north-south oriented flight lines recorded on June 17th 2007. The sixth line is recorded on 26th of June, because of large cloud cover on the first data take. The HyMap data was received as radiometric corrected data. As a first pre-processing step, three bad bands have been removed. These were the first band of the VIR spectrometer and the first and second band of the NIR spectrometer (band nr. 1, 33 and 34), leaving 125 bands.

Next, the data was corrected for atmospheric influences and converted to reflectance with ATCOR atmospheric correction software (Richter, 2007). The atmospheric correction was optimised using field spectra of bright homogeneous surfaces recorded during the overflight on June 17th (a concrete parking roof and a tennis court).

Several clouds and shadows caused by clouds covered the study area during data acquisition. With a special module within ATCOR it is possible to remove the cloud shadows. This allows retrieval of some spectral information of the shaded pixels and avoids having to discard those areas for further data processing. The methodology applied in this algorithm to retrieve a normal spectrum from the shadowed spectrum is described in Richter and Müller (2005). The cloud removal module is applied to subsets containing the affected areas. The corrected subsets are then merged into their original image lines.

Since HyMap has a broad field of view of 61°, view angle effects influence the measured spectra. Schiefer et al. (2005) describe such effects and present a solution for the across track brightness gradient. A brightness gradient can also be noticed in the HyMap data set of the Munich study area. Because the images were recorded in the morning between 8:45 and 10:15 the objects in the image were illuminated from the east. As a result of this solar angle, the sensor viewing angle and the north-south flight direction, the images show a brightness gradient increasing from east to west. This can be noticed in the radiance image in figure 4.5, where the left side of the subset is slightly brighter than the right side. Figure 4.6 shows in the left graph the mean reflectance for each column of each HyMap flight line, confirming a brightness gradient of up to 7 % reflectance. The effect is less strong in flight line six (only 2 %), because this line is recorded at June 26th around 11:30. The brightness gradient has been corrected with a simple nadir normalisation included in the ATCOR software. This approach normalises each pixel according to the sensor viewing angle.

The last step of pre-processing the HyMap data was the geo-referencing. Within this step, the imagery was corrected for the roll, pitch and yawn of the airplane during the data take. The location and airplane movements have been recorded during the overflight. The geo-correction
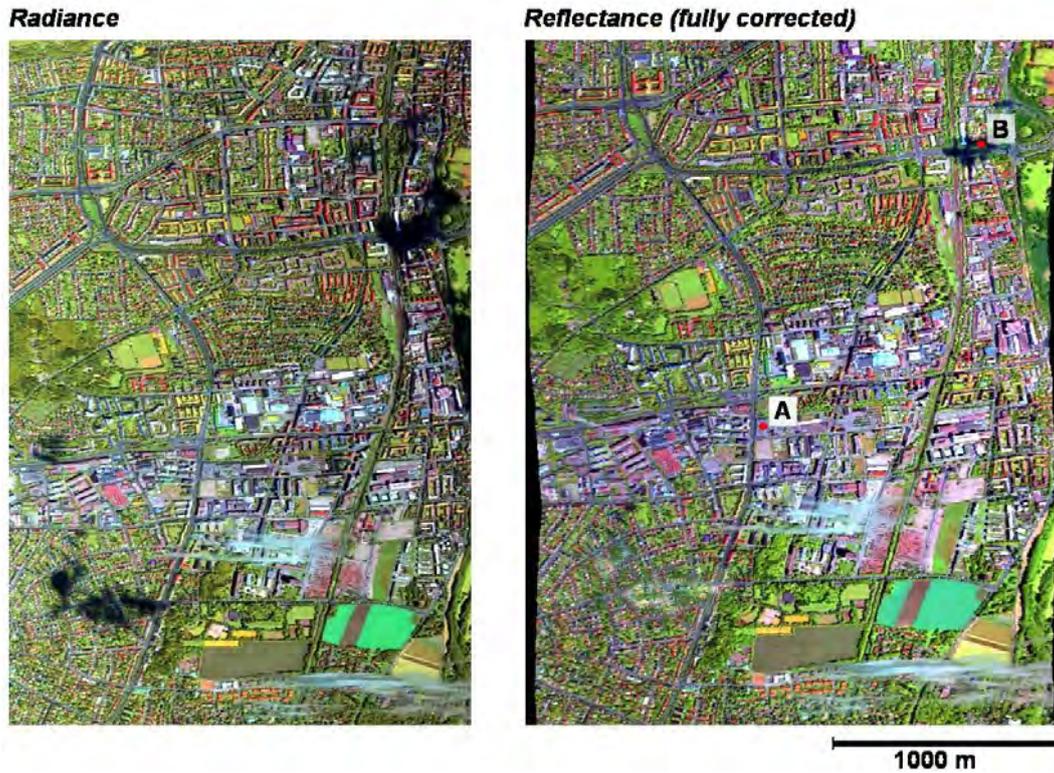
Figure 4.5: *Subset of the third HyMap flight line. Left, the uncorrected radiance image. Right, the fully corrected reflectance spectrum (atmospheric correction, cloud shadow removal, nadir normalisation and geometric correction applied).*
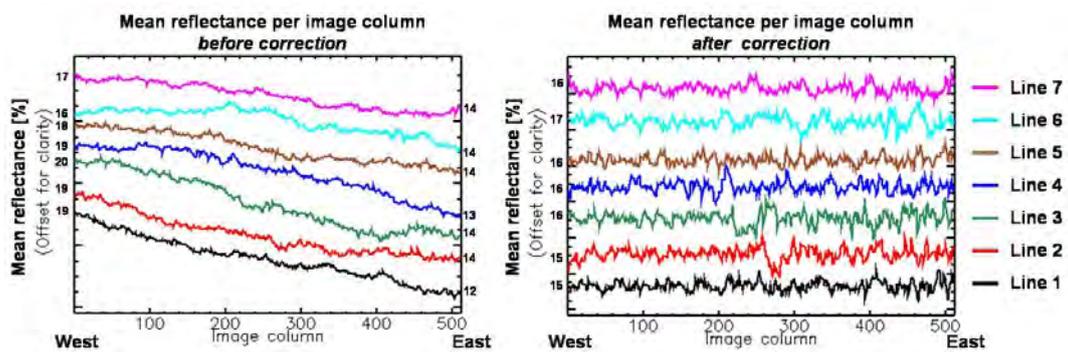


Figure 4.6: *Mean reflectance per image column showing an across track brightness gradient (left) and the mean reflectance per image column after nadir normalisation (right).*

42
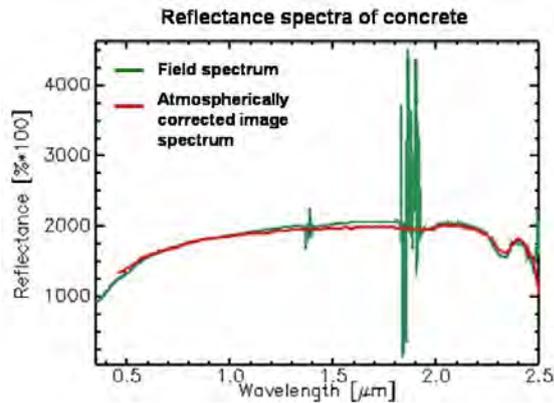
Figure 4.7: *Comparison of a field reflectance spectrum and an image reflectance spectrum (after atmospheric correction) of concrete.*
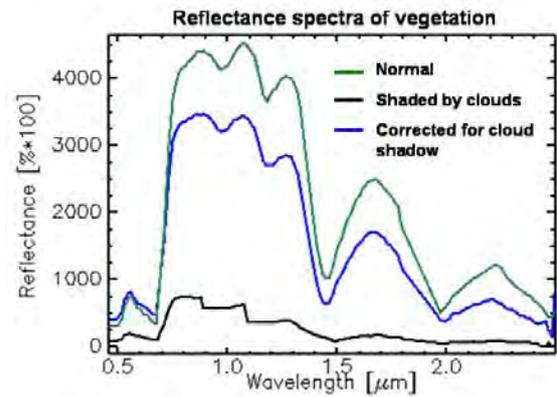


Figure 4.8: *Reflectance spectra of vegetation without shadow, shaded vegetation and a shadow-removed vegetation reflectance spectrum.*

and referencing to the UTM WGS 84 coordinate system was done with the software OR-THO (Müller et al., 2005). Additional ground control points have been used to improve geo-registration. The pixel size is 4 x 4 m$^2$. The data was resampled using a nearest neighbourhood interpolation, leaving the spectra intact.

In figure 4.5 the results of the pre-processing of HyMap are presented. On the left a subset of the radiance image is shown with band 81 in red, band 19 in green and band 7 in blue. This band combination is also applied to the final reflectance image on the right. As a quality assessment of the atmospheric correction a reflectance spectrum of concrete from this image (marked with A in figure 4.5) is compared with the mean concrete spectrum measured with the field spectrometer. Figure 4.7 shows both spectra, which are in good agreement. In figure 4.8 three reflectance spectra are shown which indicate the effect of the cloud shadow removal. The first spectrum is a normal image vegetation spectrum outside the cloud shadow. The second spectrum shows a vegetation spectrum within a cloud shadow. The third spectrum shows a vegetation spectrum which is corrected for the cloud shadow. The albedo of the corrected spectrum is not as high as the normal vegetation spectrum, which can also be caused by natural variation in albedo among vegetation. However, the shape of the spectrum and most of the albedo could be restored with this correction step. This made the spectral information within the cloud shadows available for further spectral analysis. Still some very deep shadows could not be completely removed such as in the upper right of the subset in figure 4.5 (marked with B).

The nadir normalisation effectively normalised the albedo of the east and west side of the flight lines. This is confirmed by the average reflectance per image column for the different flight lines as shown on the right in figure 4.6.

For the subset shown in figure 4.5, a strong geo-correction was not needed because for this flight line the roll, pitch and yawn of the airplane were relatively small. The main effect of the geo-correction which can be seen in this figure is the effect of geo-referencing: expanding the image in all directions. During the data take of the other flight lines the airplane movements were sometimes larger. In general the geo-correction of all flight lines could be carried out successfully, with an overall RMSE for all flight lines of 0.8 pixels (see also section 4.3.3).

However, several lines of pixels in the fourth flight line could not be corrected, due to severe turbulence during data acquisition. The GPS system was not able to record the airplane positions accurately enough in those image lines.

Summarising, the quality of the hyperspectral data set after pre-processing is good, both spectrally and spatially. In figure 4.9 those areas are indicated where attention is needed during the following processing steps, especially spectral analysis. Figure 4.9 indicates areas with cloud cover, the areas where a removal of cloud shadows is carried out and the areas where the geo-correction was unsatisfactory.

### 4.3.2 Pre-processing of the height data

The HRSC height data as derived by DLR-RM-OS from HRSC stereo imagery (Scholten et al., 2003) is a digital elevation model (DEM) containing both terrain and object height. Only the height of the objects (buildings and trees) is needed for this study. Therefore a normalised digital elevation model (nDEM) needs to be calculated by subtracting the surface height (digital terrain model, DTM) from the HRSC-DEM. The DTM for Munich is retrieved from the DLR-SRTM database (Habermeyer et al., 2008) with a spatial resolution of 20 x 20 m$^2$. The first step is thus to resample the DTM to the resolution of the height data (1 x 1 m$^2$). To avoid staircases in the resampled DTM a bilinear interpolation method was applied for the resampling and the resampled terrain height was smoothed with a low pass filter of 7 x 7 pixels. This improved DTM is subtracted of the HRSC DEM. The nDEM thus retrieved is resampled to 4 x 4 m$^2$ pixels to match the HyMap data. A nearest neighbour resampling approach is used, because this resulted in crisper object borders than when using a pixel aggregating resampling approach.

To create a building mask, all objects higher than 6 m are selected. Of course trees are also included in those objects. But because they are spectrally so different from buildings this is not a problem.

Figure 4.10 gives an impression of the height data. The original HRSC height data and the derived object height map are shown for an area next to the river Isar. In the original height data it can be seen that there is a steep slope parallel to the river. In the object height image this height difference is corrected for. Only a line of trees mark the slope in this image.

The height of the objects in the nDEM was validated at 124 buildings randomly spread in the test area. The height of these buildings was manually determined based on the height difference between the building roof and the surrounding ground in the original HRSC DEM. The average absolute height difference between the nDEM and the reference is 1.82 m ($\sigma$ 1.68 m). This is less than one building floor.

In figure 4.11 the HRSC-derived building mask is compared to the high quality building vector data of the municipality of Munich (DFK building mask). Because the height data is 4 years older than the building mask, several newer buildings are missing (e.g. see A in figure 4.11). Other buildings which are missing in the HRSC-mask are actually underground car parks which are also included in the DFK-mask (e.g. at B in figure 4.11). They are usually covered with lawns and can therefore not be recognised in remote sensing data. Low buildings (e.g. detached and semi-detached houses) are not always included in the building mask (e.g. around C in figure 4.11). In general the buildings are slightly larger than in the municipal building map, which is visible in figure 4.11 by small green lines between streets and buildings (both in white). Bridges are falsely included as buildings because they are high (see D in figure 4.11) and
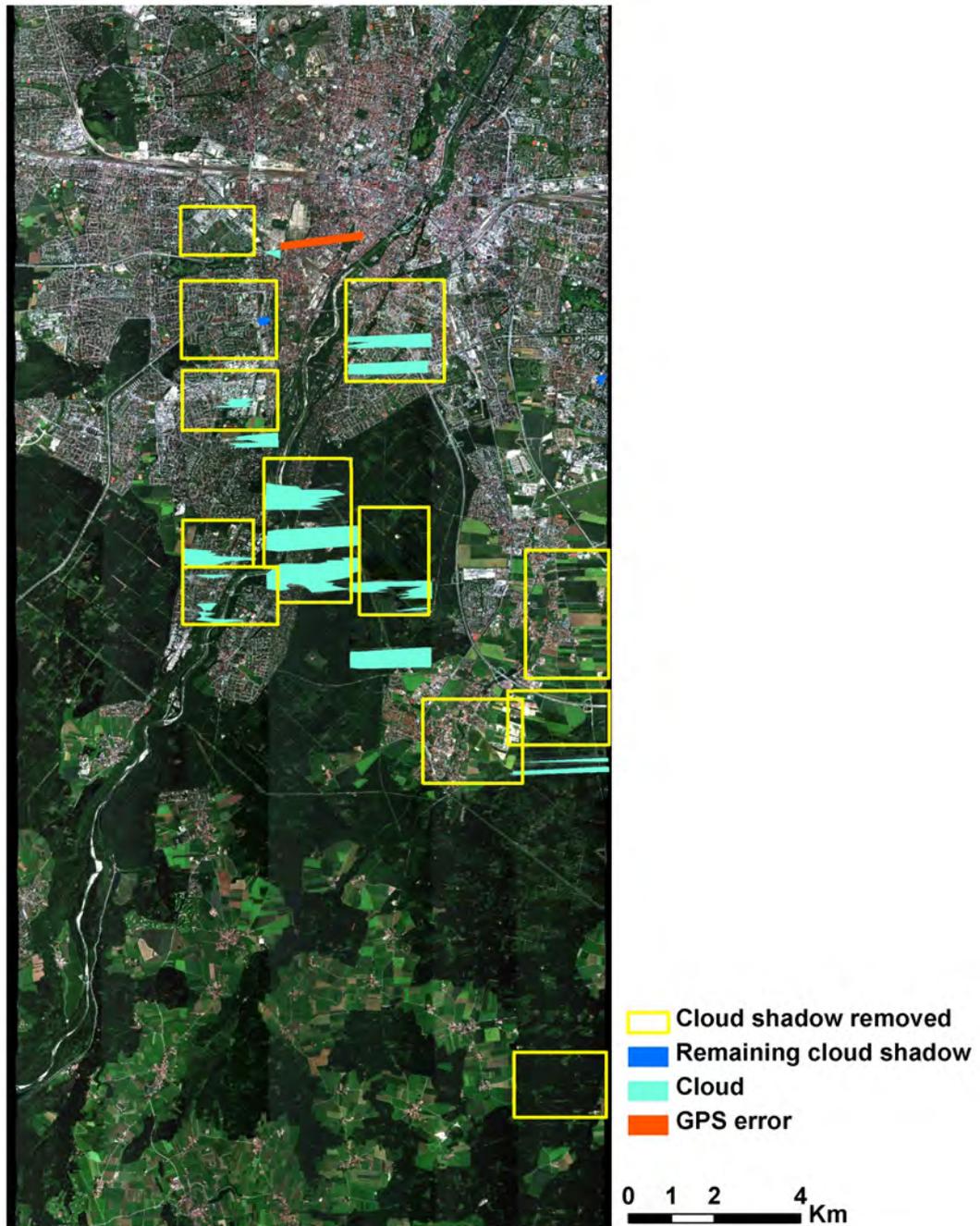
Figure 4.9: *Location of cloud cover, cloud shadow correction and GPS-errors in the HyMap data.*
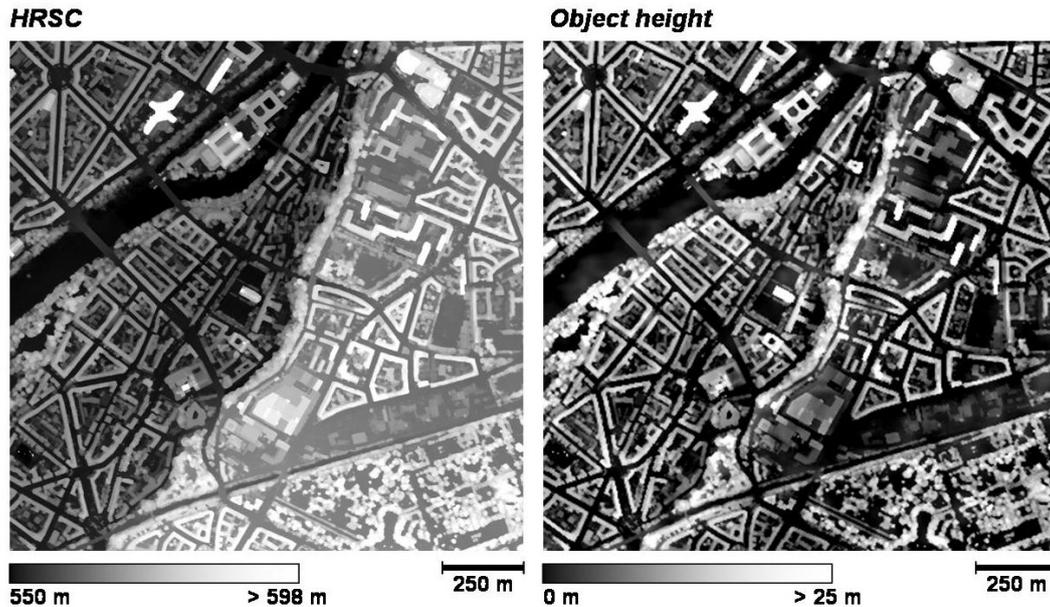
Figure 4.10: *The original HRSC height data next to the derived object height for a subset around the river Isar*

several open areas (fields, squares) where the DEM normalisation was not perfect are included as well (outside subset of figure 4.11). Nevertheless, the quality of the HRSC building mask is satisfactory for most parts of the data set.

### 4.3.3 Co-registration of the data sets

An accurate co-registration of the four data sets (HyMap, nDEM, building block vectors and ortho-photos) is of crucial importance. With a 4 meter pixel size, a difference between two data sets of more than a pixel can cause for a whole building to be displaced. Therefore extra effort has been made to co-register the different data sets. The nDEM, 3K-nadir images and the vector data of building blocks and buildings have shown a perfect fit to each other and an IKONOS image of 1 meter spatial resolution that has been geo-referenced with an accuracy of less than one meter. The HyMap imagery was less accurate: quality varied throughout the images. Because of drifting of the IMU and severe aircraft movements during the data take, the geo-coding based on the recorded IMU data did not perfectly fit the 3K-nadir images. For each HyMap flight line between 34 and 69 ground control points were collected based on the 3K-nadir images. Based on those points a first degree polynominal transformation with nearest neighbour resampling was applied to improve the co-registration of the HyMap data to the other data sets.

In table 4.2 the result of the co-registration of the HyMap flight lines to the other data sets is listed by the root mean squared error (RMSE). The average RMSE for all 7 flight lines is 0.8, with a maximum of 0.94 (line 4) and a minimum of 0.68 (line 3). Geo-referencing with a mean RMSE of less than one pixel is a good result for airborne sensor data (Schläpfer and Richter, 2002). However, in further analysis, especially sub-pixel analysis, one should still be aware of co-registration errors.

46
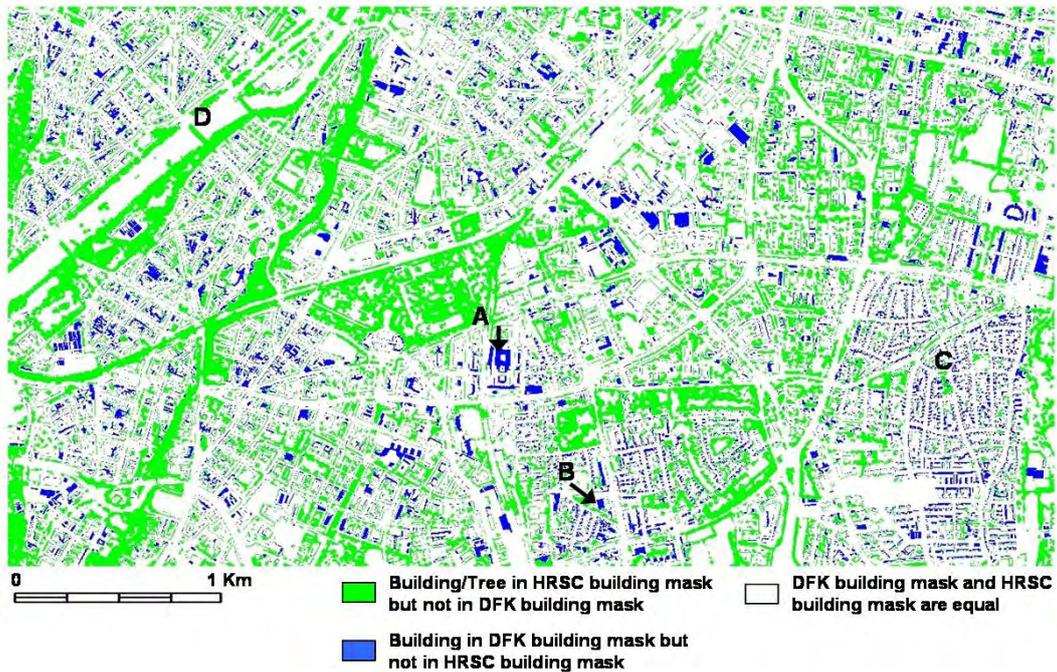
Figure 4.11: *Comparison between DFK building mask and HRSC building mask*

Table 4.2: *Number of additional ground control points used for the co-registration of the HyMap flight lines to the other data sets and the resulting RMSE for each flight line.*

|  | Number of additional ground control points | RMSE (pixel) |
|---|---|---|
| Line 1 | 34 | 0.71 |
| Line 2 | No additional correction | 0.68 |
| Line 3 | No additional correction | 0.68 |
| Line 4 | 36 | 0.94 |
| Line 5 | 41 | 0.71 |
| Line 6 | 69 | 0.91 |
| Line 7 | 39 | 0.83 |

# 5 Methods

This chapter describes the methods and techniques that are applied to characterise the urban micro climate. The first two sections deal with the remote sensing methods. The final two sections concern the approaches and techniques that describe the urban micro climate based on the hyperspectral products.

## 5.1 Material identification based on airborne hyperspectral data

The type of surface cover is an important factor in the urban micro climatic system, as explained in section 3.2.1. Different surfaces have a different heat capacity, conductivity and other properties which influence the energy balance. Thus, if the surface material can be identified based on the spectral information in a hyperspectral image, these properties, which are material specific, can be assigned to each pixel. Therefore, a detailed material map is needed as an input parameter of the urban micro climate model (see section 5.4). Additionally, information about the spatial configuration of urban objects and the urban structural type can be retrieved from a material map. This information is required for both the urban micro climate model and the calculation of spatial indicators (see section 5.3).

### 5.1.1 Methods for hyperspectral land cover mapping

Literature reports on many possible methods for urban land cover mapping with remote sensing. The suitability of the method depends on the spatial and spectral resolution of the available data, the thematic detail of the land cover classes and the spectral variety of the classes present in the study area. Several approaches which have been applied to urban hyperspectral remote sensing have been mentioned in section 3.3.4. They are discussed into more detail here in order to support the selection of the most suitable method for this research.

For traditional, statistical classification approaches a pixel is often represented as a point in the n-dimensional feature space, with n being the number of spectral bands. The location of the point is assigned based on the reflection values in the different bands (Lillesand et al., 2004). Points close together have similar spectral characteristics and are therefore assigned to the same class. Different approaches exist to define how close the points should be together to assign them to the same class, such as a minimum distance to mean or a parallelepiped classifier. Though such statistical classification approaches are often applied to multispectral data (e.g. Madhavan et al., 2001), they are not very suitable for hyperspectral data. Because of the Hughes phenomenon (Hughes, 1968) the classification performance levels off after a certain number of bands and then even decreases. Also the number of training samples increases exponentially

with the number of bands. Thus a data reduction of the hyperspectral data is needed. In the urban environment is the spectral variation within classes large. This results in overlapping pixel class clouds within the spectral feature space, which makes statistical classification difficult. Another disadvantage is that these methods can assign only one class to each pixel. This does not do justice to the fact that in many landscapes (especially urban ones) pixels can contain more than one surface material. Additionally, the physical information of the spectrum (i.e. the absorption features resulting from the mineral and chemical composition of the material) is not used.

Quantitative classification approaches especially make use of the shape of the spectrum and the information absorption features provide. For a quantitative comparison of image reflectance spectra with a known reference spectra two groups of methods are available: spectral matching techniques and sub-pixel classification techniques (Van der Meer, 2006). Spectral matching techniques assess the similarity of an image spectrum to a known class spectrum. Several similarity measures of varying complexity have been developed, such as spectral information divergence (SID, Chang (2000)), Euclidean distance (ED) and spectral angle mapper (SAM, Kruse et al. (1993)). The spectral angle mapper is probably the best known of the spectral similarity measures. It regards the image spectrum and the known reference spectrum as vectors in the feature space and compares the angles between them. Because it compares the angles between the spectra, it is relatively insensible for albedo differences, which are caused by shade or inclined roofs for example. SAM has for example been used by Bhaskaran et al. (2004) for the mapping of roof materials to assess the vulnerability of the roofs for hailstorms.

The second methodology for quantitative comparison of spectra consists of sub-pixel classification techniques. The most common one of those techniques is linear spectral mixture analysis (LSMA). It is based on the concept that the spectrum of an image pixel represents the abundance of different materials within the pixel. In figure 5.1 this concept is shown with a simple example. If the area within the instantaneous field of view of the sensor is covered with two materials A and B in a ration of 30 to 70 % then the spectral signature of material A contributes to 30 % of the spectrum of the pixel and the spectrum of material B contributes to 70 % to the image spectrum. The information about the mixture of materials is considered to be sub-pixel information. To find the right combination of materials and spectra, mixed spectra are modelled based on known spectra of pure materials (also called endmembers). The modelled spectra are compared to the image spectrum until a matching spectrum is found and the mixed pixel is unmixed (see also section 5.1.2). Linear spectral unmixing has been applied often for urban area mapping with hyperspectral data e.g. in Ben-Dor et al. (2001); Roessner et al. (2001).

Non-linear unmixing approaches also exist. In these approaches the contribution of different materials to a spectrum is considered to be non-linear. This is more in accordance with reality, especially in urban areas where scattered reflection of neighbouring objects (also from walls) influence the spectrum recorded by the sensor (Borel et al., 2009). Also sensor characteristics and atmospheric scattering contribute to the non-linearity of the recorded mixed spectrum. However, for the applications in this thesis the accuracy that can be reached with linear spectral unmixing suffices. Therefore the possibilities of complex non-linear mixing models are not further explored in this thesis.

Next to statistic and quantitative spectral classifications non-parametric classification approaches gain popularity. Examples of such approaches are artificial neural networks (ANN), support vector machines (SVM) and classification trees. Artificial neural networks automati-
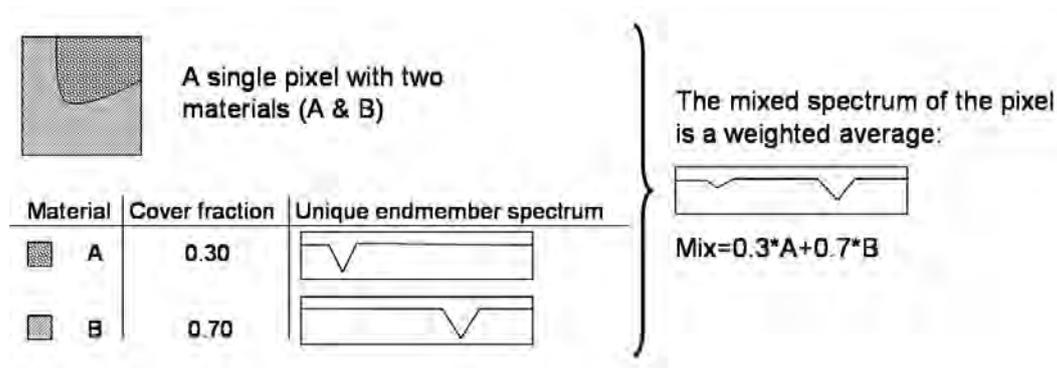
Figure 5.1: *Principle of linear spectral mixing and unmixing (adapted after Van der Meer and de Jong (2003)).*

cally generate a classification model (a neural net) based on training data. The network is then improved by iteratively classifying the signal of the training samples and back-propagating the error. The most common neural network algorithm is the multi-layer perceptron (MLP). This algorithm has also been used for sub-pixel analysis (e.g. Van de Voorde et al., 2009). In comparison with traditional classifiers artificial neural networks often achieve better accuracies (e.g. in comparison to a maximum likelihood classifier in Berberoglu et al. (2000)). Disadvantages of the neural network are that the neural network is a black box which most of the time does not provide the user with any insight in the features on which the classification is based and training is required for each new data set.

Support vector machines and classification trees are interesting because of the possibility to combine different kinds of features (e.g. spatial characteristics can be integrated in the classification scheme quite easily). Support vector machines separate two classes by a hyperplane which is placed in the n-dimensional feature space in a way that it optimally separates the training data of the two classes. Therefore only two classes can be evaluated at the time. Van der Linden (2008) applied SVM on the first twenty principal components of a hyperspectral image of Berlin, using the spectral information of each segment to map vegetation, built-up area, impervious surfaces, pervious surfaces and water.

A classification tree (decision tree) approach is a sequence of class separations, where a pixel is assigned to one of the next branches of the tree, finally resulting in a class label. For example Stein (2009) developed a classification tree for the recognition of fourteen urban materials in Munich based on the presence and absence of characteristic spectral features (absorption features, band ratios etc.). Classification trees are often based on expert knowledge though methods to automatically generate decision trees exist as well (e.g. Wang and Li, 2008). A disadvantage is that they usually do not provide sub-pixel information.

From the above it can be concluded that statistical classification methods are less suitable for material mapping with hyperspectral data because they have a limited ability to process high dimensional data and do not take the physical properties of the spectrum into account. Both quantitative spectral classifications and non-parametric classifications are well suited for the analysis of hyperspectral data and have been successfully applied to urban areas. For this study a linear spectral unmixing approach is selected to identify urban surface materials. Especially

the possibility to retrieve sub-pixel information is of advantage to the implementation into the micro-climate model and for the calculation of indicators.

## 5.1.2 Theory of linear spectral unmixing

In linear spectral mixture analysis (LSMA) the spectrum of a pixel is expressed as follows:

$$a_{ij} = Bx_{ij} + \varepsilon_{ij} \qquad (5.1)$$

where $a_{ij}$ is a vector of $n$ elements describing the image spectrum of the pixel in row $i$ and column $j$, with $n$ the number of spectral bands; $B$ is a matrix of $n$ rows and $m$ colums with $n$ the number of spectral bands and $m$ the number of endmembers; $x_{ij}$ is a vector of $m$ elements containing the fraction to which each endmember contributes to the spectrum $a_{ij}$; $\varepsilon_{ij}$ is an error term (Schowengerdt, 1997). An endmember is the spectrum of a pure, non-mixed material. In an ideal case an endmember is available for each material that comes up within the image. The objective for linear spectral unmixing is to find the best endmember combination by minimising the error $\varepsilon$. This error is commonly expressed as the root mean squared error (RMSE) which is calculated as follows:

$$RMS_{ij} = \sqrt{\frac{\sum\limits_{k=1}^{n} (a_{ij}(k) - a_{ij}^*(k))^2}{n}}. \qquad (5.2)$$

where $n$ is the number of bands, $a_{ij}$ the image reflectance spectrum of pixel $i, j$ at band $k$ and $a_{ij}^*$ the modeled reflectance of pixel $i, j$ at band $k$ (Van der Meer and de Jong, 2003).

In LMSA approaches equation 5.1 is solved for each image pixel using all the endmembers. This is computational intensive. It is also unrealistic that for a whole scene all materials occur everywhere. Therefore, multi endmember spectral mixture analysis (MESMA) methods have been developed (e.g. Roberts et al., 1998; Roessner et al., 2001; Bachmann, 2007; Franke et al., 2009). Within these unmixing methods, the number of endmembers within a pixel is constrained to a limited number of endmembers (usually two or three) to model the spectrum. Combinations of all possible endmembers are tested, or a pre-selection of endmembers can be made, e.g. based on the neighbouring pixels. With MESMA the selection of the best modelled spectrum is commonly based on the RMSE as well.

An important step of each spectral unmixing analysis is the identification of endmembers. All materials that are present in the image should be available for the unmixing in an endmember library. The spectra of the endmembers are retrieved from field spectra, spectral libraries or the image. Image spectra are preferable as endmembers because they contain the same illumination conditions and sensor noise as the spectra that need to be unmixed.

The linear spectral unmixing approach that has been applied in this study is a MESMA approach developed by the German Research Centre for Geosciences (GFZ) which has been developed especially for urban applications (Roessner et al., 2001; Segl et al., 2003). The algorithm has been successfully applied to study areas in Berlin, Potsdam and Dresden (Heiden, 2004; Bochow et al., 2007a). Furthermore, the algorithm is continuously improved. It is implemented in a series of C-binaries which run from a Linux-shell and was provided by GFZ for use in this

research. In cooperation with GFZ the algorithm was further improved for its application in Munich (see section 5.1.3). The algorithm can be carried out automatically or semi-automatically. The GFZ-approach consists of three steps: image endmember identification, identification of pure pixels (seedlings) and the actual unmixing.

The first step is to identify the endmembers within the image. This is done with a maximum likelihood feature classifier. The spectral features of urban materials can be numerically described by band ratios, absorption depth and absorption wavelength (Van der Meer, 2004). The characteristic spectral features of common German urban materials have been analysed by Heiden et al. (2007). An overview of spectral characteristics of a selection of common urban materials is given in table 3.5. The maximum likelihood feature classifier compares the features of the known materials with those of the image spectra and derives the likelihood that the pixel belongs to that class for all materials. It has been trained with spectra from Dresden, Potsdam, Berlin and the data sets of Munich used in this study. Only the pixels with a very high likelihood are selected as endmember. Using features to classify spectra is advantageous in that it is relatively insensitive to albedo differences and within class variations (e.g. caused by ageing). However, the unmixing algorithm is not insensitive to this. Therefore, a cluster analysis is applied to the spectra of the pixels selected as endmembers. In this process, the number of clusters per class can be specified by the user. For each cluster an average spectrum is calculated which is stored in the endmember library.

The second step is the identification of seedlings. These are pure pixels that are the starting point for the sequential unmixing. Based on the endmember library another maximum likelihood classification is executed. Only a selection of spectral bands is used (see section 5.1.3) and the pixels are assigned to a class based on the Mahalenobis distance. Then the pixels which are classified with a very short Mahalenobis distance are selected as pure seedlings.

The third step is the actual spectral unmixing. It is a fully constraint iterative unmixing algorithm using also spatial information. The endmember fractions ($x_{ij}$ in equation 5.1) have to be between zero and one and also sum to unity. In several iterations the whole image is unmixed. How this is implemented is graphically described in figure 5.2. First the pixels next to the pure seedlings are addressed. For these pixels a mixture of materials that includes the material of the neighbouring seedlings is assumed. The mixture with the lowest RMSE is selected. In the next iteration, the neighbouring pixels of the newly unmixed pixels are addressed, again assuming a mixture which includes the material of the already identified neighbouring pixels. Since it is a MESMA approach, the number of endmembers in the mixing model is limited, in this case to two endmembers. The result of the unmixing is an abundance map for each class. An abundance map of a certain material (class) provides the fraction of the pixel that is covered with that material.

It is possible to include a building mask in all three of the described steps in the GFZ-unmixing approach. This option is provided because several materials are both used to cover roofs and non-built surfaces, such as bitumen and asphalt, red clay roofing tiles and red loose chippings (which are actually crushed tiles) or concrete roofing and concrete roads. Since it are the material characteristics which determine the spectra and not the function (e.g. building or road), these classes are spectrally hard to distinguish. For many applications, however, it is important to separate between buildings and non-built surfaces. Therefore the unmixing algorithm makes use of a-priori information on the location of buildings in the form of a building mask.
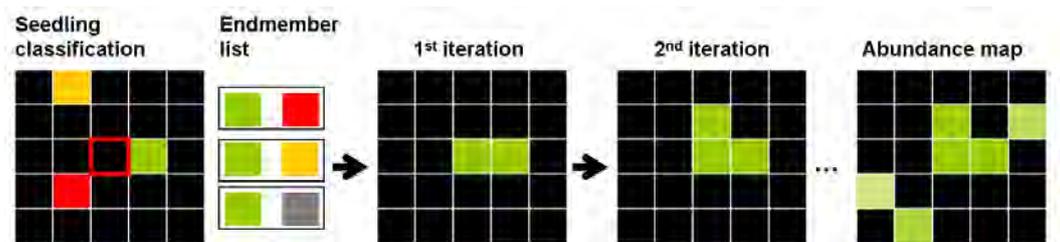
Figure 5.2: *Iterative unmixing. See text for description. Adapted after Roessner et al. (2001)*

The building mask constraints the assignment of non-built surface materials to pixels within the building mask and vice versa during endmember selection and seedling identification. A buffer around the buildings allows the assignment of both materials at building edges. During the spectral unmixing step, the building mask constraints the endmembers that are selected for the modelled spectra. Within the masked buildings only combinations of roof materials are tested, while only combinations with non-built materials are used outside the masked buildings. Within the buffer, all materials combinations are evaluated.

## 5.1.3  Application of linear spectral unmixing

In the following paragraphs the application of the GFZ-unmixing approach for the Munich data sets is described. First the implemented classification scheme is explained and after that the application of the algorithm during the three steps mentioned in the previous section will be dealt with.

The GFZ-unmixing approach is semi-automatic. The user has to define settings and prepare the input. If desired, intermediate results can be adapted manually between the steps. To analyse the influence of the different possibilities, various tests have been carried out on the test area around the eastern railway station (see section 4.1 for a description of this area). In the following paragraphs the different options and tested approaches are described. A very important option is the additional use of a building mask (see previous section). The algorithm is applied with and without a building mask using the settings and parameters described in the next sections. The results of the various tests and the final material identification are presented in section 6.1.

### 5.1.3.1  Classification scheme

The classification scheme applied in this study is presented in table 5.1. It is based on the classification scheme published in Heiden et al. (2007) and consists of three levels of land cover classes. The first level consists of broad land cover classes that are closely related to planning parameters. These classes are subdivided into the classes of the second level. The second level includes various classes of roof materials (metal, tiles etc.), different types of non-built surface types (asphalt, concrete etc.) etc. The classes of level II can be split up into different materials at level III. The classes included in this level are selected based on their spectral characteristics. For urban climate analysis a classification at material level (level III) is desired, because each material has its own thermal properties (see section 3.2.1 and 5.4). Although the thermal properties of, for example, normal polyethylene surfaces (e.g. on sports fields) will

hardly differ from green polyethylene surfaces, they do have a quite different spectral signature (different reflection in the green part of the spectrum). Therefore, they have to be separately addressed in the spectral unmixing approach and they are listed separately in the list of classes at level III. A shadow class is also added for the benefit of the spectral unmixing. Of course shadow is not a real surface cover, but because of the shadow too little spectral information of the shaded surface is available to classify it. Nevertheless, the difference between vegetation and non vegetated shaded areas can usually be distinguished.

The GFZ-unmixing approach aims at the identification of materials at level III. The results are aggregated to level II for the visualization of the material identification, because a land cover map with more than 35 classes is difficult to interpret. In most cases the variety of classes present in level II will be of enough detail for urban planners. The materials at level III of the classification scheme are required for the urban micro climate model and the material identification is aggregated to level I for the preparation of the indicators (see section 5.3).

### 5.1.3.2 Endmember classification

As explained in section 5.1.2, image endmembers are selected using a maximum likelihood feature classifier. This classifier has been trained with image and field spectra of known materials from training areas in Dresden, Berlin and Potsdam. Image spectra from the Munich HyMap data set have also been included so as to improve the achievements of the feature classifier. Close examination of the image spectra of Munich has shown that some HyMap spectral bands are of poor quality and added artefacts to the spectra. Three spectra with such artefacts are shown in figure 5.3. The artefacts occur mainly at the first and last bands of the four spectrometers (of which the HyMap sensor is composed) and at the bands prior and after the water band interpolations of the atmospheric correction. As figure 5.3 shows, not all spectra contain artefacts in all bad bands and also the strength of the artefacts varies. This means that it is not possible to correct the spectra by applying a gain or offset to selected bands in the whole the data set. Therefore, a third version of the feature classifier was trained to recognize the materials without using features in band 16, 17, 30, 40, 43, 56, 59, 69, 91 and 95 to 97.

The input for the feature classifier is the hyperspectral image and the building mask. As described above, the result of the feature classifier is the probability that a pixel belongs to a certain class. A threshold on this probability assures that only pure pixels are selected. It is also possible to constraint the number of selected endmembers for each class. It is important to set the parameters in a way that only pure pixels are selected, but a significant amount of pixels per class are present as well. The probability threshold is the most important parameter to regulate this. The selection of the probability threshold depends on the size of the image, the variety and coverage of the different materials and the quality and within class variation of the spectra. If the number of selected pure pixels is too high, the probability threshold can be set higher to increase the quality of the selected pixels and reduce their number. If the probability threshold is set too high, small classes are not included in the endmember selection. In the test area this was for example the case for soil. After several tests this threshold was set at 70 % for the test area. This means that a pixel should belong to a class with a probability of at least 70 % according to the feature classifier in order to be selected as a pure pixel from which the endmember can be derived. Since it is not possible to adjust the probability threshold per class, the algorithm provides the the possibility to manually add endmember pixels of small

Table 5.1: *Classification scheme*

| Level I | Level II | Level III |
|---|---|---|
| Buildings | roofing tiles | red roofing tiles |
| | | dark roofing tiles |
| | | grey roofing tiles |
| | roofing concrete | red roofing concrete |
| | | bright roofing concrete |
| | roofing metal | roofing aluminum |
| | | roofing copper |
| | | roofing zinc |
| | | roofing coated metal |
| | roofing synthetic/glass | polyvinyl chloride (PVC) |
| | | polyethylene |
| | | roofing glass |
| | roofing bitumen/tar | dark roofing bitumen |
| | | red roofing bitumen |
| | | roofing tar |
| | vegetated roof | vegetated roof |
| | roofing gravel | roofing gravel |
| | unknown | facade |
| | | unknown |
| Non-built impervious surface | concrete | concrete |
| | asphalt | asphalt |
| | tartan / synthetic turf / polyethylene surfaces | tartan |
| | | synthetic turf |
| | | polyethylene surface |
| | | green polyethylene surface |
| Partially impervious surface | permeable paving | cobblestone pavement |
| | | red concrete pavement |
| | | brick pavement |
| | loose chippings | red loose chippings |
| | | dark loose chippings |
| | | grey loose chippings |
| | railway tracks | railway tracks |
| Bare soil | sand/soil | siliceous sand |
| | | soil |
| Water | water | river |
| | | lake |
| | | pool |
| Vegetation | trees | deciduous trees |
| | | coniferous trees |
| | lawn | lawn |
| | | dry vegetation |
| Shadow | shadow | shadow on vegetation |
| | | shadow on other surfaces |
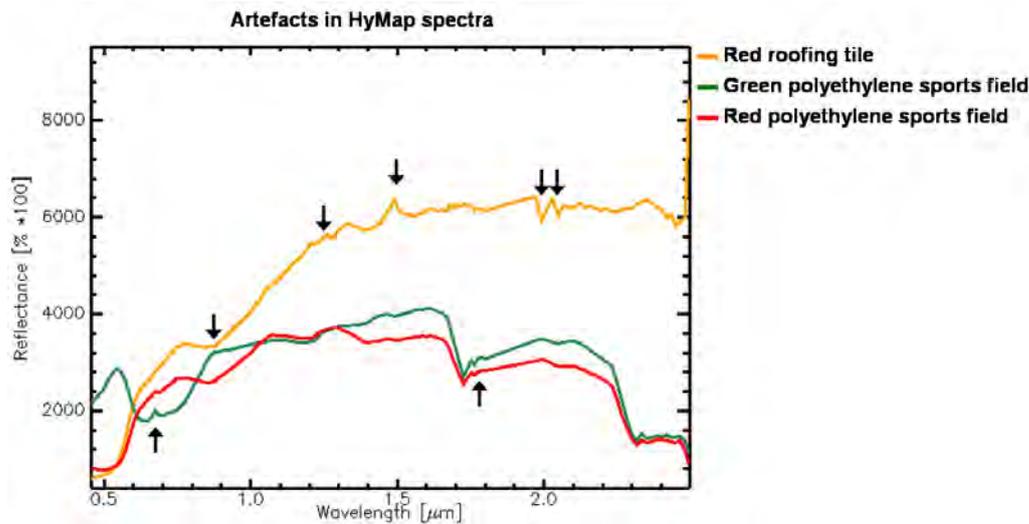
Figure 5.3: *Three examples of HyMap spectra with artefacts (artefacts are indicated with an arrow).*

classes to the endmember map. This option was used for the classes soil and tartan and red loose chippings.

The use of a building mask influences the selection of pure pixels as well. If a building mask is not used, it might happen that for example no red loose chippings are identified but only red roofing tiles, because these materials are spectrally similar. Therefore the number of selected pure pixels is slightly higher when using a building mask.

After selecting the endmember pixels an endmember library containing one spectrum for each endmember-material has to be created. In section 5.1.2 it has already been described that a cluster analysis is used to define subclasses according to the within class variability. No constraints were set on the number of subclasses. The criterion for separating the spectra in another cluster is set relatively strict. The result is a large number of subclasses for classes with a large spectral variability, such as aluminium or vegetation and a low number of subclasses for classes with a low spectral variability such as roofing tiles.

### 5.1.3.3 Seedling selection

As described in section 5.1.2, a maximum likelihood classifier is used to select seedlings. The location of each class in the feature space is defined by the average endmember spectrum. The within class variation (or size of the class pixel cloud in feature space) is described by the maximum Mahalanobis distance of all endmember pixels of the class. A pixel is selected as a seedling if its Mahalenobis distance is smaller than the maximum Mahalanobis distance of the class. The algorithm provides the possibility to reduce the maximum Mahalenobis distance. This can improve the quality of the selected endmembers but also reduces the number of seedlings. A low number of seedlings usually results in a lower number of unmixed pixels within the next step. A Mahalenobis distance of 90 % of the maximum distance of each class proved to give the best results for the test area.

Table 5.2: *Scheme for the evaluation of selected seedling classes according to their height and neigh-bourhood. If the requirements are not met the alternative class is assigned to the seedling pixel.*

| Class | Requirements | | Alternative class |
| --- | --- | --- | --- |
| | Height > 4m | Neighbourhood | |
| Red roofing tiles | yes | roof | Red loose chippings |
| Red loose chippings | no | n.a. | Red roofing tiles |
| Bright roofing concrete | yes | roof | Concrete |
| Concrete | no | n.a. | Bright roofing concrete |
| Lawn | no | n.a. | Trees |
| Trees | yes | n.a. | Lawn |

Also the seedling selection was carried out both with and without a building mask. Because the building mask does not perfectly fit the HyMap data (see section 4.3.3) the use of a building mask – although it benefits the separation of spectrally similar materials – results in new inaccuracies. Therefore, an additional hybrid solution is tested. In this approach the height data is only considered for those classes where confusion typically occurs between buildings and non-built area (see section 5.1.2). The classification of vegetation into trees and lawn can be improved by the evaluation of the height data as well. The seedlings are first derived without a building mask. Then the seedlings of eight classes are adapted to the height data according to the scheme in table 5.2. The requirements that are set for each of the selected seedling classes are based on the expected height and the most likely category (level I of the classification scheme) of neighbouring seedling pixels. If these requirements are not met the alternative class is selected. The results of the three different approaches to identify the seedlings are presented in section 6.1.

### 5.1.3.4 Iterative unmixing

The last step is the iterative unmixing of the image. As explained in section 5.1.2, the unmixing algorithm uses the seedlings as a starting point. Next to the seedling map also the hyperspectral image, the endmember library and optionally the building mask are needed as input data. The neighbourhood of the pixel under consideration determines one of the two endmembers that are used for the unmixing. The second endmember is selected freely or is constrained to roof or no roof material in case a building mask is used. However, some endmembers are very suitable for the unmixing model to solve the equation, but are not likely to occur. One example is water. In an urban area it is not likely that there is water in one pixel and not in its neighbouring pixels. But because of its low reflectance it is often added to the modelled spectrum to reduce the RMS error, instead of shadow and asphalt which have a dark spectrum as well. To avoid this, the algorithm can take into account a list of endmembers that are not allowed to be part of a mixture if they do not occur in the neighbourhood as well. For the test area all water endmembers and railway track endmembers were included in this list.

The threshold for the RMS error for acceptance of the modelled spectrum is set to a maximum RMS error 10%. A lower threshold was found to be unnecessary because the mean RMS error

was already below 2% with this threshold (see also 6.1). If the RMS threshold is set lower, the computation time increases almost exponentially.

Finally the number of iterations has to be determined. If there are not so many seedlings, more iterations are needed. Because additional iterations did not add so much computation time, it was practically left unconstrained and set to 30 iterations.

### 5.1.4 Validation concept

Knowledge about the quality of the generated material map is very important for its further use in calculating of spatial indicators and applying it in the urban micro climate model. Therefore, a validation concept is presented in this section. It allows insight in the accuracy of the intermediate products (endmembers and seedlings) and in the abundance maps.

The accuracy assessment is carried out by making a comparison with a reference data set. The reference data is assumed to represent the ground truth perfectly. Thus it is assumed as well that all differences can be attributed to errors in the calculated products. However, this is sometimes incorrect and can lead to an underestimation of the classification accuracy (Congalton, 1991; Carlotto, 2009). Also the reference data is not likely to be perfect, although it is more detailed than the calculated product. The scale of the reference data set plays an important role. Commonly, the reference data set has a smaller pixel size than the calculated product. This allows the representation of smaller objects. However, it is generally impossible for a data set to recognise objects smaller than the pixel size (Lechner et al., 2009). Nevertheless, for validation approaches the comparison of the calculated product with a reference data set considered 'ground truth' is well established (Foody, 2002) and therefore upheld in this study as well. In the following sections it is described how the reference data is created. Because no accuracy assessment has been carried out on the reference data, the reader can get an impression of the quality of this data.

During the development of the validation concept it has been taken into consideration that other errors than classification and unmixing errors might occur, such as errors in co-registration of the reference data set and the calculated products. In the following sections the validation concepts are described and an indication of how these problems are dealt with is given.

#### 5.1.4.1 Validation of endmembers and seedlings

The assessment of the accuracy of the endmembers and seedlings is important because they are the main input for the next steps in the unmixing chain. In the endmember and seedling maps one class is assigned to each pixel. This allows a pixel based comparison to a reference data set and the calculation of a confusion matrix.

For a pixel to pixel comparison of a reference data set one should be absolutely certain that the pixel in the reference data set describes the same area in the real world as the pixel in the calculated map. With a co-registration error of 0.8 pixel in average, this will not always be the case. Therefore the following approach is implemented to evaluate the accuracy of the endmember and seedling maps.

The CLUSTER-reference data set consists of clusters of pixels instead of a reference set of classified single pixels in order to reduce errors caused by misregistration of the reference data set and the HyMap data. 200 clusters are randomly selected within the test area for the accuracy

assessment after which they are manually classified. Half of the clusters are buildings; the other half of the clusters are non-built areas. The size of each cluster is at least 200 m$^2$ (more than 15 pixels). Each cluster is checked so that it only includes one surface material within the HyMap data. Then one class is assigned to each cluster based on aerial photographs and field surveys. By doing this, a difference between the reference cluster and the endmember or seedling pixels can be attributed to a classification error, and so co-registration errors are excluded. The reasoning for this is as follows: each endmember or seedling pixel is assumed to be a pure pixel, not a mixture. Also, all pixels within the reference cluster are pure pixels. Thus, even if the calculated pixel does not exactly match the location in the reference area, the class will still be the same as in the reference cluster if the classification is correct.

The endmember and seedling pixels are automatically compared to the clusters. The class of the reference cluster and the class that has been assigned to the majority of the endmembers or seedlings are compared and entered into the confusion matrix. If no endmembers or seedlings are present within the cluster, it is discarded and the number of validation samples is reduced. Based on the confusion matrix the user, producer and overall accuracy are calculated. Additionally information is collected on the number of endmember or seedling pixels within each cluster that have the dominant class. The result of the accuracy assessment of endmembers and seedlings against the CLUSTER-reference data can be found in section 6.1.

### 5.1.4.2 Validation of abundances

The validation of the pixel abundances is important because the abundances are the input for both the calculation of the spatial indicators as well as for the micro climate model. However, validation of abundances is not straight forward. The RMS error that is provided for each pixel by the spectral mixture analysis provides information on the quality of the unmixing model, not on the thematic accuracy of the abundances. It explains how well the modelled spectrum fits the image spectrum and not how well the modelled spectrum explains the ground truth.

Since more than one class can be assigned to a pixel the use of a standard confusion matrix is impossible. Specially adapted accuracy measures are needed (Foody, 2002). For example Pontius and Cheuk (2006); Silvan-Cardenas and Wang (2008) have developed confusion matrices especially for soft classifications. However, such matrices are not easy to interpret. More intuitively understandable are area based validations of the fractional covers. Such an approach is often applied in the accuracy assessment of spectral unmixing results (e.g. Lee and Lathrop, 2005; Powell et al., 2007; Weng et al., 2008). Reference fractional covers are calculated for a pixel or a cluster of pixels. Then the differences between the reference data and the modelled fractions are calculated. Common measures to express these differences are the correlation coefficient $R^2$, the mean absolute error (MAE) and the RMSE.

Because of the possibility to compare the results with many other studies and the relatively easy interpretation of the measures, an area based validation approach is developed for this study. The BLOCK-reference data set consists of fourteen manually classified building blocks located in the test area (see section 4.1). They were created as a vector data set by digitizing aerial images and manually assigning class labels based on the aerial images and field surveys. The vector dataset was then converted to raster. Surface cover fractions were calculated by dividing the area of a class by the size of the validation area (i.e. 4 x 4 m or larger, see below).
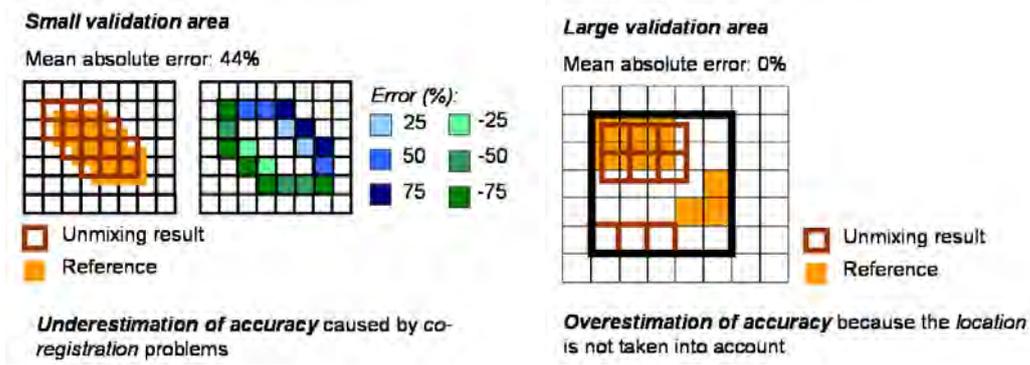
Figure 5.4: *Illustration of the influence of the size of the validation area on the measured accuracy of abundance maps, showing the possible underestimation of the accuracy when the validation area is small (left) and the possible overestimation of the accuracy when the validation area is large (right).*

It is important to note that the size of the validation area influences the measured accuracy. 5.4 (left) shows that small sample areas can underestimate the accuracy due to co-registration errors. In the given example the co-registration error is only a half pixel but this can still result into a MAE of 44%. A larger sample size is insensitive to such co-registration errors, but might overestimate the accuracy when errors of omission and commission within the validation area outbalance each other, as is shown in 5.4 (right). This illustrates that the most suitable size of the validation area is a trade-off between the risk of co-registration errors and the risk of outbalancing omission and commission errors. In Heldens et al. (2009b) different sizes of validation areas have been tested. Depending on the application, validation areas of 3x3 pixels and larger were found suitable because they are less sensible of co-registration errors than single pixels. The abundance maps will be used at pixel level in the micro climate simulations and at building block level for the calculation of the spatial indicators. Therefore, validation areas of 3x3 pixel clusters and a building block are selected for this study.

The actual validation consists of the comparison between the abundances resulting from the iterative unmixing and the abundances of the BLOCK-reference data set. For each sample area (i.e. a 3x3 pixel cluster or a building block) the difference is calculated for each class. The results are displayed in section 6.1. Based on the calculated differences the following measures are calculated after Powell et al. (2007):

$$MAE = \frac{\sum\limits_{i=1}^{n} |z_{ik} - z_{ik}^*|}{n} \tag{5.3}$$

$$Bias = \frac{\sum\limits_{i=1}^{n} z_{ik} - z_{ik}^*}{n} \tag{5.4}$$

where $z_{ik}$ is the fraction of material $k$ in validation sample $i$ of the unmixing result, $z_{ik}^*$ is the fraction of material $k$ in validation area $i$ in the reference data and $n$ is the total number of

validation samples. The MAE provides information on the size of the differences, whereas the bias provides information on over- or underestimation of the abundances in comparison to the reference. These measures are calculated for each class and are presented in section 6.1 as well. When interpreting the mean absolute error and bias, one should be aware that the error also depends on the size of the class. If the total abundance of a class in the validation area is low, the absolute errors are also low. This also goes the other way around: the mean absolute error of more frequent materials is larger even if the same cover fraction (in percentage) was falsely identified. Therefore, the total abundance of each class in the validation area and the whole test area should be considered during the interpretation of the accuracy assessment results.

# 5.2 Additional hyperspectral products

Apart from the surface materials, the urban micro climate model needs two more input parameters to which hyperspectral remote sensing can contribute. These parameters are surface albedo and leaf area density (LAD). This section deals with how albedo and LAD are derived from the HyMap data.

## 5.2.1 Albedo

Albedo is defined as the bi-hemispherical reflectance of a surface (Schaepman-Strub et al., 2006) and is equal to the reflected short wave radiation $K\uparrow$ introduced in 3.2.1. It is an important parameter for climate models because it controls the surface energy budget (Govaerts et al., 2008, see also sections 3.2 and 3.2.1).

When using remote sensing, albedo is calculated as the ration of the total reflected energy of the surface to the total incident energy on the surface (Van der Meer and de Jong, 2003). Surface reflectance, as measured by remote sensors, can be a substitute for surface albedo when integrated over the wavelengths (Richter, 2007).

Albedo is, similar to reflectance (see 3.3.1), a property of the surface material which depends on the ability of the surface to reflect, absorb and transmit radiation, and on the bidirectional reflectance distribution function (BRDF) of the surface. The BRDF describes the reflection of a beam of incoming radiation from one direction into another (Schaepman-Strub et al., 2006). Because of the BRDF the albedo of a surface measured by a remote sensor varies depending on the viewing angle of the sensor, the solar angle during data collection and the orientation of the surface.

This study tests two approaches to calculate the surface albedo. The first approach uses the albedo product included in the ATCOR software, whereas the second approach consists of a simple reflectance average.

Within ATCOR the surface albedo is calculated during the atmospheric correction using the following equation (Richter, 2007):

$$a = \frac{\int_{0.3\mu m}^{2.5\mu m} \rho(\lambda)d\lambda}{\int_{0.3\mu m}^{2.5\mu m} d\lambda} \tag{5.5}$$

where $a$ is the surface albedo and $\rho(\lambda)$ is the reflectance at wavelength $\lambda$. The surface reflectance is interpolated for spectral bands that are not available. For HyMap data this is the case for the spectral region between 0.3 $\mu$m and 0.45 $\mu$m (Richter, 2007).

The reflectance average, which functions as a second method to calculate the surface albedo, is the mean of the spectral reflectance of all spectral bands of the atmospherically corrected HyMap image. This is accomplished with the image processing software IDL/ENVI (ITT Visual Information Solutions, 2007). The advantage of this approach is that the albedo can be calculated very fast and at any time after the pre-processing of the data.

In section 6.2.1 the results of both approaches are presented and compared.

## 5.2.2 Leaf area index and leaf area density

Vegetation has a large influence on the (micro) climate (see section 3.2.1). Evapotranspiration is the most important process in which vegetation influences the air temperature and the humidity (Kuttler, 1998). Plant structure plays an important role in this. The larger the leaf surface, the more evaporation can take place. The orientation of the leaves and the vertical leaf structure (e.g. overlapping leaves, leaf area at different heights) are important as well. In many remote sensing studies research has been conducted on the relationship between spectral characteristics and plant structure. Leaf area index (LAI) is one of the parameters that can be estimated based on spectral reflectance and it provides information on the plant structure. LAI expresses the leaf area per unit of ground surface area. In the ENVI-met model, the structure of the plants is described by the leaf area density (LAD, see also section 5.4) at different heights. This parameter expresses the leaf area per unit of ground surface at different heights of the plant. Lalic and Mihailovic (2004) provide an empirical relationship between LAI and LAD for various deciduous and coniferous trees:

$$LAI = \int_0^h L(z)dz \qquad (5.6)$$

where $L(z)$ is the leaf area density at height $z$ of the tree and can be calculated as follows:

$$LAI = \int_0^h L_m \left(\frac{h - z_m}{h - z}\right)^2 exp\left[n(1 - \frac{h - z_m}{h - z})\right] dz \qquad (5.7)$$

with $n = \begin{cases} 6, & \text{for } 0 \leq z < z_m \\ \frac{1}{2}, & \text{for } z_m \leq z \leq h \end{cases}$

where $L_m$ is the maximum leaf area density of the tree at the heigth $z_m$ and $h$ is the total height of the tree. The height $z_m$ (usually at the broadest part of the tree crown) depends on the tree species. Since information about the different tree species is not available the $z_m$ is assumed to be at $0.7h$ for all trees, i.e. the maximum leaf area density is assumed at slightly over two-thirds of the total height of the tree.

Thus, in order to calculate the LAD required by ENVI-met the LAI has to be derived from the HyMap data. Zheng and Moskal (2009) provide an overview of different methods that are used to retrieve the leaf area index with remote sensing. These methods can be divided in two categories. The first category is based on the correlation between spectral vegetation indices and LAI. The second category uses inverse modelling.

There are many spectral vegetation indices available in literature. A selection of those indices is listed in table 5.3. Most of them make use of the ratio between the reflectance in the NIR and the red part of the spectrum. The red part of a vegetation spectrum is strongly influenced by the chlorophyll content. The NIR part of a vegetation spectrum is influenced by the reflectance and scattering within the leaf structure. Field measurements are used to correlate the values of the vegetation indices to LAI, as is for example done in Soudani et al. (2006) and Haboudane et al. (2004).

Table 5.3: *Selection of common vegetation indices implemented in the AS Toolbox (Dorigo et al., 2006). $R_x$ is the reflectance at wavelength x in nm, L= Soil coefficient with default value 0.5.*

| Vegetation index | Reference | Calculation |
|---|---|---|
| NDVI - Normalised Difference Vegetation Index | Rouse et al. (1973) | $\frac{R_{864}-R_{671}}{R_{864}+R_{671}}$ |
| RVI - Ration Vegetation Index | Pearson and Miller (1972) | $\frac{R_{864}}{R_{671}}$ |
| SAVI - Soil adjusted vegetation index | Huete (1988) | $(1+L)\frac{R_{864}-R_{671}}{R_{864}+R_{671}+L}$ |
| MSAVI - Modified Soil adjusted vegetation index | Qi et al. (1994) | $0.5*(2R_{800}+1-\sqrt{(2*R_{800}+1)^2-8*(R_{800}-R_{670})})$ |
| REIP - Red Edge Inflection Point | Guyot and Major (1988) | $700+\frac{740}{100}*\frac{R_i-R_{701}}{R_{740}+R_{701}}, R_i=0.5\frac{R_{780}}{R_{670}}$ |

Especially when hyperspectral data is available inverse radiative transfer modelling is often applied, e.g. for agriculture (Dorigo, 2007) or forestry (Kötz, 2006). A plant radiative transfer model simulates the reflectance at different wavelengths, while taking into account various plant characteristics, such as LAI. A well known example of a plant radiative transfer model is PROSPECT/SAIL (Jacquemoud and Baret, 1990; Jacquemoud et al., 2009). Also the widely used LAI map of the satellite based sensor MODIS is calculated with a radiative transfer model (Knyazikhin et al., 1999). For the pixels where this is not possible, LAI is estimated based on empirical relations between NDVI and LAI.

It should be noted that most approaches to retrieve LAI and other vegetation parameters from remote sensing focus on agricultural crops and (production) forests. The relatively small and dispersed patches of urban vegetation contain a large variety of species and often suffer from water stress and physical damages by construction works etc. (Damm, 2008). Therefore, approaches to retrieve vegetation parameters that have been developed for agriculture and forestry should be applied with care to urban vegetation.

Although the application of a radiative transfer model has great potential to retrieve accurate LAI, the application of such a complex model is outside the scope of this thesis. Therefore, the LAI is calculated based on vegetation indices. Unfortunately, no field measurements of LAI are available to establish empirical relationships for this study. In literature, empirical relationships between LAI and a vegetation index are provided for different types of vegetation. Several of these empirical relations are implemented in the AS Toolbox (Dorigo et al., 2006). This toolbox, developed by the imaging spectroscopy working group at DLR, provides a series of algorithms for the (pre-)processing of field and image spectra with IDL/ENVI, including a large

Table 5.4: *Selected empirical relationships between LAI and vegetation indices implemented in AS Toolbox (adapted after Dorigo et al., 2006)*

| Name and Reference | Calculation | Original field of application |
|---|---|---|
| LAI NDVI (Wang et al., 2005) | $9.7929 * NDVI - 0.4314$ | Deciduous forest |
| LAI RVI (Liu et al., 1997) | $0.475(RVI - 2.781)$ | Boreal forest |
| LAI MSAVI (Haboudane et al., 2004) | $0.663e^{4.2731} * MSAVI$ | Crops (wheat, corn, soybean) |
| LAI REIP (Danson and Plummer, 1995) | $e^{logREIP - \frac{log710.1}{0.0084}}$ | Coniferous forest |

number of vegetation indices. In table 5.4 four LAI measures are listed which are selected to calculate the LAI for a small test area by using the AS Toolbox. The backup algorithm of the widely accepted MODIS LAI product is also tested. This approach is based on different lookup tables for different biomes (Knyazikhin et al., 1999). Of course there is no biome for urban areas. Therefore, the biomes shrub land, broad leaf forest and needle leaf forest are selected to represent the different types of vegetation within the urban area. The lookup tables for these biomes are listed in table 5.5. The results are presented in section 6.2.2.

Summarizing, the approach to calculate the LAD required by ENVI-met consists of three steps. Firstly the vegetation indices are calculated (see table 5.3), secondly the LAI is estimated based on the vegetation indices (see table 5.4 and 5.5) and finally the LAD is calculated based on the LAI and equation 5.7. The LAI is only calculated for pure vegetation pixels. Non-vegetation pixels are masked out based on the material classification (see section 5.1). The LAD is only calculated for pixels that are dominantly classified as trees in the material classification, because the empirical leaf area density function as developed by Lalic and Mihailovic (2004) is only valid for trees. The height data is used to provide the maximum height of the tree required in equation 5.7. The results of the LAI and LAD calculations are presented in section 6.2.2.

## 5.2.3 Validation concept

The surface albedo can be measured with a pyranometer which is specially made for this purpose, but remote sensors can measure albedo according to the definition in Schaepman-Strub et al. (2006) as well. Therefore, additional measurements of albedo for validation were considered unnecessary. In the assessment of the quality of the retrieved albedo values, however, the sensor-properties which influence the measurement of albedo as a surface property need to be considered .

The validation of LAI and LAD is based on comparisons with values in literature, because field measurements of LAI are not available. The selection of the best suitable approach for

Table 5.5: *LAI-NDVI lookup table for the biomes shrub land, broad leaf forest and needle leaf forest (after Knyazikhin et al., 1999).*

| NDVI | LAI | | |
|---|---|---|---|
| | *Shrubland (biome 2)* | *Broad leaf forest (biome 5)* | *Needle leaf forest (biome 6)* |
| 0.025 | 0 | 0 | 0 |
| 0.075 | 0 | 0 | 0 |
| 0.125 | 0.2663 | 0.1516 | 0.1579 |
| 0.175 | 0.3456 | 0.1973 | 0.2239 |
| 0.225 | 0.4357 | 0.2686 | 0.324 |
| 0.275 | 0.5213 | 0.3732 | 0.4393 |
| 0.325 | 0.6057 | 0.5034 | 0.5629 |
| 0.375 | 0.6951 | 0.6475 | 0.664 |
| 0.425 | 0.8028 | 0.7641 | 0.7218 |
| 0.475 | 0.9313 | 0.9166 | 0.8812 |
| 0.525 | 1.102 | 1.091 | 1.086 |
| 0.575 | 1.31 | 1.305 | 1.381 |
| 0.625 | 1.598 | 1.683 | 1.899 |
| 0.675 | 1.932 | 2.636 | 2.575 |
| 0.725 | 2.466 | 3.557 | 3.298 |
| 0.775 | 3.426 | 4.761 | 4.042 |
| 0.825 | 4.638 | 5.52 | 5.303 |
| 0.875 | 6.328 | 6.091 | 6.501 |
| 0.925 | 6.328 | 6.091 | 6.501 |
| 0.975 | 6.328 | 6.091 | 6.501 |

the estimation of LAI is made by comparing reference values of LAI reported in other studies. A difficulty with this is that most studies regarding LAI focus on agricultural or forest areas. Accuracy assessments in literature where field measurements were available reported values for the agreement coefficient $r^2$ between 0.54 and 0.98 for the estimation of LAI based on vegetation indices for different crops with hyperspectral AISA data (e.g. Haboudane et al., 2004).

## 5.3 Spatial indicators

Spatial characteristics aggregated over a larger area (e.g. area of impervious surface in a building block) are often used to describe urban areas in urban planning. They can be used as spatial indicators, because they describe a complex spatial situation within said areas with a single value. This makes it easier to compare different areas. A combination of values of different spatial indicators is typical for an urban structural type (see section 3.1.3). A relation to the urban micro climate has been documented in literature for many spatial indicators (see section 3.2.2), which makes it just to use them as micro climatic indicators. Therefore, the mapping of spatial indicators at a building block level is selected as one approach to characterise the urban structural types and their micro climate.

### 5.3.1 Selection of relevant spatial indicators

Common spatial indicators used in German planning are building density, vegetation density and imperviousness (Pauleit and Duhme, 2000b; Breuste et al., 1996; Heber and Lehmann, 1993). They describe basic spatial features of building blocks or other reference areas. In literature, a strong relationship between urban climate and building density, vegetation density and impervious surface has been reported (e.g. Zhang et al., 2009b, see also section 3.2.2). Building volume and vegetation volume are useful to distinguish between high and low buildings and trees and lawns. This is important information in order to be able to distinguish between urban structural types such as row house development and regular block development (see section 3.1.3). The building and vegetation volume also have a large effect on the urban micro climate, e.g. on the height to width ratio (H/W ratio) to describe street canyons or the influence of buildings and trees on wind flows (see section 3.2.1). The roofing material that is used in a building block is also a relevant spatial indicator, since it influences the urban micro climate (Henry and Dicks, 1987; Hoyano et al., 1999). However, so far it is not commonly used in urban planning because of the difficulties in acquiring the information. Roof material is one of the descriptive characteristics of an urban structural type, because the roofing material is related to the building type and building period that are used to classify the urban structural types. Indicators that describe the spatial organisation of buildings and vegetation (e.g. spatial metrics as applied in Herold et al. (2003b) and Huang et al. (2007)) are relevant as well. The spatial organisation is exemplary for some urban structural types (e.g. regular block development) and also strongly influences the aspects of the urban micro climate, such as the wind flow (Eliasson et al., 2006). Still, the currently available spatial metrics (e.g. complexity and compactness used in Huang et al. (2007)) are often difficult to interpret. This makes them unsuitable for urban planning applications, because urban planners prefer indicators and maps that are easily to comprehensible and explicable in the communication with politicians and citizens (Klein et al., 2010). They are therefore left out of this study.

As a result, the following six spatial indicators are selected for this study: building density, vegetation density, imperviousness, building volume, vegetation volume and roofing material. In table 5.6 the selected indicators and their definitions are listed. The next section describes how the spatial indicators are derived at the building block level based on the available data.

Table 5.6: *Overview of six selected spatial indicators*

| Indicator | Definition | Unit |
|---|---|---|
| building density | percentage built up area per building block area | % |
| vegetation density | percentage vegetation per building block area | % |
| imperviousness | percentage impervious surface per building block area | % |
| building volume | average building volume per building block area | $m^3/m^2$ |
| vegetation volume | average vegetation volume per building block area | $m^3/m^2$ |
| roofing material | abundance of the different roofing materials within the building block | % |

## 5.3.2  Calculation of spatial indicators

In urban planning, the common approach to map spatial indicators is by digitising aerial photographs and field surveys. This is very time and labour intensive and mapping of large areas such as a metropole like Munich is almost impossible. Therefore, (semi-)automatic mapping of spatial indicators based on remote sensing has been the topic of several studies reported on in literature. The main focus lies on mapping the impervious surface, vegetation and buildings. For example, the vegetation-impervious-soil (VIS) approach (Ridd, 1995) focuses on mapping the abundance of impervious surface and vegetation in urban areas (e.g. Weng et al., 2008, see also section 3.3.2). A disadvantage of this approach is that soil and bright impervious surfaces are often confused, especially when multispectral remote sensing data is used (Lu and Weng, 2006). There is also no possibility to distinguish between built and non-built impervious surfaces when this concept is used. In multispectral remote sensing a spectral building index has been used to map buildings for which a ratio of the spectral reflectance in the NIR and SWIR regions of the spectrum is used (Zha et al., 2003). When hyperspectral remote sensing data is available, buildings are mapped in multiple classes which each have their own characteristic spectrum, often separating different roof materials (e.g. Roessner et al., 2001; Franke et al., 2009; Ben-Dor et al., 2001). Therefore, the derived material abundances (see section 5.1) provide the basis for the calculation of the selected spatial indicators in this study as well. The classification scheme in table 5.1 shows that the materials can be grouped into roofing materials (i.e. buildings), impervious and partially impervious non-built surfaces, and vegetation. This scheme is used to calculate the building block characteristics.

The reference unit for calculating the spatial indicators is provided by the building block vector data set of the municipality of Munich (see section 4.2). Using IDL/ENVI software (ITT Visual Information Solutions, 2007) the characteristics are automatically calculated for the building blocks based on the material abundances and height data.

The building density (BD) is calculated based on the total abundance of roof materials:

$$BD = \frac{\sum_{i=1}^{n} abu_{roof}(i)}{n} 100\%$$ (5.8)

where $abu_{roof}(i)$ is the abundance of roofing material in the pixel $i$ in percentage and $n$ is the total number of pixels within the building block.

The vegetation density (VD) is calculated similarly to the building density :

$$VD = \frac{\sum_{i=1}^{n} abu_{veg}(i)}{n} 100\%$$ (5.9)

where $abu_{veg}$ is the abundance of vegetation in the pixel $i$.

The imperviousness is based on the combined abundance of built-up area, fully sealed surfaces and partially sealed surfaces. Because a part of the rain water seeps through partially sealed surfaces, they are only included for 50% in the calculation of imperviousness:

$$IMP = \frac{\sum_{i=1}^{n} abu_{roof}(i) + \sum_{i=1}^{n} abu_{sealed}(i) + 0.5 \sum_{i=1}^{n} abu_{part.sealed}(i)}{n} 100\%$$ (5.10)

where $abu_{sealed}$ is the abundance of fully sealed, non-built surfaces and $abu_{part.sealed}$ the abundance of partially sealed surfaces such as cobble stones or loose chippings.

In addition to the material abundances also height data is required for the calculation of the building volume (BV) and the vegetation volume (VV). They are calculated according to the equations 5.11 and 5.12:

$$BV = \frac{\sum_{i=1}^{n} abu_{roof}(i) * h(i)}{n} 100\%$$ (5.11)

$$VV = \frac{\sum_{i=1}^{n} abu_{veg}(i) * h(i)}{n} 100\%$$ (5.12)

where $h(i)$ is the height of pixel $i$.

In order to calculate the percentage of roof material per building block the materials are aggregated to level II material categories as defined in the classification scheme (see table 5.1). For each of the seven roof material categories the average abundance within the building block is then calculated by using the following equation:

$$Roofmat(x) = \frac{\sum_{i=1}^{n} abu_{roof(x)}(i)}{n} 100\%$$ (5.13)

where $x$ represents the different roof material categories.

The results of the calculation of the spatial indicators is presented in 6.3.

### 5.3.3 Validation concept

Knowledge of the accuracy of the spatial characteristics is important if they are used for further analysis, such as for urban climate characterisation. Therefore, a validation of the spatial indicators is carried out. The approach that is implemented is similar to that of other remote sensing studies concerned with imperviousness and vegetation density, namely in comparing the remote sensing based indicators to manually estimated indicators based on a very detailed source, such as aerial photographs or field surveys (e.g. in Wu and Murray, 2003).

Two data sets are used in this study for the accuracy assessment of the spatial indicators. The first is the BLOCK-reference data set containing fourteen digitised building blocks which is also used for the accuracy assessment of the material abundances (see section 5.1.4.2). The surface materials for these building blocks are determined by making use of field surveys and aerial photographs. Based on the material maps of the BLOCK-reference indicators are calculated using the methods described in section 5.3.2. The indicator values of the BLOCK-reference are then compared to the HyMap spatial indicators. The differences are expressed as the mean absolute error (MAE) and the bias (i.e. the mean error) to analyse the magnitude and the under- and overestimation of the spatial indicators, which is similar to the analysis of the material abundances described in section 5.1.4.2.

The second data set to which the calculated spatial indicators are compared to are the indicators provided by the municipality of Munich (see section 4.2). This data set contains values for building density, vegetation density and imperviousness for each building block. First the quality of this municipal data set is assessed by a comparison with the indicator values of the BLOCK-reference data set. Then the HyMap-based indicators are compared to the building block characteristics of the municipality. The results of this comparison are presented in section 6.3.

## 5.4 Micro climate simulations

Micro climate simulations can help urban planners gain more insight in the climatic situation of selected building blocks. Hyperspectral remote sensing can support the acquisition of input parameters for such simulations. Several numerical models have been developed for the simulation of the urban micro climate (see also 3.2.2). They differ in their objectives and complexity and therefore also in the required input parameters. URBAN3 (Terjung and O'Rourke, 1980) for example focuses on modelling the surface energy fluxes. MISKAM (Eichhorn, 1989) aims at the modelling of wind flow around obstacles. ENVI-met (Bruse and Fleer, 1998) models the interaction between vegetation, atmosphere and urban surfaces, providing a possibility to analyse many aspects of the urban micro climate and their interactions at once. Additionally, ENVI-met is freely available at www.envi-met.com and continuously improved at the university of Mainz. Because of these characteristics, ENVI-met was selected to simulate the urban micro climate within this study.

A beta-version of ENVI-met V4 is used for this study, which is provided directly by the developers and it is expected to be available online in the summer of 2010. A description of the model is given in the next section. General preparations which are required for the simulations are described in section 5.4.2. In section 5.4.3 the generation of the ENVI-met model input based on the hyperspectral data products is explained. Section 5.4.4 focuses on the validation concept for the simulations.

### 5.4.1 Model description

The following description of ENVI-met is based on Bruse and Fleer (1998), www.envi-met.com and experiences with ENVI-met $V4\beta$, unless stated otherwise. It should be noted that the aim of this section is to give the reader a general understanding of ENVI-met in order to understand and discuss the implementation of the hyperspectral data products in this particular urban micro climate model. Therefore, the text below does not provide a complete overview of all the possibilities of the model, but only of those that are relevant to this study. The reader is referred to www.envi-met.com for a full description of the latest version of ENVI-met.

ENVI-met is a 3D numerical, non-hydrostatic micro climate model which simulates the interaction between atmosphere, vegetation and urban surfaces over time. The objective of the model is to offer a tool to urban planners and architects to analyse the interactions of buildings and vegetation with the micro climate by allowing the simulation of different scenarios (Bruse, 2000). It simulates the micro climate over time for a user defined urban environment and provides the user with simulated climate variables such as temperature and humidity for each time step. The influence of small scale changes on the micro climate can be simulated, such as the effect of planting trees or changing roof materials. Various applications of ENVI-met have been listed in literature. For example Ali-Toudert and Mayer (2007) simulated the influence of the geometry of street canyons and vegetation on thermal comfort. Hien and Jusuf (2008) used ENVI-met to predict the effects of a new building plan on the ambient temperature. Wania (2007) applied ENVI-met to study how trees influence the air quality in street canyons.

ENVI-met runs at a regular PC with Windows XP and consists of three software tools with graphical user interfaces to create the simulation area (ENVI-eddy), to run the model (ENVI-met) and to display the results (LEONARDO). The model is based on a 3D grid with typical
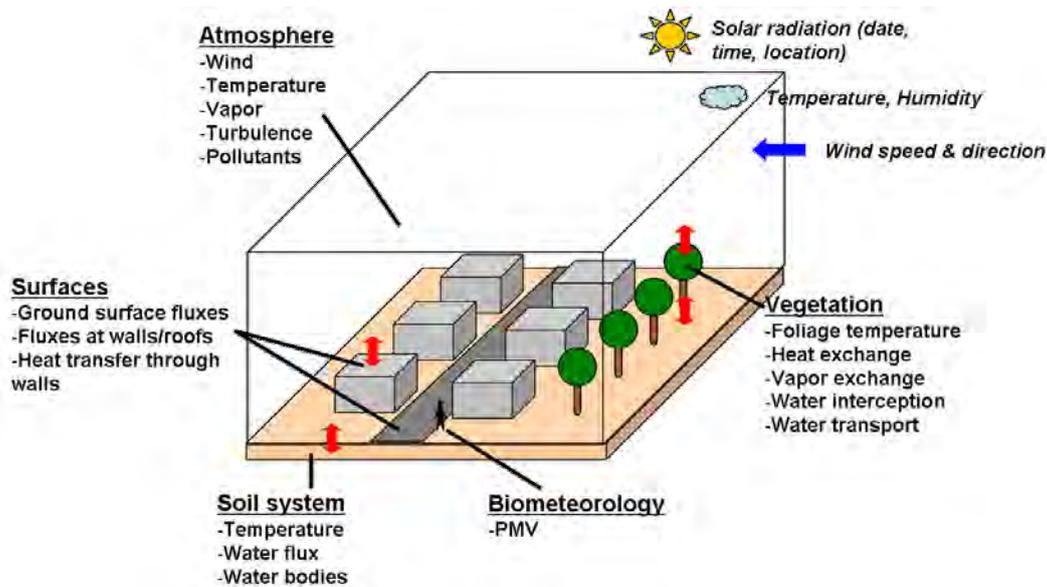
Figure 5.5: *Schematic overview of the ENVI-met model showing the 3D simulation area with its different sub-models and their main parameters. The parameters in italics are initial parameters. The red arrows indicate an exchange between the sub-models (Adapted after www.envi-met.com).*

grid sizes between 0.5 m and 10 m in x and y direction and grid heights between 1 and 5 meters to represent a synthetic or real simulation area.

The model consists of five sub-models for the atmosphere, the soil system, the vegetation, the surfaces and biometeorology. Each sub-model is calculated for each grid cell and time step, taking into account spatial configuration, surface and plant characteristics and the parameters calculated in the other sub-models. A schematic overview of the various sub-models and their parameters is given in figure 5.5. There is a difference between fixed input parameters, initial parameters (written in italics in figure 5.5) and modelled parameters (all other parameters in figure 5.5).

The fixed input parameters are the spatial configuration of the simulation area and the thermal and hydrological characteristics of surfaces and plants. The simulation area is described by the area input file which contains the location and height of buildings, the location of vegetation and different soil types. Also the type of the plants and the materials which are used for the roofs and walls are indicated. The simulation area is usually created manually in the editor-software ENVI-eddy, but can also be generated with any other software by directly describing the simulation area in the ENVI-met binary-format (see section 5.4.3). An overview of the grid-based 3D simulation area containing six buildings, four trees and an asphalt road is given in figure 5.6. Each object is composed of grid cells. By doing this, buildings can be assigned different materials for walls and roofs. To model the influence of the urban objects and surfaces on the micro climate accordingly, their thermal and hydrological properties are stored in additional databases. For example, for each plant type the plant height and the leaf area density are included. For soil types and materials for walls and roofs among others the albedo and thermal conductivity are indicated. Several plants, soil and facade types are included in ENVI-met, but
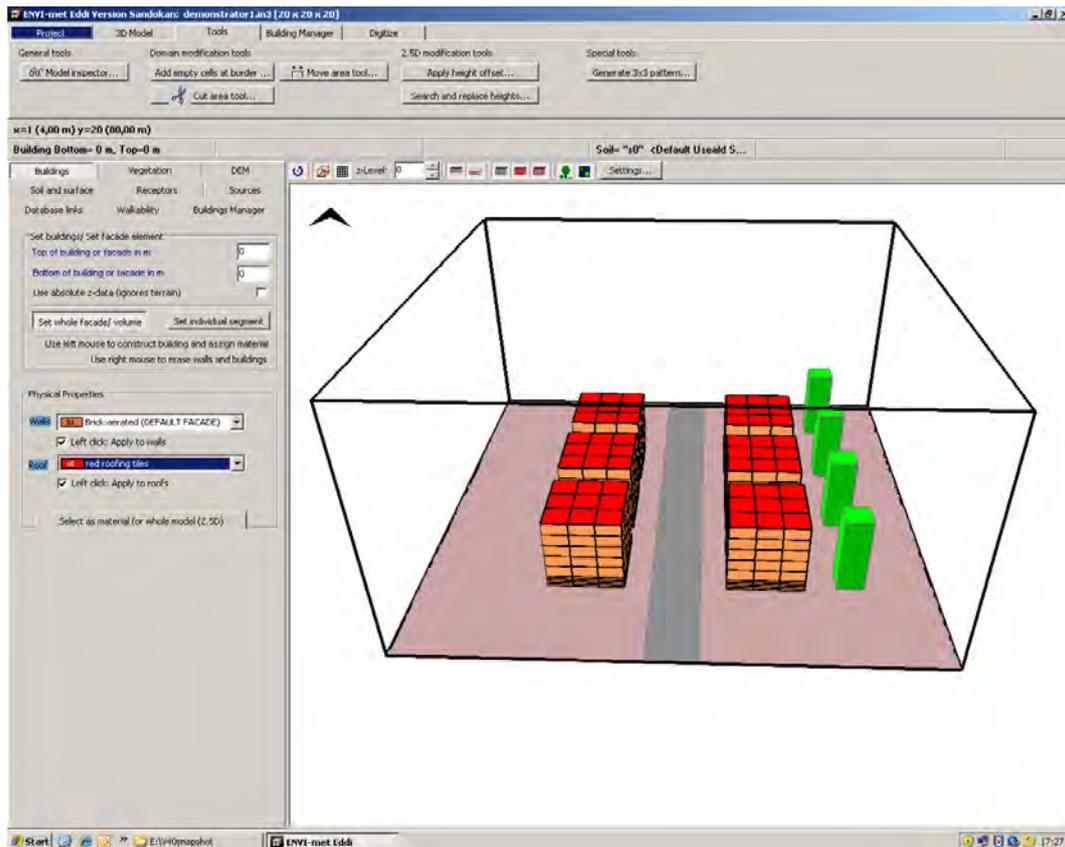
Figure 5.6: *Screen shot of a 3D simulation area in the ENVI-met Editor*

the user can add ones himself. These databases are independent of the simulation area, although all materials and plants included in the simulation area have to be included in the databases as well. The basic databases used in this study are described in section 5.4.2. They are adapted for each simulation area to accommodate within class variation of plants and surface materials (e.g. albedo). The approach for creating the adapted databases is described in section 5.4.3.

The initial parameters are needed to start up the simulations and are used to describe the weather conditions at the starting time of simulation, such as initial wind speed and direction, temperature and humidity. The starting date and time of the simulation are needed to calculate the solar radiation. Additional initial values and model constraints can be assigned to each of the sub-models if other than default values are desired. These initial parameters are written in a configuration file which, combined with the area input file and the data bases, forms the input for the ENVI-met model. The configuration file not only contains initial meteorological parameters but also simulation settings, such as the duration of the simulation and the file location for input and output files. The configuration file that is used in this study is described in section 5.4.2.

There is a vast number of modelled parameters in the ENVI-met model. In figure 5.5 the modelled parameters are generalised per sub-model for clarity. These parameters are updated every time step (between 5 and 10 seconds) and saved for a user defined time interval (e.g. each simulated hour). The original numerical model equations implemented in ENVI-met to

Table 5.7: *Attributes required by ENVI-met V4β to describe the properties of roof and wall materials (facades), plant types, soil types and soil profiles*

| Database | Facades | Plants | Soils | Profile |
|---|---|---|---|---|
| Attributes | ID | ID | ID | ID |
| | Reflection | C3 or C4 plant type | Sealed/unsealed | Roughness length of the surface |
| | Absorption | Deciduous (1), coniferous (2) or grass (3) plant type | Volumetric water content at saturation* | Short wave albedo of the surface |
| | Transmission | Minimum stomata resistance of the plant (400 for trees and 200 for grass) | Volumetric water content at field capacity* | Long wave emissivity of the surface |
| | Emissivity | Short wave albedo | Volumetric water content at wilting point* | Soil type at 14 different depths between -0.005m and -1.75m (using SOIL id) |
| | K-value | Plant height | Matrix potential at saturation* | |
| | Specific heat capacity | Total depth of the root zone | Hydraulic conductivity at saturation* | |
| | Thickness | Leaf area density at 10 data points | Volumetric heat capacity** | |
| | | Root area density at 10 data points | Clapp & Hornberger Constant* | |
| | | | Heat conductivity** | |

\* only for pervious surface materials (bare soils, sand)
\*\* only for impervious surface materials

calculate these parameters for the different sub-models can be found in Bruse and Fleer (1998) and the most recent version can be found on www.envi-met.com. The output contains a value for each grid cell of the 3D simulation area for each parameter and time step. The software tool LEONARDO or any other software can be used to display and analyse the binary output files. The results can for example be displayed spatially (e.g. temperature at height z) or over time (e.g. temperature change during the day).

## 5.4.2 General simulation settings

This section describes the two kinds of input data for the ENVI-met model that are the same for all simulations in this study: the basic databases containing properties of roofs, facades, soils and vegetation and the configuration file containing the model settings.

**Basic databases**

In table 5.7 an overview is given of the attributes of the four different databases that are required by ENVI-met. The ID of each database entry is used in the area input file to describe the soil profile, the vegetation and the roof and wall material of each grid cell in the simulation area (see also 5.4.3). The default entries of ENVI-met V4β are complemented with the materials which are used to describe the urban area with the hyperspectral data according to the classification scheme in section 5.1.3.1. By doing this, the material maps derived by the GFZ-unmixing approach (see section 5.1) can be used directly to describe the model area for the micro climate model (5.4.3). The basic databases for facades, plants, soils and profiles can be found in appendix C.

The basic facade database contains the thermal and optical properties of wall and roof materials. The facade database is extended by the roofing materials of the classification scheme in table 5.1. The thermal properties (K-value and specific heat capacity) are based on literarely values (Clarke, 2001; National Physics Laboratory, 2009). The thickness of the material is estimated. HyMap spectral libraries are used to calculate the average albedo of each of the roof materials. These spectral libraries were created to train the feature classifier described in section 5.1.3.2 and contain 20 to 400 pure spectra per material, depending on the abundance of the class. The albedo is calculated as the mean reflectance of the spectrum (see also section 5.2.1) and then averaged for all spectra of the class. These albedo values are used as a default in the basic facade database. Because the reflection (albedo), the transmission and the absorption of a material have to sum to 100 % and the transmission is assumed to be zero for all materials except glass, the values for the absorption follow from the albedo. A standard value of 90% is used for the emissivity of all materials except for the metal roofing materials. They have a much lower emissivity; between 0 % and 20 %. The emissivity values are based on values reported on in literature (Clarke, 2001).

For the basic plant database the default plant database provided in ENVI-met V4$\beta$ is used. This database is extended during the generation of the area-based model input according to the characteristics of the vegetation identified by the hyperspectral and height data (section 5.4.3).

To describe the soil system, two databases are used in ENVI-met. The soil database lists the properties of each soil type (see table 5.7). The profile database describes the vertical profile of the soil, indicating the soil type at each height. In the simulation area the profiles from this database are assigned to each grid cell to describe the soil properties. The default soil and profile databases of ENVI-met V4$\beta$ are expanded with three synthetic sealed surface materials (tartan, synthetic turf and polyethylene). Also three types of partially sealed surface materials (cobblestone and concrete pavements, loose chippings) are added, although a differentiation between sealed and partially sealed surfaces is not possible in ENVI-met V4$\beta$. The volumetric heat capacity and the heat conductivity of these surface types are based on values found in literature (Clarke, 2001; National Physics Laboratory, 2009). The albedo of these surfaces is derived from the average albedo of these materials in the HyMap training data set, calculated similarly to the albedo of the roofing materials.

**Configuration file**

The configuration file contains initial parameters for the micro climate simulation and general simulation settings. An overview of the values and settings used in this study is given in table 5.8.

The simulation settings provide temporal information about the simulation, in addition to the file locations of the input and output files. The simulation starts at 03:00 in the morning. This time is selected to start the simulations before dawn, which starts around 04:30 in the middle of June in Munich. The total simulated time is one day. The status quo of the modelled micro climate is saved every hour. An important aspect of every spatial model is how the model borders are handled. The solution in ENVI-met consists of so-called nesting grids. This is a ring of additional grid cells around the actual simulation area with default values. This allows the simulation of the micro climate to include the borders of the original simulation area.

Table 5.8: *Simulation settings, initial parameters and sub-model boundary parameters used in the configuration file. 1 clo = 0.155 $KW^2/W$.*

|  | **Parameter** | **Value** |
|---|---|---|
| Simulation settings | Total simulation time | 24 hours |
|  | Time interval output | 60 minutes |
|  | Nesting grids | yes |
| Initial parameters | Simulation start date | June 17th 2007 |
|  | Simulation start time | 03:00 |
|  | Wind speed [m/s] | 3.5 |
|  | Wind direction [degree] | 245 |
|  | Roughness length [m] | 0.1 |
|  | Initial temperature of atmosphere [K] | 287 |
|  | Specific humidity at 2500m [g water / kg air] | 7 |
|  | Relative humidity in 2 m [% ] | 50 |
| Boundary parameters for sub-models: biometeorology | Walking speed [m/s] | 0.83 |
|  | Energy exchange [W/$m^2$] | 116 |
|  | Mechanic factor | 0.0 |
|  | Heat transfer resistance cloths [clo] | 0.5 |

The initial parameters that are used in this study are based on measurements by the meteorological station of the Technical University of Munich in the Theresienstraße near the city centre of Munich. The measurements are recorded every 15 minutes and are online available in graphical form back until the year 1999 (www.meteo.physik.uni-muenchen.de). The measured values of air temperature, wind speed and wind direction at 03:00 at June 17th 2007 are used as starting point for the simulations. The other parameters were not measured by the meteorological station and default values provided by ENVI-met are used (see table 5.8).

The default settings are used for all sub-models, except for the biometeorology model, where the properties of a person walking through the model environment are given. These properties are used to calculate the Predicted Mean Vote (PMV); an index of the thermal comfort of a person (see also section 3.2.2). The values for the properties listed in table 5.8 are typical values for a person walking with 3 km/h wearing light summer clothes (www.envi-met.com).

### 5.4.3 Automatic generation of ENVI-met input parameters

The editing of the model input with ENVI-Eddy (the editor software of ENVI-met) is a tedious, time consuming job, especially considering complex urban structures. The availability of digital maps of materials, buildings and vegetation height gives the opportunity to automate this process. The availability of additional hyperspectral products such as albedo and LAI/LAD provides the possibility to adjust the basic databases of plants and facades to actually measured values. In figure 5.7 a flowchart of the automatic generation of the ENVI-met area input file is presented. The approach is implemented in IDL/ENVI and requires the material classification (dominant and secondary class, see section 5.1), the object height data (see section 4.3.2) and the albedo and LAI products (see section 5.2) as its input. The area input file required by ENVI-

met V4$\beta$ consists of information layers concerning buildings, vegetation and soil. Each pixel in the material map corresponds with one grid cell in the simulation area. The height of the grid cells is defined by the highest object within the model area, because the maximum number of grids cells in the z direction is 36.

The first step is the identification of the pixel surface cover (see figure 5.7 and figure B.1 in appendix B for a detailed flowchart of this step). The sub-pixel information of the material map and the object height are used for this. Because there are small co-registration errors between the height data and the material map derived from the HyMap data, sub-pixel information supports the accurate assignment of the surface material. The height data is used to separate buildings and trees from non-built surfaces and lawns. Then the appropriate surface cover is assigned. Roof materials and trees are the expected surface cover for pixels with a height of more than two meters. If the dominant surface cover of the pixel does not belong to one of these classes, the surface cover class of the second class is used. In a final case where the second class is also not a roof material or tree, the dominant roof material or tree of the Von Neumann neighbourhood is assigned.The low objects are classified in a similar manner. Only then a non-built surface material (e.g. asphalt) or lawn is needed. The results of this first step are a building map, a non-built surfaces map and a vegetation map (including both trees and lawns).

The second step is to assign profile IDs to the non-built surfaces. The proper soil profile is selected based on the top soil of the profile, which is the same surface material as in the material classification. Before assigning IDs a majority filter is applied. A default soil profile is assigned to all pixels that are covered with buildings or vegetation. The profile IDs are stored in the soil information layer (see the detailed flowchart in figure B.2 in appendix B).

The third step is to assign vegetation IDs to the entries in the vegetation map. This step is also illustrated in figure 5.7 and in detail in figure B.3 in appendix B. The vegetation ID is assigned based on plant type (deciduous, coniferous or grass), plant height, albedo and LAD (see also table 5.7). The latter two parameters are only calculated for pure vegetation pixels. The LAD can only be calculated for trees (see section 5.2.2). Default values are assumed for albedo and leaf area density in mixed pixels. If the difference to all existing IDs for one of the parameters is larger than predefined thresholds, a new entry is added to the plant database. The location of the vegetation and their IDs are stored in the vegetation information layer.

The fourth step is to adjust the building map to the ENVI-met V4$\beta$ requirements and limitations (see figure 5.7). A detailed flowchart of this step can again be found in figure B.4 in appendix B. ENVI-met is very sensitive to captured grids, which are non-built grid cells that are completely surrounded by building pixels. Such captured grids cause numeric errors in the model and have to be removed. This is done by either re-classifying the captured grid as a building or by removing the buildings from one of the surrounding pixels, depending on the form of the building. Thereafter an image segmentation using an IDL/ENVI-routine (ITT Visual Information Solutions, 2007) is carried out to identify separate buildings. The average height of the building is assigned to the whole building, to reduce the complexity of the model environment. Then building walls are identified based on the height difference between two neighbouring pixels. Before assigning IDs to the roofing material a majority filter is applied to smooth the classification of roofing materials. The albedo of the roof material is evaluated for pure pixels and compared to the values of the same material in the database. If the difference is more than 4%, a new entry with an adapted albedo value is added to the database for that material. This is
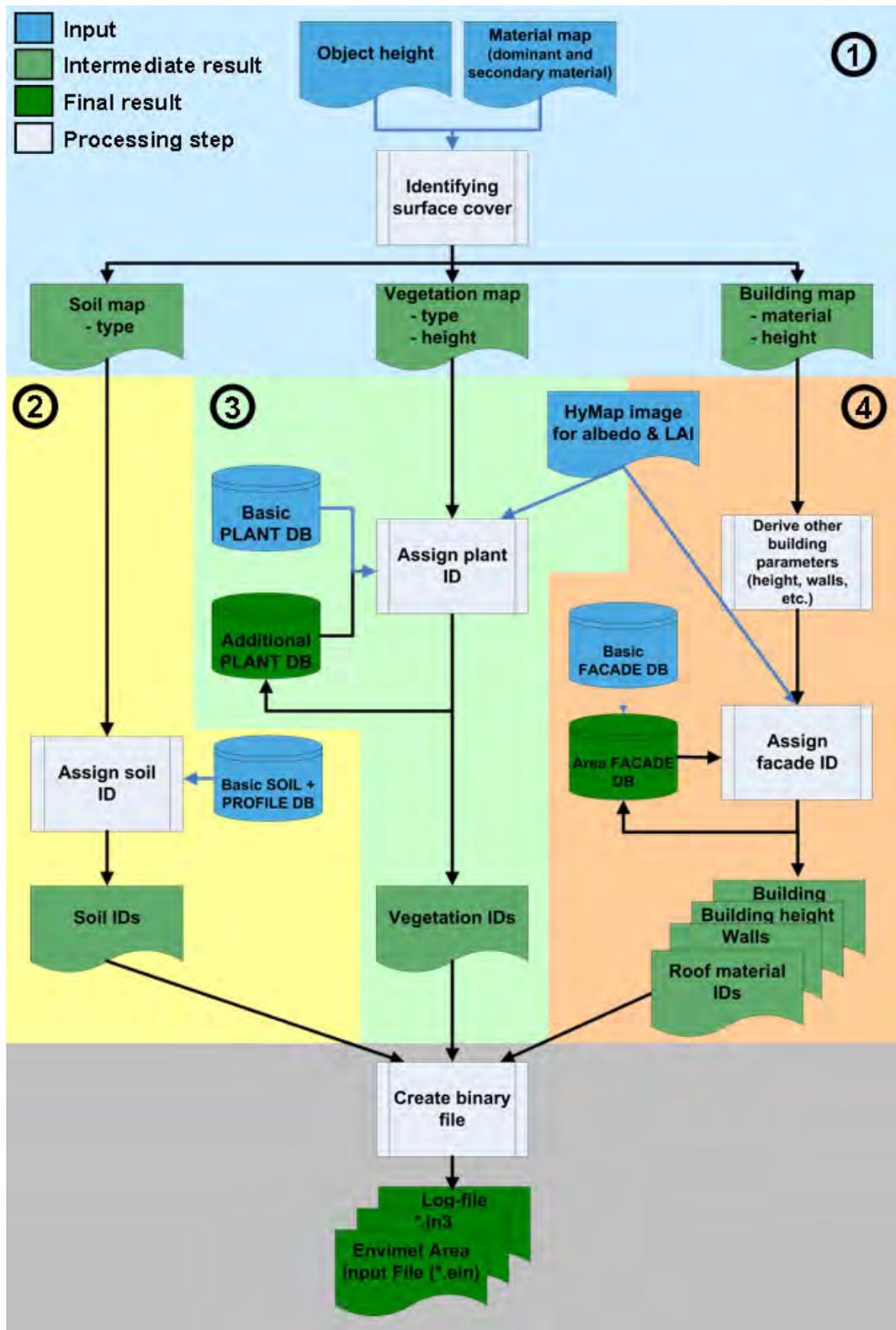
Figure 5.7: *Flowchart of the algorithm to generate the ENVI-met area input file. Detailed flowcharts of the processes in step 1, 2, 3 and 4 can be found in appendix B.*

especially expected to improve the representation of reality for materials with large within-class variation such as aluminium or roofing tiles of different ages. Because there is no information available on the material that is used for the building walls, a default material is assigned to all walls.

The building, vegetation and soil information are stored in a binary file in ENVI-met V4$\beta$ format together with a header file. The header includes as its most important entries the number and size of the grid cells in x,y, and z direction and the geographical location of the model area.

With the approach described here 16 ENVI-met area input files are created for the 15 simulation areas described in section 4.1 and the area around the meteorological station in the Theresienstraße (see appendix A for the location and aerial photographs of these areas).

## 5.4.4 Validation concept

Validation of the micro climate simulations is needed to gain insight in the quality of the results and to indicate the meaning of the simulated values for urban planners. The quality of the simulation results depends on the quality of the model and the input data. An accuracy estimation of the input data for the hyperspectral data products is given in section 6.1.3 and for the height data in section 4.3.2 . Assessment of the quality of the model is only possible on a limited scale within this study because extensive meteorological measurements are not available. Therefore it relies on literary validations of the model as well.

The accuracy of ENVI-met is among others assessed in Samaali et al. (2007) and Lauk (2009). Samaali et al. (2007) carried out a validation of the vegetation radiant fluxes by comparing ENVI-met simulations with simulations of the extensively validated SAIL model and field measurements of soybean canopy. The differences were within acceptable ranges for most parameters. Lauk (2009) compared measurements of temperature and wind speed and direction with ENVI-met simulation results. That study showed that temperature and wind direction are modelled accurately, whereas for wind speed an error range of 10 % should be taken into account. The study also revealed that the model is sensitive to surface properties such as albedo and emissivity. A 10 % decrease of the surface albedo results in a 4°increase of surface temperature.

Within the scope of this thesis only a simple accuracy assessment can be carried out. The assessment consists of a comparison between the modelled surface temperature and the surface temperature measured by the Daedalus thermal band. The results of this accuracy assessment are presented in section 6.4.2. The evaluation of other climate parameters was not possible because of a lack of reference data.

# 6 Results

This chapter presents the results of the implementation of the conceptual framework for the case study of Munich. Similar to the chapter on methodology (chapter 5) this chapter describes the remote sensing products in the first two sections. In section 6.3 the spatial indicators are presented and in section 6.4 the results of the micro climate simulations are revealed.

## 6.1 Material identification based on airborne hyperspectral data

This section first presents the results of the different steps of the material identification for the test area. The unmixing approach is adapted and transferred to the study area based on the (intermediate) results of the test area, demonstrating the potential of this technique to map large urban areas.

### 6.1.1 Endmembers

The first step of the material identification is the endmember identification with the feature classifier (section 5.1.3.2). In figure 6.1 a small subset of the endmember image is presented next to a HyMap false color composite of the same area for comparison. The endmember image shows which pixels are used to retrieve the endmember spectra. Many lawn pixels are selected from the large sports field in the centre of the subset. Quite some pixels of roofing zinc (blue in the HyMap image) have also been selected, from a large building. In the lower part of the endmember image several single roofing tile pixels are selected. These pixels are located on a long but small building (red in the HyMap image) which therefore does not contain that many pure pixels.

Table 6.1 shows the the number of selected pixels, the number of identified classes and the overall accuracy of the endmembers pixels selected with the untrained (i.e. not with Munich spectra) feature classifier, the trained feature classifier and the feature classifier trained without bad bands. The feature classifier trained with Dresden, Berlin and Potsdam spectra already reaches an overall accuracy of 65 %. By training the feature classifier with Munich image spectra this can be improved to 77 %. Most of this improvement has to be attributed to the addition of surface materials which especially occur in Munich, such as dark roofing tiles or bright asphalt. A further 2 % increase of the overall accuracy of the endmembers could be reached by removing bad bands from the training data set (see section 5.1.3.2). This version of the feature classifier is selected for use in this thesis.

Another important parameter for the selection of endmember pixels is the use of a building mask. In table 6.2 the number of selected pixels, the number of identified classes and the overall
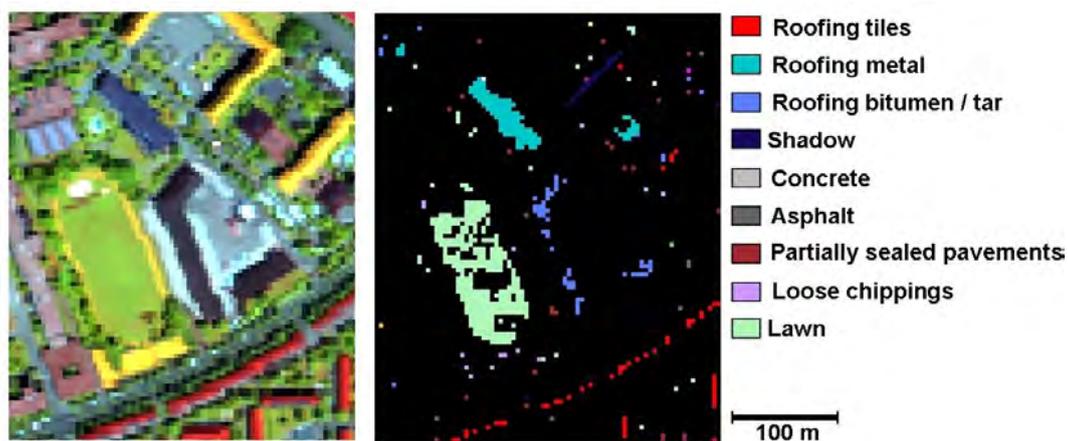
Figure 6.1: *Subset of the endmember image indicating the pixels selected as endmembers for each class. On the left the HyMap image of the subset for comparison (false color composite: RGB=b81,b19,b7)*

accuracy of the selected endmembers pixels are listed for three approaches; with and without buiding mask. The number of selected pixels is higher when a building mask is used. When looking at the overall accuracy of the three cases in comparison to the CLUSTER-reference data set, the selected endmember pixels have an overall accuracy of almost 80 %. Only minor differences in overall accuracy exist between the different approaches. Confusion exists among dark roofing materials, asphalt and concrete, and trees and lawn. However, for the sake of interpretation of this accuracy assessment it should be noted that only a limited number of reference samples was available (see table 6.2). Because the selected endmember pixels cover only about 6 % of the image, no endmember pixel was selected at all in many of the digitised reference clusters (see section 5.1.4) and samples had to be discarded. Therefore, a more important indicator for differences between the endmember identification with and without a building mask is the number of classes and pixels that can be identified. With a building mask more pixels are identified. Moreover, several important classes are not recognised or only a few pixels of these classes are selected. For example, with the HRSC-building mask 26 soil pixels, 237 coniferous tree pixels and 2000 red loose chipping pixels are identified. Because the building mask provides a priori information on the class of the pixel, the probability of identifying the material increases. Because of that, more pixels reach the probability threshold and are selected as endmember pixels. Without a building mask soil pixels are not identified at all and less than 50 pixels are identified as coniferous trees and less than 100 pixels as red loose chippings. Since the spectra of only three or more neighbouring pixels are included and a significant amount of pixels is required to represent the within-class variation, a larger number of selected endmember pixels is preferable. Therefore, the endmember selection using a building mask is preferred over the approach without a building mask. The DFK-building mask and the HRSC building mask are almost equally suited to support the endmember identification. The endmembers identified with the support of the DFK-building mask are used for the test area.

After the selection of the pure endmember pixels with the feature classifier based on the HyMap image, the spectra of these pixels are clustered into subclasses (see section 5.1.3.2).

Table 6.1: *Number and accuracy of the selected endmember pixels with 'untrained' and trained classifier. The 'untrained' classifier is trained with spectra from Dresden, Berlin and Potsdam but not from Munich. The DFK- building mask is used in all three approaches*

|  | Number of end-member pixels selected | Number of classes automatically detected | Overall accuracy [%] (number of reference samples) |
|---|---|---|---|
| 'Untrained' classifier | 41493 (4.8 %) | 24 | 66 (94) |
| Trained classifier | 53618 (6.2 %) | 30 | 77 (101) |
| Trained classifier without bad bands | 56682 (6.4 % ) | 48 | 79 (107) |

Table 6.2: *Number and accuracy of the selected endmember pixels for the three different approaches regarding the building mask*

|  | Number of end-member pixels selected | Number of classes automatically detected | Overall accuracy [%] (number of reference samples) |
|---|---|---|---|
| Without building mask | 48382 (5.6 % ) | 44 | 79 (89) |
| With DFK-building mask | 56682 (6.4 % ) | 48 | 79 (107) |
| With HRSC-building mask | 54786 (6.6 % ) | 48 | 78 (101) |

The average spectrum of each subclass is included in the endmember library. Figure 6.2 shows the subclass endmembers of clay roofing tiles and pvc. The general shape and location of the features are similar for each of the subclasses. The variation in albedo is caused by BRDF effects of the different roof inclinations and the sun/sensor geometry. For clay roofing tiles ageing also plays a role (Heiden, 2004): older roofing tiles have a lower albedo. Different colours of the material cause different reflection values in the visible part of the spectrum for PVC.

## 6.1.2 Seedlings

Three approaches have been tested for the identification of seedlings. The classification of the materials is carried out with and without the a priori knowledge of a building mask and additionally a hybrid solution is tested where the height is considered only for those classes that are commonly confused (see section 5.1.3.3). In this hybrid approach seedling pixels are identified in exactly the same way as without a building mask and corrected afterwards. This results in the same number of seedling pixels for those approaches, namely 41 % of the pixels of the test area. With the DFK-building mask 40 % of the pixels are identified as seedlings. By using the
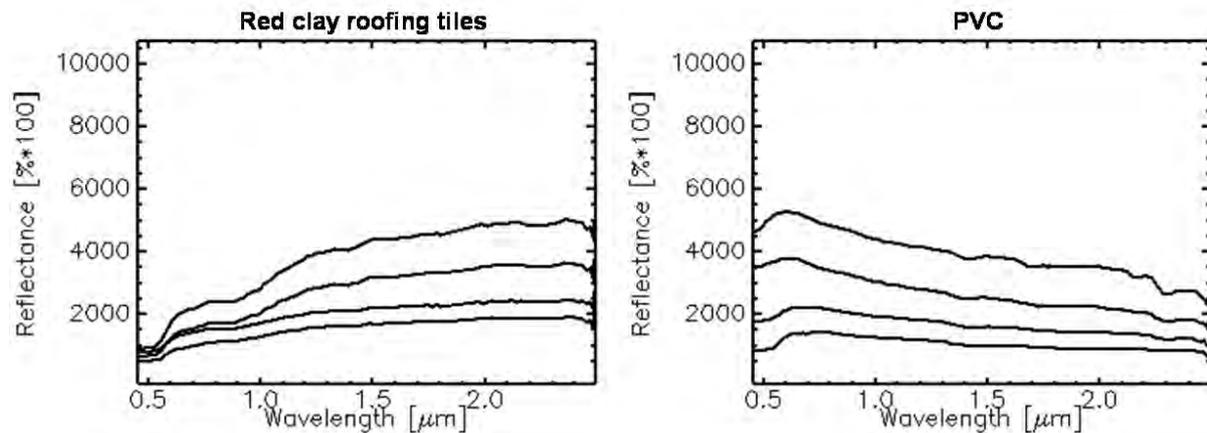
Figure 6.2: *Subclass endmember spectra of clay roofing tiles (left) and PVC (right)*

approach described in section 5.1.4 the accuracy of the seedling pixels is assessed by comparing them to the CLUSTER-reference data set. The result is presented in table 6.3. It shows that the overall accuracy of the seedling pixels selected without a building mask is the lowest, although it is still 73 %. By adapting the classes of the seedling pixels according to their height in the hybrid approach, the overall accuracy can be improved with 8 % to 81 %. The seedlings identified with support of the DFK building mask have the highest overall accuracy (86 %). The user and producer accuracies for a selection of classes are shown in table 6.3. Synthetic non-built surfaces, bare soil and loose chippings are not included in this selection, because seedling pixels were present in too few reference samples. One or two representative materials are selected of the roofing materials of each material category (level II, see table 5.1).

Mineral roofing materials (tiles, concrete) have good user and producer accuracies of above 89 %. One sample of concrete roofing tiles is assigned wrongly to the facade class in the hybrid approach, which reduces the producer accuracy to 75 %. The identification of metal roofing materials also show very high user and producer accuracies. Only aluminium is shown in table 6.3, but also zinc and copper have a user and producer accuracy of 100 % in all three approaches. Synthetic roofing materials show accuracies of around 80 %. Confusion occurs with bitumen and tar and within the synthetic roofing materials. Seedlings of hydrocarbon roofing materials (bitumen, tar) show clearly different accuracies for those identified without mask and those identified with the support of a building mask or height data. The user accuracy is in all cases higher than the producer accuracy. This means that there is an error of omission: bitumen and/or tar seedlings are not recognised. Those that have been assigned to the class of bitumen and tar indeed belong to that class in 67 % to 100 % of the cases. Missing bitumen and tar seedlings are wrongly assigned to synthetic or metal roofs and to asphalt. The confusion between hydrocarbon roofing materials and asphalt is reduced when using a building mask or height data, although it should be noted that the number of samples (6 for tar and 7 for bitumen) is too little to draw a definite conclusion.

Seedlings of concrete surfaces show a slightly higher user accuracy than producer accuracy in all three approaches. Confusion occurs mainly with asphalt, but also to a lesser extend with soil. The confusion between the bright concrete and the usually dark asphalt can occur because

Table 6.3: *Seedling accuracy of the three different approaches. UA=user accuracy; PA= producer accuracy.*

| | Seedlings derived with without building mask | | | Seedlings derived DFK-building mask | | | Seedlings derived with hybrid approach | | |
|---|---|---|---|---|---|---|---|---|---|
| | **UA [%]** | **PA [%]** | **Nr of samples** | **UA [%]** | **PA [%]** | **Nr of samples** | **UA [%]** | **PA [%]** | **Nr of samples** |
| Red roofing tiles | 100 | 96 | 27 | 96 | 96 | 28 | 100 | 97 | 29 |
| Red roofing concrete | 100 | 100 | 4 | 100 | 100 | 4 | 100 | 75 | 4 |
| Dark roofing tiles | 100 | 89 | 9 | 100 | 90 | 10 | 100 | 89 | 9 |
| Concrete roof | 100 | 94 | 18 | 100 | 100 | 18 | 100 | 100 | 18 |
| Roofing aluminium | 100 | 100 | 3 | 100 | 100 | 3 | 100 | 100 | 3 |
| Roofing PVC | 80 | 80 | 5 | 80 | 80 | 5 | 80 | 80 | 5 |
| Roofing polyethylene | 67 | 80 | 5 | 83 | 100 | 5 | 80 | 80 | 5 |
| Roofing bitumen | 67 | 29 | 7 | 100 | 29 | 7 | 100 | 29 | 7 |
| Tar | 75 | 50 | 6 | 100 | 33 | 6 | 100 | 33 | 6 |
| concrete | 80 | 57 | 7 | 71 | 71 | 7 | 83 | 71 | 7 |
| Asphalt | 89 | 60 | 28 | 95 | 68 | 28 | 89 | 61 | 28 |
| Cobble stone pavement | 10 | 100 | 1 | 17 | 100 | 1 | 10 | 100 | 1 |
| River | 100 | 100 | 2 | 100 | 100 | 2 | 100 | 100 | 2 |
| Trees | 100 | 43 | 30 | 100 | 97 | 33 | 97 | 94 | 32 |
| Lawn | 47 | 100 | 16 | 100 | 100 | 17 | 89 | 100 | 16 |
| *Overall accuracy* | *73* | | | *86* | | | *81* | | |

the asphalt of many roads is relatively old in Munich. Ageing increases the albedo of asphalt (Herold and Roberts, 2005) which can lead to the confusion with concrete. Similar to concrete asphalt has a higher user accuracy than producer accuracy. Asphalt pixels are wrongly assigned to concrete for the above mentioned reason, but also to cobble stone and railway tracks. Not many cobblestone seedlings are identified. It is difficult to find pure pixels of this material, because cobblestone pavements are usually applied on smaller roads and footpaths. Cobblestone seedlings were identified only within one reference sample and this sample was identified correctly in all three approaches. However, this class has large errors of commission, where mainly asphalt pixels are assigned to the cobblestone class.

Vegetation is identified correctly in almost 100 % of the samples. However, the separation between trees and lawn is not spotless for the approach without a building mask. The height data supports this separation for the hybrid approach and increases the user and producer accuracy of the identification of lawn and trees from 89 % to 100 %.

The accuracy assessment of the seedling maps shows that the approaches to identify the seedlings which were supported with a building mask or height data are more accurate than the seedling identification without a building mask or height data. Improvements in the correct identification of hydrocarbon roofing materials and asphalt are especially found, as well as a considerable improvement in the separation between trees and lawn. Because the seedlings derived with the DFK-building mask have the highest overall accuracy, this approach is used as input for the following step, the iterative unmixing.

### 6.1.3 Material abundances

The iterative unmixing described in section 5.1.3.4 is the last step in the identification of the materials. The result is an abundance map for each material class. For visualisation purposes, these abundance maps are summarized into a map of the dominant class, a map of the second class, a map of the abundance of the dominant class and a map of the abundance of the second class per pixel. Figure 6.3 presents these four maps for a small subset of the test area and shows the full information content of the unmixing result at sub-pixel level. Pure pixels appear black in the second class image on the right. The information about the abundance of the two classes is shown in the abundance images in figure 6.3. The abundance of the dominant class is given on the left. Pure pixels appear white in this image, but they appear black in the abundance image of the second class. These images show that mixed pixels often occur at the borders of objects, such as buildings. The sports field marked with the red arrow also contains mixed pixels. The running track of red loose chippings around the sports field is about 6 meters wide, only 2 meters wider than the pixel size of HyMap. The chance of one pixel being completely covered by the track is small. With the unmixing analysis the track can also be identified if it is only partially covered by the pixel. The dominant material alternates between lawn and red loose chippings, as it does for the material of the second class, which allows the detection of the small track. Between larger objects a border of mixed pixels can often be seen, e.g. between the building and the parking lot marked with the green arrow. The border between the pure bitumen pixels of the building and the pure concrete pixels of the parking lot consists of mixed pixels with concrete as their dominant class and bitumen as their second class.

The dominant class of the test area is shown in figure 6.4. More than 99% of the pixels in the test area could be unmixed, 44% of which are pure pixels. The variation surface covers is clearly visible, as is the variation in building and vegetation structures. Roofing tiles (clay and concrete) are the most common roofing material. In block developments, for example in the upper left part of the image, a considerable amount of metal roofing is also found. In the centre of the image the Eastern railway station with its railway tracks can be clearly recognised. In the adjacent (former) industrial areas almost no roofing tiles have been used. There, more often bitumen, concrete and synthetic roofing materials have been applied. An analysis of typical roofing materials for the different urban structural types is provided in section 6.3. Large buildings can be very well identified. Urban structural types with smaller buildings such as the detached and semi-detached houses in the south-west of the test area are more difficult to identify. Most houses do not take up a complete pixel. Additionally, they are often covered by tree crowns or shade of surrounding trees, which makes the identification of the roofing materials more difficult.

The mean RMSE of the unmixing result of the test area is 1.53 %. Half of the pixels in the image could be unmixed with an RMSE of less than 0.9 %. This means that the unmixing model is very accurate. In order to analyse the thematic accuracy an area based validation is carried out according to the approach described in section 5.1.4. The mean absolute error (MAE) and the bias of the calculated abundances in comparison to the BLOCK-reference data are shown in table 6.4. All classes that have been identified during the unmixing step are included in the analysis. The validation is carried out at two scale levels. The first scale is the building block level, where a building block contains about 550 pixels on average. This level is relevant to the use of the material abundances when calculating the spatial indicators. The overall MAE is
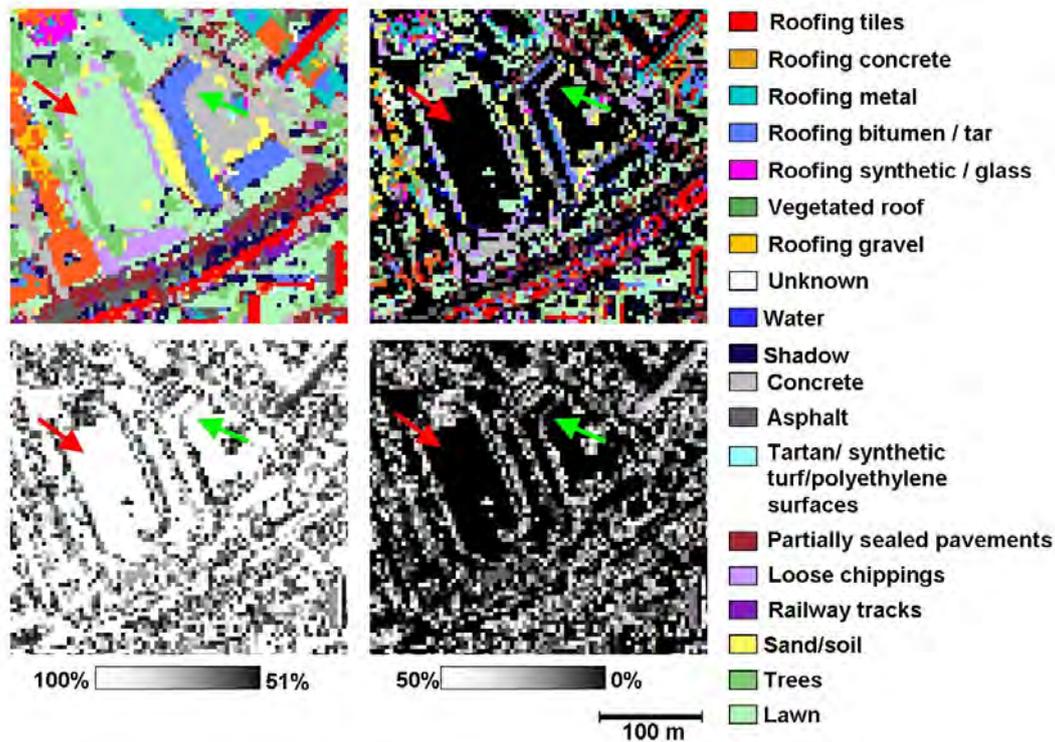
Figure 6.3: *Detail of the unmixing results. The upper two images show the dominant class (left) and the second class (right). The lower two images show the abundances of the dominant class (left) and the second class (right) in %.*

2.2 % abundance for the area based validation per building block. The other level focuses on clusters of 3x3 pixels. This level is relevant to the implementation of the material abundances into the micro climate model. The overall MAE for this level is 16 % abundance. There are two ways to explain why the MAE at the 3x3 pixel cluster level is almost 14 % higher than the MAE at building block level. The first is that spatial errors are balanced out in large validation areas and so the accuracy can be overestimated. The other is that small co-registration errors increase the spatial errors in small validation areas and cause an underestimation of the accuracy. In Heldens et al. (2009b) these influences have been investigated in more detail.

The bias can be used to gain insight in the nature of the error, especially at the 3 x 3 pixel level. If the bias is small, it can be assumed that the error is mainly caused by a co-registration error between the reference data and the unmixing result, as is the case for PVC. However, if the bias is large confusion with other classes also play a role. This is for example the case for roofing bitumen and tar. These materials are overestimated, because they are incorrectly assigned to shaded roofs of other materials (e.g. tiles). The shadow strongly reduces the overall albedo of all materials. Because a spectrum of bitumen and tar usually has a very low albedo and therefore almost no recognisable features it can easily be confused with a shaded spectrum of for example roofing tiles or metal.

At building block level the MAE is below 5 % for 29 out of 31 classes. Thus, for the material abundance aggregated at building block level an average error margin of +/- 5 % has to be taken
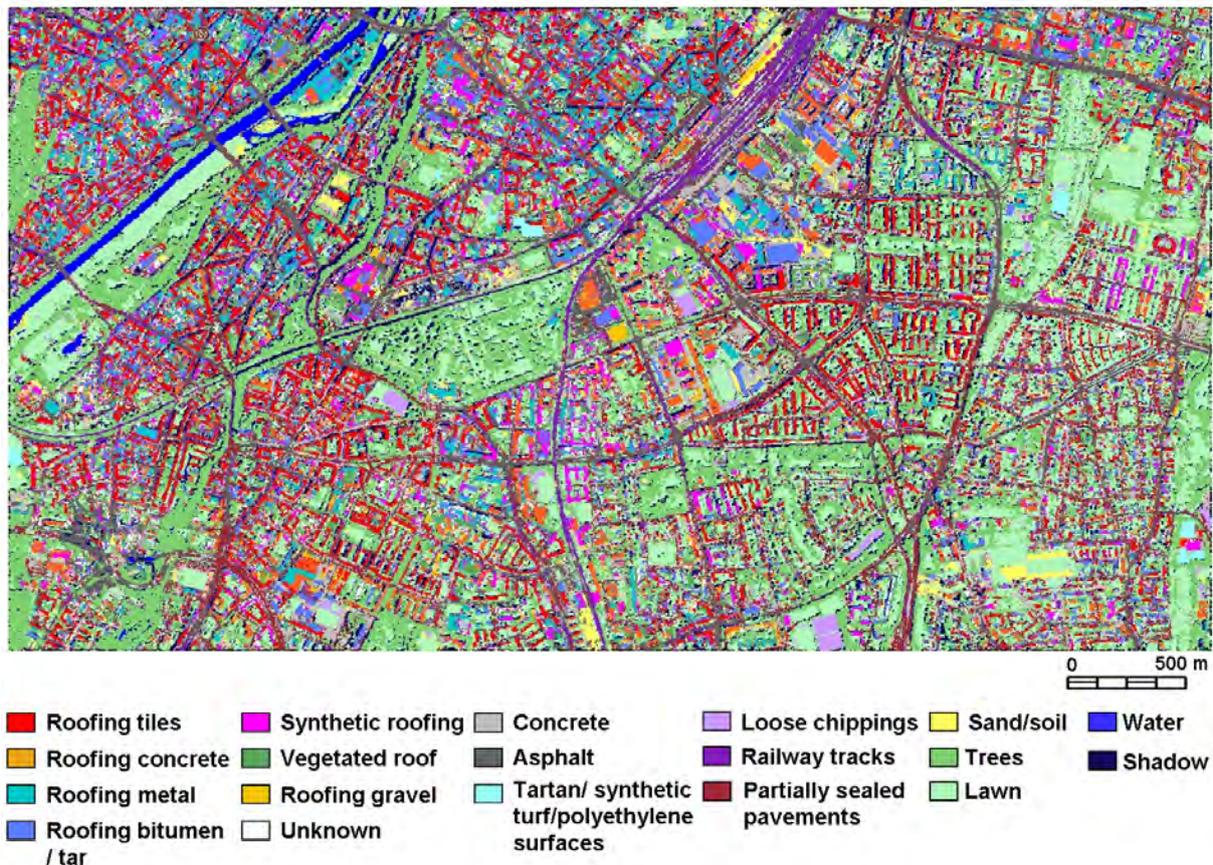
Figure 6.4: *Unmixing result of the test area (dominant class)*

into account for the fractional cover. For 3 x 3 pixels this error margin is less than +/- 20 % for 25 out of 31 classes. This means that with the applied unmixing approach almost all materials could be identified with high accuracy. In order to gain more insight in the accuracy of the material abundance map three classes with lesser accuracy are selected and discussed below.

Trees show an MAE of 10.3 % at building block level and 22.9 % at 3 x 3 pixel cluster level. Compared to the BLOCK-reference the abundance of trees is underestimated (bias = -9.4% at building block). This can be explained by a confusion with lawn (which is slightly overestimated), by the high amount of shaded vegetation and by the building mask. Both vegetation types (trees and lawn) are frequently obscured by shadows cast by buildings and trees, resulting in a 4.8% abundance of shaded vegetation in the whole test area. The building mask does not fit the HyMap data perfectly (see section 4.3.3). This small co-registration error causes vegetation adjacent to buildings to be forced to being mapped as a roof material. Most of this vegetation is then identified as vegetated roof. Additionally, some underground car parks are included in the DFK-building mask. They are commonly covered with vegetation and so these areas are also identified in the reference data. However, the building mask forces a building material in these areas and thus vegetated roof is assigned, causing an underestimation of lawn and trees and an overestimation of vegetated roofs.

Concrete has an MAE of 8.0 % at building block level and 18.8 % at 3 x 3 pixel cluster level.

Table 6.4: *Accuracy of material abundances evaluated at 3x3 pixels scale and at building block scale*

| Class | Total abundance in the validation area [%] | 3x3 pixel cluster | | Building block | |
|---|---|---|---|---|---|
| | | MAE | Bias | MAE | Bias |
| Red roofing tiles | 9,2 | 17,0 | 2,7 | 3,1 | 1,4 |
| Dark roofing tiles | 6,1 | 20,1 | -10,1 | 4,1 | -3,5 |
| Red roofing concrete | 4,1 | 13,7 | 2,0 | 1,1 | 0,4 |
| Bright roofing concrete | 1,1 | 37,6 | -32,3 | 1,9 | -1,7 |
| Roofing aluminium | 1,4 | 7,5 | 4,2 | 0,9 | 0,4 |
| Roofing copper | 0,2 | 25,3 | -19,0 | 0,3 | -0,3 |
| Roofing zinc | 0,7 | 12,0 | -3,7 | 1,0 | -0,5 |
| Roofing coated metal | 0,0 | 15,5 | -14,8 | 0,6 | -0,6 |
| Polyvinyl chloride (PVC) | 5,8 | 18,0 | -0,7 | 1,8 | -0,7 |
| Polyethylene | 1,0 | 14,3 | 0,6 | 0,4 | 0,1 |
| Dark roofing bitumen | 1,3 | 14,8 | 4,9 | 1,4 | 0,2 |
| Red roofing bitumen | 0,3 | 17,8 | 1,0 | 0,7 | -0,1 |
| Roofing tar | 4,5 | 17,5 | 16,8 | 4,4 | 4,4 |
| Vegetated roof | 3,1 | 19,1 | 10,6 | 2,2 | 2,2 |
| Roofing gravel | 1,7 | 37,7 | 37,7 | 1,7 | 1,7 |
| Facade/unknown | 4,6 | 10,7 | 9,3 | 0,8 | 0,8 |
| Concrete | 1,6 | 18,8 | -15,7 | 8,0 | -7,8 |
| Asphalt | 4,9 | 16,3 | -1,5 | 3,9 | 1,6 |
| Synthetic turf | 0,1 | 4,8 | 4,8 | 0,1 | 0,1 |
| Green polyethylene surface | 0,0 | 4,7 | 4,7 | 0,0 | 0,0 |
| Cobblestone pavement | 2,1 | 17,7 | 17,4 | 2,1 | 2,1 |
| Red concrete pavement | 0,7 | 14,0 | 14,0 | 0,7 | 0,7 |
| Red loose chippings | 1,9 | 11,1 | 5,1 | 1,8 | 1,5 |
| Railway tracks | 0,9 | 21,0 | 21,0 | 0,9 | 0,9 |
| Siliceous sand | 0,4 | 6,8 | 2,3 | 0,4 | 0,2 |
| Soil | 0,3 | 9,7 | 2,4 | 0,3 | 0,2 |
| River | 0,6 | 5,9 | 5,9 | 0,6 | 0,6 |
| Trees | 16,3 | 22,9 | -13,0 | 10,3 | -9,4 |
| Lawn | 18,4 | 18,3 | 8,3 | 4,3 | 1,9 |
| Shadow on vegetation | 4,6 | 15,7 | 14,6 | 4,5 | 4,5 |
| Shadow | 1,6 | 9,6 | 9,5 | 1,6 | 1,6 |
| *Overall* | | *16,0* | *2,9* | *2,1* | *0,1* |

The underestimation of concrete (bias = -7.8%) can be partly explained by confusion with asphalt, which shows a small overestimation (bias = 1.6%). This confusion already occurred during seedling classification (see previous section) because of the similarity between spectra of concrete and old asphalt. Another part of the underestimation of concrete can be explained by the fact that concrete surfaces (mainly streets) are relatively often covered by shadows cast by adjacent buildings. 1.6 % of the whole test area is identified as shaded surface.

The accuracy of the class railway tracks is not explicitly visible in table 6.4. The MAE is 0.9 % and 21.0 % for the building block and the 3 x 3 pixel cluster, respectively. In the validation area railway track has been identified in only 0.9 % of the area. However, in the whole test area this class covers 2.6 %. This is more than can be expected when looking at the amount of railway tracks in the image (in comparison: dark roofing tiles cover 2.6 % of the test area as well). A close look at the abundance image of the test area shows that this class is scattered over the whole the image. This is assumed to be the result of the mixed nature of the class and not of an error in the unmixing algorithm. A railway track exists of multiple surface materials including the rails, soil and vegetation. Therefore, the endmember spectrum of the class railway shows similarities to all of these materials. This makes it a very suitable endmember to add

to the modelled mixed spectrum in order to improve the RMSE. The railway endmember is frequently added to pixels that contain a mixture of vegetation and asphalt or concrete. Although the railway class is thus often overestimated, actual railway tracks are mainly correctly identified in the unmixing result, as can be seen in figure figure 6.4.

It is difficult to compare the results of this study with the results of other urban material classifications presented in literature. Firstly, because only a few studies were published in which airborne hyperspectral data was used in urban mapping with such high thematic detail and second because accuracies of sub-pixel classifications cannot be directly compared to full-pixel classification accuracy assessments (e.g. a confusion matrix). A few studies to which the results of this thesis may be compared are Franke et al. (2009), Bhaskaran et al. (2004) and Ben-Dor et al. (2001). In Franke et al. (2009) a MESMA approach was applied so as to identify of 24 urban surface cover types, among which eleven roof materials by making use of HyMap data. Ben-Dor et al. (2001) also used a spectral unmixing approach to identify ten urban surface cover types based on CASI hyperspectral scanner data. Bhaskaran et al. (2004) used a spectral angle mapper (SAM) approach to identify five different roof materials in a HyMap image of Sydney. Although different materials are present, since the studies were carried out in different parts of the world, they also found that it is possible to separate the urban materials accurately with the use of the hyperspectral data. However, in these studies confusion of dark roofing materials with shadow and asphalt also occurred frequently. Franke et al. (2009) and Ben-Dor et al. (2001) both applied a sub-pixel mapping approach: they provided the accuracy assessment only for the dominant material in each pixel. Therefore, the mean absolute error calculated in this study cannot be compared to the results of those studies.

### 6.1.4  Application of the unmixing approach for large areas

The results of the identification of materials for the test area show that the applied approach works well for a small test area. However, the advantage of remote sensing is the large spatial coverage and the ability of automatic processing of large data sets. Therefore the unmixing approach described in the previous sections is transferred to the complete study area covering almost the whole city of Munich. The study area includes seven flight lines, each with a length of 12 km (see chapter 4 for a full description), thus covering a region of 252 km$^2$.

The settings that were found to be optimal for the test area could not all be applied to the large area directly due to data availability and computation time. The following paragraph therefore describes the changed settings for endmember selection, seedling selection and iterative unmixing.

Because the study area is very extensive, the seven HyMap flight lines are processed separately for computational reasons. The endmembers are identified with the trained feature classifier (bad bands excluded) for each of these flight lines separately, allowing image specific spectral characteristics to be included in the endmember spectra. The approach with the HRSC-building mask is selected, because a DFK-building mask was not available for the whole study area. A probability threshold of 80 % is applied. This is higher than the threshold used for the test area and is selected to improve the quality of the endmembers. Because the area is much larger than the test area, there is no risk of too few endmember pixels being selected. No classes were manually added, in order to keep the number of manual interactions as low as possible.

Table 6.5: *Statistics of endmembers, seedlings and RMSE for each flight line of the study area*

| | % pixels selected as EM | % pixels selected as seedling | Mean RMSE [% reflectance] | % pixels unclassified | % pure pixels |
|---|---|---|---|---|---|
| Line 1 | 5.4 | 58.2 | 0.71 | 0.9 | 71.6 |
| Line 2 | 6.2 | 54.7 | 0.74 | 0.9 | 69.5 |
| Line 3 | 6.6 | 52.5 | 0.77 | 0.3 | 69.5 |
| Line 4 | 7.9 | 50.4 | 0.72 | 1.2 | 70.6 |
| Line 5 | 6.3 | 46.0 | 0.82 | 0.2 | 63.9 |
| Line 6 | 7.8 | 61.0 | 0.65 | 0.7 | 76.0 |
| Line 7 | 6.5 | 57.3 | 0.70 | 0.8 | 71.4 |
| *Mean* | *6.7* | *54.3* | *0.73* | *0.7* | *70.4* |

An unconstrained number of endmembers requires too much computation time when unmixing of the complete study area. Therefore, the number of subclasses for this large area is constraint to a maximum of ten after testing.

The hybrid approach is selected for the identification of the seedlings. The test area showed that this considerably improves the accuracy of the seedlings when no DFK-building mask is used.

The flight lines are divided into even smaller parts for the iterative unmixing, because of the computation time. After the unmixing analysis all subsets are mosaicked to form the result of the complete study area. As for the test area the maximally allowed RMS error is set to 10 %. The number of iterations is reduced to 20, to save computation time.

Table 6.5 lists the percentage of selected endmembers and seedlings for each flight line. The number of endmembers is slightly higher than in the test area. Also the number of seedlings is higher than in the test area. This can be explained by the large forests south of Munich, which are also covered by the flight lines. Many pure tree pixels are available here, for example: in the first flight line the seedlings of the tree class cover 19 % of the image, which is a third of all the seedlings in this flight line. In order to assess the accuracy of the seedlings for the whole study area, a mosaic of line 5, 6 and 7 is created so as to allow comparison with the CLUSTER-reference data as described in section 5.1.4. The overall accuracy of the seedlings is 80.3 %, which is comparable to the overall accuracy of seedlings derived with the hybrid approach for the test area (81 % ).

The mean RMSE per flight line is indicated in table 6.5, as well as the percentage of pixels that could not be unmixed and the number of pure pixels in each flight line. The mean RMSE is very low with values of about 0.7 % for each flight line. This low RMSE value is influenced by the high number of pure pixels which cover 70.4 % of whole study area.

Figure 6.5 shows the result of the unmixing in a spatial form and summarized in a dominant class image. Areas with cloud cover and severe geometric inaccuracy are masked out (see for more explanation section 4.3.1). The image clearly shows the different structures in the city. Two remarkable line structures are the river Isar which flows from south to north accompanied by large green areas and the large railway tracks from west to east. The city centre is densely built

with tiles and metal as main roofing materials. Towards the outskirts of the city the building density decreases strongly. A pattern of single small and larger buildings can be seen there, accompanied by large parks or other green areas. Several industrial areas can be identified by the large buildings and mainly synthetic or bitumen roofing materials, for example south of the railway tracks in the middle of the image or west of the Isar (south of the city centre).

The subset in figure 6.5 shows the area around the castle Nymphenburg and the Nymphenburger Channel. It clearly shows the main road crossing the channel (north-south direction) as well as the building blocks of detached and semi-detached houses and small multi-storey buildings. This illustrates that the unmixing approach is also able to map urban surface materials accurately for a large area with only minimal manual interaction.

Some of the agricultural fields could not be identified (black areas in the south-east). On these fields crops are in several growing stages, which were not represented by the endmembers. The unmixing algorithm focuses on urban surface materials and is therefore less suitable for the mapping of agricultural land.

Another remarkable effect is the visibility of the different flight lines within the classification mosaic. The shaded area is much larger on the eastern side of the flight lines, for example. This can be directly related to the sensor's broad field of view and the sun-sensor angle. This also plays a role in the test area, but becomes more visible in the forests.

In the large study area the classes railway track and vegetated roof are overestimated, which is similar to the test area. This is more frequently the case in urban structural types with small buildings and a lot of vegetation such as detached and semi-detached houses. Those have a large number of mixed pixels which resemble the railway track endmember because they contain both vegetation and a road or building .

A mosaic to cover the reference data set was created for the abundances just like the one for the endmembers and the seedlings. This mosaic was used for an assessment of the accuracy of the abundances following the approach described in 5.1.4. With an overall mean absolute error of 2.3 % at building block level (bias = 0.1 %) and 22.0 % at the 3x3 pixel cluster level the accuracy is comparable with the that of the abundances in the test area. It should be noted however, that the areas where the effects and inaccuracies described above occur most frequently are mainly outside this test area.
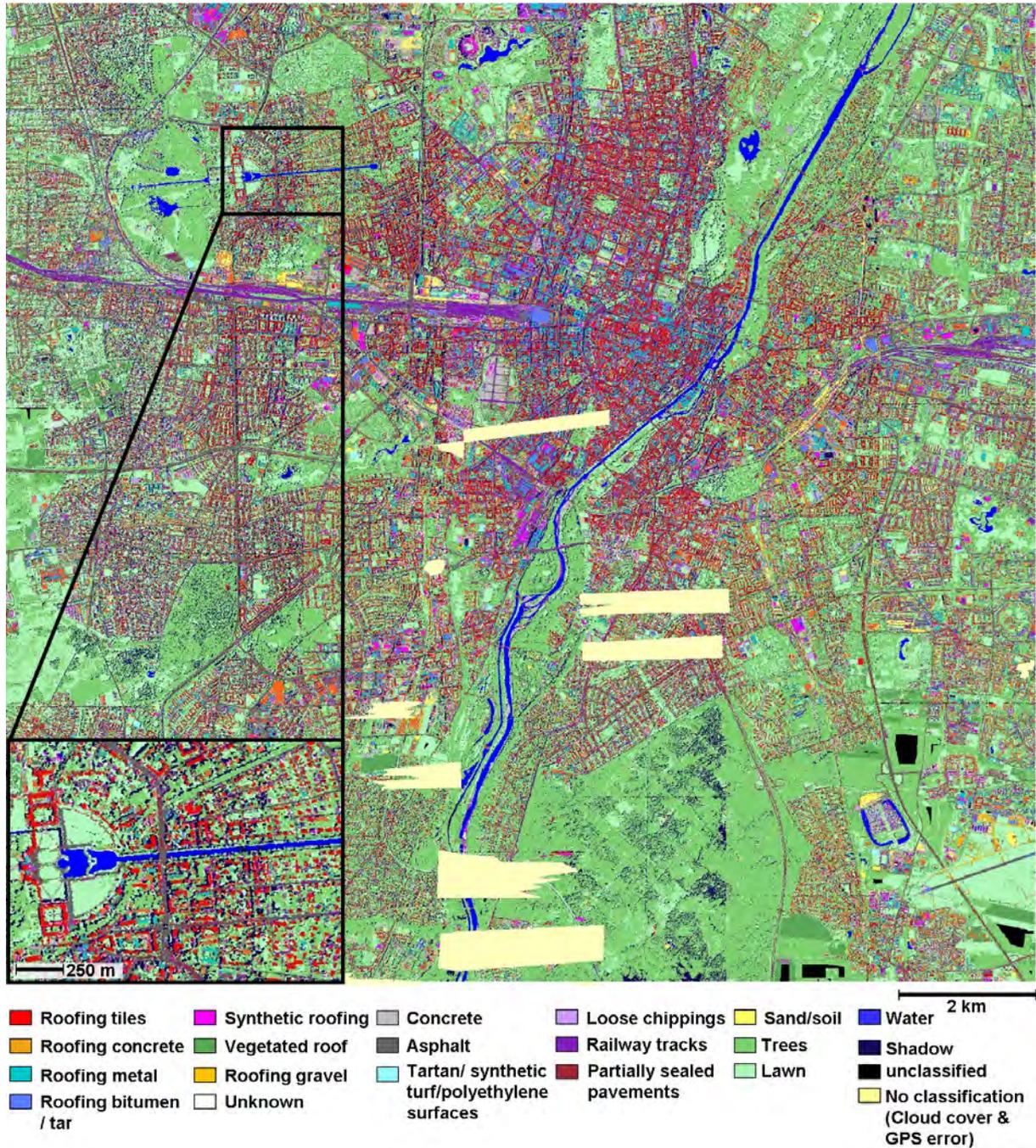
Figure 6.5: *Unmixing result of the study area (dominant class)*

# 6.2 Additional hyperspectral data products

This section presents the results of two hyperspectral products that are required as input parameters by micro climate models. Section 6.2.1 compares the results of the two approaches to calculate surface albedo as described in section 5.2.1. Section 6.2.2 shows the results of the different approaches to calculate leaf area index as described in section 5.2.2 and the subsequently calculated leaf area density.

## 6.2.1 Albedo

Figure 6.6 gives the results of the two different albedo calculations as described in section 5.2.1 for a part of a HyMap flight line in the west of Munich. The differences between the two approaches to calculate albedo are minor. The general pattern of different albedo values for different land cover types is similar in both images. However, where the albedo is rather equally distributed in the average reflectance image there is a clear gradient in albedo in the ATCOR albedo image. In this image, the albedo increased from east to west. This is caused by the large viewing angle of the HyMap sensor. This effect is corrected for during pre-processing by using the nadir normalisation module in ATCOR (see section 4.3.1). In the ATCOR software the nadir normalisation can only be applied after the calculation of albedo. Calculating the albedo based on the average reflectance can be done at every moment in the processing chain; also after the nadir normalisation, as was done here. It is preferable to use a nadir normalised image for the calculation of albedo, for in that case the influence of the sun/sensor geometry is reduced and the albedo value mainly represents the material properties. Only the material specific albedo is required by the ENVI-met model, because the model simulated the changing sun-angle itself. Therefore, and because of its flexible and easy calculation, the average reflectance based albedo is selected for the following steps.

## 6.2.2 Leaf area index and leaf area density

The leaf area index (LAI) is calculated with different vegetation indices as described in section 5.2.2. Figure 6.7 shows the LAI maps for a small subset. There are large differences in the absolute values of the LAI and also in the patterns within the area for the different LAI calculations. Both NDVI based LAI maps show the highest LAI values. The LAI-NDVI of the MODIS backup algorithm shows a little bit more variation within the image, e.g. along roads and other mixed pixels. The LAI RVI map shows higher LAI values for lawns than for trees. A similar pattern but one with even lower values for trees (LAI < 2) is mapped by the LAI MSAVI approach, which was originally developed for crop analysis. Such low LAI values are unlikely for healthy deciduous trees in Summer. The LAI REIP was developed for coniferous forests and it shows overall low LAI values. Only a few trees have higher LAI values.

Before selecting the best approach as input for the leaf area density calculation it should be noted that the variations of LAI values of single trees in urban areas can be very large. Damm (2008) measured LAI values between 2 and 9 for chestnut trees in Berlin, for example. Because there are no LAI field measurements for the Munich area available, it is difficult to judge what LAI values are correct and thus which method is most suitable. In addition it should be mentioned that LAI values higher than 6 do not influence the reflectance spectrum any further
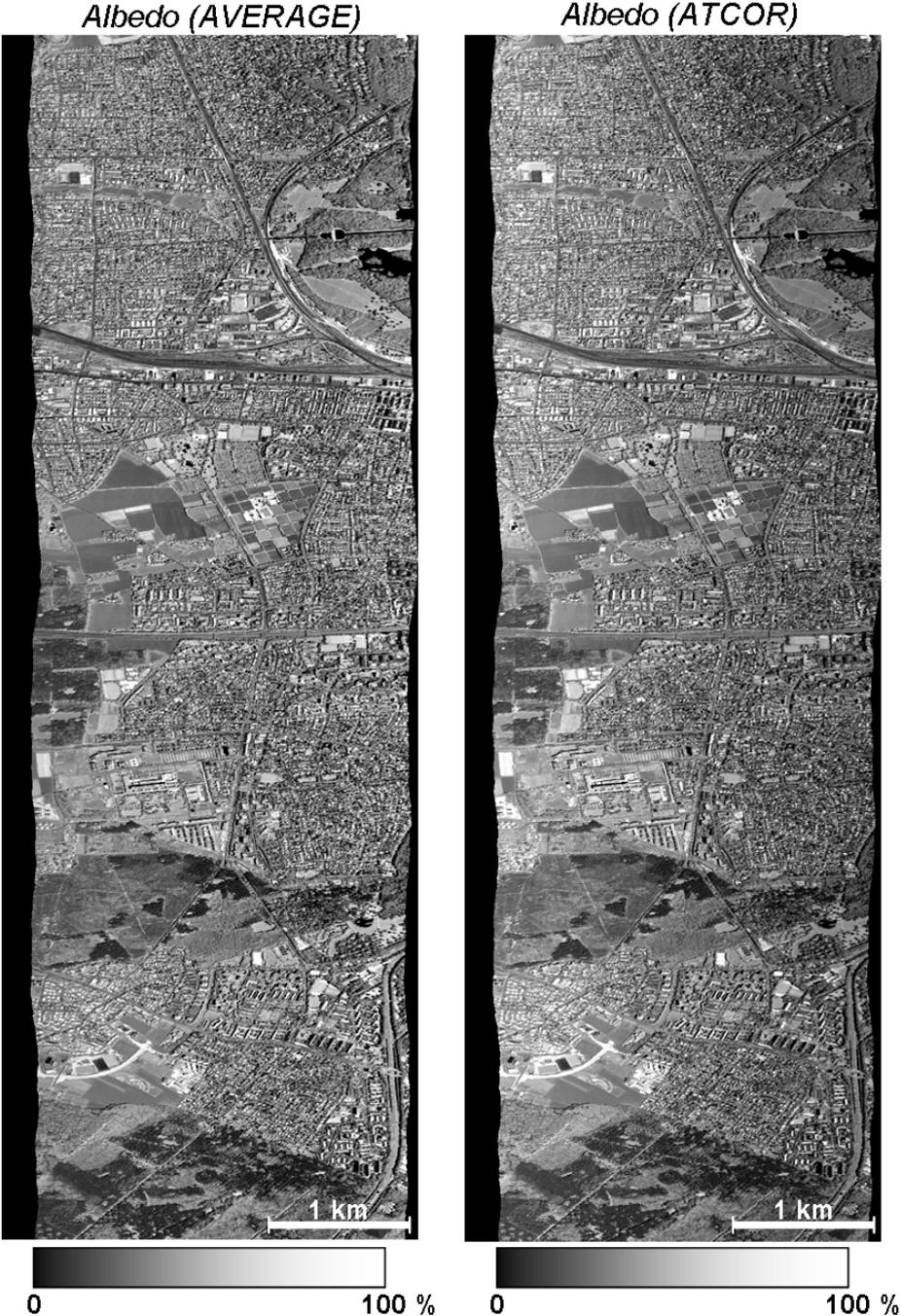
Figure 6.6: *Comparison between mean reflectance (left) and albedo calculated with ATCOR software (right).*
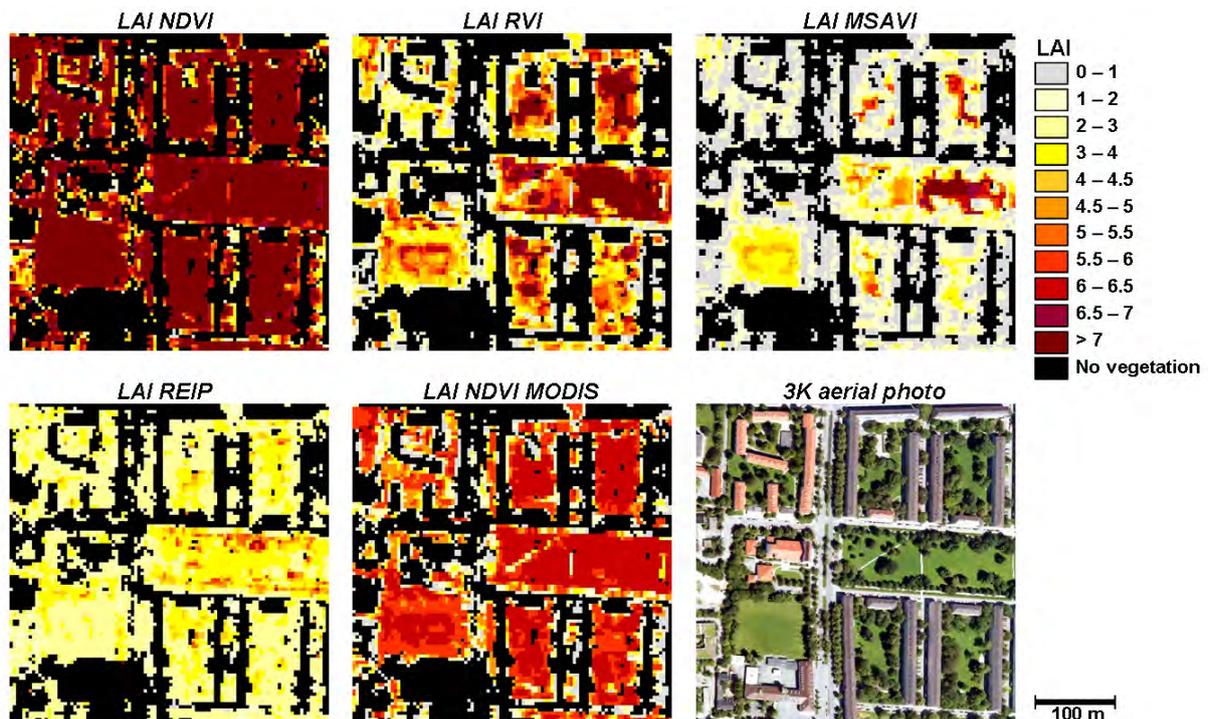
Figure 6.7: *Comparison of LAI-NDVI (Wang et al., 2005), LAI-RVI (Liu et al., 1997), LAI-MSAVI (Haboudane et al., 2004), LAI-REIP (Danson and Plummer, 1995) and LAI-NDVI MODIS (Knyazikhin et al., 1999). 3K aerial photograph for orientation.*

and so a saturation of the measurable LAI value occurs with remote sensing (Haboudane et al., 2004).

When assuming that healthy lawn has a LAI of at least 2.5 and deciduous trees have a LAI higher than 5 (Scurlock et al., 2001), one of the two NDVI-based approaches is preferred. The fact that the MSAVI, REIP and RVI based approaches are originally developed for crops and (mainly) coniferous forests, supports this preference. The NDVI-MODIS based LAI measure is selected for further use because of the application for different vegetation types and the fact that it is a generally accepted approach as part of the MODIS-LAI algorithm.

The leaf area density (LAD) is calculated according equation 5.7 using the calculated LAI and the height of the pixel. The height at which the maximum LAD of the tree can be found is set to $0.7h$ for all trees, where $h$ is the total height of the tree. ENVI-met requires the leaf area density to be calculated at ten points, equally spread over the total height of the tree. In figure 6.8 the LAD for four exemplary trees is shown, with the height of the tree at the y-axis and the LAD at the x-axis. By doing this, the curve follows the shape of the tree with low leaf area density at the stem and higher densities at the crown of the tree. Trees with similar a leaf area index (for example tree A and B) show a different crown density as a result of their different heights. The curves are similar to those calculated and measured by Lalic and Mihailovic (2004) and those available in ENVI-met.
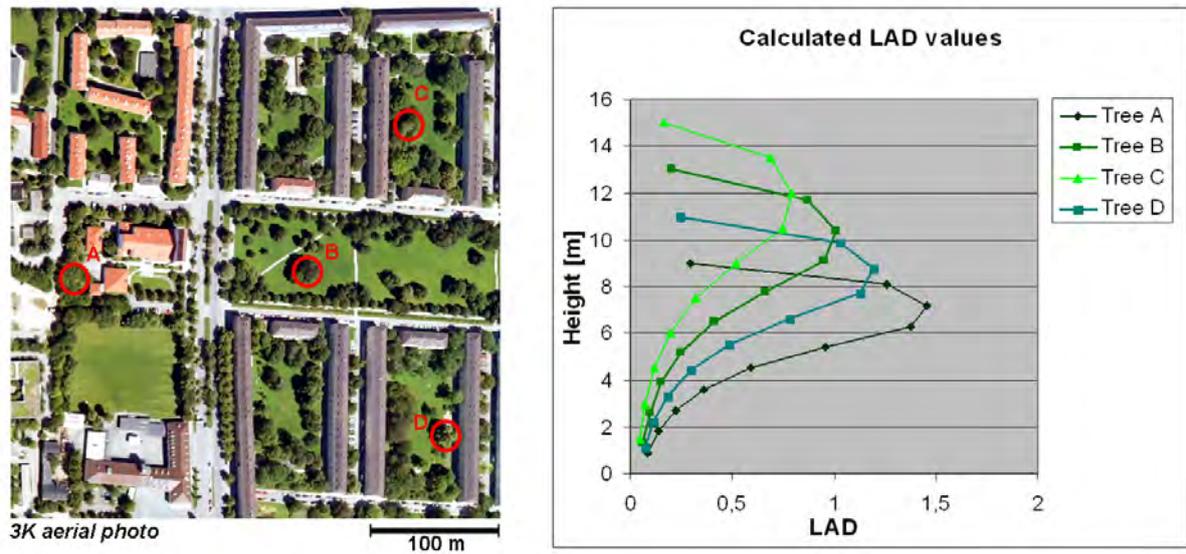
Figure 6.8: *Calculated leaf area density (LAD) for four exemplary trees : A (height: 9 m , LAI: 6.1), B (height: 13 m , LAI: 6.1), C (height: 15 m , LAI: 5.5) and D (height: 11 m , LAI: 6.1). The tree locations are indicated in the aerial photograph (left).*

# 6.3 Spatial indicators

In the following section the result of the mapping of spatial indicators is presented. Firstly, the derived maps of the spatial indicators and their accuracy are dealt with. Next, the relation to urban structural types is addressed.

### 6.3.1 Mapping spatial indicators

Figure 6.9 and 6.10 present two of the calculated indicators for the study area. No indicators were calculated for building blocks with cloud cover or large GPS errors.

The imperviousness map (figure 6.9) clearly shows the contrast between the city centre and the large parks. Also remarkable are the highly impervious building blocks along the main railway tracks from east to west in the middle of the study area. The tracks themselves are left out. Along the railway many discounters and car resalers are located. The large industrial areas such as the Siemens industrial area in Obersendling (mid-south of the study area) and the BMW factory (red building block in the north of the study area) can also be seen.

The building volume map of Munich (figure 6.10) further emphasises on the city centre with its high and large buildings surrounded by low volume residential areas (mainly detached and semi-detached houses). Outside the city centre, along the railway tracks and the industrial areas of for example BMW and Siemens higher building volumes can be found. The parks, which could be easily recognised in the imperviousness map, have low building volumes just like the surrounding residential areas.

Figure 6.11 shows three of the spatial indicators in more detail. The selected area includes the Ostbahnhof (A) and the Eastern Cementary (Ostfriedhof, B). No indicators are calculated for the transport network. North of the railway tracks dense block development is the dominant urban structural type (C). This area is characterised by high imperviousness and low vegetation density. The most frequently used roofing materials are tiles and metal. Directly east of the railway track there is a former industrial area with a mixture of urban structural types including large storage halls and large multi-storey buildings (D). This area is characterised by high imperviousness and low vegetation density as well. However, the dominant roofing materials here are bitumen and concrete. The south eastern part of the subset in figure 6.11 is dominated by detached and semi-detached houses (E). This reflects in a lower imperviousness, higher vegetation density and a large variety of roof materials, which is however still dominated by roofing tiles.

A comparison with BLOCK-reference data and with indicators provided by the municipality of Munich is carried out to assess the accuracy. The indicators for the study area and for the test area are compared. The material map of the test area was created under optimal conditions, using accurate a priori information on building locations. Height information was only used to improve the quality of the seedlings of the material map of the study area (see section 5.1.3 and 6.1.2 for more details). As a cross-validation, the indicators provided by the municipality were compared to the reference data as well. The results of the accuracy assessment are presented in figure 6.12 and figure 6.13.

The mean absolute error is 5.4 % for building density, 3.7 % for vegetation density, 3.2 % for imperviousness, 0.53 $m^3m^2$ for building volume and 0.4 $m^3m^2$ for vegetation volume. The
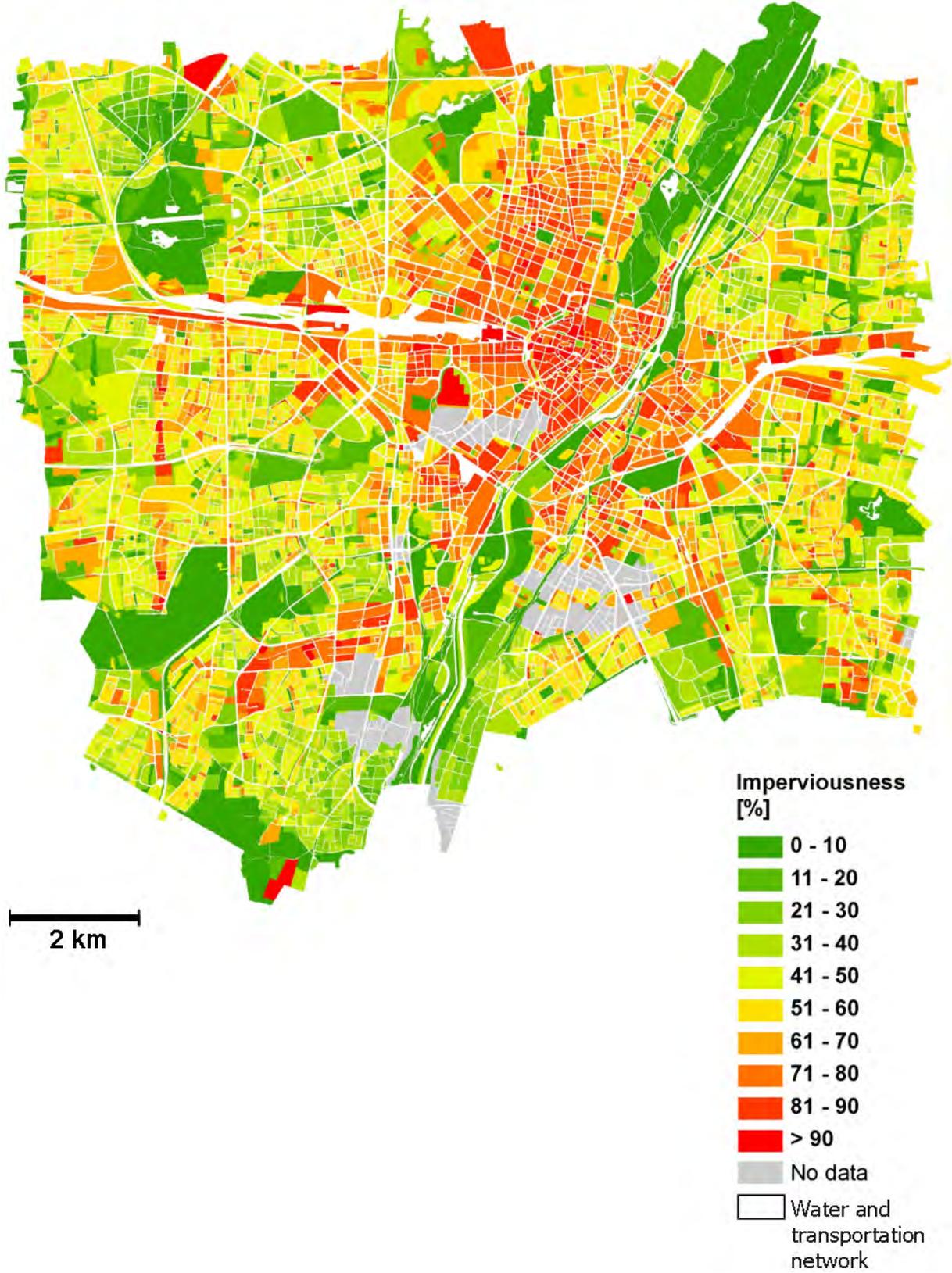
Figure 6.9: *Percentage of impervious surface per building block in the study area*
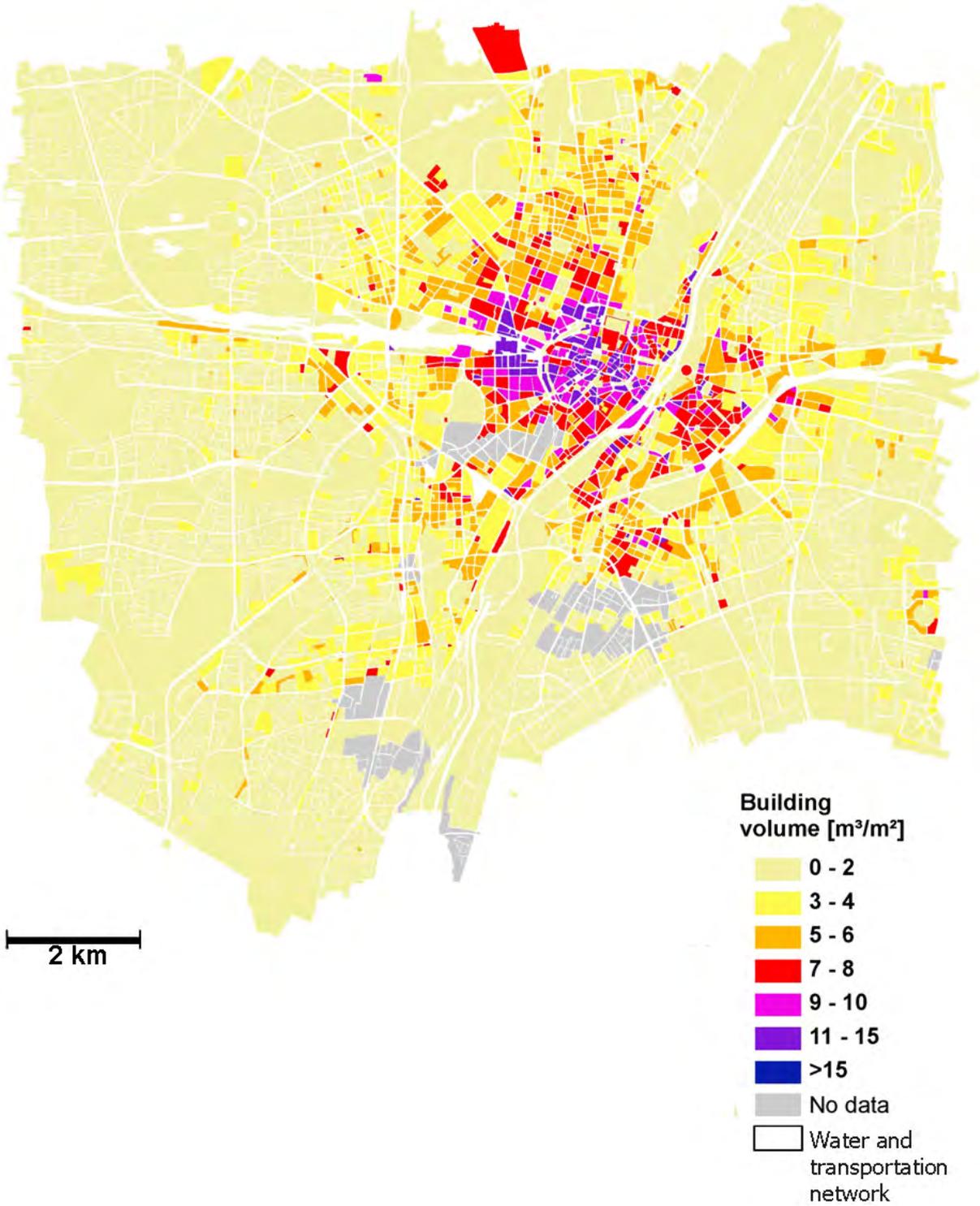
Figure 6.10: *Building volume per building block in the study area*
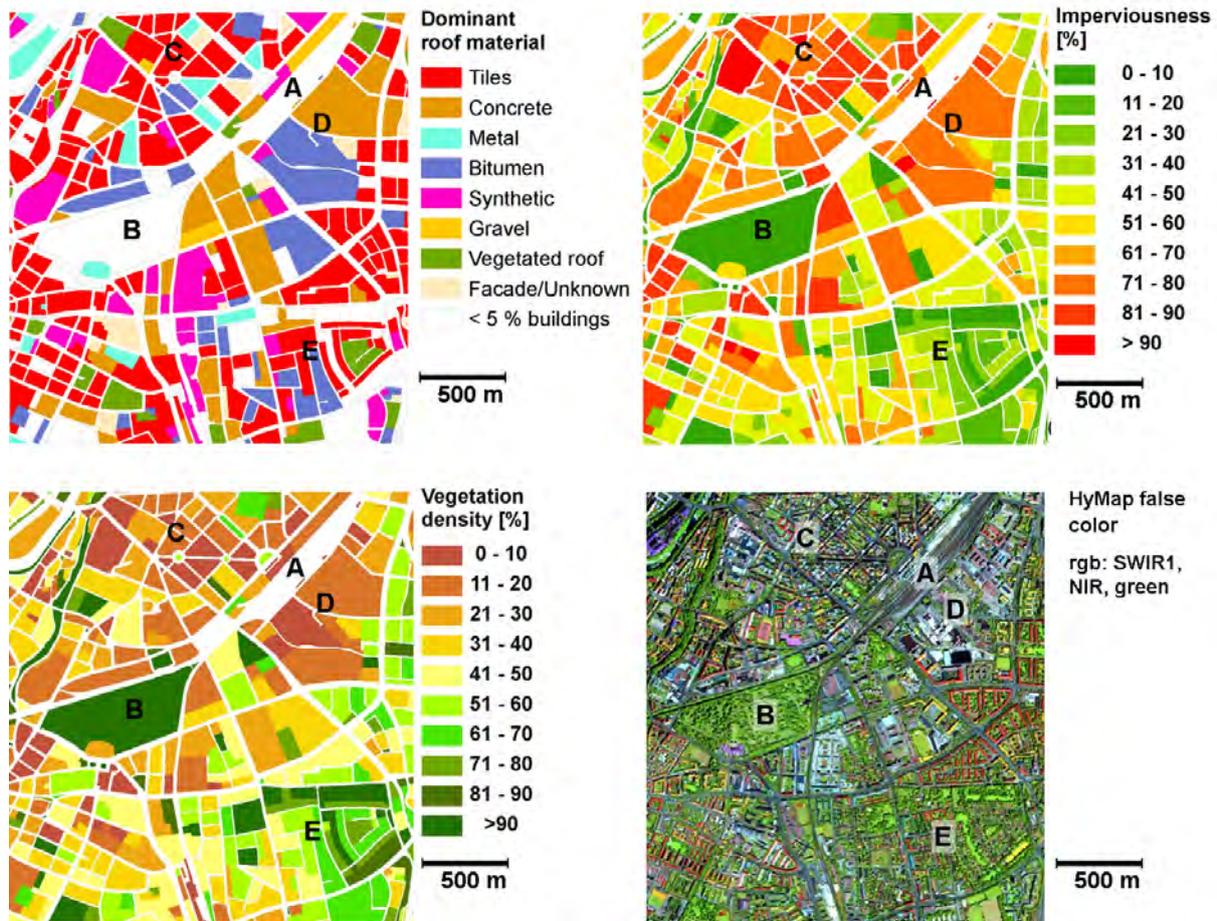
Figure 6.11: *Detail of the indicators dominant roof material, imperviousness and vegetation density. False colour HyMap image for orientation. The reader is referred to the text for more information on the locations indicated by the letters.*

producer accuracy of the dominant roofing material is 71 %. This shows that the indicators based on the hyperspectral products and height data are able to represent the selected indicators accurately. On average an error margin of less than +/- 5 % has to be taken into account for the indicators building density, vegetation density and imperviousness.

Figure 6.12 shows the differences between the calculated indicators in the test area and the reference building blocks, allowing more insight in the nature of the differences. The figure shows that for most building blocks the building density is slightly overestimated (bias = 4.2 %) and vegetation density is underestimated (bias = -3.2 %). The imperviousness of the HyMap-based indicators is both overestimated and underestimated in an equal number of blocks, resulting in a bias of only -0.4 %. The HyMap-based imperviousness is underestimated for six out of seven building blocks with imperviousness higher than 50 % in the reference data. The opposite effect can be noticed for the seven building blocks with imperviousness lower than 50 %. For those building blocks the HyMap-based values show an overestimation of imperviousness. Building and vegetation volume both show only minor differences to the reference values.

The overestimation of building density can be attributed to the use of the building mask. Because of inaccuracies of the building mask as a result of the vector-raster conversion, the area identified as buildings during the spectral unmixing is larger than the area in the reference data. This explains the underestimation of vegetation density as well, because vegetation pixels that are erroneously located inside the building mask are identified as vegetated roof. In addition to these small areas larger areas are assigned to buildings that look like vegetation in the remote sensing images. They are actually underground parking garages. These are included in the building mask and are therefore responsible for more vegetated roofs resulting in higher building density and imperviousness. Although this results in an overestimation of the building density and an underestimation for the vegetation density, it is not wrong to include these underground parking garages in the imperviousness. Imperviousness is used to express the area of the surface which does not allows the percolation of water. This number is important to calculating the right dimensions of for example sewers and rainwater drainage systems. Since underground constructions prevent rainwater from seeping through into the ground water as well, it is justified to include the areas of underground parking garages in the calculation of imperviousness.

The differences between the HyMap-based indicators and the reference are higher for the whole study area (mean absolute error is 10 % for building density, 10 % for vegetation density and 7 % for imperviousness), but they do follow the same pattern. The number of pixels identified falsely as vegetated roofs is larger because no building mask was used (see also section 6.1.4). This results in an overestimation of the building density and an underestimation of vegetation density. It also causes a lower producer accuracy for the dominant roofing material per building block of 50 %, whereas this is 71 % for the test area.

A comparison of municipal indicators with the reference data in figure 6.12 shows that the differences between the municipality data and reference data are larger than those between the HyMap-based indicators and the reference data. The mean absolute error of the HyMap-based indicators in the test area is in general about 3 % less than the MAE of the municipality indicators. Also the pattern of the differences varies from that of the HyMap-based indicators. Where the HyMap indicators show an overestimation for building density in 12 of 14 building blocks, the municipality data shows much more variation: in 5 building blocks the building density is overestimated, in 9 it is underestimated compared to the BLOCK-reference data set.

Figure 6.13 allows a closer look on the accuracy of the spatial indicators at several levels. Scatter plots provide a comparison of the HyMap-based indicators with the BLOCK-reference (14 building blocks) and the municipality of Munich for three indicators (the same 14 reference blocks and all 909 building blocks). The indicators of the municipality are only available in steps of 5 %. The black lines show the overall trend of correlation for each of the indicators. The blue line indicates the one-to-one trendline, which would occur when both indicator data sets have equal values for each building block. The scatter plots on the left show that the agreement of the HyMap-based indicators with the reference is good for all indicator levels. The same 14 building blocks as contained in the reference are shown in the middle scatter plots in figure 6.13, comparing the HyMap-based indicators with those of the municipality of Munich. The agreement with the trendline is weaker and shows a general overestimation of low indicator values and an underestimation of high values. The scatter plots on the left show a similar situation for all 909 building blocks in the test area. Because the agreement of the HyMap-
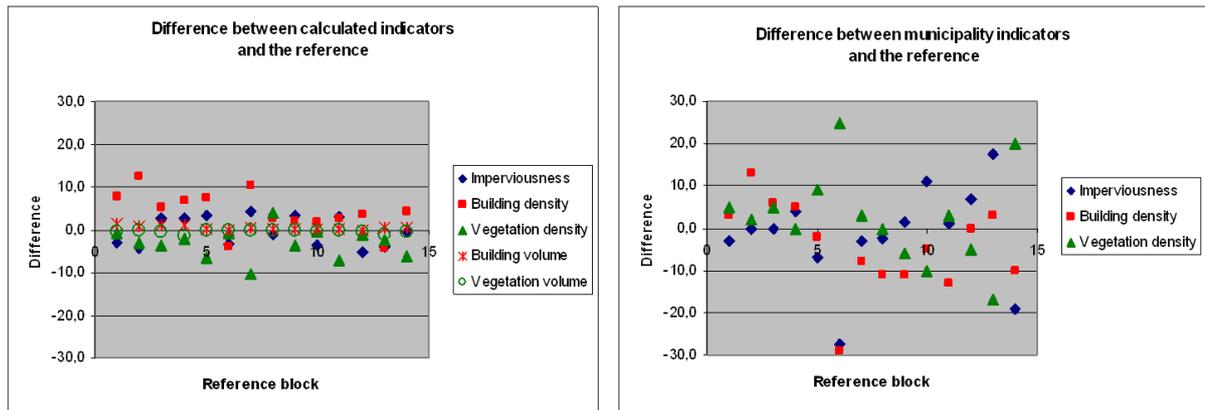
Figure 6.12: *Comparison of HyMap-based indicators with the reference (left) and the indicators of the municipality of Munich with the reference for the same 14 reference building blocks (right)*

based indicators with the reference is better than that of the indicators of the municipality, the over- and underestimation probably have to be attributed to the municipality data and not to the HyMap-based data. The large number of building blocks that have a vegetation density of 100 % in the municipality data in the right scatter plot, but varying values in the HyMap-based data are likely to be urban green. These urban structural types are usually very small and surrounded by roads or buildings. Thus, a co-registration error in the building block map with the HyMap data easily results in large vegetation density errors. This can also be an explanation for the relatively large number of building blocks that have a building density and imperviousness of 0 % in the municipality data, but varying values in the HyMap data.

## 6.3.2 Characterisation of urban structural types

The different urban structural types have regular values for the selected spatial indicators, as is suggested by figure 6.11. This is illustrated in more detail by figure 6.14 and table 6.6. Figure 6.14 shows the dominant roof material for the different urban structural types. The figure is based on over 900 building blocks in the test area. The total of the bar for each urban structural type is equal to the mean building density. This graphic does not only show differences in mean building density for urban structural types, but also in the roofing materials which are dominantly used. The dominant material for residential urban structural types (a1 to a7), which have usually smaller buildings is roofing tiles. The roofing materials vary more for urban structural types with larger buildings such as the multi-storey types (a7, b1). Typical flat roof materials such as bitumen and synthetic materials are used for the storage halls (b2, b3).

In table 6.6 the mean and standard deviation for each spatial indicators per urban structural type is listed. These values allow a clear differentiation between the urban structural types, especially when they are combined. An example is the separation between row houses and regular block development. These two urban structural types have similar values for building density, vegetation density, imperviousness and dominant roofing materials. However, building volume is the differentiating factor with clearly higher values for regular block developments (which commonly have 4-6 floors) than for row houses (with usually only 2-3 floors). A supervised
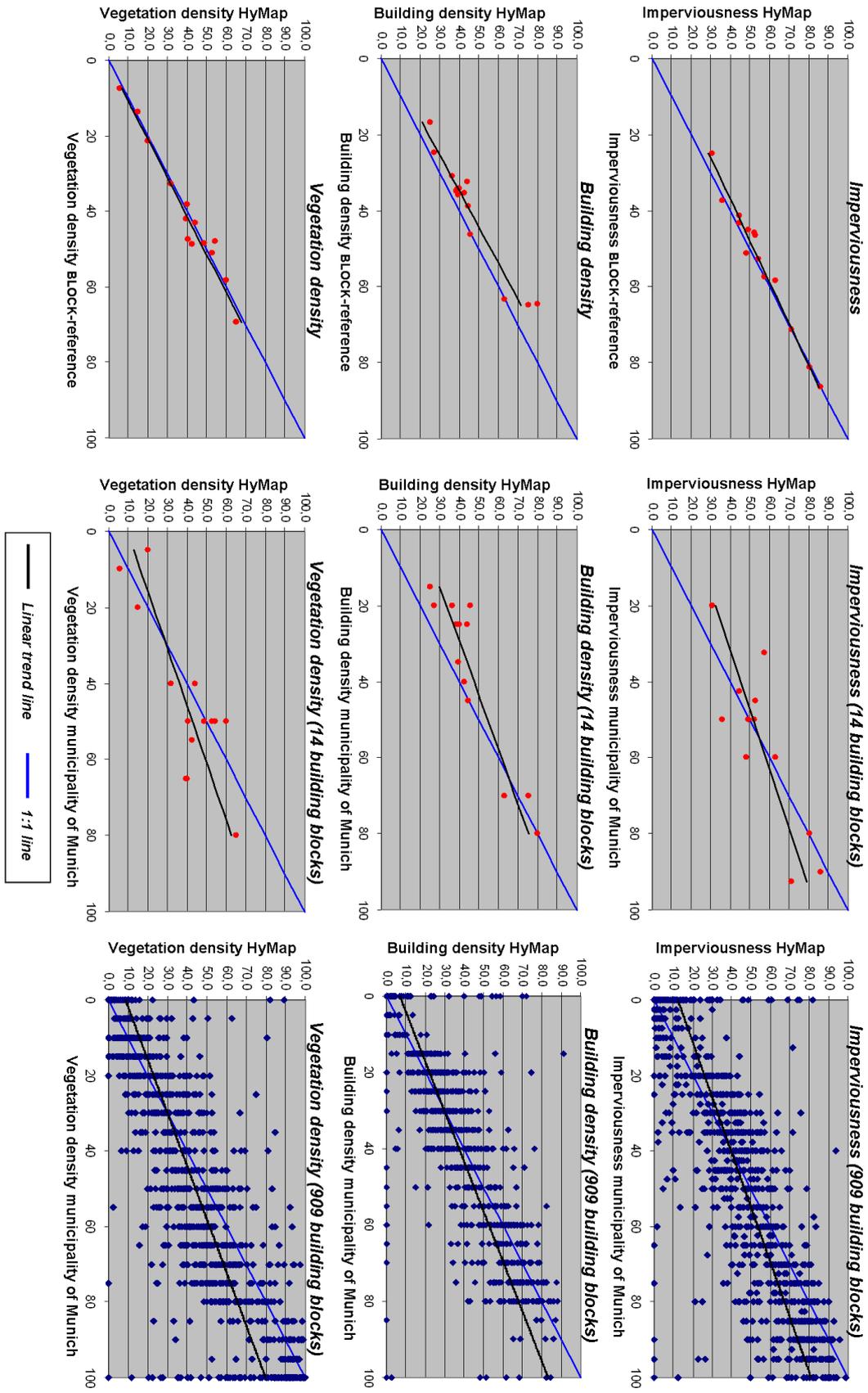
Figure 6.13: *Direct comparison of HyMap-based indicators with the BLOCK-reference and the indicators of the municipality of Munich*
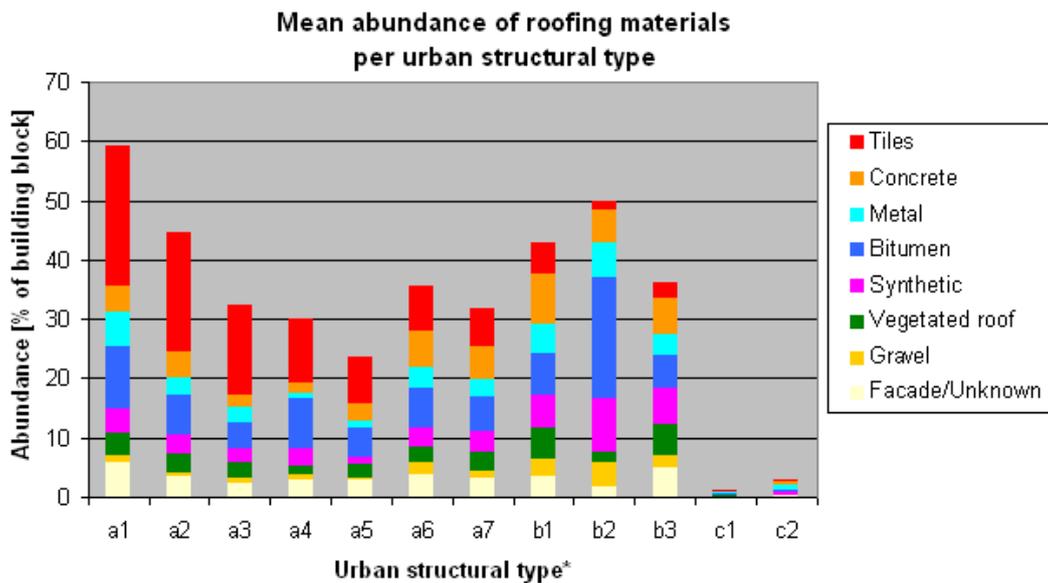
Figure 6.14: *Mean abundance of roofing materials for the different urban structural types. * a1=dense block development, a2=perimeter block development, a3=regular block development, a4=row house development, a5=detached and semi-detached housing, a6=high rise buildings, a7=small multi-storey buildings, b1=large multi-storey buildings, b2=large halls and storage buildings, b3=small halls and storage buildings, c1=parks and urban green, c2=sports fields*

classification based on the minimum difference was able to identify 60 % of urban structural types of the building blocks in the test area correctly, by using the mean of the six presented indicators. This confirms that the spatial indicators can be used to identify the urban structural types. Tests with supervised classifications making use of the standard deviation indicate that the classification accuracy can be improved. However, the development of a classification approach for urban structural types was not pursued any further in this thesis. The reader is referred to ongoing research of Bochow et al. (2007a) and Wurm et al. (2009), which focuses on the classification of urban structural types by using hyperspectral and very high resolution data, respectively.

Although the mean values of the selected spatial indicators allow a good separation between the different urban structural types, the standard deviations are quite large for some indicators and urban structural types. This is on the one hand an additional description of the urban structural type. It is valuable information that the building density for building blocks assigned to the urban structural type of large storage halls can vary widely. On the other hand, this illustrates the variety of building blocks assigned to one urban structural type and the difficulty to objectively classify them based on a few spatial indicators.

Table 6.6: *Mean and standard deviation σ for the different urban structural types for building density (BD, in % ), vegetation density (VD, in % ), imperviousness (IMP, in % ), building volume (BV, in $m^3/m^2$), vegetation volume (VV, in $m^3/m^2$) and dominant roof material (MAT)*

| Urban structural type (number of samples) | Spatial indicator* | | | | | | | | | | |
|---|---|---|---|---|---|---|---|---|---|---|---|
| | BD | σ | VD | σ | IMP | σ | BV | σ | VV | σ | MAT |
| Dense block development (210) | 59 | 18 | 18 | 15 | 71 | 17 | 7.20 | 3.10 | 1.19 | 1.23 | tiles |
| Perimeter block development (60) | 45 | 14 | 37 | 16 | 56 | 15 | 5.28 | 2.27 | 1.88 | 1.25 | tiles |
| Regular block development (80) | 33 | 14 | 46 | 15 | 45 | 14 | 3.10 | 2.21 | 2.45 | 1.43 | tiles |
| Row house development (49) | 30 | 7 | 49 | 10 | 44 | 9 | 1.42 | 0.83 | 1.27 | 0.64 | tiles |
| Detached and semi-detached houses (80) | 24 | 8 | 54 | 13 | 37 | 11 | 0.93 | 0.54 | 1.86 | 1.75 | tiles |
| High rise buildings (35) | 36 | 17 | 43 | 20 | 47 | 19 | 5.09 | 4.22 | 2.35 | 1.50 | tiles |
| Small multi-storey buildings (80) | 32 | 16 | 44 | 20 | 47 | 20 | 2.52 | 2.09 | 2.43 | 2.81 | tiles |
| Large multi-storey buildings (41) | 43 | 14 | 29 | 16 | 61 | 17 | 5.75 | 2.66 | 1.65 | 1.41 | concrete |
| Large halls and storage buildings (5) | 51 | 25 | 9 | 6 | 79 | 16 | 4.03 | 1.93 | 0.47 | 0.42 | bitumen |
| Small halls and storage buildings (20) | 37 | 19 | 27 | 13 | 60 | 16 | 3.42 | 3.51 | 1.29 | 0.94 | concrete |
| Parks and urban green (136) | 2 | 5 | 79 | 20 | 13 | 15 | 0.16 | 0.61 | 6.63 | 4.69 | tiles |
| Sports fields (21) | 4 | 5 | 67 | 23 | 22 | 18 | 0.25 | 0.55 | 2.66 | 1.50 | synthetic |

# 6.4 Micro climate simulations

A more detailed way to characterise urban micro climate in comparison to spatial indicators are micro climate simulations. The urban micro climate model ENVI-met is used for the simulations in this study. The input data for this model is automatically generated from hyperspectral data products and height data as described in section 5.4.

## 6.4.1 Model input

In figure 6.15 the different layers of input data are shown combined with a 3D view of the simulation area in the ENVI-met software and a 3K aerial photo for orientation. 45 new building IDs have been generated for this subset, because the difference with the albedo values of existing building IDs (roof materials) was too large. This mainly concerned roofing tiles and metal roofs such as aluminium and zinc. These two material categories are often applied to inclined roofs, which strongly influences the albedo recorded by HyMap. In addition, metal roofs are strongly influenced by material specific BRDF effects. The building input data does represent the building and roof material pattern well, since it is supported by smoothing of roof materials. An exception is the omission of a part of the buildings in the building block in the middle west of the subset. This building was missing in the height data and therefore not included in the automatic process. Another, more important spatial characteristic that cannot be realistically included in the ENVI-met model are inclined roofs. If an inclined roof would be modelled within a grid based environment the roof would look like a staircase. The same is true for diagonal building walls, as can be seen in the 3D image. This is a common way to represent buildings in remote sensing applications. However, for the modelling of micro climate this will influence the simulation results (see below).

The second input layer contains the vegetation IDs. 47 new IDs were added for the example in figure 6.15, based on plant height, albedo and leaf area density. The third input layer provides information about different soil/surface types. All pixels on which buildings or vegetation are located have been assigned a default soil type. Streets and other non-built surfaces were assigned surface materials according to the material map. A difficulty of using remote sensing data can be seen here. The most eastern street in the subset going from north to south is lined by several trees. These trees prevent the view on the street from an airborne perspective. As a result, these trees are identified, but the street below the tree crowns is not. This results in the ENVI-met input data lacking a street with sealed surface.

The fourth input layer describes the building heights and locations of walls as shown in the most left subset in figure 6.15. The wall locations and heights are directly derived from the height data.

The input data for the simulation area shown and described above is one of the sixteen areas which have been selected to be simulated by ENVI-met. The locations of these simulation areas are shown in 4.2. An aerial photograph and the 3D ENVI-met simulation area in appendix A give an overview of the variation of urban structural types in the selected areas. The automated generation of the input data for the ENVI-met model allowed fast preparation of each of these areas. However, urban structural types with small buildings such as detached and semi-detached housing caused some difficulties. Within the material map, the buildings in these areas are often difficult to recognise because of the many tree crowns that (partly) cover the buildings.
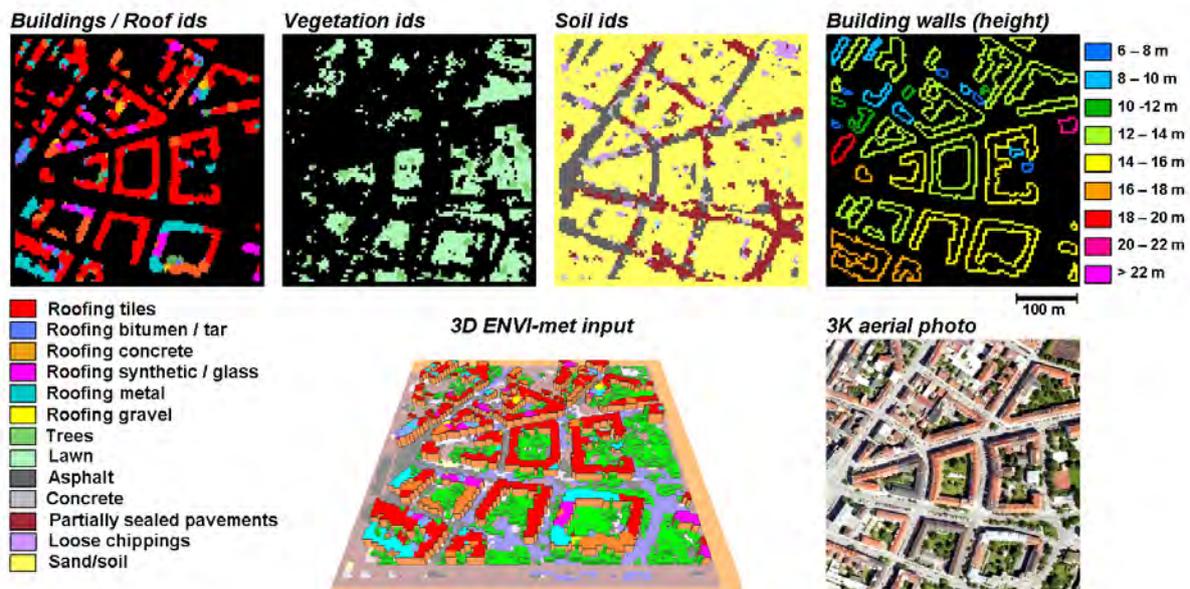
Figure 6.15: *Generated input for ENVI-met based on the hyperspectral products and height data.*

In addition, the height data is less accurate in these areas (see also section 4.3.2). As a result, several small buildings are not included in the model input, especially in detached and semi-detached housing areas (e.g. subset 8 in appendix 4.2).

## 6.4.2 ENVI-met simulations

Having prepared the input data for the ENVI-met model, the simulation can commence. The model configuration listed in table 5.8 is applied to all simulations that are presented in the following text unless stated otherwise.

Like many climate models, ENVI-met is a very computational intensive model. A simulation run of 24 hours for an area of 400 m x 400 m (or 114x114x36 grid cells) takes between 130 and 140 hours or five to six days on a fast computer (SUN 64GB RAM, two 3 Ghz quadcore processors). The model does not use the multiple processing cores. However, one instance of the model can be run on each processing core. This allows the simultaneous processing of multiple simulation areas. Still, the computation time was a limiting factor in this study, constraining the number and size of the simulation areas and scenarios that could be simulated.

The results produced by a single simulation run are numerous. Results are generated for each grid cell in x-, y- and z-direction and at each time step for each climate parameter. Figure 6.16 shows maps of the parameters air temperature, wind (speed and direction) and predicted mean vote (PMV) at a height of 1.5 m at the hottest time of the day (14:00) as an example.

The air temperature pattern in figure 6.16 is mainly dominated by the wind. The wind was set to come from the south-west and is strongly influenced by the buildings. The streets are corrIDors (canyons) for the wind, resulting in stronger wind through the streets. Inside the building blocks, the wind speed is much lower. Following this pattern the air temperature is
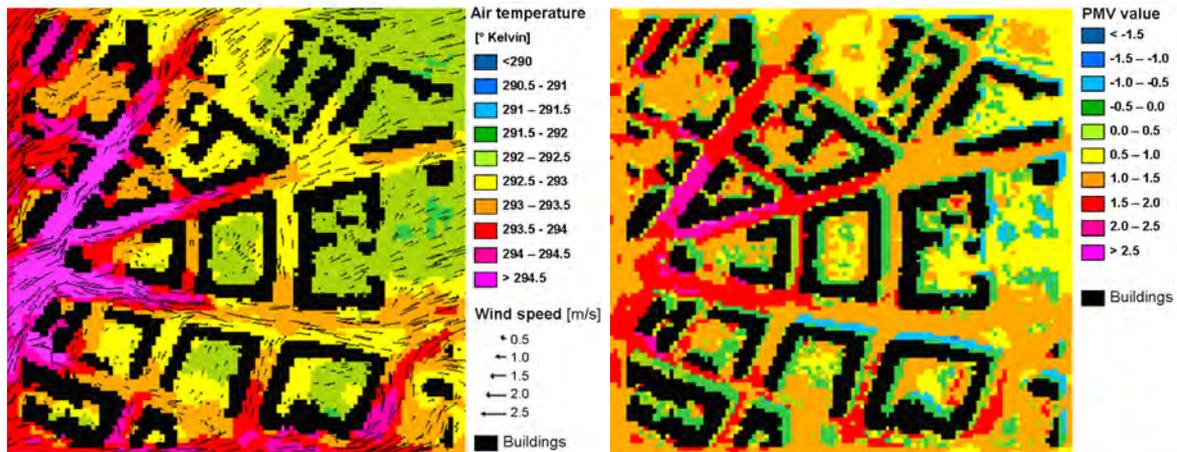
Figure 6.16: *Exemplary ENVI-met simulation results: simulated air temperature and wind speed at 14:00 and 1.5 m height (left) and predicted mean vote (PMV) at the same time and height (right).*

lower inside building blocks and at the leeward sides of the buildings. However, it should be noted that the maximum difference in air temperature is not more than five degrees.

The predicted mean vote (PMV) is a human comfort index based on climate parameters and the human physiology (Fanger, 1970; Bouyer et al., 2007). The information provided by human comfort indices is very interesting to urban planners, because it shows in which areas inhabitants are likely to feel uncomfortable and planning activities could be considered with just one number. A PMV-value of zero means that the test person would feel comfortable. If the value is negative, a person would feel cold and positive values indicate that a person would feel warm. The minimum and maximum values (3 and -3) indicate very uncomfortable circumstances. The PMV by definition strongly depends on air temperature. This explains why the places that will be considered cold are in the (wind) shadows of the buildings in figure 6.16. Also near and below vegetation the PMV shows negative values. Figure 6.16 shows that areas which will be perceived as (too) warm are mainly located on the west side of the buildings where both warm air an direct sunlight heat up the environment.

The advantage of hyperspectral remote sensing is that it is able to rapidly, objectively and mainly automatically perform detailed surface material mapping in urban areas, as shown in section 6.1. Thereby more detail on the actual situation of a building block can be provided with less effort than when the information has to be obtained through field surveys, aerial photograph interpretation and manual editing of the simulation area in ENVI-Eddy. In order to conclude weather or not this level of detail is also an advantage to the micro climate simulations an analysis is made so as to evaluate the influence of different surface materials on the micro climate. The influence of roofing materials and of other surface materials are then analysed separately in two series of scenario studies. Unfortunately, it was not possible to carry out a scenario with changed building configuration due to technical problems.

The simulation area presented in figures 6.15 and 6.16 is manually adapted to four different scenarios to be able to analyse the influence of roofing materials on the micro climate. The first scenario in figure 6.17 is the original situation. In the second scenario, the roofing material of

the centre building block is changed from mainly clay roofing tiles into aluminium. In the third and fourth scenario the roofing material of the middle building block is changed into bitumen and polyethylene respectively. The simulation results showed that these changes were of almost no influence to the wind and humidity and only of minor, local influence to the air temperature. Changes in air temperature reached not further than the changed building block in horizontal direction and only a few meters in vertical directions. However, the change of roofing materials did influence the surface temperature of the buildings. This is shown in figure 6.17 for 14:00. This figure shows that the surface temperature of an aluminium roof at this time of the day is comparable to the roofing tiles and the surface temperature of the polyethylene roof is slightly higher. The bitumen roof reaches surface temperatures which are almost ten degrees higher than that of the aluminium roof at midday. In order to describe the influence of different roofing materials in more detail, the simulated roof surface temperatures of three other areas (subset 1, 4 and 13; see appendix A) are analysed over the complete simulation time of 24 hours. For each building pixel the roof surface temperature is extracted for every simulated hour. The average surface temperature is calculated per roofing material and plotted against time. The result is shown in figure 6.18. The total temperature span the different roof materials cover is almost 15 degrees. The standard deviation is largest at the hottest time of the day. For bitumen, polyethylene, PVC, zinc and copper the maximum standard deviation lies between 3.5 and 6 degrees. For aluminium, concrete and clay tiles it lies between 16.5 and 20.5 degrees. According to the simulation results, copper and zinc have the highest surface temperature at midday. Synthetic materials (polyethylene and PVC) and bitumen reach medium surface temperatures. Clay tiles clearly have the lowest surface temperature at midday. In addition there are slight shifts in the time of the maximum temperature between the different roofing materials. Bitumen, PVC and polyethylene reach their maximum surface temperature earlier than concrete and clay tiles, whereas the metal roofing materials reach their maximum surface temperature later in the afternoon.

Besides the roof surface temperature the 3D images in figure 6.17 also show the surface temperature of walls. In the stairs-like shape of the walls the grid (pixel) based input data can be recognised. So a wall from south-west to north-east consists of a sequence of south and east facing walls. As can be seen in figure 6.17 the orientation of the wall influences the surface temperature of the walls, resulting in hot south-facing walls and cooler east-facing walls. While a diagonal wall in general would have one surface temperature in the real world, in the model it has varying temperatures. If inclined roofs would be simulated in this pixel-based way this effect would be even stronger, because the roof surface would consist of fully exposed horizontal surfaces and barely exposed vertical surfaces. In addition to its influence on temperature, such a stair-like representation of diagonal building walls and inclined roofs influences the wind flow in a different way than a smooth wall or roof, especially if the pixel size is large.

The second analysis focuses on the influence of varying non-built surface cover. In addition the influence of surface cover in neighbouring building blocks on a building block of interest is studied. Again four scenarios are manually created based on the subset of figure 6.15 and 6.16. The scenarios are shown on the left in figure 6.19. The first scenario is again the original situation. The middle building block serves as the reference for which the effect of changes in the neighbourhood are assessed. In the second scenario, all vegetation is removed in two building blocks south of the middle building block and is replaced by an impervious asphalt
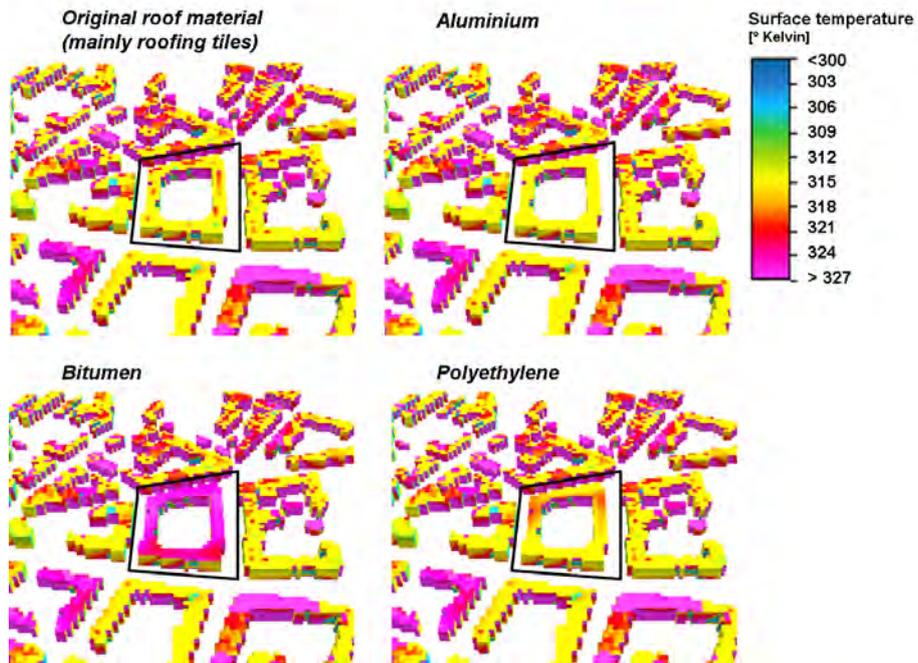
Figure 6.17: *Simulated surface temperatures of buildings with different roof materials*
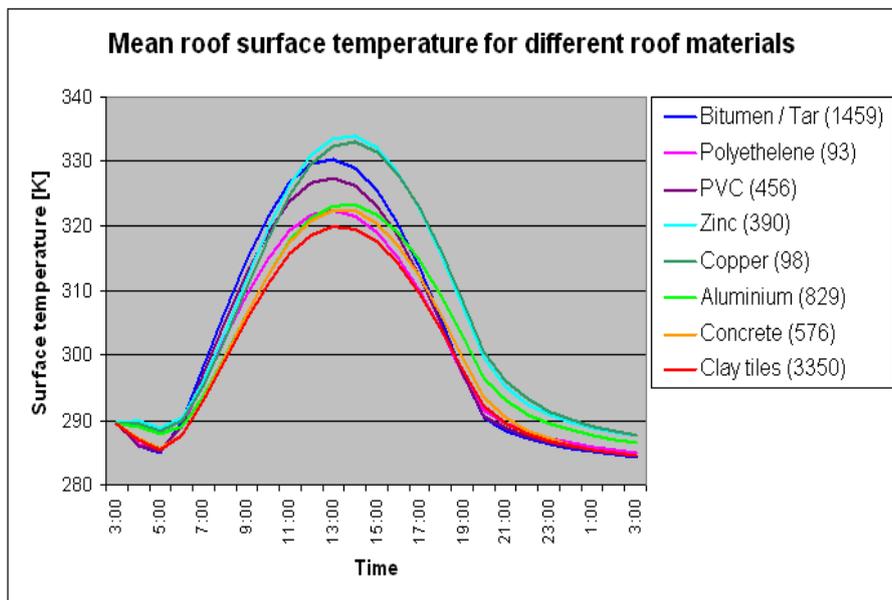


Figure 6.18: *Mean simulated roof temperatures for different roof materials throughout the day. The number of roof pixels that contributed to the mean are given in brackets.*

111
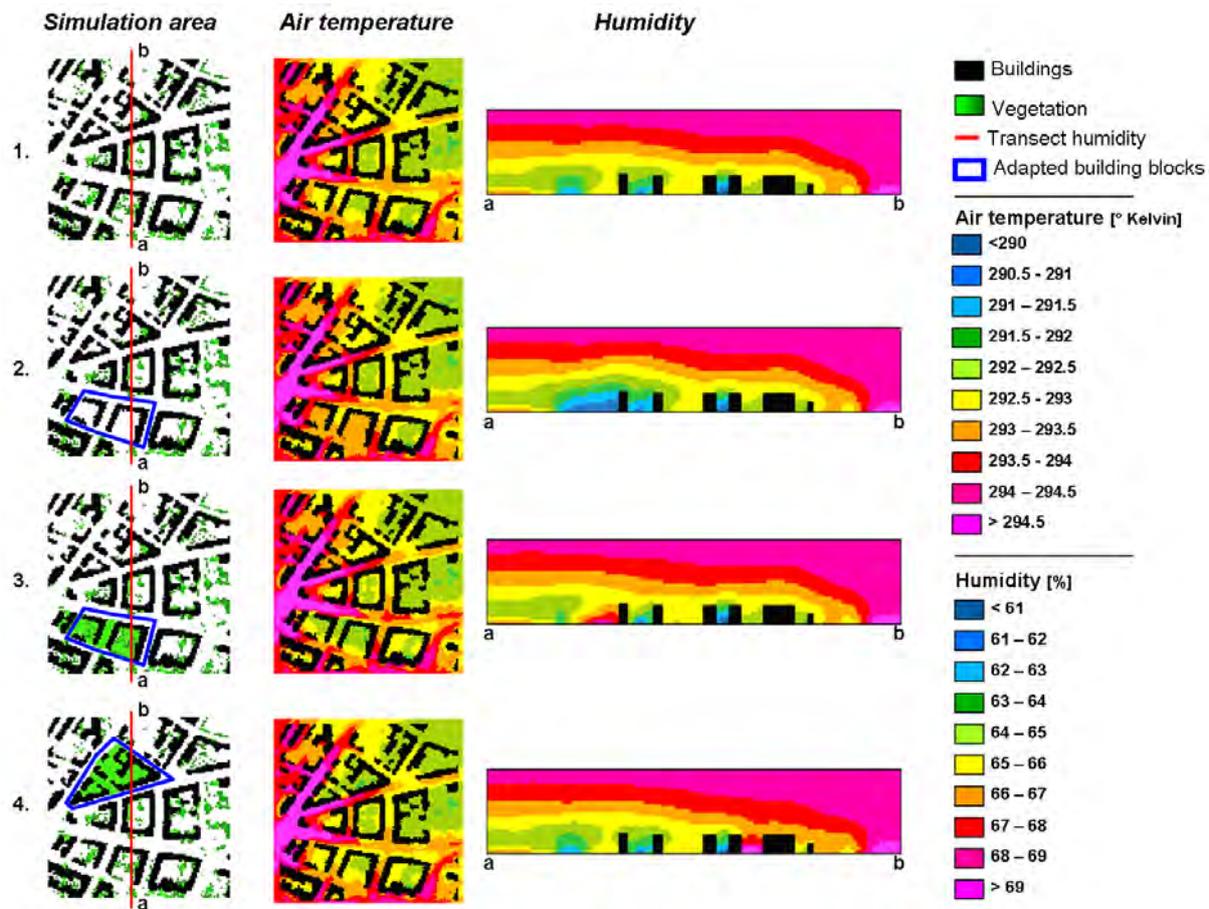
Figure 6.19: *Air temperature (at 1.5 m height) and humIDity at 14:00 for the original simulation area (1), a scenario where two building blocks are paved with asphalt (2) and two scenarios where the non-built areas within the building blocks are replaced with trees (3,4).*

surface. In the third scenario the opposite environment of the second scenario is created. The non-built space in these two building blocks is completely planted with trees. In the fourth scenario, the trees are planted within two building blocks north of the test area, in order to assess if changes on different locations have a different effect on the micro climate in the middle building block. The results of the simulations for the parameters air temperature and humidity at 14:00 are shown in figure 6.19. The air temperature is shown at a height of 1.5 m. The humidity is shown in a transect from *a* to *b*; showing the humidity at different heights. The results show that the changes almost solely influence the temperature and humidity in the building block they were made in. The air temperature decreases with 0.5 - 1 degree in the altered building blocks in the third and fourth scenario where more trees were included. In the second scenario, where the impervious surface was increased, the temperature increases with 0.5 - 1 degree compared to the original scenario. The humidity in the scenarios where trees were added increased within these building blocks with a maximum of 4 %. In the building block where the non-built surfaces were replaced by asphalt the humidity decreases with up to 4 %. The changes of humidity reach to the same height as the buildings (which are about 14 m high in this area).
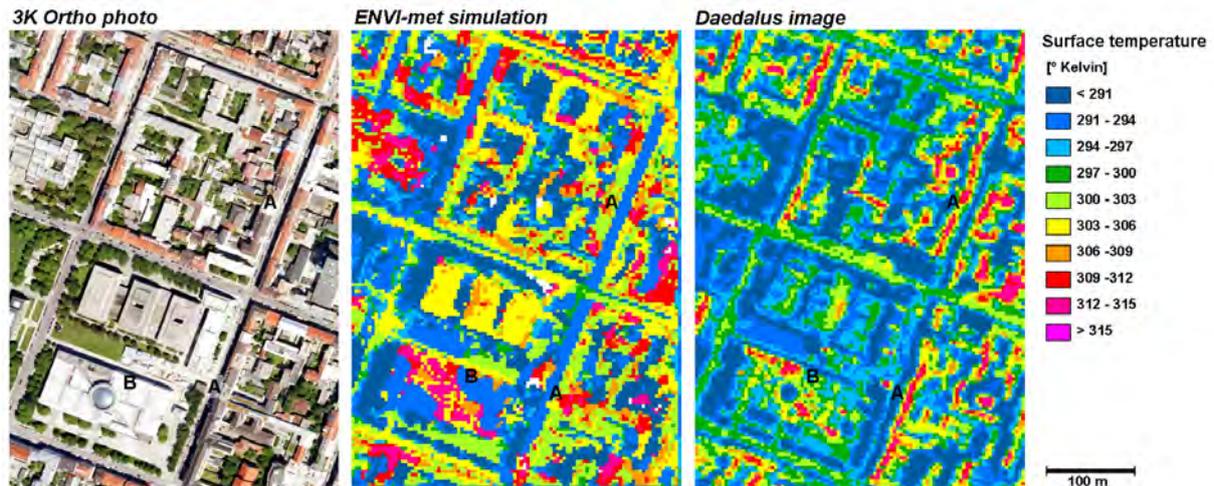
Figure 6.20: *Comparison of surface temperature simulated with ENVI-met (centre) and recorded by the thermal Daedalus scanner (right). 3K orthophoto (left) for orientation. For more information on the location indicated with A and B the reader is referred to the text.*

In order to judge the value of these results for urban planning information about the accuracy of the simulation results is required. As has already been stated in section 5.4.4 only a simple comparison in surface temperature can be drawn out in the context of this thesis because of the lack of extensive meteorological data.

The simulated surface temperatures have been compared with the surface temperature recorded by the Daedalus thermal band (see section 4.2 for a description of this data set). The two images are shown in figure 6.20 with an additional 3K ortho photo of the area for orientation. The Daedalus image was recorded simultaneously with the HyMap images at about 9:30 in the morning of June 17th 2007. The simulation results of this date and time are used for the comparison. The two images show large differences, but the pattern of buildings, which mainly have higher surface temperatures than the other surfaces, is recognisable in both images. The main differences are caused by the fact that all buildings have flat roofs in the ENVI-met simulations. In the Daedalus image buildings have inclined roofs resulting in illuminated and shaded roof sides, for the illumination comes from the east at this time of day. Additionally, bright building facades are included in the Daedalus image because of the viewing angle of the sensor. These effects can for example be recognised at the locations marked with A in figure 6.20. At the same location in the simulated surface temperature map, the buildings appear to be much larger and warmer because the complete roof surface is illuminated and heated. On the other hand are the relative differences between roofs with different roof materials quite accurately simulated. A good example is the building of the Pinakothek der Moderne museum, marked with B in figure 6.20. Its roof construction consists of two different materials of which the pattern is realistically simulated, although the absolute difference between the two roof materials in the simulated images is larger than in the Daedalus image.

In conclusion, the simulations of the selected areas and scenarios showed that with the remote sensing products as the main source for the model input data simulation of all important

climate parameters is possible. A comparison of one of these parameters, the surface temperature, showed that the general trend is correct, although there are differences in the absolute values. The scenario studies showed that different surface cover types (vegetation, impervious surface, etc.) influence the micro climate within the building block. Different roof materials mainly influence the surface temperatures of the building they are applied to and do not have noticeable effects on the rest of the building block. Synthetic, mineral and metal roofing materials show different maximum surface temperatures at different times of the day. This is useful information for architects, e.g. to estimate the need for airconditioning or isolation.

# 7 Discussion

This chapter discusses the selected methods and achieved results according to the three main aspects of the conceptual framework: first the potential of the hyperspectral data to map urban characteristics with high spatial and thematic detail is addressed (section 7.1), then the use of these derived remote sensing products for the calculation of spatial indicators and micro climate simulations to characterise urban micro climate is discussed (section 7.2). Third, the potential of the use of urban structural types as a framework for micro climate characterisation to suit the needs of urban planners is demonstrated in section 7.3. Then, the experiences with the various aspects are combined and the applicability of the conceptual framework as a whole is evaluated in section 7.4.

## 7.1 Mapping urban characteristics with airborne hyperspectral data

To support the characterisation of urban micro climate information about the urban characteristics influencing the micro climate is required (see sections 2 and 3.2.1). In this thesis hyperspectral remote sensing, supported by height data, was used to derive this information. The main focus was on the surface material map, but additional products (albedo and LAI) were also derived. This section discusses these products and the methodology to derive them from a remote sensing perspective. In the next section (section 7.2) the ability of these products to support the characterisation of urban micro climate will be discussed.

### 7.1.1 Material mapping

A sub-pixel approach is selected for the material mapping in order to handle the heterogeneity of the urban area and its relatively small objects. The multiple endmember spectral mixture analysis approach developed especially for urban areas by GFZ Potsdam (Roessner et al., 2001; Segl et al., 2003) was applied first to a test area and then to the whole study area of the city of Munich (see section 5.1).

The results in section 6.1 showed that the selected linear spectral unmixing approach was able to map abundances of surface materials accurately. In the test area 40 % of the pixels are identified as seedlings with an overall accuracy of 86 %. The iterative unmixing is carried out by taking these pure pixels as a starting point. The mathematical accuracy of the unmixing model is very high: 99 % of the pixels could be unmixed with an average RMSE of less than 1.6 %. The urban objects (buildings, vegetation, roads etc.) could be identified accurately and allowed a realistic mapping of the urban structure. The accuracy assessment of the material abundances showed that the mean absolute error is on average 16 % abundance for 3 x 3 pixels

and 2.1 % abundance per building block. This is a very good result, meaning that on average only an error margin of +/- 2.1 % fractional cover has to be taken into account for the estimated abundance of surface materials per building block. However, there are differences in accuracy of the surface materials. Roofing tiles and metal roofing materials could be recognised very accurately. On the other hand, dark materials (asphalt, bitumen) were frequently confused with shaded surfaces, which has already been addressed by Segl et al. (2003). Nevertheless, the applied approach allows a separation between shaded vegetation and other shaded surfaces. This is most important to micro climate characterisation. Therefore, this thesis did not focus on the reduction of shadow any further. Yet increasing the identification of shaded impervious surfaces (built and non-built) by removing the shadow within the urban area prior to unmixing is likely to be advantageous, e.g. with the deshadowing module in ATCOR (Richter and Müller, 2005).

In areas with many trees (such as detached and semi-detached housing areas) tree crowns are obscuring the view on small houses or streets. This is not so much the result of the unmixing approach as well as a general characteristic of remote sensing during summer (cf. Heiden (2004) and Van der Linden and Hostert (2009)). Further it could be observed from the presented results in section 6.1 that badly defined endmembers or classes strongly influence the final results. This turned out to be the case for the class railway tracks, for example. The use of a priori information on the location of buildings (i.e. a building mask) improved the identification of all roofing materials, but especially those materials that are used both as roofing materials and on non-built surfaces (e.g. tiles and red loose chippings). In this study the use and quality of the building mask turned out to be one of the most important factors for the accuracy of the unmixing results. Therefore, the influence of the building mask is discussed in more detail in the following paragraphs.

A priori information on the location of buildings has been proven to increase the number of selected endmembers and to improve the accuracy of seedlings by 8 to 13 % to an overall accuracy of 86 %. The use of a building mask constraints the possible endmember combinations during the spectral unmixing. This prevents bitumen roofing materials from being assigned to asphalt streets for example. In accordance to Segl et al. (2003) and Heiden (2004) it can thus be stated that adding spatial information to the spectral information improves the unmixing results. Two different sources for a priori information on buildings have been used in this study: a building mask derived from the municipal cadastre data (DFK-mask) and object height derived from the HRSC-height data which also includes trees. Both data sets considerably improve the results in contrast to when no building mask is used at all. However, the two building masks both have their own advantages and limitations based on their different sources.

The object height data has the advantage that besides the location of buildings, it also contains the height of buildings and trees. Yet, the DEM normalisation required for the retrieval of the object height from the overall elevation caused some inaccuracies as the result of the low spatial resolution of the available DTM. This effect occurs mainly in the east of the study area, which has a slightly higher elevation. This causes difficulties in areas with low buildings (see also section 4.3.2). A more advanced object extraction method, e.g. including a pre-classification of surfaces, could improve the object height data set. Because the digital elevation model was derived from stereo data, a few buildings are lacking or are only partially included. This is likely to be caused by surrounding higher buildings that are blocking the view on a measurement point

in some of the stereo images (which are all taken from different viewing angles), so that no height can be calculated for these points (Mayer, 2004). Of course also another, more accurate source of height data, such as laser scanning data, would increase the quality of the object data. However, such highly detailed height data is not yet widely available at moderate prices and is therefore less suitable for area wide applications in urban planning.

The DFK-mask is a highly accurate data set, because it is based on the cadastral map. Since all buildings are included, it is the preferred building mask for this study. However, the conversion from vector data to raster caused a slight increase in the area of buildings. For underground car parks were included as buildings in the DFK-building mask, the number of vegetated roofs is slightly overestimated in the unmixing results with this building mask.

Next to the source of the building mask, the advantage of using such an external data set is dominated by the quality of the co-registration with the hyperspectral data. Despite efforts to improve the co-registration of the data sets as described in section 4.3.3, regional differences between the hyperspectral data and the building information persist. Van der Linden and Hostert (2009) indicated that this has to be attributed to the viewing angle of the HyMap sensor. The off-nadir viewing angles result in a displacement of buildings at the borders of the flight lines. This causes co-registration errors, especially when overlayed with a building mask. In the GFZ-unmixing approach, pixels within the building mask are forced to be mapped as a roof material. Pixels outside the building mask are mapped as vegetation or impervious non-built surfaces. Co-registration errors lead to an overestimation of impervious surfaces because vegetation inside the building mask (e.g. next to a building) is mapped as vegetated roof and buildings outside the building mask are assigned to an impervious non-built surface material (e.g. concrete). To min-imise such confusion but still optimise the separation of spectrally similar materials on built and non-built objects (which is the objective of the building mask), the hybrid solution was applied. The success of the hybrid approach in identifying the seedlings (see section 6.1.2) suggests that the use of object height data is even more preferable than the use of a building mask with only building information, because it strongly improved the separation between trees and lawn as well. Improving the object height map regarding the DEM normalisation and identification of all buildings would thus provide most advantage to further increase the accuracy of the material identification.

The transferability of the GFZ-unmixing algorithm is an important aspect in its application to the Munich region. The unmixing algorithm was originally developed for and applied to small sites in the cities of Dresden, Potsdam and Berlin. However, with the high degree of au-tomatisation good conditions are available to transfer the algorithm to other regions. Especially the automatic selection of image endmembers with the feature classifier is of great advantage. Image-based endmember spectra are preferable for subsequent unmixing because possible im-age artefacts are included in the endmembers and do not cause larger RMSE during unmixing. Identification of endmembers of urban materials is complicated by the large within-class varia-tion. The spectral variation is caused by shadow cast by other objects, by BRDF effects of the materials and by objects-geometry (e.g. because of inclined roofs). For several surface materi-als spectral characteristics vary because of ageing (e.g. asphalt or clay roofing tiles). In order to obtain accurate unmixing results, endmember spectra of all variations of the material (bright, shaded, old, new, etc.) should be available. The feature classifier is able to identify the spec-tra by characteristic features that are independent from the absolute albedo. This enables the

identification of surface materials under different conditions of sun/sensor geometry and roof inclinations and increases the transferability of the classifier. The subsequent clustering algorithm then creates an endmember for each subclass to cover the complete variation of the class for the unmixing algorithm. Because the feature classifier was trained on a large spectral library of ten thousands of field and image spectra from Dresden, Potsdam and Berlin the endmembers of the Munich test area could be identified with an accuracy of 65 % (section 6.1.1) without any adaptation. Providing the feature classifier with additional Munich image spectra and removing bad bands could improve the accuracy of the automatically identified endmembers to almost 80 %. Only few classes could not be automatically identified and had to be added manually. A possible way to improve the feature classifier even further is to train the classifier with even more spectra. This way more variations of each material will be familiar to the classifier and features that are more suitable to separate the classes can be selected. However, here one should be careful to not include spectra with sensor or atmospheric correction artefacts. Because the features are identified based on mathematical separability, these artefacts might be inappropriately used as characteristic material features. Alternatively, therefore, physical feature classifiers might be considered for endmember retrieval, for example the feature classifier presented by Stein et al. (2009). The feature classifier described in this publication enables the identification of 13 urban materials based on physical based spectral features (e.g. absorption features of minerals) instead of mathematical features. However, it is still to be tested if the number of physical features is sufficient to separate the large number of materials as is available in the unmixing approach of GFZ (i.e. >30 classes).

The transfer of the unmixing approach from the test area in Munich to a large area of 7 flight lines and 252 km$^2$ covering almost the entire city of Munich could be carried out easily and with an almost similar accuracy to the test area. This can be attributed to the high degree of automatisation of the GFZ-approach. The quality of the available a priori information on buildings is the main source of errors for the unmixing results in this large area. The preferred DFK-mask was unavailable for the larger area. The fact that detached and semi-detached housing are the most common urban structural type in Munich outside the city centre makes the less accurate identification of small building by the HRSC-mask (see above) become a bigger issue. Therefore, the hybrid solution is applied. Manual interaction was reduced so as to process this large data set within acceptable time and thus no additional endmembers were added. Outside the densely built areas this resulted in an overestimation of the classes railway track and vegetated roof (see section 6.1.4). The automatic feature classifier could not identify sufficient endmembers for the occasional agricultural fields, which can be explained by the focus of the classifier on urban materials. Manually adding agricultural endmember spectra was not considered necessary in this context.

## 7.1.2 Additional products

Two additional products are derived from the hyperspectral data for the ENVI-met model: surface albedo and leaf area index. The results of the albedo calculation in section 6.2.1 showed that the calculation of surface albedo can be done accurately by averaging the reflectance in all HyMap wavelengths. This approach is preferred over the approach implemented in ATCOR because it can be applied to fully pre-processed data, including nadir normalisation. However,

sensor viewing angle, inclination of roofs, orientation of buildings and shadows cast by neighbouring objects, all influence the albedo as recorded by the sensor, although the material properties of the surface do not change. Because of the nadir-normalisation the influence of the sensor viewing angle is minimised but influences of roof inclination and orientation for example still exist. A BRDF-correction could help to derive normalised albedo values representing the actual surface properties and not its geometry. For example Feingersh et al. (2009) developed such a BRDF correction algorithm, which is planned to be operationally available within the coming years. However, such a correction is not straight forward, because knowledge on the surface topography and the BRDF characteristics of surface materials is required. This effort should only be made if the micro climate model is very sensitive to albedo inaccuracies (see also section 7.2).

The leaf area index is needed to calculated the leaf area density, which is required by the ENVI-met model. Leaf area index (LAI) is a common remote sensing product. However, the urban environment is only seldom the object of interest. Therefore, no vegetation index based relationships have been developed for the estimation of the LAI of urban vegetation, but only for crops, forests and grasslands. Because no field measurements were available to establish such a relationship within this thesis, the NDVI-based MODIS-backup algorithm was selected because of its applicability for various biomes and wide acceptance. Although Damm (2008) showed that estimating the LAI of urban trees is difficult, the mapping of the LAI in this study was found sufficient to calculate the LAD with values comparable to those documented in the literature.

## 7.2 Micro climate characterisation with the derived remote sensing products

The second aspect of the concept presented in chapter 2 is concerned with the use of the remote sensing products to support micro climate characterisation by spatial indicators and modelling. The remote sensing products were used to create maps of six climate relevant spatial indicators at building block level and to support urban micro climate modelling with ENVI-met (see section 6.3 and 6.4). The following discusses the potential of the remote sensing products to support these two approaches and their ability to characterise urban micro climate based on the derived hyperspectral products (materials, albedo, LAI).

### 7.2.1 Spatial indicators

The six selected spatial indicators are able to represent the urban structure at building block level very accurately. The differences between urban structural types and their heterogeneity could be demonstrated. Typical values of the spatial indicators could be derived for each of the twelve selected urban structural types. For certain urban structural types several indicators show larger standard deviations, e.g. for small multi-storey buildings. Although this makes an objective separation of the urban structural types more difficult, the standard deviation is also an additional feature which characterises the urban structural type.

The accuracy of the spatial indicators is considered to be very high. This confirms that the derived sub-pixel material map is of sufficient quality to support the calculation of spatial indicators at building block level. Especially the accuracy of the percentage of impervious surface is very high. The identification of the dominant roof material is troubled by co-registration errors in the building mask during the material identification. Vegetation was identified as vegetated roof, resulting in a dominant roofing material of vegetated roof in building blocks with high vegetation density such as detached and semi-detached housing areas. As a result, the building density in these building blocks is overestimated, while the vegetation density is underestimated.

Because only 14 building blocks were available in the highly detailed BLOCK-reference a comparison with the indicators currently used by the municipality of Munich was made. However, the comparison of the municipality indicators with the reference showed that the municipality data is less accurate and more variable than the HyMap-based indicators (cf. figure 6.12). Therefore, one should be careful in drawing conclusions from these comparisons. The comparison with the municipal indicators (figure 6.13) suggests underestimation of high values of the indicators and overestimation of low values in the HyMap-based indicators. It is possible that small under- and overestimation of the indicators indeed occur. A comparison between the imperviousness of the reference and HyMap-based indicators shows a similar trend. Also literature frequently reports on the underestimation of high imperviousness and overestimation of low imperviousness for approaches based on linear unmixing (e.g. Pu et al., 2008; Wu and Murray, 2003). Wu and Murray (2003) attributed this to the fully constrained linear unmixing model. However, it is more likely that the differences between the HyMap-based indicators and the municipality indicators have to be attributed to the method with which the municipality indicators are derived, namely by visual interpretation of aerial images. Powell et al. (2004) studied the influence of the interpreters on the classification of land cover. They found that, although

on average all interpreters reach an equal accuracy, there were large differences in the classes they assigned. Especially assigning the fractional cover of a class (such as vegetation density or percentage impervious surface) was found to be a highly subjective task, for which the resulting percentages differed greatly among interpreters. Using the remote sensing based approach to map the spatial indicators retrieves objective and repeatable results. Especially when monitoring large areas and over multiple years this is a great strength of remote sensing techniques and it facilitates the comparison of the derived maps.

The spatial indicators play an important role in describing the urban area for planning, e.g. by characterising building blocks after urban structural types (section 6.3.2). The spatial indicators selected in this study are all familiar to the urban planners within the REFINA project in the Munich region and are considered relevant to monitoring of the urban development (Heldens et al., 2009a).

The spatial characteristics that the indicators describe strongly influence the urban micro climate. The importance of these indicators can be illustrated by the extensive number of studies concerning their influence on the urban climate (e.g. Kuttler, 1998; Helbig et al., 1999; Kolokotroni and Giridharan, 2008; Zhang et al., 2009a). Because of their importance to the urban micro climate and their existing application in the urban planning praxis, spatial indicators can bridge the gap between the disciplines of micro climate analysis and urban planning. The spatial indicators can provide a means to describe the characteristics influencing urban micro climate in a way that is suitable and comprehensible to urban planners. How this can be accomplished is demonstrated in section 7.3.

## 7.2.2 Micro climate simulations with ENVI-met

A simulation run with the micro climate model ENVI-met provides extensive information for the micro climate characterisation of multiple building blocks at a time. One simulation run requires much computation time and a large number of input parameters to describe the area. The advantage of the use of the hyperspectral data products is that it allows the retrieval of many input parameters with only one data source, such as albedo, leaf area density and a large range of surface materials to which the relevant thermal properties can then be assigned. Because all of these input parameters and the object height data are available in digital form, the simulation area can be generated without any manual interaction in ENVI-met format, saving extensive manual editing efforts.

The quality of the sub-pixel material map is sufficient to represent the study area accurately in the ENVI-met 3D model environment. Of course improvements to the material identification as discussed in section 7.1.1 will enhance the representation of the real situation in ENVI-met even further. However, minor co-registration errors between the height data and the material map are no problem for the creation of the ENVI-met files. Because the buildings are identified by using the height data and both the dominant and second class are examined to find a suitable material (i.e. a roofing material) small co-registration errors are overcome by using the sub-pixel information. The object height turned out to be one of the aspects that strongly influence the ENVI-met simulations of wind flow. Therefore, the improvement of the height data, especially regarding the height of small buildings, will enhance the accuracy of the simulations.

Tree crowns covering streets and small buildings are of more concern, making it hard to de-

tect these objects with remote sensing accordingly and include them in the area description for ENVI-met. In ENVI-met the tree crown should be located at the grid cell where the stem is. ENVI-met then models the influence of the tree crown according to the height and leaf area density of the tree. Usage of remote sensing images recorded in winter could help to identify both the tree stem and the streets or buildings, allowing a view on the object below through leafless tree crowns. Commonly, like in this study, summer images are used, because the sun/sensor geometry is more favourable during that season, e.g. because of less shadows. Such effects have to be taken care of when using winter images.

A large percentage (6.4 %) of the test area is identified as shaded surface in the surface material map. Usually, this would mean that no information on the actual surface material is available for the automatic representation of the study area in ENVI-met format. However, in many cases the other endmember can provide necessary information on the surface cover. Also shaded vegetation can often be separated from other shaded surfaces by the GFZ-unmixing algorithm, which reduces the negative effect of shaded surfaces.

The albedo and leaf area index are additionally derived from the hyperspectral data in order to provide more realistic surface properties for the ENVI-met model. However, these parameters can only be used when calculated for pure pixels. Since albedo is part of the description of a certain surface material in the ENVI-met facade-database, there is no use in including the albedo of a pixel which contains two surface materials. For these pixels a default albedo value is assigned according to the average albedo of known pure pixels of the material. The accuracy of the calculated albedo surfaces is sufficient for application in the ENVI-met model. The influence of the surface albedo mainly concerns the surface temperature.

For the leaf area density solely pure vegetation pixels can be used as well. Another background (i.e. asphalt or soil) as would be the case in mixed pixels, influences the LAI value calculated with vegetation indices (Haboudane et al., 2004). An equation for the calculation of leaf area density (LAD) is available only for trees (Lalic and Mihailovic, 2004). The accuracy of the leaf area index of trees is high enough to calculate representative LAD values. Default values provided by ENVI-met are used for all other vegetation pixels.

From the many simulation runs carried out during this study, small classification errors of the surface material or inaccuracies in the estimated albedo and LAI do not seem to strongly influence the simulation results. An extensive sensitivity analysis of the ENVI-met model regarding these input parameters is still required to confirm this. The same is true for the thermal properties of materials and soils. So far, values published in literature have been used. An analysis of the possible variation within similar materials (e.g. because of weathering) could probably result in more accurate surface properties. However, this is only useful if small differences in the surface properties significantly influence the simulation results.

The results in sections 6.4 showed that all urban characteristics described by the hyperspectral data are of importance to modelling with ENVI-met. Differences in surface covers (e.g. asphalt or trees, see figure 6.19) cause different micro climate characteristics (e.g. temperature, humidity). The use of different roof materials causes differences in surface temperatures of the buildings and as a result they are responsible for different indoor temperatures. This is important because it influences the climate inside the building, including the need for air conditioning etc. Therefore it is useful information for architects and construction engineers to learn which roofing materials are advantageous and which not. However, only the upper part of the roof

can be included in the ENVI-met model. Remote sensing cannot measure the amount and type of insulation used for example. Also ENVI-met is not (yet) able to model multiple layers of roofing material and insulation in detail.

Within this thesis it was not possible to carry out a complete accuracy assessment of the model results. The comparison of simulated surface temperature with the Daedalus surface temperature in section 6.4 showed similar patterns of surface temperatures. But, because ENVI-met needs buildings to be described with flat roofs, differences in both relative and absolute surface temperatures occurred especially on buildings with inclined roofs.

A close look at the maximum air temperatures suggests that the ENVI-met model underestimates the maximum daily temperature. The simulation of a sunny summer day reached a maximum temperature of only 20°Celsius. A discussion with the ENVI-met developers revealed that this effect can be reduced by using the forcing option. This is an option in ENVI-met where hourly measured values (e.g. from a weather station in the surroundings) are provided to the model and then used instead of the model average. Without providing these values the average temperature is calculated with the simulated situation in the whole area each hour, including cool and warm areas. This average is used as a starting point for the next round of simulations. If the simulation area contains a lot of shaded areas, the average is too low and a realistic maximum temperature will not be reached. The same effect occurs in other parameters such as humidity. Unfortunately, it was not possible to evaluate the advantage of the forcing option within this study, due to time and data constraints.

Another important aspect that influences the simulation results is the location within the simulation area. This is shown by a test in which each of the 95 building blocks in the 16 simulation areas are assigned to a quadrant according to their location in the simulation area. For all blocks in each quadrant, mean values are calculated for the climate parameters. In figure 7.1 the result of this test is shown for air temperature at 1.5 m above ground. Next to the figure, the location of the quadrants is indicated. The graphic shows that the location of the building block significantly influences the air temperature. Building blocks located in the south-west of the simulation area (quadrant 1) have a clearly higher average air temperature than the building blocks in the north-east of the simulation area (quadrant 9). This effect can also be noticed in figure 6.16, for example. Although it is common for the air temperature to be controlled by the wind, the influence is rather strong in this case. This effect might be reduced when the forcing option is used. The location differences are a combination of the selected wind direction, the heating of the bare soil in the nesting grids in the south-west and the obstruction of the wind by buildings, creating a wind shadow in the north-east of the simulation area. Nesting grids are used to allow the modelling of the micro climate at the borders of the model environment in ENVI-met. More tests are required to analyse if the location within the simulation area is still as large with different simulation parameters, such as an altered wind direction and the use of the forcing option.

Nevertheless, the ENVI-met model provides the possibility to gain insight in the micro climatic situation of selected building blocks in a visual and comprehensible way. When using the automatic generation of the simulation areas based on the remote sensing products presented in this thesis, realistic areas can be simulated with minimal effort saving field surveys and tedious manual editing.
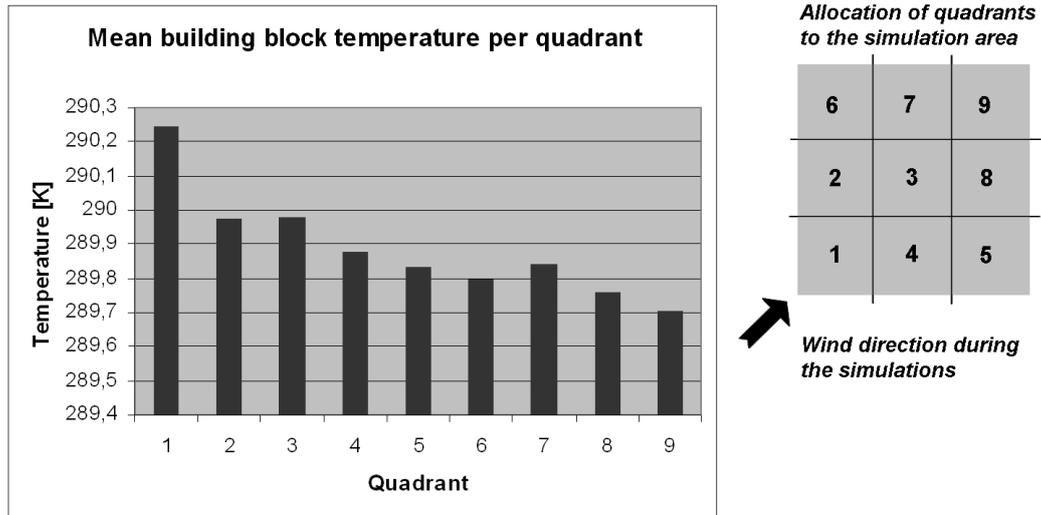
Figure 7.1: *Mean building block temperature per quadrant at 1.5 m above ground. The graphic on the right displays the allocation of quadrants to the different parts of the simulation area. During the simulations the wind came from the south-west with a speed of 3.5 m/s at 2 m above ground.*

# 7.3 Demonstration of urban structural types as framework for micro climate characterisation

In order to meet the needs of urban planners urban structural types were suggested as a framework for micro climate characterisation. Because of their suitable scale for both urban planning and micro climate analysis, building blocks are used as the unit to present the results of the micro climate characterisations. In this section it is demonstrated how urban structural types can be used for micro climate characterisation. The first part takes a closer look at two building blocks of different urban structural types with their spatial and climatic characteristics. Next, two examples show how the urban micro climate can be characterised within the framework of urban structural types based on the spatial indicators and simulation results.

Tables 7.1 and 7.2 give an overview of the generated spatial and climatic characteristics for two exemplary building blocks of different urban structural types. Table 7.1 shows a regular block development. The buildings of this block are mainly characterised by roofing tiles, both red clay tiles (32 % of the roofs) and concrete tiles (33.8 %). For this building block, the building density and vegetation density are almost equal. More than half of the block is covered with sealed surfaces. The building volume (3.31 m$^3$/m$^2$) is similar to the average building volume for regular block development (3.10 m$^3$/m$^2$). The vegetation volume is low in comparison with the average vegetation volume for regular block development, indicating that the number of trees is not very high.

A selection of climate parameters of this regular block development resulting from the ENVI-met simulations and aggregated for the building block is presented in table 7.1. The figure next to the table shows the spatial configuration of air temperature and wind flow. The mean air temperature of one day in the block is almost 289.8 degrees Kelvin (16.8 degrees Celsius). At a height of 20 m, about five meters above the buildings, the mean temperature decreased with almost 0.2 degrees. In this building block the warmest time of day is around 14:00. The mean wind speed within the building block is 0.69 m/s. Above the top of the roofs, at a height of 20 m, this increases to 4.21 m/s. This, together with the map of air temperature and wind flow in the table, illustrates how important the buildings and their configuration are to the wind flow. The most western building shields the rest of the building block from the wind; the wind flows around the block. This also prevents warmer air from reaching the inner building block area. This result in differences of up to 1.5 degrees between the building block and the big road to its north at the warmest time of the day, according to the model simulations. Closely related to the air temperature and the wind speed is the predicted mean vote (PMV). The mean value of 0.6 for this building block indicates that a test subject would feel warm but not uncomfortably hot (which would be the case at a PMV value of 3). A humidity of 71.2 % within the building block is quite high. Above the roofs, the mean humidity is 1 % lower. As a last climate parameter, the mean simulated surface temperature is presented. The surface temperature is much higher than the air temperature. For roof surfaces only, the mean surface temperature is 297.9 degrees Kelvin (24.9 degrees Celsius). The average of all surfaces lies almost 5 degrees lower. The vegetated surfaces are mainly responsible for this lower surface temperature.

In table 7.2 the same information is provided for a dense block development. The main roofing materials of this building block are clay tiles and metal. The building density and impervi-

Table 7.1: *Spatial and climatic characteristics of an exemplary building block of regular block development (BD: building density, VD: vegetation density, IMP: imperviousness, BV: building volume, VV: vegetation volume, $T_{block}$: air temperature within the building block, $T_{surf}$: surface temperature within the building block and $v_{wind}$: wind speed within the building block).*
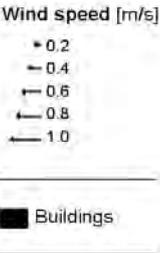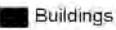


| Regular block development | |
|---|---|
| **Spatial indicators** | |
| roofing material [% of all buildings] | |
| *roofing tiles* | *32* |
| *concrete* | *33.8* |
| *metal* | *0.2* |
| *synthetic* | *0.5* |
| *bitumen* | *15.3* |
| *vegetated* | *14.7* |
| *gravel* | *0.6* |
| *facade / unknown* | *2.9* |
| BD [% ] | 43.4 |
| VD [% ] | 41.8 |
| IMP [% ] | 52.4 |
| BV [$m^3/m^2$] | 3.31 |
| VV [$m^3/m^2$] | 1.77 |
| **Climate parameters** | |
| mean $T_{air}$ (1.5 m) [K] | 289.767 |
| mean $T_{air}$ (20 m) [K] | 289.574 |
| max. $T_{air}$ (1.5 m) [K] | 292.780 |
| time of max. $T_{air}$ | 14:00 |
| mean $v_{wind}$ (1.5 m) [m/s] | 0.69 |
| mean $v_{wind}$ (20 m) [m/s] | 4.21 |
| max. PMV (1.5 m) | 0.6 |
| mean humidity (1.5 m) [% ] | 71.16 |
| mean humidity (20 m) [% ] | 70.04 |
| mean $T_{surf}$ (all surfaces) [K] | 293.217 |
| mean $T_{surf}$ (only roofs) [K] | 297.866 |

Table 7.2: *Spatial and climatic characteristics of an exemplary building block of dense block development (BD: building density, VD: vegetation density, IMP: imperviousness, BV: building volume, VV: vegetation volume, $T_{block}$: air temperature within the building block, $T_{surf}$: surface temperature within the building block and $v_{wind}$: wind speed within the building block).*



| Dense block development | |
|---|---|
| **Spatial indicators** | |
| roofing material [% of all buildings] | |
| *roofing tiles* | *32.7* |
| *concrete* | *2.6* |
| *metal* | *11.1* |
| *synthetic* | *7.9* |
| *bitumen* | *20.5* |
| *vegetated* | *11.2* |
| *gravel* | *0.3* |
| *facade / unknown* | *13.7* |
| BD [% ] | 78.8 |
| VD [% ] | 16.3 |
| IMP [% ] | 82.1 |
| BV [$m^3/m^2$] | 10.68 |
| VV [$m^3/m^2$] | 1.33 |
| **Climate parameters** | |
| mean $T_{air}$ (1.5 m) [K] | 290.589 |
| mean $T_{air}$ (20 m) [K] | 290.691 |
| max. $T_{air}$ (1.5 m) [K] | 293.850 |
| time of max. $T_{air}$ | 15:00 |
| mean $v_{wind}$ (1.5 m) [m/s] | 0.07 |
| mean $v_{wind}$ (20 m) [m/s] | 2.51 |
| max. PMV (1.5 m) | 0.8 |
| mean humidity (1.5 m) [% ] | 66.28 |
| mean humidity (20 m) [% ] | 65.86 |
| mean $T_{surf}$ (all surfaces) [K] | 298.264 |
| mean $T_{surf}$ (only roofs) [K] | 301.323 |

127

ousness of the dense block development are almost twice as high as the values that have been found for the exemplary regular block development in table 7.1. As a trade-off, the vegetation density is less than half of the vegetation density in the regular block development. Also the building volume of this dense block development is high, even higher than the average building volume found for dense block developments, which is 7.2 $m^3/m^2$. However, the vegetation volume is comparable to that of the regular block development. This illustrates that the vegetation volume does not only depend on the height of the vegetation but also on the total vegetation density. A large lawn with small bushes can thus reach the same vegetation volume as a small vegetation patch with only a few high trees.

The climate parameters resulting from the micro climate simulations indicate that the exemplary dense block development is warmer and less humid than the exemplary regular block development. The mean air temperatures both at 1.5 m and 20 m height are about one degree higher. The time of the maximum air temperature shifted more towards the afternoon. A large difference between the two building blocks in table 7.1 and 7.2 can be found in the wind speed. Inside the building block of a dense block development this is only 0.07 m/s, against a speed of 0.69 m/s for the regular block development. The surface temperature of the exemplary dense block development is almost five degrees higher than in the building block in table 7.1. This is likely to be the result of the larger imperviousness and the larger amount of bitumen roofs (which has a high heat capacity).

The two tables show that there are considerable differences in the micro climate characteristics of two urban structural types. In the following two examples it is therefore shown how the micro climate can be characterised within the framework of urban structural types, based on the information provided by the spatial indicators and micro climate simulations. They provide information about the simulated climate characteristics of urban structural types in relation to their spatial characteristics as described by the indicators. At the same time they give information on the variation between and within the urban structural types.

The first example shows an analysis of the air temperature at 1.5 m above ground during the day for the twelve different urban structural types. The hourly mean temperature is calculated for all building blocks, averaged for each of the structural types and displayed in figure 7.2. The curves show differences in the maximum temperature at midday and in the speed with which the building blocks warm up and cool down (steepness of the curves). Still, the differences between the urban structural types are all within one degree. In addition, one should be aware that the standard deviation is almost of the same magnitude, ranging from 0.15 for sports fields (c2) to 0.7 for high rise buildings (a6). The difference between the maximum and minimum temperature of the day is around five degrees. This is not as high as could be expected from a cloud free summer day. This underestimation of the maximum temperature has already been addressed in the previous section (section 7.2).

Figure 7.2a shows the results for the urban structural types with a mainly residential use. According to the simulation results, row house development (a4) has the highest maximum temperature followed by dense block development (a1) and high rise buildings (a6). Perimeter block developments (a2) and regular block developments (a3) have the lowest temperatures. This does not completely meet the expectations, because urban structural types with high vegetation densities such as detached and semi-detached houses (a5) or row house development (a4) were expected to show the lowest mean air temperatures. This has to be attributed to the loca-
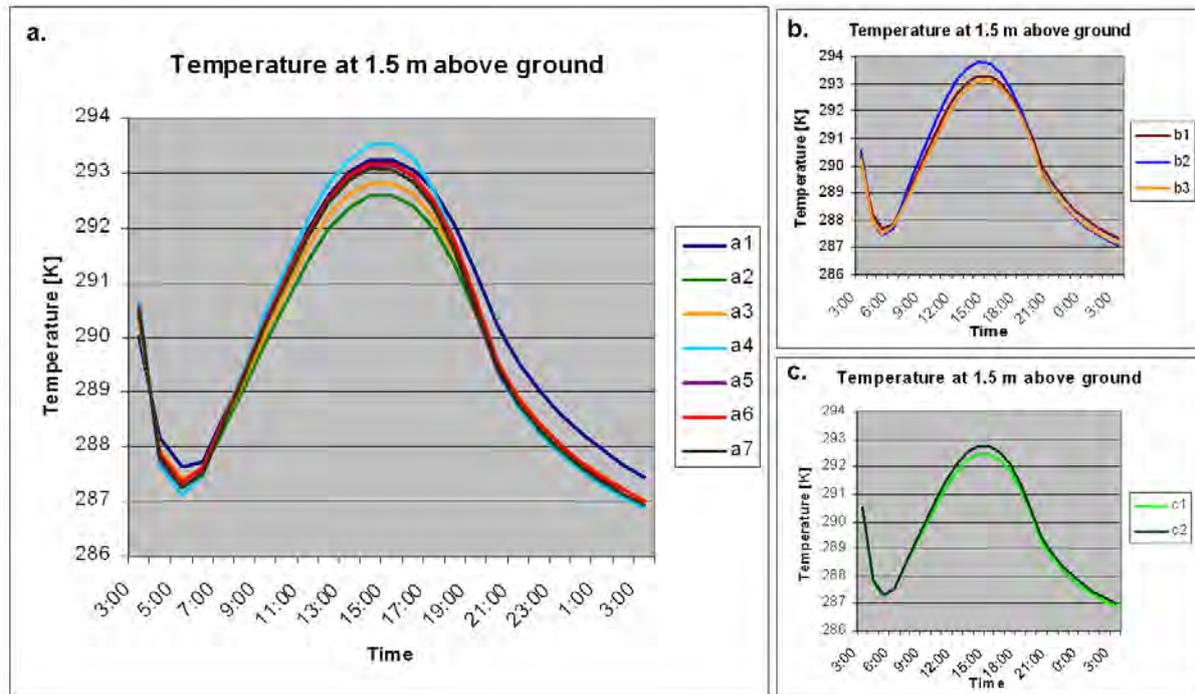
Figure 7.2: *Mean building block temperature during the day for different urban structural types. a: mainly residential structural types (a1=dense block development, a2=perimeter block development, a3=regular block development, a4=row house development, a5=detached and semi-detached housing, a6=high rise buildings, a7=small multi-storey buildings); b: mainly commercial/industrial structural types (b1=large multi-storey buildings, b2=large halls and storage buildings, b3=small halls and storage buildings) and c: recreationally used structural types (c1=parks and urban green, c2=sports fields).*

tion of the building blocks within the simulation area (see also figure 7.1). All building blocks of the row house development urban structural type are located in the south-west of their simulation areas (quadrants 6,7,8 or 9), where the air temperatures were significantly lower. Half of the building blocks belonging to perimeter block development were located in the hottest quadrants, quadrant number 1 and 2.

The temperature course of three mainly commercially used urban structural types is given in figure 7.2. Large halls and storage buildings (b2) show a higher maximum temperature than the other two types. Large multi-storey buildings (b1) seem to cool down slowest, according to the simulation results. Although no significant amount of building blocks was available for these urban structural types (one for small and large halls and storage buildings, five for large multi-storey buildings), these simulation results do meet the expectations.

The maximum temperature of urban green and sports fields (in figure 7.2c) is lower than that of most of the built up urban structural types, as could be expected. There is a slight difference between the parks and urban green (c1), which have vegetation densities of up to 100 %, and sports fields (c2) which usually contain some buildings or (partially) impervious sports courts.

The second example shows how an analysis of the correlation of climate parameters and spatial indicators can be used for the characterisation of the micro climate of urban structural types. Four climate parameters (surface temperature, air temperature, wind speed and humidity) are selected and correlated with spatial indicators. The simulated parameters are aggregated per building block to allow a comparison between building blocks. Based on this hourly average, the day mean and maximum are calculated for each building block and parameter.By grouping the building blocks according to their urban structural type, for example the similarity of urban structural types in such a correlation can be analysed. In figure 7.3 and 7.4 four scatter plots are presented. The first scatter plot (figure 7.3a) shows the relation between imperviousness and surface temperature, for which quite a strong positive linear correlation can be observed ($R^2$= 0.84). A similar correlation was found in other studies (e.g. Yuan and Bauer, 2007; Zhang et al., 2009b). The positive correlation between imperviousness and air temperature, displayed in figure 7.3b is rather weak ($R^2$=0.34). The air temperature is not only influenced by the surface cover but also by climate parameters such as wind and humidity (Kuttler, 1998). Figure 7.4a shows the correlation between the building volume and the wind speed. After the correlation between imperviousness and surface temperature this is the strongest correlation that has been found between the selected micro climate parameters and spatial indicators ($R^2$=0.59). It indicates that ENVI-met simulates on average lower wind speeds for building blocks with higher building volumes (i.e. larger and/or higher buildings). The last scatter plot, which is shown in figure 7.4b, presents the correlation between vegetation density and humidity. At a building block level this positive correlation is not so strong ($2^{nd}$ polynomial $R^2$=0.4). Nevertheless, the simulation results show that an increase of humidity over vegetation patches can be observed locally (as is shown in figure 6.19).

In order to provide information about the micro climate characteristics of the different urban structural types, the building blocks in the scatter plots are marked accordingly. This makes several observations possible. Firstly, there are large differences between the urban structural types in the shape of the clusters they formed. For example parks (c1) and detached and semi-detached houses (a5) form relatively tight clusters with few outliers. Perimeter block developments (a2) on the other hand form loose clusters, covering a large range of building volumes and wind speeds for example. Secondly, the location of the building blocks within the clusters of their urban structural types varies for the different types and scatter plots. For instance in figure 7.3a where the building blocks of dense block developments (a1) vary mainly in surface temperature whereas the imperviousness is more similar, giving the cluster of this urban structural type a vertical shape. In contrast, the shape of the cluster of detached and semi-detached houses (a5) is more horizontal and the blocks vary more in imperviousness than in temperature. In figure 7.4a this is exactly the other way around. Here the dense block development (a1) cluster is more horizontally shaped, covering a large range of the spatial indicator building volume and a small range of wind speeds, whereas the cluster of detached and semi-detached houses (a5) is vertical (with a varying climate parameter with similar spatial indicator). Thirdly, one can observe that the orientation of the clusters of the urban structural types towards each other is similar for the four scatter plots. Urban green (c1) and sports fields (c2) are the opposite of dense block development (a1), at the extremes of the scatter plots. The building blocks of detached and semi-detached houses (a5) are located in the middle but slightly closer towards urban green (c1), where as large multi storey buildings (b1) are located closer to the cluster of dense

130
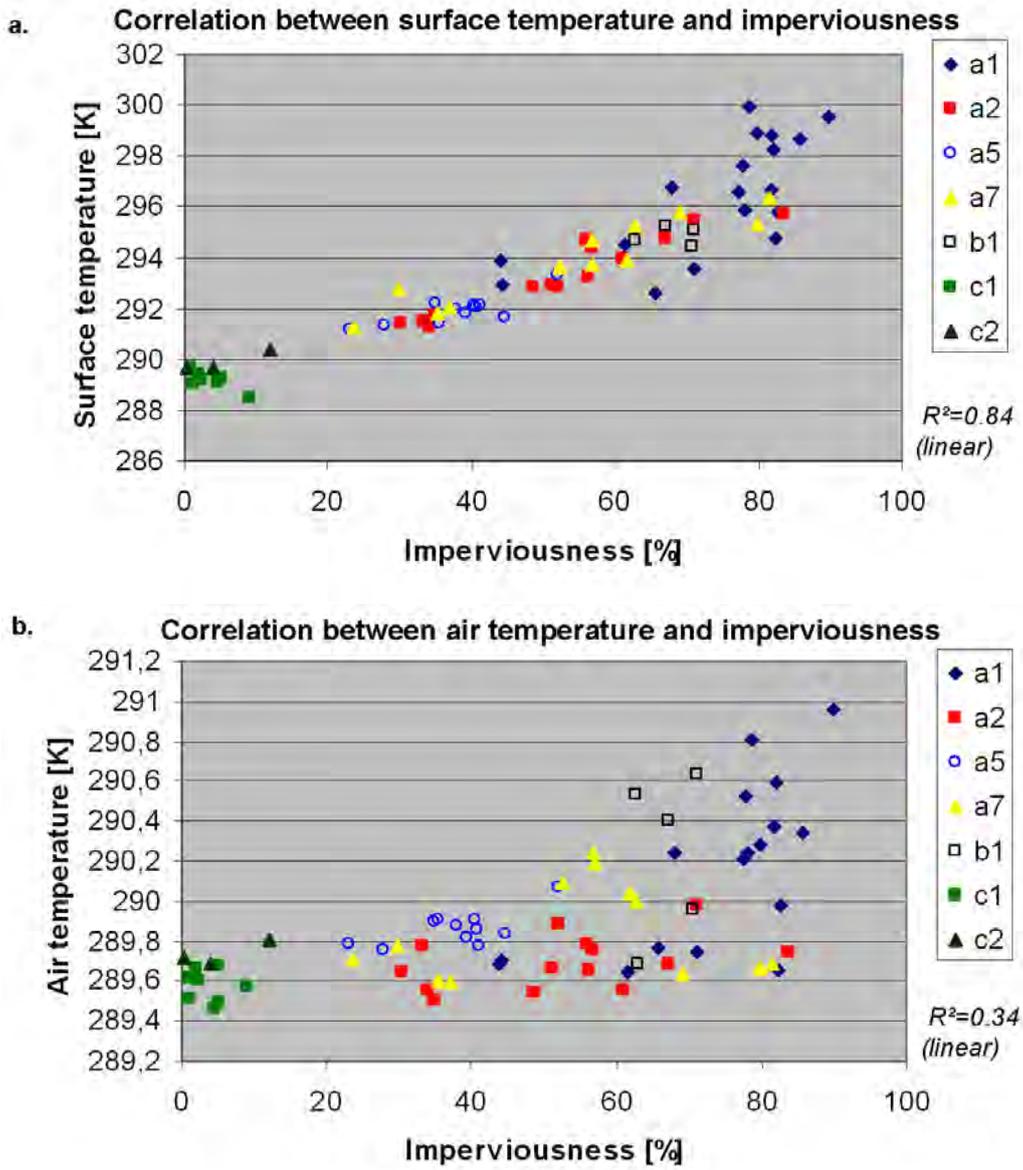
Figure 7.3: *Correlation between the spatial indicator imperviousness and climate parameters surface temperature and air temperature at 1.5 m, for a selection of urban structural types. See figure 7.2 for an explanation of the abbreviations for the urban structural types.*
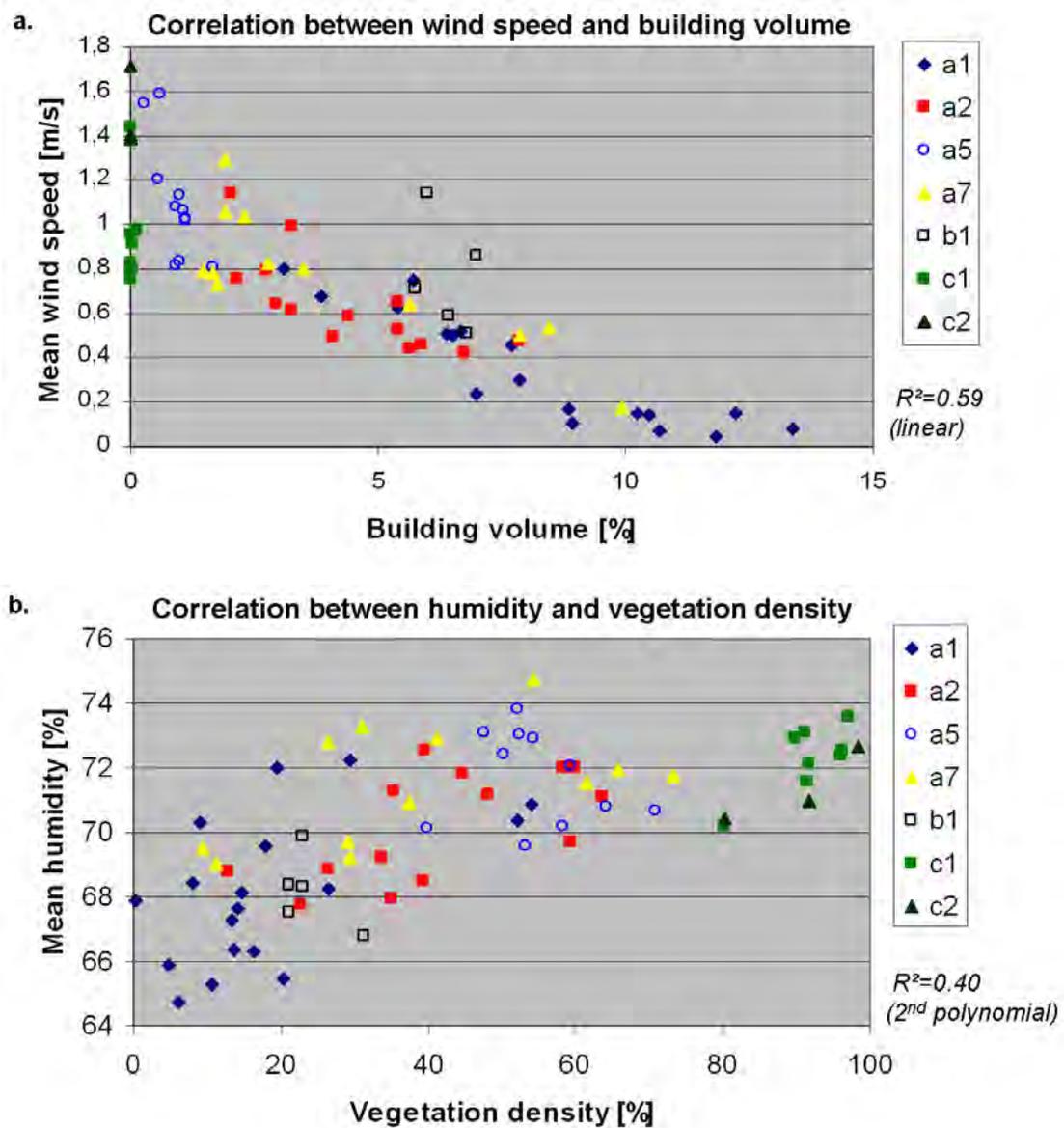
Figure 7.4: *Correlation between the spatial indicators building volume and vegetation density and the climate parameters wind speed and humidity at 1.5 m, for a selection of urban structural types. See figure 7.2 for an explanation of the abbreviations for the urban structural types.*

block development (a1). Perimeter block developments (a2) and small multi-storey buildings (a7) cover almost the whole range between urban green (c1) and dense block development (a1).

The examples in this section show that typical differences between the urban structural types exists, both in the simulated climate parameters and in the spatial indicators. The differences between the urban structural types are less obvious for the selected climate parameters (mean wind speed, mean humidity, max temperature, max PMV) than for the spatial indicators (cf. section 6.3.2). This can be partially explained by the fact that the total variation of the climate parameters is smaller: impervious surfaces in the different building blocks span almost the complete range from 0 to 100 % of impervious surface for example, while all humidity values are within 10 %. Also the complexity of the urban micro climate system plays a role. The effect of one spatial indicator, e.g. imperviousness, can be mitigated by another, e.g. building configuration. The scatter plots in the figures 7.3 and 7.4 show that the various samples of each urban structural type are grouped. For the parks and sport fields this grouping is very tight, for regular block development the grouping is looser. In each scatter plot regions can be assigned to all urban structural types, although they are partly overlapping.

An existing categorising system, such as that of urban structural types, is preferable for the use in urban planning for the characterisation of the urban micro climate. The approach presented in this study can generate information that shows how the urban micro climate in different urban structural types can be characterised. It allows urban planners to gain insight in the differences in the climatic situation in building blocks of different urban structural types and at the same time allows the analysis of the heterogeneity of micro climate within building blocks of the same urban structural type. Such knowledge is valuable for the development of mitigating and climate improving planning activities: for urban structural types with homogeneous micro climatic characteristics one type of activity (e.g. increasing urban green) is likely to be sufficient, whereas for more heterogeneous urban structural types a variety of measures is required (e.g. increase of urban green and regulation of the building alignment).

## 7.4 Evaluation of the conceptual framework

The conceptual framework presented in chapter 2 aimed at providing an approach in which the advantages of hyperspectral remote sensing can be fully employed to support micro climate characterisation. An important objective for the development of this conceptual framework was to consider the needs and requirements of urban planners. They need to use the micro climate information to be able to take the micro climatic situation in the city into account in the spatial plans. The time span of this Phd research was not long enough to evaluate the use of the derived micro climate information in the planning praxis. This can easily take several years, since the development of spatial plans is a slow process. However, the REFINA project (Klein et al., 2010), within which this research was carried out, enabled the discussion of remote sensing products with urban planners in the Munich region and made an evaluation of this conceptual framework possible.

With these experiences and the validation results presented in this thesis it can be stated that the conceptual framework meets its objectives. The full potential of hyperspectral remote sensing is used, providing a highly detailed mapping of surface materials. The requirements of urban planners are taken into account by several aspects.

The spatial scale of the analysis is selected in a way that it fits to the zoning plans and the influences of micro climate. Most micro climatic effects occur within the building block (see section 6.4.2). The remote sensing products can easily be aggregated to this level. At the building block level a relation with urban structural types and spatial indicators is possible, as is demonstrated in section 7.3. This relationship between well-known planning concepts and the urban micro climate can increase the understanding of the micro climate system among urban planners.

The remote sensing products provide a time efficient means to acquire most of the necessary input parameters for micro climate modelling and the calculation of spatial indicators. This saves valuable time of municipalities and climatologists because the amount of field surveys can be reduced drastically. In addition, the spatial indicators and micro climate simulation results are presented in understandable maps and graphics. Urban planners often need to show politicians or citizens the information on which they based the development of a new spatial plan. Therefore it is of great advantage if this information is mainly self-explicable and looks good (Heldens et al., 2009a).

The conceptual framework developed in this thesis is a first step towards providing urban planners with the advantages of hyperspectral remote sensing. However, there are several aspects that have to be taken into account when transformation of this approach from an experimental one into an operational approach is desired.

Because of the high standard of the remote sensing techniques applied in the approach, remote sensing expert knowledge is required to ensure a high level of accuracy. Most of the steps in the approach are automated or part of a chain of automatic processes. The transfer of the unmixing approach to the large study area also showed that good results can be retrieved with minimal manual interaction. However, a certain level of knowledge about the applied techniques seems necessary to evaluate the intermediate results and carry out enhancements where needed.

Urban planners need to be supported by a climatologist for the correct interpretation of the results in the context of the urban micro climate. Although the ENVI-met model is easy to

use and produces apparently easily interpretable simulation results, a micro climate expert can judge the model results more accurately. In addition, a climatologist is required to support urban planners in the development of mitigating measures to improve the urban micro climate, e.g. to assess the multiple effects of one action.

Finally, airborne hyperspectral remote sensing, although with much potential, is an expensive data set. Many municipalities find such data too expensive (Klein et al., 2010), among others because they need remote sensing experts as well to assist them with the interpretation of the hyperspectral image cube. It should become an objective to the hyperspectral community to convince potential users of the large and valuable amount of information that can be retrieved from one hyperspectral data set. Not only can information be derived to support micro climate analysis, but also to map the health of urban vegetation (Damm, 2008), the urban ecosystem (Bochow et al., 2006) and much more, making the hyperspectral data worth the money.

The conceptual framework and its implementation as presented in this thesis are not limited to Munich, but likely to be transferable to other German and northern-European cities without many problems. In other regions, the applied material identification algorithm needs to be trained to recognise local surface materials. An alternative for urban structural types might have to be considered for non-western countries because the use of such a framework is depending on planning traditions and practice. Other micro climate models might also be considered for the simulation of the urban micro climate, because the input parameters are relevant for urban micro climate in general and because they are used by many models. Of course in that case the automated generation of the input data developed especially for the ENVI-met model needs to be adapted to the new micro climate model.

# 8 Summary and conclusions

For this thesis the following two objectives were set: (1) develop a conceptual framework for the use of airborne hyperspectral remote sensing to support urban micro climate characterisation for urban planning and (2) analyse the potential of airborne hyperspectral remote sensing for this task by implementing the conceptual framework in a case study in Munich.

The conceptual framework proposes the use of hyperspectral remote sensing to identify surface materials that are representative of urban objects. Spatial characteristics can be mapped at a local scale to provide basic information for urban micro climate analysis, e.g. for spatial indicators to describe building blocks or as detailed input parameters to a micro climate model. Urban structural types are identified as a suitable framework for micro climate characterisation because this is a well known and commonly used scheme to describe the urban area for planning purposes. The building block is selected as a reference area because it fits both the spatial scale of planning activities and that of micro climate studies. The spatial indicators and model simulation results can then be used and combined for the characterisation of the micro climate situation of urban structural types.

The conceptual framework was successfully implemented in a case study in the city of Munich. A multiple endmember spectral mixture analysis approach developed by Roessner et al. (2001) and Segl et al. (2003) was applied to airborne hyperspectral HyMap data to map sub-pixel surface materials. The algorithm was found to be easily transferable to the Munich region, even for a large area of seven flight lines. This can be attributed to the large degree of automatisation of the GFZ-unmixing approach and the feature classifier which makes use of a very large spectral library for the identification of endmembers. The algorithm was supported by a priori information on building locations to enable separation between different urban objects covered with the same materials (e.g. asphalt streets and bitumen roofs) which cannot be separated spectrally. For the more than 25 different surface materials the mean absolute error was on average 2.2 % abundance per building block and 16 % abundance per cluster of 3 x 3 pixels. The a priori information on the location of buildings was identified as one of the most important factors influencing the accuracy of the material identification.

In addition to the sub-pixel material map, surface albedo and the leaf area index were derived. Although field measurements for validation of these results were lacking, the products could be successfully used as input parameters for the micro climate model. The surface albedo was found to be strongly influenced by the sun-sensor angle and building orientation. Leaf area index in urban areas has to be measured with care because of the high number of mixed pixels. Nevertheless, leaf area density as required by ENVI-met could be successfully retrieved from the leaf area index calculated for the trees.

The products derived from the airborne hyperspectral remote sensing were used in two approaches to characterise the urban micro climate: the calculation of spatial indicators and micro

climate simulations. Previous studies showed the relation of urban characteristics with climate parameters. A selection of spatial indicators describing these urban characteristics was calculated per building block, based on the material map and object height data. Building density, vegetation density, imperviousness, building volume and vegetation volume could be calculated with a mean absolute error of less than 5 %. The dominant roof material per building block reached an overall accuracy of 71 %.

For the simulation of the urban micro climate the model ENVI-met (Bruse and Fleer, 1998) was selected. Based on the sub-pixel material map, surface albedo, leaf area index and object height data the simulation areas could automatically be described in the file format of the ENVI-met software. This saves tedious manual editing and therefore allowed to create 16 different simulation areas of 400 x 400 m covering 95 building blocks on which micro climate simulations were carried out. The hyperspectral products were able to describe the selected areas accurately. However, streets aligned with trees could not be represented very well because the tree crowns dominate the hyperspectral image and obscure the streets. Also errors in the height data caused some inaccuracies. The buildings were all modelled with flat roofs because inclined roofs cannot yet be modelled by ENVI-met nor represented by the available height data. The validation of the simulated climate parameters showed that the flat roofs did influence the simulated surface temperature. In addition, analysis revealed that the location of a building block within the simulation area in the ENVI-met model in combination with the fixed wind direction strongly influences the values of the simulated climate parameters. This demonstrates the need of accurate, area wide spatial information.

During the implementation of the conceptual framework in the case study of the city of Munich, several insights were gained regarding the potential of airborne hyperspectral data to support urban micro climate analysis and the applicability of the developed conceptual framework.

The hyperspectral data is not only able to provide standard products such as albedo and LAI, but also enables a detailed description of the study area by sub-pixel material mapping. Object height data is required for the mapping of the urban characteristics so as to analyse the urban micro climate. The use of a priori information on the building locations, either derived from height data or from the municipal vector data, enhances the accuracy of the sub-pixel material mapping significantly. The sub-pixel material map provides the possibility to assign the correct material to objects derived from the height data, even though small co-registration errors between the two data sets exists.

The conceptual framework has proven to be applicable to the case study. The full potential of the hyperspectral data could be used by deriving a large range of climate relevant input parameters and a highly detailed material map. The use of the remote sensing products saves valuable time for urban planners and climatologists because field surveys and manual inserting of input data in the micro climate model become mainly obsolete. The characterisation of the urban micro climate with the derived remote sensing products results in understandable maps and graphics at a suitable scale and with a large spatial extend, meeting the needs of urban planners. It is demonstrated how the spatial indicators and the micro climate simulation results can be combined to characterise the urban micro climate for urban structural types. Relating the urban micro climate system to these concepts well known to urban planners eases the communication between urban planners and climatologist. The conceptual framework was implemented in a se-

ries of largely automated steps. However, expert knowledge of both remote sensing specialists and climatologists is required for the meaningful use of remote sensing based micro climate information in urban planning.

Because of the satisfactory results of the case study, it is promising to expand the conceptual framework towards an operational approach. By doing this, urban planners can be provided with validated information on the micro climate characteristics of urban structural types in general and for the micro climate in selected building blocks.

Further research is primarily needed on the sensitivity of the micro climate model regarding the remote sensing products. Hereby also the location of the area of interest within the simulation area should be considered. To improve the usability of the micro climate characterisations for urban planning purposes, a more thorough accuracy assessment of the simulated climate parameters would be advantageous. The general relation between the building block characteristics and climate parameters should be studied for more cities as well, to support the use of these characteristics as climate indicators.

Although the accuracy of the remote sensing products was good, certain aspects can be enhanced. For the material map, the identification of streets below tree crowns is an important aspect which needs to be improved to meet the requirements of the ENVI-met model. Research into the use of multi-temporal leaf-on leaf-off images might be a way to do so. Improvements to the a priori information of building location and the quality of endmembers can increase the accuracy of the material map even more. For the leaf area index field measurements are required to assess the accuracy. Radiative transfer modelling of this parameter might be considered if the influence of this parameter on the ENVI-met model is large enough. More research on the surface albedo is required concerning the BRDF effect and its importance in the ENVI-met model. A BRDF-correction, e.g. as proposed in Feingersh et al. (2009), might be considered.

This thesis focused on the potential of reflective hyperspectral remote sensing. It would be interesting to explore the potential of hyperspectral sensors with additional thermal bands (e.g. ARES or TASI) as well. From the extra thermal information a better separation between surface materials can be expected. Additional products can be derived, which are useful input parameters for micro climate modelling, such as surface emissivity or heat storage capacity.

# Acknowledgements

# Bibliography

Ali-Toudert, F. and Mayer, H. (2007). Effects of asymmetry, galleries, overhanging facades and vegetation on thermal comfort in urban street canyons. *Solar Energy*, 81(6):742–754.

Arnfield, A. J. (2003). Two decades of urban climate research: a review of turbulence, exchanges of energy and water, and the urban heat island. *International Journal of Climatology*, 23:1–26.

Arthur-Hartranfta, S. T., Carlson, T. N., and Clarke, K. C. (2003). Satellite and ground-based microclimate and hydrologic analyses coupled with a regional urban growth model. *Remote Sensing of Environment*, 86:385–400.

Bachmann, M. (2007). *Automatisierte Ableitung von Bodenbedeckungsgraden durch MESMA-Entmischung*. PhD thesis, Julius-Maximilians-Universität Würzburg.

Bassani, C., Cavalli, R. M., Cavalcante, F., Cuomo, V., Palombo, A., Pascucci, S., and Pignatti, S. (2007). Deterioration status of asbestos-cement roofing sheets assessed by analyzing hyperspectral data. *Remote Sensing of Environment*, 109:361–378.

Bayerisches Staatsministerium für Umwelt, Gesundheit und Verbraucherschutz (2008). *Luftreinhalte-/Aktionsplan für die Stadt München, 2. Fortschreibung*. http://www.muenchen.info/pia/spezial/zweitefortschreibung.pdf. Date of access: 10-08-2009.

Ben-Dor, E., Levin, N., and Saaroni, H. (2001). A spectral based recognition of the urban environment using the visible and near-infrared spectral region (0.4-1.1$\mu$m). A case study over Tel-Aviv, Israel. *International Journal of Remote Sensing*, 22(11):2193–2218.

Ben-Dor, E. and Saaroni, H. (1997). Airborne video thermal radiometry as a tool for monitoring microscale structures of the urban heat island. *International Journal of Remote Sensing*, 18(14):3039–3053.

Benediktsson, J., Palmason, J., Sveinsson, J., and Chanussot, J. (2004). Decision level fusion in classification of hyperspectral data from urban areas. In *International Geoscience and Remote Sensing Symposium (IGARSS)*, volume 1, pages 73–76, St Martin d'Heres, France.

Berberoglu, S., Lloyd, C., Atkinson, P., and Curran, P. (2000). The integration of spectral and textural information using neural networks for land cover mapping in the mediterranean. *Computers and Geosciences*, 26:385–396.

Berlekamp, L.-R. and Pranzas, N. (1986). Methode zur Erfassung der Bodenversiegelung von städtischen Wohngebieten - ein Beitrag zu Hamburger Landschaftsprogramm. *Natur und Landschaft*, 61:92–95.

Bhaskaran, S., Datt, B., Forster, B., Neal, T., and Brown, M. (2004). Integrating imaging spectroscopy (445-2543 nm) and geographic information systems for post-disaster management: a case of hailstorm damage in Sydney. *International Journal of Remote Sensing*, 25(13):2625–2639.

Bochow, M., Peisker, T., Segl, K., and Kaufmann, H. (2006). Modelling of urban biotope types from hyperspectral imagery using a fuzzy logic approach. In *EARSeL SIG Remote Sensing of Land Use & Land Cover*.

Bochow, M., Segl, K., and Kaufmann, H. (2007a). Automating the build-up process of feature-based fuzzy logic models for the identification of urban biotopes from hyperspectral remote sensing data. In *Urban Remote Sensing Joint Event*, Paris, France.

Bochow, M., Segl, K., and Kaufmann, H. (2007b). An update system for urban biotope maps based on hyperspectral remote sensing data. In *Proceedings of the 5th EARSeL Workshop on Imaging Spectroscopy.*, Bruge, Belgium.

Borel, C., Ewald, K., Manzardo, M., Wamsley, C., and Jacobson, J. (2009). Adjoint radiosity based algorithms for retrieving target reflectances in urban area shadows. In Ben Dor, E., editor, *Proceedings of the 6th EARSeL Imaging Spectroscopy SIG Workshop*, Tel Aviv, Israel.

Bouyer, J., Vinet, J., Delpech, P., and Carré, S. (2007). Thermal comfort assessment in semi-outdoor environments: Application to comfort study in stadia. *Journal of Wind Engineering and Industrial Aerodynamics*, 95(9-11):963–976.

Breuste, J., Keidel, T., Meinel, G., Münchow, B., Netzban, M., and Schramm, M. (1996). Erfassung und Bewertung des Versiegelungsgrades befestigter Flächen. Technical Report 12/1996, UFZ-Umweltforschungszentrum.

BRIDGE (2009). *http://www.bridge-fp7.eu/*. Newsletter November 2009. Date of access: 19-01-2010.

Bruse, M. (2000). Anwendung von mikroskaligen simulationsmodellen in der stadtplanung. In Bernhard, L. and Küger, T., editors, *Simulation raumbezogener Prozesse: Methoden und Anwendung*. University of Münster.

Bruse, M. and Fleer, H. (1998). Simulating surface-plant-air interactions inside urban environments with a three dimensional numerical model. *Environmental Modelling and Software*, 13(3-4):373–384.

Bruzzone, L. and Carlin, L. (2006). A multilevel context-based system for classification of very high spation resolution images. *IEEE Transactions on Geoscience and Remote Sensing*, 44(9):2587–2600.

Bundesministerium für Bildung und Forschung (2009). *Forschung zu Klimaschutz und Klimawirkungen*. http://www.bmbf.de/de/8493.php. Date of access: 10-08-2009.

Bundesministerium für Verkehr, Bau und Stadtentwicklung (2009). *Baugesetzsbuch*. http://bundesrecht.juris.de/bbaug/BJNR003410960.html. Date of access: 10-08-2009.

Campbell, S. and Fainstein, S. S., editors (2003). *Readings in planning theory*. Blackwell Publishing, second edition.

Carlotto, M. J. (2009). Effect of errors in ground truth on classification accuracy. *International Journal of Remote Sensing*, 30(18):4831–4849.

Cavalli, R. M., Fusilli, L., Pascucci, S., Pignatti, S., and Santini, F. (2008). Hyperspectral sensor data capability for retrieving complex urban land cover in comparison with multispectral data: Venice city case study (Italy). *Sensors*, 8:3299–3320.

Chang, C. (2000). An information theoretic-based approach to spectral variability, similarity and disciminability for hyperspectral image analysis. *IEEE Transactions on Information Theory*, 46:1927–1932.

Chen, C.-M., Hepner, G., and Forster, R. (2003). Fusion of hyperspectral and radar data using the IHS transformation to enhance urban surface features. *ISPRS Journal of Photogrammetry and Remote Sensing*, 58:19–30.

Chen, J. and Hepner, G. F. (2001). Investigation of imaging spectroscopy for discriminating urban land covers and surface materials. In *AVIRIS Workshop Proceedings*, Pasadena CA, USA.

Chen, X. L., Zhao, H. M., Li, P. X., and Yin, Z. Y. (2006). Remote sensing image-based analysis of the relationship between urban heat island and land use/cover changes. *Remote Sensing of Environment*, 104(2):133–146.

Clarke, J. (2001). *Energy simulation and Building Design*. ButterworthHeinemann.

Cocks, T., Jenssen, R., Stewart, A., Wilson, I., and Shields, T. (1998). The hymap airborne hyperspectral sensor: the system, calibration and performance. In *Proceedings of the 1st EARSeL Workshop on Imaging Spectroscopy*, Zurich, Swiss.

Commission for Climatology (2009). *World Meteorological Organization*. http://www.wmo.int/. Date of access: 11-08-2009.

Congalton, R. G. (1991). A review of assessing the accuracy of classifications of remotely sensed data. *Remote Sensing of Environment*, 37(1):35–46.

Damm, A. (2008). *Hyperspektrale Fernerkundung zur Ableitung pflanzenphysiologischer Parameter von Stadtbäumen - Strahlungstransfermodellierung für Berliner Kastanienbestände*. PhD thesis, Humboldt-Universität zu Berlin - Geographisches Institut.

Danson, F. M. and Plummer, S. E. (1995). Red-edge response to forest leaf area index. *International Journal of Remote Sensing*, 16(1):183–188.

Dell'Acqua, F., Gamba, P., and Trianni., G. (2005). A preliminary study on separability of paving materials in shadowed hyperspectral pixels from a central urban area. In Moeller, M. and Wentz, E., editors, *ISPRS Joint Conferences - 3rd International Symposium Remote Sensing and Data Fusion Over Urban Areas (URBAN 2005) and 5th International Symposium Remote Sensing of Urban Areas (URS 2005)*, Tempe AZ, USA.

145

Deutsche Meteorologische Gesellschaft (2007). *Stellingnahme der Deutschen Meteorologischen Gesellschaft zur Klimaproblematik, 09.10.2007.* www.dmg-ev.de/gesellschaft/stellungnahmen/Klimastatement_dmg_2007_09_10_c2.pdf. Date of access: 10-12-2009.

Deutscher Wetterdienst (2009). *Der KLIMA-Report 2008*. http://www.dwd.de. Date of access: 19-01-2010.

Dorigo, W. (2007). *Retrieving canopy variables by radiative transfer model inversion. A regional approach for imaging spectrometer data.* PhD thesis, Technischen Universität München.

Dorigo, W., Bachmann, M., and Heldens, W. (2006). *AS Toolbox & Processing of field spectra.* German Aerospace Center (DLR), German Remote Sensing Data Center. Version 1.12.

Durieux, L., Lagabrielle, E., and Nelson, A. (2008). A method for monitoring building construction in urban sprawl areas using object-based analysis of Spot 5 images and existing GIS data. *ISPRS Journal of Photogrammetry and Remote Sensing*, 63(4):399–408.

Eichhorn, J. (1989). *Entwicklung und Anwendung eines dreidimensionalen mikroskaligen Stadtklima-Modells*. PhD thesis, University of Mainz.

Eliasson, I. (2000). The use of climate knowledge in urban planning. *Landscape and Urban Planning*, 48:31–44.

Eliasson, I., Offerle, B., Grimmond, C., and Lindqvist, S. (2006). Wind fields and turbulence statistics in an urban street canyon. *Atmospheric Environment*, 40(1):1–16.

Esch, T., Himmler, V., Schorcht, G., Thiel, M., Wehrmann, T., Bachofer, F., Conrad, C., Schmidt, M., and Dech, S. (2009a). Large-area assessment of impervious surface based on integrated analysis of single-date Landsat-7 images and geospatial vector data. *Remote Sensing of Environment*, 113:1678–1690.

Esch, T., Taubenböck, H., Heldens, W., Thiel, M., Wurm, M., Klein, D., Dech, S., Roth, A., and Schmidt, M. (2009b). Monitoring and assessment of urban environments using space-borne earth observation data. In Krek, Rumor, Ziatanova, and Fendels, editors, *Urban and Regional Data Management*, pages 385–398, Ljubljana, Slovenia. Taylor & Francis Group.

Fan, H. and Sailor, D. J. (2005). Modeling the impacts of anthropogenic heating on the urban climate of Philadelphia: a comparison of implementations in two PBL schemes. *Atmospheric Environment*, 39(1):73–84.

Fanger, P. (1970). *Thermal Comfort - Analysis and Applications in Environmental Engineering*. McGraw-Hill Book Co., New York.

Fehrenbach, U., Scherer, D., and Parlow, E. (2001). Automated classification of planning objectives for the consideration of climate and air quality in urban and regional planning for the example of the region of Basel/Switzerland. *Atmospheric Environment*, 35:5605–5615.

Feingersh, T., Schläpfer, D., and Ben-Dor, E. (2009). BREF-COR – Towards operational BRDF correction for imaging spectrometer data. In Ben Dor, E., editor, *Proceedings of the 6th EARSeL Imaging Spectroscopy SIG Workshop*, Tel Aviv, Israel.

Fischer, H. S. (2002). *Flächencharakterisierung der im Rahmen der Stadtbiotopkartierung erfassten Struktureinheiten*. Ifanos Landschaftsökologie, im Auftrag der Landeshauptstadt München.

Foody, G. M. (2002). Status of land cover classification accuracy assessment. *Remote Sensing of Environment*, 80:186–201.

Franke, J., Roberts, D. A., Halligan, K., and Menz, G. (2009). Hierarchical Multiple Endmember Spectral Mixture Analysis (MESMA) of hyperspectral imagery for urban environments. *Remote Sensing of Environment*, 113:1678–1690.

Frey, C., Rigo, G., and Parlow, E. (2007). Urban radiation balance of two coastal cities in a hot and dry environment. *International Journal of Remote Sensing*, 28:2695–2712.

Gamba, P., Dell'Aqua, F., Lisini, G., and Trianni, G. (2007). Improved VHR urban area mapping exploiting object boundaries. *IEEE Transactions on Geoscience and Remote Sensing*, 45:2676–2682.

Gluch, R., Quattrochi, D. A., and Luvall, J. C. (2006). A multi-scale approach to urban thermal analysis. *Remote Sensing of Environment*, 104(2):123–132.

Gómez, F., Tamarit, N., and Jabaloyes, J. (2001). Green zones, bioclimatics studies and human comfort in the future development of urban planning. *Landscape and Urban Planning*, 55(3):151–161.

Gomez-Chova, L., Fernández-Prieto, D., Calpe, J., Soria, E., Vila, J., and Camps-Valls, G. (2006). Urban monitoring using multi-temporal sar and multi-spectral data. *Pattern Recognition Letters*, 27(4):234–243.

Govaerts, Y., Lattanzio, A., Taberner, M., and Pinty, B. (2008). Generating global surface albedo products from multiple geostationary satellites. *Remote Sensing of Environment*, 112(6):2804–2816.

Greiwe, A., Bochow, M., and Ehlers, M. (2004). Segmentbasierte Fusion geometrisch hochaufgelöster und hyperspektraler Daten zur Verbesserung der Klassifikationsgüte am Beispiel einer urbane Szene. *Photogrammetrie, Fernerkundung, GeoInformation*, 6.

Guyot, G.and Baret, F. and Major, D. (1988). High spectral resolution: determination of spectral shifts between the red and the near infrared. *International Archives of Photogrammetry and Remote Sensing*, 11:750–760.

Habermeyer, M., Marschalk, U., and Roth, A. (2008). Digital elevation model database W42 - A scalable system for spatial data. In *The International Archives of the Photogrammetry, Remote Sensing and Spatial Information Sciences, International Society for Photogrammetry and Remote Sensing, ISPRS Conference 2008*, Peking, China.

Haboudane, D., Miller, J. R., Pattey, E., Zarco-Tejada, P. J., and Strachan, I. B. (2004). Hyperspectral vegetation indices and novel algorithms for predicting green LAI of crop canopies: Modeling and validation in the context of precision agriculture. *Remote Sensing of Environment*, 90(3):337–352.

Hanschke, U. and Beddig, D. (2005). *Flächentypen. Eine Beschreibung der im Informationssystem Stadt und Umwelt (ISU) der Sensatsverwaltung für Stadtentwickelung erfassten und verwalteten Struktur- und Flächennutzungskategorien von Berlin.* Senatsverwaltung für Stadtentwicklung, III F, Berlin.

Heber, B. and Lehmann, I. (1993). Stadtstrukturelle Orientierungswerte für die Bodenversiegelung in Wohngebieten. Technical Report 05-1993, Institut für Ökologische Raumentwicklung e.V. Dresden.

Heiden, U. (2004). *Analyse hyperspektraler Flugzeugscannerdaten zur ökologischen Charakterisierung städtischer Biotope.* PhD thesis, Technischen Universität Berlin.

Heiden, U., Segl, K., Roessner, S., and Kaufmann, H. (2007). Determination of robust spectral features for identification of urban surface materials in hyperspectral remote sensing data. *Remote Sensing of Environment*, 111:537–552.

Helbig, A., Baumüller, J., and Kerschgens, M., editors (1999). *Stadtklima und Luftreinhaltung.* Springer Verlag, second edition.

Heldens, W., Esch, T., Heiden, U., and Dech, S. (2008). Potential of hyperspectral remote sensing for characterisation of urban structure in munich. In Jürgens, C., editor, *Remote Sensing - New Challenges of High Resolution. Proceedings of the EARSeL Joint Workshop Bochum, March 5-7 2008*, pages 94–103, Bochum, Germany. CD-ROM.

Heldens, W., Esch, T., Heiden, U., Müller, A., and Dech, S. (2009a). Exploring the demands on hyperspectral data products for urban planning: a case study in the Munich region. In Ben Dor, E., editor, *Proceedings of the 6th EARSeL Imaging Spectroscopy SIG Workshop*, Tel Aviv, Israel.

Heldens, W., Heiden, U., Bachmann, M., Esch, T., Müller, A., and Dech, S. (2009b). Scaling issues in validation of abundance maps derived from hymap data of and urban area. In Ben Dor, E., editor, *Proceedings of the 6th EARSeL Imaging Spectroscopy SIG Workshop*, Tel Aviv, Israel.

Henry, J. A. and Dicks, S. E. (1987). Association of urban temperatures with land use and surface materials. *Landscape and Urban Planning*, 14:21–29.

Hepner, G. F., Houshmand, B., Kulikov, I., and Bryant, N. (1998). Investigation of the integration of AVIRIS and IFSAR for urban analysis. *Photogrammetric Engineering and Remote Sensing*, 64(8):813–820.

Herold, M., Gardner, M. E., and Roberts, D. A. (2003a). Spectral resolution requirements for mapping urban areas. *IEEE Transactions on Geoscience and Remote Sensing*, 41(9):1907–1919.

Herold, M., Liu, X., and Clarke, K. C. (2003b). Spatial metrics and image texture for mapping urban land use. *Photogrammetric Engineering and Remote Sensing*, 69:991–1001.

Herold, M. and Roberts, D. (2005). Spectral characteristics of asphalt road aging and detoration: implications for remote-sensing applications. *Applied Optics*, 44(20):4327–4334.

Herold, M., Roberts, D. A., Gardner, M. E., and Dennison, P. E. (2004). Spectrometry for urban area remote sensing - development and analysis of a spectral library from 350 to 2400 nm. *Remote Sensing of Environment*, 91:304–319.

Hidding, M., Van den Brink, A., Heinen, J., and Kragting, J. (2002). *Planning voor stad en land*. Uitgeverij Coutinho, second, revised edition.

Hien, W. N. and Jusuf, S. K. (2008). GIS-based greenery evaluation on campus master plan. *Landscape and Urban Planning*, 84(2):166–182.

Höppe, P. (1999). The physiological equivalent temperature - a universal index for the biometeorological assessment of the thermal environment. *International Journal of Biometeorology*, 43(2):71–75.

Hoyano, A., Iino, A., Ono, M., and Tanighchi, S. (1999). Analysis of the influence of urban form and materials on sensible heat flux - a case study of Japan's largest housing development 'Tama New Town'. *Atmospheric Environment*, 33:3931–3939.

Huang, J., Lu, X., and Sellers, J. M. (2007). A global comparative analysis of urban form: Applying spatial metrics and remote sensing. *Landscape and Urban Planning*, 82:184–197.

Huete, A. (1988). A soil-adjusted vegetation index (SAVI). *Remote Sensing of Environment*, 83:195–213.

Hughes, G. (1968). On the mean accuracy of statistical pattern recognizers. *IEEE Transactions on Information Theory*, 14:55–63.

Inglada, J. (2007). Automatic recognition of man-made objects in high resolution optical remote sensing images by SVM classification of geometric image features. *ISPRS Journal of Photogrammetry and Remote Sensing*, 62(3):236–248.

ITT Visual Information Solutions (2007). *IDL 7.0 and ENVI 4.5 Users' Guide*.

Jacquemoud, S. and Baret, F. (1990). PROSPECT: A model of leaf optical properties spectra. *Remote Sensing of Environment*, 34:75–91.

Jacquemoud, S., Verhoef, W., Baret, F., Bacour, C., Zarco-Tejada, P., Asner, G., François, C., and Ustin, S. (2009). PROSPECT + SAIL models: A review of use for vegetation characterization. *Remote Sensing of Environment*, 113:S56 – S66.

Jain, S. and Jain, R. K. (2006). A remote sensing approach to establish relationships among different land covers at the micro level. *International Journal of Remote Sensing*, 27(13):2667–2682.

Jat, M. K., Garg, P. K., and Khare, D. (2008). Modelling of urban growth using spatial analysis techniques: a case study of Ajmer city (India). *International Journal of Remote Sensing*, 29(2):543–567.

Jenerette, G. D., Harlan, S. L., Brazel, A., Jones, N., Larsen, L., and Stefanov, W. L. (2007). Regional relationships between surface temperature, vegetation, and human settlement in a rapidly urbanizing ecosystem. *Landscape Ecology*, 22(3):353–365.

Jung, A., Tökei, L., and Kardeván, P. (2007). Application of airborne hyperspectral and thermal images to analyse urban microclimate. *Applied Ecology and Environmental Research*, 5:165–175.

Karssenberg, D. and De Jong, K. (2005). Dynamic environmental modelling in GIS: 1. Modelling in three spatial dimensions. *International Journal of Geographical Information Science*, 19(5):559–579.

Kato, S. and Yamaguchi, Y. (2007). Estimation of storage heat flux in an urban area using ASTER data. *Remote Sensing of Environment*, 110(1):1–17.

Klein, D., Esch, T., Heldens, W., Himmler, V., and Schmidt, M. (2009). Zum Stand der Flächeninanspruchnahme in Deutschland – Neue Beobachtungstechniken und Ergebnisse des Refina-Projekts Flächenbarometer. In Deutsches Institut für Urbanistik (Difu), editor, *Methoden und Konzepte zur Flächen- und Standortbewertung für ein nachhaltiges Flächenmanagement -REFINA-Veröffentlichungsreihe B̈eiträge aus der REFINA-Forschung; Band 2.*, Berlin.

Klein, D., Klein, R., Wettemann, J., Heldens, W., Himmler, V., and Esch, T. (2010). Entwicklund und Evaluierung eines Flächenbarometes als Grundlage für ein nachhaltiges Flächenmanagement. Endbericht.

Kleinschmit, B., Hostert, P., Coenradie, B., Haag, L., and Damm, A. (2007). Entwicklung und Umsetzung eines hybriden Verfahrensansatzes zur Versiegelungskartierung in Berlin. Technical report, Senatsverwaltung für Stadtentwicklung.

Knox, P. L. and Marston, S. A. (2001). *Places and regions in global context: human geography*. Prentice Hall, Inc., second edition.

Knyazikhin, Y., Glassy, J., Privette, J. L., Tian, Y., Lotsch, A., Zhang, Y., Wang, Y., Morisette, J. T., Votava, P., Myneni, R., Nemani, R. R., and Running, S. W. (1999). *MODIS Leaf Area Index (LAI) and Fraction of Photosynthetically Active Radiation Absorbed by Vegetation (FPAR) Product (MOD15)*. http://modis.gsfc.nasa.gov/data/atbd/atbd_mod15.pdf. Algorithm Theoretical Basis Document. Date of access: 20-01-2010.

Kolokotroni, M. and Giridharan, R. (2008). Urban heat island intensity in London: An investigation of the impact of physical characteristics on changes in outdoor air temperature during summer. *Solar Energy*, 82:986–998.

Kötz, B. (2006). *Estimating biophysical and biochemical properties over heterogeneous vegetation canopies. Radiative transfer modeling in forest canopies based on imaging spectrometry and LIDAR.* PhD thesis, Universität Zürich.

Krayenhoff, E. S. and Voogt, J. A. (2007). A microscale three-dimensional urban energy balance model for studying surface temperatures. *Boundary-Layer Meteorology*, 123:433–461.

Kruse, F., Lefkoff, A., Boardman, J., Heidebrecht, K., Shapiro, A., Barloon, P., and Goetz, A. (1993). The spectral image processing system (SIPS)–interactive visualization and analysis of imaging spectrometer data. *Remote Sensing of Environment*, 44(2-3):145–163.

Kurz, F., Müller, R., Stephani, M., Reinartz, P., and Schroeder, M. (2007). Calibration of a wide angle digital camera system for near real time scenarios. In Heipke, C., Jacobsen, K., and Gerke, M., editors, *ISPRS Workshop 2007, High Resolution Earth Imaging for Geospatial Information*, Hannover, Germany.

Kuttler, W. (1998). Stadtklima. In Sukkop, H. and Wittig, R., editors, *Stadtökologie*, pages 125–167. Gustav Fischer Verlag.

Kuttler, W. (2004). Stadtklima. Teil 1: Grundzüge und Ursachen. *Beitragsserie: Klimaänderung und Klimaschutz*, pages 1–13.

Lacherade, S., Miesch, C., Briottet, X., and Le Men, H. (2005). Spectral variability and bidirectional reflectance behaviour of urban materials at a 20 cm spatial resolution in the visible and near-infrared wavelengths. A case study over Toulouse (France). *International Journal of Remote Sensing*, 26:3859 – 3866.

Lalic, B. and Mihailovic, D. T. (2004). An empirical relation describing leaf-area density inside the forest for environmental modeling. *Journal of Applied Meteorology*, 43(4):641–645.

Lauk, C. (2009). *Mikroklimasimulation am Beispiel der Fraunhofer Freilandversuchsstelle in Holzkirchen.* Master's thesis, Universität Stuttgart.

Lechner, A. M., Stein, A., Jones, S. D., and Ferwerda, J. G. (2009). Remote sensing of small and linear features: Quantifying the effects of patch size and length, grid position and detectability on land cover mapping. *Remote Sensing of Environment*, 113(10):2194–2204.

Lee, S. and Lathrop, R. G. (2005). Sub-pixel estimation of urban land cover components with linear mixture model analysis and Landsat Thematic Mapper imagery. *International Journal of Remote Sensing*, 26(22):4885–4905.

Lillesand, T. M., Kiefer, R. W., and Chipman, J. W. (2004). *Remote Sensing and Image Interpretation.* Wiley International, fifth edition.

Liu, J., Chen, J., Cihlar, J., and Park, W. (1997). A process-based boreal ecosystem productivity simulator using remote sensing inputs. *Remote Sensing of Environment*, 62:158–175.

Lizarazo, I. (2008). SVM-based segmentation and classification of remotely sensed data. *International Journal of Remote Sensing*, 29(24):7277–7283.

151

Lu, D. S. and Weng, Q. H. (2006). Use of impervious surface in urban land-use classification. *Remote Sensing of Environment*, 102(1-2):146–160.

Madhavan, B. B., Kubo, S., Kurisaki, N., and Sivakumar, T. V. L. N. (2001). Appraising the anatomy and spatial growth of the Bangkok Metropolitan area using a vegetation-impervious-soil model through remote sensing. *International Journal of Remote Sensing*, 22(5):789–806.

Madhok, V. and Landgrebe, D. (1999). Supplementing hyperspectral data with digital elevation. In *IGARSS'99*, volume I, pages 59–61, Hamburg, Germany.

Mayer, H. (1999). Air pollution in cities. *Atmospheric Environment*, 33(24-25):4029–4037.

Mayer, S. (2004). *Automatisierte Objekterkennung zur Interpretation hochauflösender Bilddaten in der Erdfernerkundung*. PhD thesis, Humboldt-Universität zu Berlin.

Müller, R., Holzwarth, S., Habermeyer, M., and Müller, A. (2005). Ortho image production within an automatic processing chain for the hyperspectral airborne scanner ares. In *Proceedings of the EARSeL Workshop 3D-Remote Sensing*, Porto, Portugal.

National Physics Laboratory (2009). *Kaye & Laby. Tables of physical & chemical constants*. http://www.kayelaby.npl.co.uk. Date of access: 23-09-2009.

Niemann, K., Goodenough, D., Marceau, D., and Hay, G. (1998). Practical alternative for fusion of hyperspectral data with high resolution imagery. In *International Geoscience and Remote Sensing Symposium (IGARSS)*, volume 1, pages 174–176, Victoria, Canada.

Offerle, B., Eliasson, I., Grimmond, C., and Holmer, B. (2007). Surface heating in relation to air temperature, wind and turbulence in an urban street canyon. *Boundary-Layer Meteorology*, 122:273–292.

Oke, T. (1987). *Boundary layer climates*. Routledge, New York.

Oke, T. (2006). Towards better scientific communication in urban climate. *Theoretical and Applied Climatology*, 84:179 – 190.

Oke, T. R. (1988). Street design and urban canopy layer climate. *Energy and Buildings*, 11(1-3):103–113.

Pauleit, S. (1998). *Das Umweltwirkgefüge städtischer Siedlungsstrukturen: Darstellung des städtischen Ökosystem durch eine Strukturtypenkartierung zur Bestimmung von Umweltqualitätszielen für die Stadtplanung*. PhD thesis, Technische Universität München.

Pauleit, S. and Duhme, F. (2000a). Assessing the environmental performance of land cover types for urban planning. *Landscape and Urban Planning*, 52(1):1–20.

Pauleit, S. and Duhme, F. (2000b). GIS assessment of Munich's urban forest structure for urban planning. *Journal of Arboriculture*, 26:133–141.

Pearson, R. and Miller, L. (1972). Remote mapping of standing crop biomass for estimation of the productivity of the short-grass prairie, Pawnee National Grasslands, Colorado. In *Proceedings of the 8th International Symposium on Remote Sensing of Environment, ERIM International*, pages 1357–1381, Ann Arbor MI, USA.

Pena, M. A. (2008). Relationships between remotely sensed surface parameters associated with the urban heat sink formation in santiago, chile. *International Journal of Remote Sensing*, 29(15):4385–4404.

Pickup and Dear (1999). An outdoor thermal confort index (OUT-SET*). Part 1 - The model and its assumptions. In *Proceedings of the 15th International Congress on Biometeorology and International Conference on Urban Climatology*, Sydney, Australia.

Pinty, B., Lavergne, T., Dickinson, R. E., Widlowski, J. L., Gobron, N., and Verstraete, M. M. (2006). Simplifying the interaction of land surfaces with radiation for relating remote sensing products to climate models. *Journal of Geophysical Research-Atmospheres*, 111:D02116.

Plaza, A., Martinez, P., Perez, R., and Plaza, J. (2004). A new approach to mixed pixel classification of hyperspectral imagery based on extended morphological profiles. *Pattern Recognition*, 37:1097–1116.

Pontius, R. and Cheuk, M. (2006). A generalized cross-tabulation matrix to compare soft-classified maps at multiple resolutions. *International Journal of Geographical Information Science*, 20(1):1–30.

Powell, R. L., Matzke, N., de Souza, C., Clark, M., Numata, I., Hess, L. L., and Roberts, D. A. (2004). Sources of error in accuracy assessment of thematic land-cover maps in the brazilian amazon. *Remote Sensing of Environment*, 90(2):221–234.

Powell, R. L., Roberts, D. A., Dennison, P. E., and Hess, L. L. (2007). Sub-pixel mapping of urban land cover using multiple endmember spectral mixture analysis: Manaus, brazil. *Remote Sensing of Environment*, 106(2):253–267.

Pu, R., Gong, P., Michishita, R., and Sasagawa, T. (2008). Spectral mixture analysis for mapping abundance of urban surface components from the Terra/ASTER data. *Remote Sensing of Environment*, 112(3):939–954.

Qi, J., Chehbouni.A, Huete, A., Kerr, Y., and Sorooshian, S. (1994). A modified soil adjusted vegetation index. *Remote Sensing of Environment*, 48:119–126.

Quattrochi, D. A. and Ridd, M. K. (1994). Measurement and analysis of thermal-energy responses from discrete urban surfaces using remote-sensing data. *International Journal of Remote Sensing*, 15(10):1991–2022.

Richter, R. (2007). *ATCOR 3 User Guide*. DLR - German Aerospace Centre, Remote Sensing Data Centre, Oberpfaffenhofen, Germany.

Richter, R. and Müller, A. (2005). De-shadowing of satellite/airborne imagery. *International Journal of Remote Sensing*, 26(15):3137–3148.

Ridd, M. K. (1995). Exploring a V-I-S (Vegetation-Impervious Surface-Soil) model for urban ecosystem analysis through remote-sensing - comparative anatomy for cities. *International Journal of Remote Sensing*, 16(12):2165–2185.

Rigo, G. and Parlow, E. (2007). Modelling the ground heat flux of an urban area using remote sensing data. *Theoretical and Applied Climatology*, 90:185–199.

Roberts, D. A., Gardner, M., Church, R., Ustin, S., Scheer, G., and Green, R. O. (1998). Mapping chaparral in the Santa Monica Mountains using multiple endmember spectral mixture models. *Remote Sensing of Environment*, 65(3):267–279.

Roberts, D. A. and Herold, M. (2004). Imaging spectrometry of urban materials. In King, P., Ramsey, M., and Swayze, G., editors, *Infrared Spectroscopy in Geochemistry, Exploration and Remote Sensing*, volume 33, pages 155–181, London, Ontario. Mineral Association of Canada.

Roessner, S., Segl, K., Heiden, U., and Kaufmann, H. (2001). Automated differentiation of urban surfaces based on airborne hyperspectral imagery. *IEEE Transactions on Geoscience and Remote Sensing*, 39(7):1525–1532.

Rouse, J., Haas, R., Schell, J., and Deering, J. (1973). Monitoring vegetation systems in the Great Plains with ERTS. In *Proceedings of the Third Symposium on Significant Results Obtained with ERTS*, pages 309–317.

Samaali, M., Courault, D., Bruse, M., Olioso, A., and Occelli, R. (2007). Analysis of a 3D boundary layer model at local scale: Validation on soybean surface radiative measurements. *Atmospheric Research*, 85(2):183–198.

Schaepman-Strub, G., Schaepman, M., Painter, T., Dangel, S., and Martonchik, J. (2006). Reflectance quantities in optical remote sensing - definitions and case studies. *Remote Sensing of Environment*, 103:27–42.

Schiefer, S., Hostert, P., and Damm, A. (2005). Analysis of view-angle effects in hyperspectral data of urban areas. In Moeller, M. and Wentz, E., editors, *ISPRS Joint Conferences - 3rd International Symposium Remote Sensing and Data Fusion Over Urban Areas (URBAN 2005) and 5th International Symposium Remote Sensing of Urban Areas (URS 2005)*, volume XXXVI, Tempe AZ, USA.

Schläpfer, D. and Richter, R. (2002). Geo-atmospheric processing of airborne imaging spectrometry data. part 1: parametric orthorectification. *International Journal of Remote Sensing*, 23(13):2609–2630.

Scholten, F., Gwinner, K., Tauch, R., and Boulgakova, O. (2003). HRSC-AX - high-resolution orthoimages and digital surface models for urban regions. In *Proceedings of the 2nd GRSS/ISPRS Joint Workshop on Remote Sensing and Data Fusion over Urban Areas (URBAN 2003).*, pages 225–229, Berlin, Germany.

Schowengerdt, R. A. (1997). *Remote Sensing. Models and methods for Image Processing.* Academic Press, second edition.

Scurlock, J., Asner, G., and Gower, S. (2001). Worldwide historical estimates and bibliography of leaf area index, 1932-2000. ORNL Technical Memorandum TM-2001/268. Oak Ridge National Laboratory, Oak Ridge, Tennessee, U.S.A.

Segl, K., Roessner, S., Heiden, U., and Kaufmann, H. (2003). Fusion of spectral and shape features for identification of urban surface cover types using reflective and thermal hyperspectral data. *ISPRS Journal of Photogrammetry and Remote Sensing*, 58:99–112.

Shashua-Bar, L., Tzamir, Y., and Hoffman, M. E. (2004). Thermal effects of building geometry and spacing on the urban canopy layer microclimate in a hot-humid climate in summer. *International Journal of Climatology*, 24:1729–1742.

Silvan-Cardenas, J. and Wang, L. (2008). Sub-pixel confusion-uncertainty matrix for assessing soft classifications. *Remote Sensing of Environment*, 112(3):1081–1095.

Small, C. (2001). Spectral dimensionality and scale of urban radiance. In *AVIRIS Workshop Proceedings*, Pasadena CA, USA.

Small, C. (2003). High spatial resolution spectral mixture analysis of urban reflectance. *Remote Sensing of Environment*, 88:170–186.

Small, C. (2006). Comparative analysis of urban reflectance and surface temperature. *Remote Sensing of Environment*, 104:168–189.

Song, M., Civco, D. L., and Hurd, J. D. (2005). A competitive pixel-object approach for land cover classification. *International Journal of Remote Sensing*, 26:4981–4997.

Soudani, K., Francois, C., le Maire, G., Le Dantec, V., and Dufrene, E. (2006). Comparative analysis of IKONOS, SPOT, and ETM+ data for leaf area index estimation in temperate coniferous and deciduous forest stands. *Remote Sensing of Environment*, 102(1-2):161–175.

Stein, E. (2009). *Entwicklung einer merkmalsbasierten Klassifikation für urbane Räume unter Verwendung von Hyperspektraldaten am Beispiel der Stadt München*. Master's thesis, Friedrich-Schiller-Universität Jena.

Stein, E., Bachmann, M., Heldens, W., Müller, A., and Schmullius, C. (2009). A spectral feature based classification algorithm for characterisation of urban surfaces in Munich. In Ben Dor, E., editor, *Proceedings of the 6th EARSeL Imaging Spectroscopy SIG Workshop*, Tel Aviv, Israel.

Stone, B. and Norman, J. M. (2006). Land use planning and surface heat island formation: A parcel-based radiation flux approach. *Atmospheric Environment*, 40(19):3561–3573.

Su, W., Li, J., Chen, Y., Liu, Z., Zhang, J., Low, T. M., Suppiah, I., and Hashim, S. A. M. (2008). Textural and local spatial statistics for the object-oriented classification of urban areas using high resolution imagery. *International Journal of Remote Sensing*, 29(11):3105–3117.

Sukkop, H. and Wittig, R., editors (1998). *Stadtökologie. Ein Fachbuch für Studium und Praxis*. Gustav Fischer, second edition.

Technical University of Munich, Meteorological Institut. */www.meteo.physik.uni-muenchen.de*. Date of access: 20-9-2009.

Terjung, W. H. and O'Rourke, P. A. (1980). Simulating the causal elements of urban heat islands. *Boundary-Layer Meteorology*, 19(1):93–118.

United Nations (2007). *Urban Population, Development and the Environment*. Economic and Social Affairs, Population Devision.

Van de Voorde, T., De Roeck, T., and Canters, F. (2009). A comparison of two spectral mixture modelling approaches for impervious surface mapping in urban areas. *International Journal of Remote Sensing*, 30(18):4785–4806.

Van der Linden, S. (2008). *Investigating the potential of hyperspectral remote sensing data for the analysis of urban imperviousness - a Berlin case study*. PhD thesis, Humboldt-Universität zu Berlin.

Van der Linden, S. and Hostert, P. (2009). The influence of urban structures on impervious surface maps from airborne hyperspectral data. *Remote Sensing of Environment*, 113(11):2298–2305.

Van der Linden, S., Janz, A., Waske, B., Eiden, M., and Hostert, P. (2007). Classifying segmented hyperspectral data from a heterogeneous urban environment. *Journal of Applied Remote Sensing*, 1:013543.

Van der Meer, F. (2004). Analysis of spectral absorption features in hyperspectral imagery. *International Journal of Applied Earth Observation*, 5:55–68.

Van der Meer, F. (2006). The effectiveness of spectral similarity measures for the analysis of hyperspectral imagery. *International Journal of Applied Earth Observation and Geoinformation*, 8(1):3–17.

Van der Meer, F. and de Jong, S. M., editors (2003). *Imaging Spectrometry*. Remote sensing and digital image processing. Kluwer Academic Press.

Voogt, J. A. and Oke, T. R. (2003). Thermal remote sensing of urban climates. *Remote Sensing of Environment*, 86(3):370–384.

Wang, Q., Adiku, S., Tenhunen, J., and Granier, A. (2005). On the relationship of NDVI with leaf area index in a deciduous forest site. *Remote Sensing of Environment*, 94(2):244–255.

Wang, Y. Y. and Li, J. (2008). Feature-selection ability of the decision-tree algorithm and the impact of feature-selection/extraction on decision-tree results based on hyperspectral data. *International Journal of Remote Sensing*, 29(10):2993–3010.

Wania, A. (2007). *Urban vegetation - detection and function evaluation for air quality assessment*. PhD thesis, Louis Pasteur University, Strassbourg.

Welch, R. (1982). Spatial resolution requirements for urban studies. *International Journal of Remote Sensing*, 3:139–146.

Wende, W., Huelsmann, W., Marty, M., Penn-Bressel, G., and Bobylev, N. (2009). Climate protection and compact urban structures in spatial planning and local construction plans in Germany. *Land Use Policy*, In press.

Weng, Q. (2009). Thermal infrared remote sensing for urban climate and environmental studies: Methods, applications, and trends. *ISPRS Journal of Photogrammetry and Remote Sensing*, 64(4):335–344.

Weng, Q., Hu, X., and Lu, D. (2008). Extracting impervious surfaces from medium spatial resolution multispectral and hyperspectral imagery: a comparison. *International Journal of Remote Sensing*, 29(11):3209–3232.

Weng, Q., Lu, D., and Schubring, J. (2004). Estimation of land surface temperature-vegetation abundance relationship for urban heat island studies. *Remote Sensing of Environment*, 89(4):467–483.

Weng, Q. and Quattrochi, D. A. (2006). Editorial: Thermal remote sensing of urban areas: An introduction to the special issue. *Remote Sensing of Environment*, 104:119–122.

Weng, Q. H. (2001). Modeling urban growth effects on surface runoff with the integration of remote sensing and GIS. *Environmental Management*, 28(6):737–748.

Weng, Q. H. and Yang, S. H. (2006). Urban air pollution patterns, land use, and thermal landscape: An examination of the linkage using GIS. *Environmental Monitoring and Assessment*, 117(1-3):463–489.

Wu, C. (2009). Quantifying high-resolution impervious surfaces using spectral mixture analysis. *International Journal of Remote Sensing*, 30(11):2915–2932.

Wu, C. and Murray, A. T. (2003). Estimating impervious surface distribution by spectral mixture analysis. *Remote Sensing of Environment*, 84(4):493–505.

Wurm, M., Taubenböck, H., Roth, A., and Dech, S. (2009). Urban structuring using multisensoral remote sensing data - by the example of german cities - cologne and dresden. In *Urban Remote Sensing Joint Event*, Shanghai, China.

www.envi met.com. Date of access: 20-9-2009.

www.münchen.de. Date of access: 25-1-2010.

Xian, G. (2008). Satellite remotely-sensed land surface parameters and their climatic effects for three metropolitan regions. *Advances in Space Research*, 41(11):1861–1869.

Xian, G. and Crane, M. (2006). An analysis of urban thermal characteristics and associated land cover in Tampa Bay and Las Vegas using Landsat satellite data. *Remote Sensing of Environment*, 104(2):147–156.

Xiao, R.-b., Ouyang, Z.-y., Zheng, H., Li, W.-f., Schienke, E. W., and Wang, X.-k. (2007). Spatial pattern of impervious surfaces and their impacts on land surface temperature in Beijing, China. *Journal of Environmental Sciences*, 19(2):250–256.

Xu, W., Wooster, M., and Grimmond, C. (2008). Modelling of urban sensible heat flux at multiple spatial scales: A demonstration using airborne hyperspectral imagery of Shanghai and a temperature-emissivity separation approach. *Remote Sensing of Environment*, 112:3493–3510.

Yoshida, H. and Omae, M. (2005). An approach for analysis of urban morphology: methods to derive morphological properties of city blocks by using an urban landscape model and their interpretations. *Computers, Environment and Urban Systems*, 29(2):223–247.

Yuan, F. and Bauer, M. E. (2007). Comparison of impervious surface area and normalized difference vegetation index as indicators of surface urban heat island effects in Landsat imagery. *Remote Sensing of Environment*, 106(3):375–386.

Zha, Y., Gao, J., and Ni, S. (2003). Use of normalized difference built-up index in automatically mapping urban areas from TM imagery. *International Journal of Remote Sensing*, 24(3):583–594.

Zhang, X., Zhong, T., Feng, X., and Wang, K. (2009a). Estimation of the relationship between vegetation patches and urban land surface temperature with remote sensing. *International Journal of Remote Sensing*, 30(8):2105–2118.

Zhang, Y., Odeh, I. O., and Han, C. (2009b). Bi-temporal characterization of land surface temperature in relation to impervious surface area, NDVI and NDBI, using a sub-pixel image analysis. *International Journal of Applied Earth Observation and Geoinformation*, 11:256–264.

Zheng, G. and Moskal, L. M. (2009). Retrieving leaf area index (LAI) using remote sensing: Theories, methods and sensors. *Sensors*, 9(4):2719–2745.

# Appendices

# A  Simulation areas

This appendix provides an overview of the 16 simulation areas which are used in this study. For each simulation area the urban structural types are indicated (see section 3.1.3), the dominant material map as derived from the hyperspectral data (described in section 5.1 and 6.1) and the ENVI-met 3D input data (section 5.4 and 6.4). The location of the simulation area within the test area is indicated in figure A.2.



**Urban structural types**
- a1 Dense block development
- a2 Perimeter block development
- a3 Regular block development
- a4 Row house development
- a5 Detached- and semi-detached houses
- a6 High rise buildings
- a7 Small multi-storey buildings
- b1 Large multi-storey buildings
- b2 Large halls and storage buildings
- b3 Small halls and storage buildings
- c1 Parks and urban green
- c2 Sports fields

**Surface materials**
- Roofing tiles
- Roofing concrete
- Roofing metal
- Roofing bitumen / tar
- Roofing synthetic / glass
- Vegetated roof
- Roofing gravel
- Unknown
- Water
- Shadow
- Concrete
- Asphalt
- Tartan/ synthetic turf/polyethylene surfaces
- Partially sealed pavements
- Loose chippings
- Railway tracks
- Sand/soil
- Trees
- Lawn



Simulation area 1          100 m

3K aerial photograph       Dominant material       ENVI-met 3D input

Figure A.1: *Simulation areas*

161

**Simulation area 2**
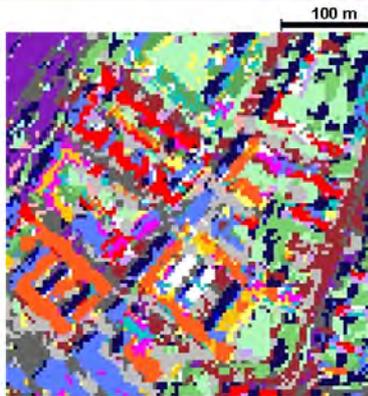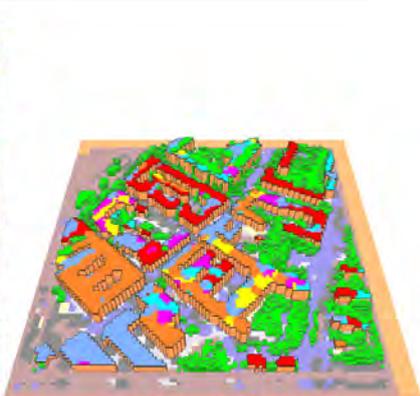


3K aerial photograph          Dominant material          ENVI-met 3D input

**Simulation area 3**
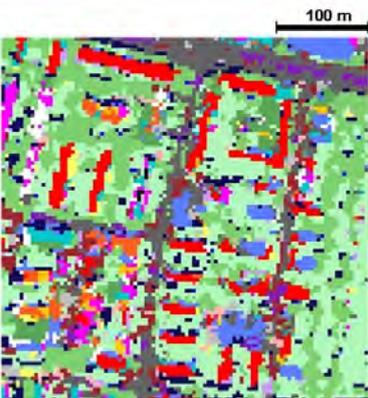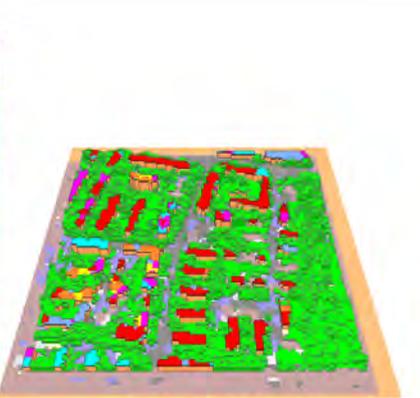


3K aerial photograph          Dominant material          ENVI-met 3D input

**Simulation area 4**
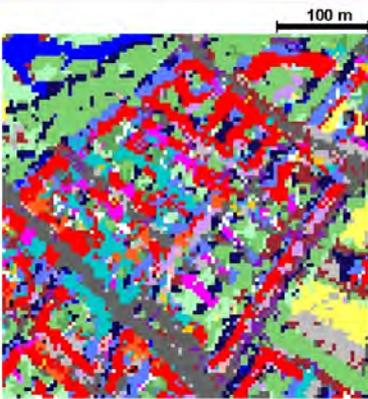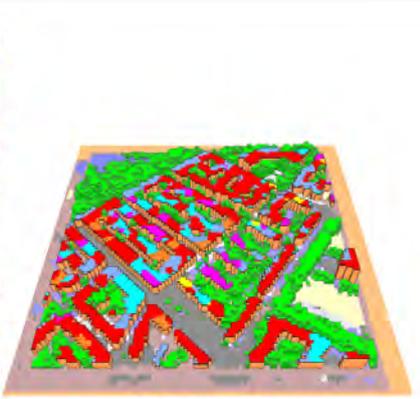


3K aerial photograph          Dominant material          ENVI-met 3D input

**Simulation area 5**



3K aerial photograph          Dominant material          ENVI-met 3D input
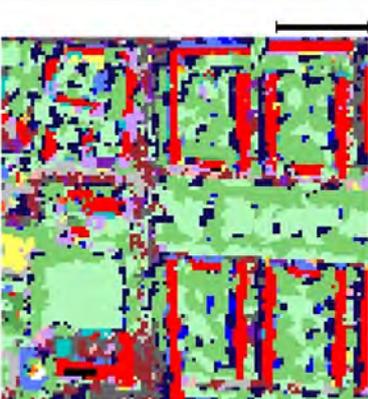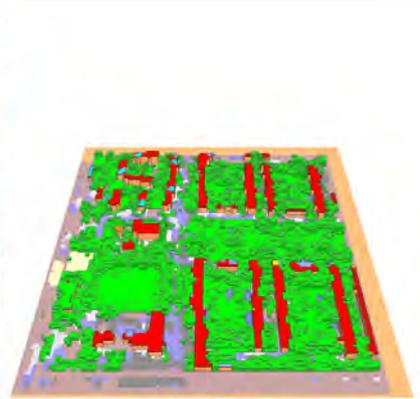
162

**Simulation area 6**

100 m
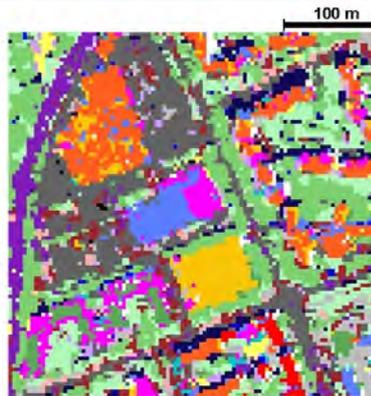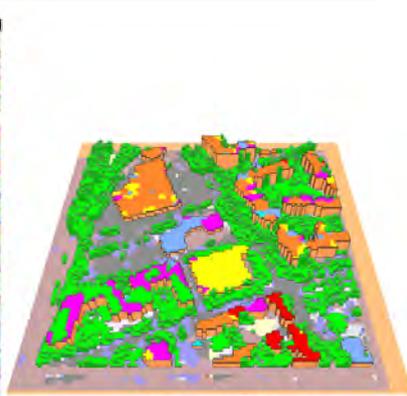
3K aerial photograph      Dominant material      ENVI-met 3D input

**Simulation area 7**

100 m
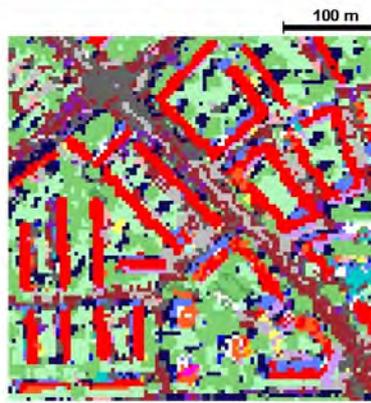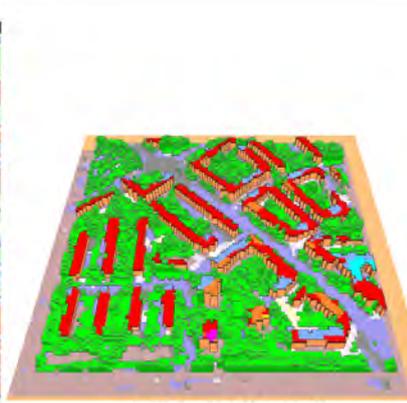
3K aerial photograph      Dominant material      ENVI-met 3D input

**Simulation area 8**

100 m
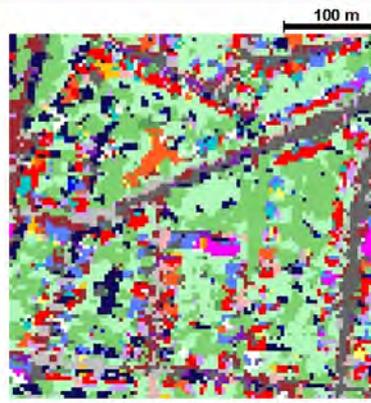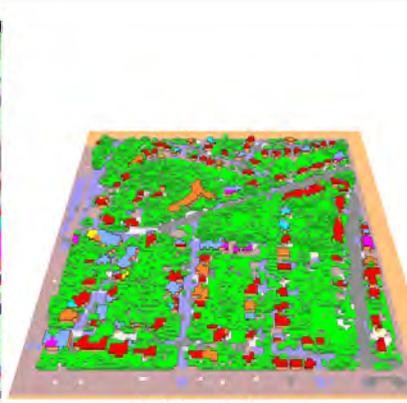
3K aerial photograph      Dominant material      ENVI-met 3D input

**Simulation area 9**

100 m

3K aerial photograph      Dominant material      ENVI-met 3D input
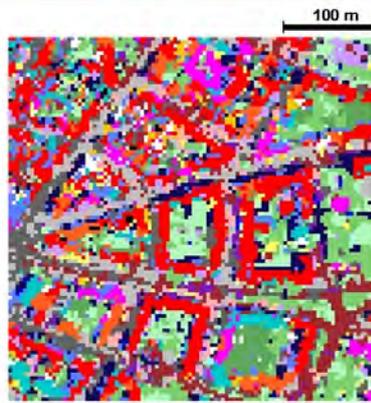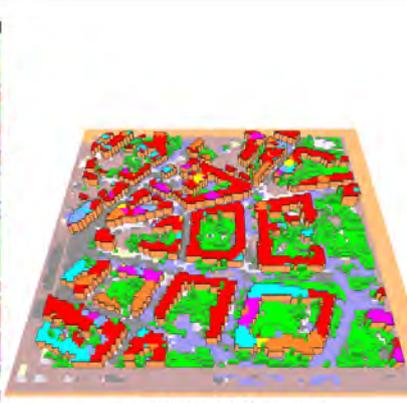
**Simulation area 10**

3K aerial photograph | Dominant material | ENVI-met 3D input
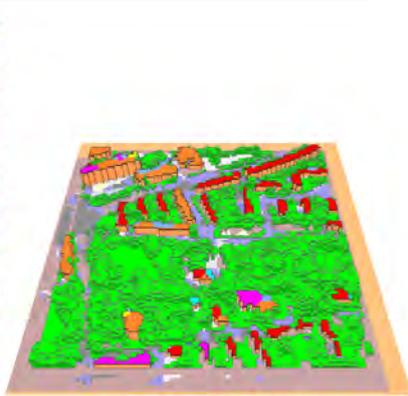
**Simulation area 11**

3K aerial photograph | Dominant material | ENVI-met 3D input
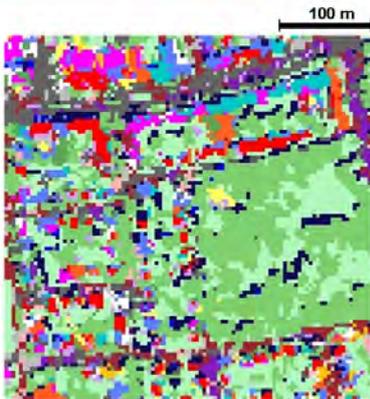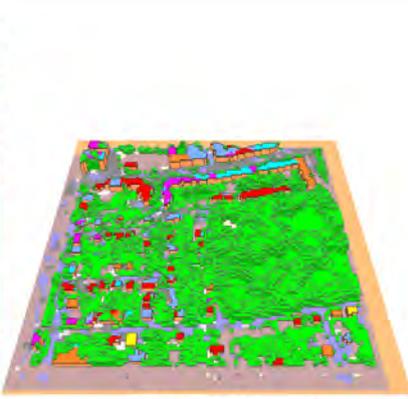
**Simulation area 12**

3K aerial photograph | Dominant material | ENVI-met 3D input
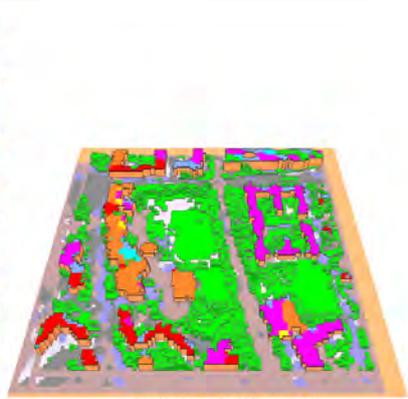
**Simulation area 13**
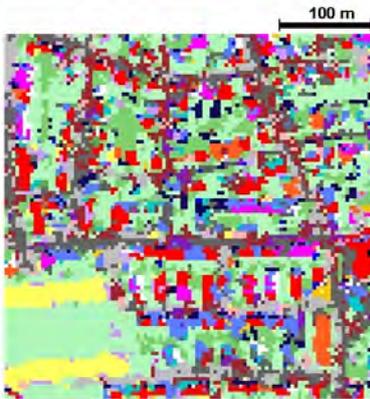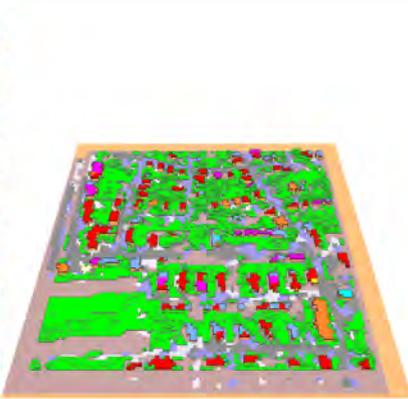
**Simulation area 14**

100 m

3K aerial photograph — Dominant material — ENVI-met 3D input
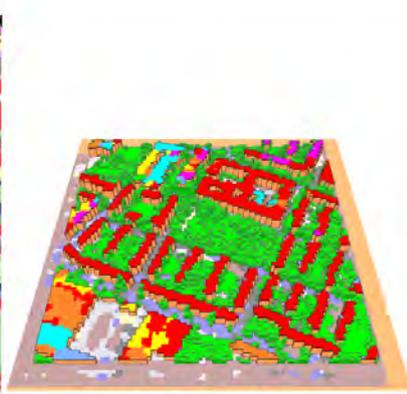
**Simulation area 15**

100 m

3K aerial photograph — Dominant material — ENVI-met 3D input
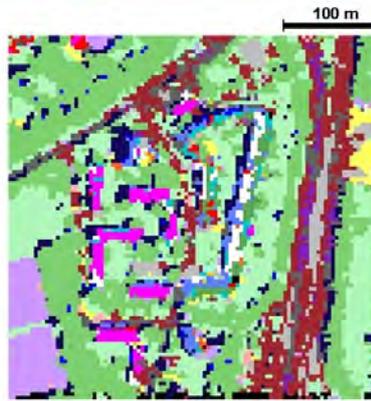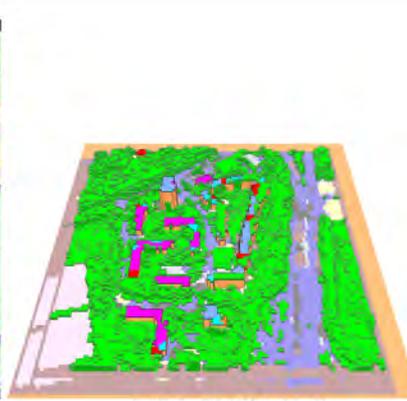
**Simulation area 16 - Theresienstraße**

100 m
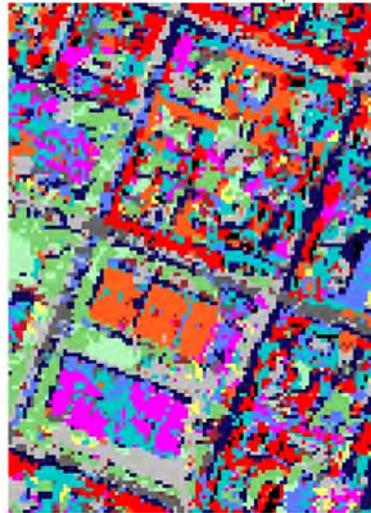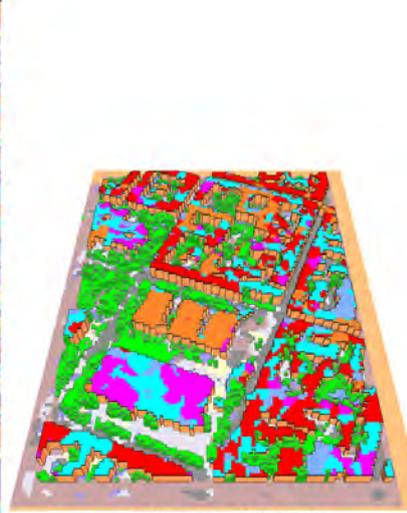
3K aerial photograph — Dominant material — ENVI-met 3D input

Figure A.2: *Location of the simulation areas within the test area in Munich*

# B Automatic generation of ENVI-met input data

In this appendix the detailed flow charts for the automatic generation of the ENVI-met input data are presented. The general approach is described in section 5.4.3.



Figure B.1: *Detailed flowchart for the identification of the surface cover type in preparation of the ENVI-met input data*
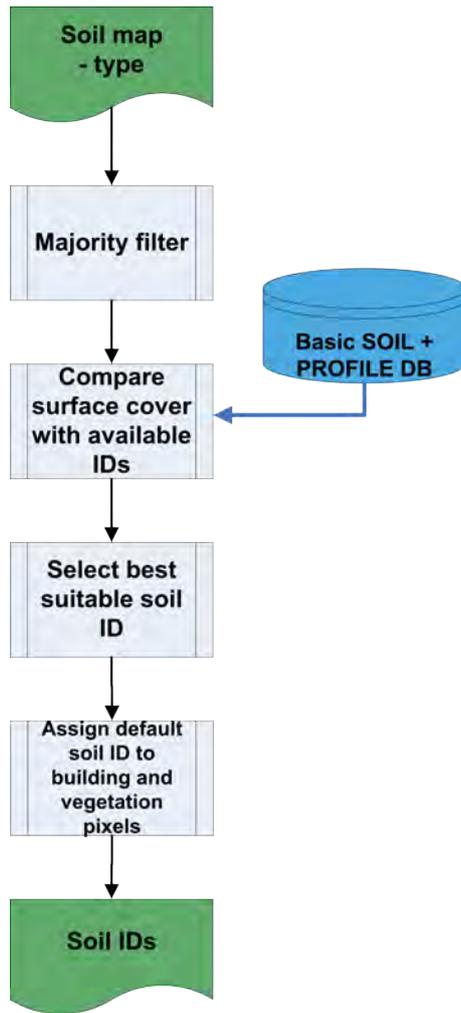
Figure B.2: *Detailed flowchart for the generation of the soil layer for ENVI-met*
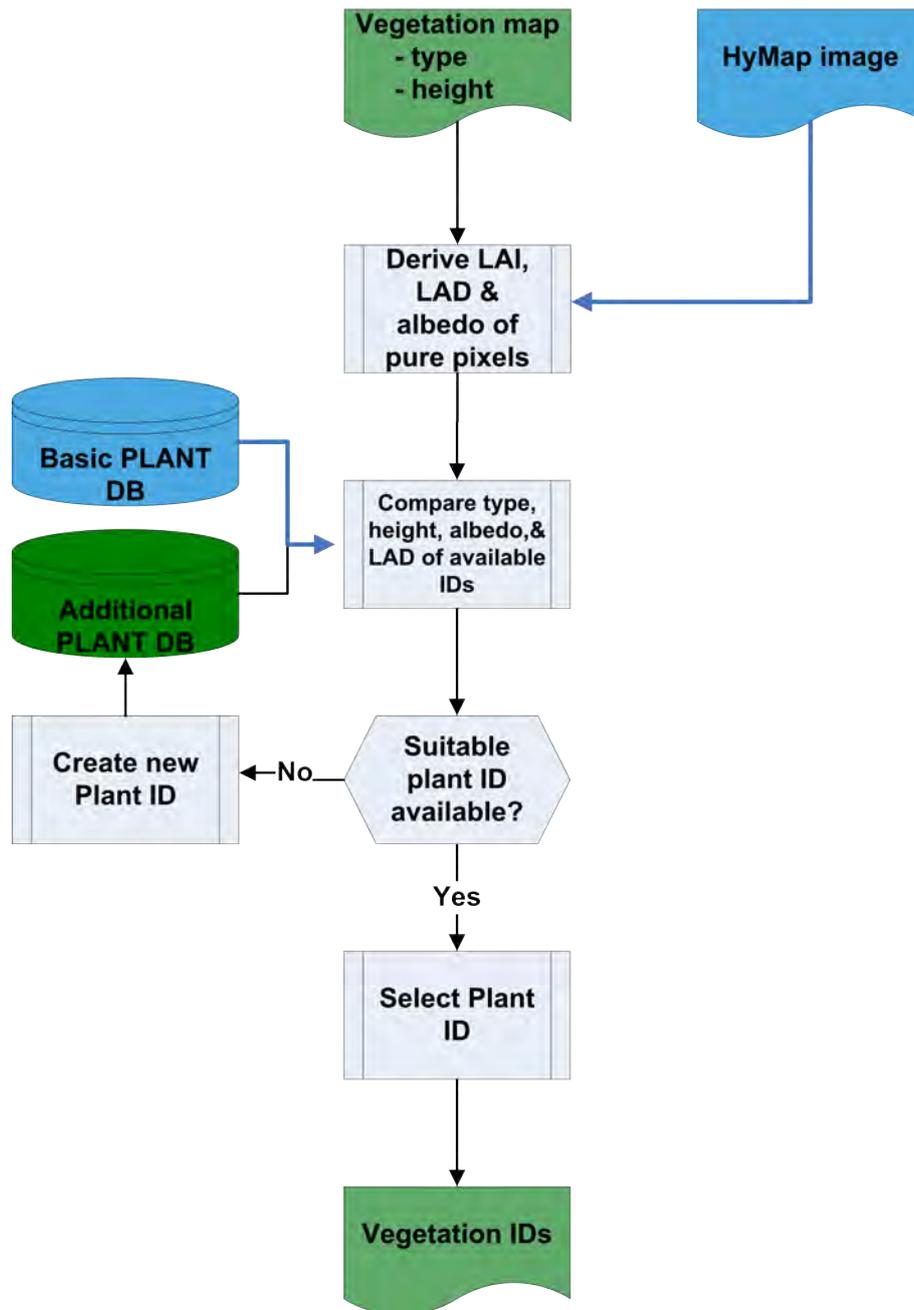
Figure B.3: *Detailed flowchart for the generation of the vegetation layer for ENVI-met*
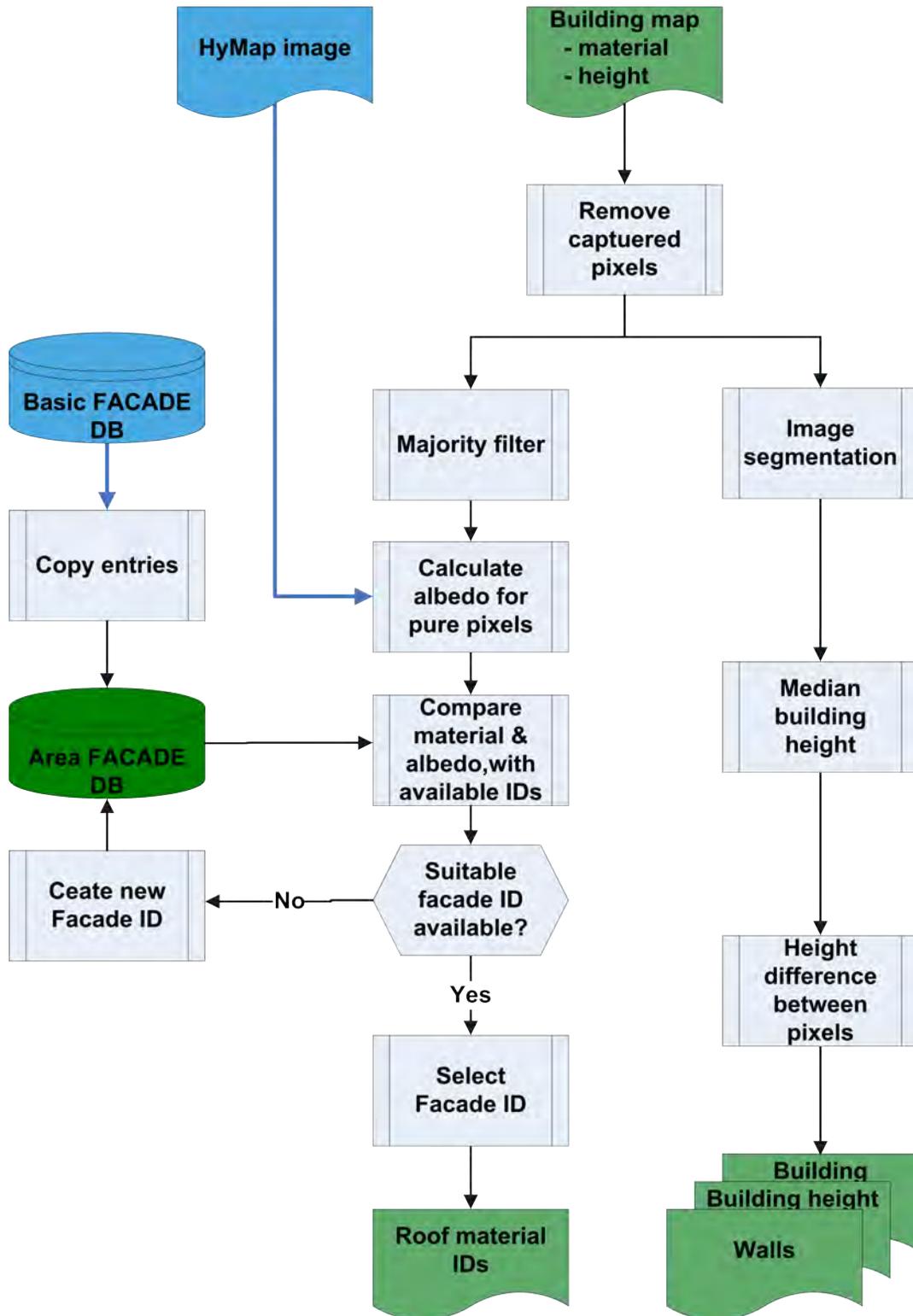
Figure B.4: *Detailed flowchart for the generation of the buildings layer for ENVI-met*

# C Basic data bases for the ENVI-met simulations

Table C.1: *Basic ENVI-met facade data base for roof and wall materials. Sources: ENVI-met; (Clarke, 2001; National Physics Laboratory, 2009) and HyMap data. This data base is expanded for each simulation area by different albedo values of the materials based on the HyMap data.*

| ID | Density [kg/m²] | Reflection [%] | Absorption [%] | Transmission [%] | Emissivity [%] | K-Value [W/(m*K)] | Specific heat capacity [J/(kg*K)] | Thickness [m] | Material Name |
|---|---|---|---|---|---|---|---|---|---|
| Tr | 1700 | 39 | 61 | 0 | 90 | 0.81 | 840 | 0.05 | red roofing tiles |
| Td | 1700 | 31 | 69 | 0 | 90 | 0.81 | 840 | 0.05 | dark roofing tiles |
| CT | 2100 | 24 | 76 | 0 | 90 | 1.1 | 840 | 0.05 | concrete tiles |
| Co | 2100 | 25 | 75 | 0 | 90 | 1.28 | 840 | 0.05 | concrete roofing (cast concrete) |
| Al | 2700 | 51 | 49 | 0 | 18 | 203 | 880 | 0.03 | Aluminium |
| Cu | 8600 | 18 | 82 | 0 | 20 | 384 | 390 | 0.03 | Copper |
| Zi | 7000 | 17 | 83 | 0 | 5 | 113 | 390 | 0.03 | Zinc |
| ST | 800 | 44 | 55 | 0 | 10 | 45 | 4800 | 0.02 | Steel |
| PV | 1200 | 20 | 80 | 0 | 90 | 0.19 | 1470 | 0.02 | PVC |
| PE | 930 | 28 | 72 | 0 | 90 | 0.4 | 1550 | 0.02 | Polyethylene |
| G4 | 2500 | 13 | 7 | 80 | 90 | 1.05 | 750 | 0.02 | clear float glass |
| Bi | 1000 | 9 | 91 | 0 | 91 | 0.17 | 1700 | 0.02 | Bitumen |
| Ta | 1000 | 7 | 93 | 0 | 91 | 0.17 | 1470 | 0.02 | Tar |
| Gr | 880 | 24 | 76 | 0 | 90 | 1.44 | 1680 | 0.05 | Roofing gravel |
| Bl | 1000 | 40 | 60 | 0 | 90 | 0.3 | 840 | 0.30 | Brick:aerated (DEFAULT FACADE) |

Table C.2: *Basic ENVI-met soil data base. Sources: ENVI-met; (Clarke, 2001; National Physics Laboratory, 2009).*

| ID | Sealed or pervious | Volumetric water content at saturation $[m^3/m^3]$ | Volumetric water content at field capacity | Volumetric water content at wilting point $[m^3/m^3]$ | Matrix potential at saturation [m] | Hydraulic conductivity at saturation $[m/s*10-6]$ | Volumetric heat capacity in $[Jm^3/K * 10^6]$ | Clapp & Hornberger constant | Heat Conductivity of the material $[W/m/K]$ | Name |
|---|---|---|---|---|---|---|---|---|---|---|
| 0 | pervious | 0.451 | 0.240 | 0.155 | -0.478 | 7.0 | 1.212 | 5.39 | 0.00 | Default soil (Loam) |
| zb | sealed | 0.000 | 0.000 | 0.000 | 0.000 | 0.0 | 2.083 | 0.00 | 1.63 | Cement Concrete |
| ak | sealed | 0.000 | 0.000 | 0.000 | 0.000 | 0.0 | 2.214 | 0.00 | 1.16 | Asphalt (with Gravel) |
| ta | sealed | 0.000 | 0.000 | 0.000 | 0.000 | 0.0 | 2.124 | 0.00 | 0.12 | Tartan (polyurethane) |
| st | sealed | 0.000 | 0.000 | 0.000 | 0.000 | 0.0 | 1.736 | 0.00 | 0.12 | Synthetic turf (polypropylene) |
| pe | sealed | 0.000 | 0.000 | 0.000 | 0.000 | 0.0 | 3.987 | 0.00 | 1.54 | Polyethylene |
| sp | sealed | 0.000 | 0.000 | 0.000 | 0.000 | 0.0 | 2.419 | 0.00 | 3.40 | Stone pavement (cobble stones) |
| cp | sealed | 0.000 | 0.000 | 0.000 | 0.000 | 0.0 | 1.764 | 0.00 | 1.10 | Concrete pavement |
| zz | sealed | 0.000 | 0.000 | 0.000 | 0.000 | 0.0 | 2.000 | 0.00 | 1.00 | Brick pavement |
| bc | sealed | 0.000 | 0.000 | 0.000 | 0.000 | 0.0 | 1.546 | 0.00 | 0.36 | Brick chippings |
| lc | sealed | 0.000 | 0.000 | 0.000 | 0.000 | 0.0 | 1.546 | 0.00 | 0.36 | Loose chippings/gravel |
| sd | pervious | 0.395 | 0.135 | 0.0068 | -0.121 | 176.0 | 1.463 | 4.05 | 0.00 | Sand |
| le | pervious | 0.451 | 0.240 | 0.155 | -0.478 | 7.0 | 1.212 | 5.39 | 0.00 | Default soil (Loam) |
| ww | water | 0.000 | 0.000 | 0.000 | 0.000 | 0.0 | 0.000 | 0.00 | 0.00 | Water |

Table C.3: *Basic ENVI-met soil profile data base. The IDs of the soil type at different depths refer to the soil types defined in table C.2. Sources: ENVI-met; (Clarke, 2001; National Physics Laboratory, 2009) and HyMap data.*

| ID | Soil type at depth | | | | | | | | | | | | | | Surface roughness length [m] | Albedo | Emissivity | Name |
|---|---|---|---|---|---|---|---|---|---|---|---|---|---|---|---|---|---|---|
| | 0.005 | 0.015 | 0.025 | 0.035 | 0.050 | 0.07 | 0.09 | 0.15 | 0.25 | 0.35 | 0.45 | 0.75 | 1.25 | 1.75 | | | | |
| s0 | le | le | le | le | le | le | le | le | le | le | le | le | le | le | 0.015 | 0.00 | 0.98 | Default Useald Soil |
| as | ak | ak | ak | ak | ak | ak | ak | ak | ak | le | le | le | le | le | 0.010 | 0.16 | 0.90 | Asphalt Road |
| co | zb | zb | zb | zb | sd | le | le | le | le | le | le | le | le | le | 0.010 | 0.22 | 0.90 | Pavement (Concrete) |
| so | le | le | le | le | le | le | le | le | le | le | le | le | le | le | 0.015 | 0.20 | 0.98 | Loamy Soil |
| sd | sd | sd | sd | sd | le | le | le | le | le | le | le | le | le | le | 0.050 | 0.38 | 0.90 | Sandy Soil |
| wa | ww | ww | ww | ww | ww | ww | ww | ww | ww | ww | ww | ww | ww | ww | 0.010 | 0.02 | 0.96 | Deep Water |
| tt | ta | ta | ta | le | le | le | le | le | le | le | le | le | le | le | 0.010 | 0.31 | 0.90 | Tartan (polyurethane) |
| ss | st | st | st | le | le | le | le | le | le | le | le | le | le | le | 0.010 | 0.13 | 0.90 | Synthetic turf (polypropylene) |
| pp | pe | pe | pe | le | le | le | le | le | le | le | le | le | le | le | 0.010 | 0.27 | 0.90 | Polyethylene |
| pa | sp | sp | sp | sp | sp | sp | sp | le | le | le | le | le | le | le | 0.010 | 0.20 | 0.90 | Stone pavement |
| cc | cp | cp | cp | cp | cp | cp | le | le | le | le | le | le | le | le | 0.010 | 0.22 | 0.90 | Concrete pavement |
| kk | zz | zz | zz | sd | le | le | le | le | le | le | le | le | le | le | 0.010 | 0.30 | 0.90 | Brick road (red) |
| bb | bc | bc | bc | bc | le | le | le | le | le | le | le | le | le | le | 0.010 | 0.31 | 0.90 | Brick chippings |
| ll | lc | lc | lc | lc | le | le | le | le | le | le | le | le | le | le | 0.010 | 0.29 | 0.90 | Loose chippings/gravel |

Table C.4: *Basic ENVI-met vegetation data base. LAD= Leaf ara density, RAD = root area density. Source: ENVI-met. This data base is expanded for each simulation area by different height, albedo and LAD values of the materials based on the HyMap and HRSC data.*

| ID | C3 or C4 type | Vegetation type | Min. stomata resistance | Albedo | Height [m] | Root zone depth [m] | | 1 | 2 | 3 | 4 | 5 | 6 | 7 | 8 | 9 | 10 | Name |
|---|---|---|---|---|---|---|---|---|---|---|---|---|---|---|---|---|---|---|
| xx | C3 | grass | 200 | 0.20 | 00.50 | 00.50 | LAD | 0.30 | 0.30 | 0.30 | 0.30 | 0.30 | 0.30 | 0.30 | 0.30 | .30 | 0.30 | Grass 50 cm aver. dense |
| | | | | | | | RAD | 0.10 | 0.10 | 0.10 | 0.10 | 0.10 | 0.10 | 0.10 | 0.10 | 0.10 | 0.10 | |
| so | C3 | grass | 70 | 0.20 | 00.63 | 1.200 | LAD | 1.58 | 0.82 | 0.38 | 0.29 | 0.27 | 0.29 | 0.33 | 0.40 | 0.52 | 0.74 | Soja 63cm |
| | | | | | | | RAD | 0.00 | 0.90 | 0.20 | 0.20 | 0.20 | 0.20 | 0.20 | 0.20 | 0.76 | 0.00 | |
| lg | C3 | grass | 200 | 0.20 | 00.18 | 03.00 | LAD | 0.30 | 0.60 | 0.90 | 1.20 | 1.50 | 1.80 | 2.00 | 1.50 | 1.00 | 0.70 | Luzerne 18cm |
| | | | | | | | RAD | 0.10 | 0.10 | 0.10 | 0.10 | 0.10 | 0.10 | 0.10 | 0.10 | 0.10 | 0.10 | |
| MO | C3 | dec. tree | 400 | 0.20 | 20.00 | 02.00 | LAD | 0.04 | 0.06 | 0.07 | 0.11 | 0.13 | 0.15 | 0.14 | 0.13 | 0.10 | 0.00 | Tree 20m aver. dense, no distinct crown layer |
| | | | | | | | RAD | 0.10 | 0.10 | 0.10 | 0.10 | 0.10 | 0.10 | 0.10 | 0.10 | 0.10 | 0.10 | |
| DO | C3 | dec. tree | 400 | 0.20 | 20.00 | 02.00 | LAD | 0.11 | 0.14 | 0.18 | 0.27 | 0.33 | 0.37 | 0.36 | 0.33 | 0.25 | 0.00 | Tree 20 m, dense, no distinct crown layer |
| | | | | | | | RAD | 0.10 | 0.10 | 0.10 | 0.10 | 0.10 | 0.10 | 0.10 | 0.10 | 0.10 | 0.10 | |
| DM | C3 | dec. tree | 400 | 0.20 | 20.00 | 02.00 | LAD | 0.08 | 0.08 | 0.08 | 0.08 | 0.25 | 1.15 | 1.06 | 1.05 | 0.92 | 0.00 | Tree 20 m dense, distinct crown layer |
| | | | | | | | RAD | 0.10 | 0.10 | 0.10 | 0.10 | 0.10 | 0.10 | 0.10 | 0.10 | 0.10 | 0.10 | |
| ds | C3 | dec. tree | 400 | 0.20 | 10.00 | 02.00 | LAD | 0.08 | 0.08 | 0.08 | 0.08 | 0.25 | 1.15 | 1.06 | 1.05 | 0.92 | 0.00 | Tree 10 m dense, distinct crown layer |
| | | | | | | | RAD | 0.10 | 0.10 | 0.10 | 0.10 | 0.10 | 0.10 | 0.10 | 0.10 | 0.10 | 0.10 | |
| sk | C3 | dec. tree | 400 | 0.20 | 15.00 | 02.00 | LAD | 0.15 | 0.15 | 0.15 | 0.15 | 0.65 | 2.15 | 2.18 | 2.05 | 1.72 | 0.00 | Tree 15 m very dense, distinct crown layer |
| | | | | | | | RAD | 0.10 | 0.10 | 0.10 | 0.10 | 0.10 | 0.10 | 0.10 | 0.10 | 0.10 | 0.10 | |
| T1 | C3 | dec. tree | 400 | 0.20 | 10.00 | 02.00 | LAD | 0.00 | 0.00 | 2.18 | 2.18 | 2.18 | 2.18 | 2.18 | 2.18 | 1.72 | 0.00 | Tree 10 m very dense, leaf-less base |
| | | | | | | | RAD | 0.10 | 0.10 | 0.10 | 0.10 | 0.10 | 0.10 | 0.10 | 0.10 | 0.10 | 0.10 | |
| ll | C3 | 01 | 400 | 0.20 | 15.00 | 02.00 | LAD | 0.04 | 0.06 | 0.07 | 0.11 | 0.13 | 0.15 | 0.14 | 0.13 | 0.10 | 0.00 | Tree, light 15 m |
| | | | | | | | RAD | 0.10 | 0.10 | 0.10 | 0.10 | 0.10 | 0.10 | 0.10 | 0.10 | 0.10 | 0.10 | |
| he | C3 | 01 | 400 | 0.20 | 02.00 | 01.00 | LAD | 2.00 | 2.00 | 2.00 | 2.00 | 2.00 | 2.00 | 2.00 | 2.00 | 2.00 | 2.00 | Hedge dense, 2m |
| | | | | | | | RAD | 0.10 | 0.10 | 0.10 | 0.10 | 0.10 | 0.10 | 0.10 | 0.10 | 0.10 | 0.10 | |

# Eidesstattliche Erklärung

Hiermit erkläre ich, dass die von mir eingereichte Dissertation zum Thema *'Use of airborne hyperspectral data and height information to support urban micro climate characterisation'* selbständig und nur unter Benutzung der in der Arbeit angegebenen Literatur und sonstigen Quellen angefertigt wurde. Wörtlich und sinngemäß übernommenes Gedankengut habe ich als solches kenntlich gemacht.

_____

Würzburg, den

# Curriculum Vitae

*Personal information*

| | |
|---|---|
| First name | Wieke |
| Family name | Heldens |
| Home address | Schmaedelstrasse 22 |
| | 81245 Munich, Germany |
| Date of Birth | September 9, 1983 |
| Place of Birth | Alphen aan den Rijn, The Netherlands |
| Nationality | Dutch |
| Marital status | single |

*Education and Trainings*

| | |
|---|---|
| Since 2006 | **Ph.D Student** within the REFINA project at the Department of Remote Sensing, Geographical Institute of the Julius-Maximilians-University, Wurzburg, Germany. Place of work: German Aerospace Centre (DLR), Oberpfaffenhofen, Germany. |
| 2006 | **Internship** at the German Aerospace Center (DLR), German Remote Sensing Data Center (DFD), Imaging Spectroscopy working group. |
| 2004 – 2006 | **Master of Science in Geo-information Science**, University of Wageningen, the Netherlands. Specialisation: GIS and remote sensing, spatial modellling. *Graduation November 2006.* |
| 2001 – 2004 | **Bachelor of Science in Landscape, Planning and Design**, University of Wageningen, the Netherlands. Specialisation: Spatial planning. *Graduation November 2004.* |
| 1995 – 2001 | **Pre-university eduction (VWO)**, Bonhoeffer College, Castricum, the Netherlands *Graduation July 2001.* |

*Publications*

Esch, T., Taubenböck, H., Heldens, W., Thiel, M., Wurm, M., Klein, D., Dech, S., Roth, A., Schmidt, M. (2009): Monitoring and assessment of urban environments using space-borne earth observation data – selected applications. In: Krek, Rumor, Zlatanova & Fendel (Eds), *Urban and Regional Data Management*, Taylor & Francis Group, London, ISBN 978-0-415-55642-2. pp. 385-398.

Heldens, W., Esch, T., Heiden, U., Dech, S. (2008): Potential of hyperspectral remote sensing for characterization of urban structure in Munich. In: Carsten Jürgens (Ed.), *Remote Sensing - New Challenges of High Resolution. Proceedings of the EARSeL Joint Workshop* Bochum, Germany, CD-ROM. pp 94-103.

Heldens, W., T. Esch, U. Heiden, A. Müller, S. Dech (2009). Exploring the demands on hyperspectral data products for urban planning: a case study in the Munich region. In: Eyal Ben Dor (Ed.), *Proceedings of the 6th EARSeL Workshop on Imaging Spectroscopy*, Tel-Aviv, Israel.

Heldens, W. (2006): *Spatio-temporal modelling of land cover using Markov theory.* MSc thesis. Wageningen University, Laboratory of Geo-Information Science and Remote Sensing

Heldens, W., Fischer, C. (2009): Development of a field guide for mineral detection using a portable spectrometer in the TIR domain. In: Eyal Ben Dor (Ed.), *Proceedings of the 6th EARSeL Workshop on Imaging Spectroscopy*, Tel-Aviv, Israel.

Heldens, W., U. Heiden, M. Bachmann, T. Esch, A. Müller, S. Dech (2009). Scaling issues in validation of abundance maps derived from HyMAP data of an urban area. In: Eyal Ben Dor (Ed.), *Proceedings of the 6th EARSeL Workshop on Imaging Spectroscopy*, Tel-Aviv, Israel.

Olesiuk, D., Bachmann, M., Habermeyer, M., Heldens, W., Zagajewski, B. (2009): Crop classification with neural networks using airborne hyperspectral imagery. In: *Annals of Geomatics Annals of Geomatics*, VII (2(32)). Polish Association for Spatial Information, pp. 107-112. ISSN 1731-5522

Stein, E., Bachmann, M., Heldens, W., Müller, A., Schmullius, C. (2009): A spectral feature based classification algorithm for characterization of urban surfaces in Munich. In: Eyal Ben Dor (Ed.), *Proceedings of the 6th EARSeL Workshop on Imaging Spectroscopy*, Tel-Aviv, Israel.